Carbon Nanotubes in Organic Solar Cells

The Faculty of Engineering of the University of Duisburg-Essen

for award of the academic degree of
Doctor Engineer

Thesis submitted
by
Dipl.-Ing. Gerhard Lackner
from Mannheim

Fakultät Ingenieurwissenschaften
Universität Duisburg-Essen

Date of submission:
13.12.2012

Vorsitzender:	Prof. Dr.-Ing. Renatus Widmann
Gutachter:	Prof. Dr. rer. nat. habil. Doru C. Lupascu
	Prof. Dr. rer. nat. habil. Martin Mkandawire

Der Lebenslauf ist in der Online-Version aus Gründen des Datenschutzes nicht enthalten.

The online version of this thesis does not contain a CV due to data privacy protection.

Acknowledgements

I would like to give a special word of thanks to Prof. Doru C. Lupascu for the wonderful guidance during my doctoral study. I am also very grateful to Prof. Martin Mkandawire, Dr. Vladimir Shvartsmann, and Dr. Richard Boucher. I would like to thank all colleagues of our workgroup UDEMat for their helpful cooperation and fruitful discussions.

I wish to say a special word of thanks to Prof. Karl Leo, Dr. Moritz Riede for the collaboration at the Institute for Applied Photo Physics (IAPP) at Technische Universität Dresden and to Dr. Jan Meiss, who initiated this cooperation, which was crucial to finish this PhD. All evaporated organic layers including the evaporated electrodes, which are mentioned in Chapter 4 and Chapter 6, were fabricated at this institute.

I thank Prof. Alexander Michaelis for his support and the collaboration with his Fraunhofer Institute for Ceramic Technologies and Systems, which made this thesis possible to be realized at all. During this time I was friendly guided by Dr. Tobias Mayer-Uhma and Dr. Ingolf Endler, which resulted in good scientific achievements and also in wonderful memories of that time.

I thank Dr. Matthias Albert from the Institute for Semiconductors and Microsystems of the Technische Universität Dresden for support and access to his laboratories, which was essential for this thesis.

I have to thank Dr. Horst Borrmann from the Max Planck Institute Chemical Physics of Solids for his ideas and support correlated with the carbonylation mentioned in Chapter 7.

I thank Prof. Giovanni Cuniberti from the Technische Universität Dresden. The time at his workgroup Environmental Nanotechnology was inspiring, motivating and full of fruitful discussions also resulting in new friendships and I would like to thank Dr. Annegret Benke, Dr. Viktor Bezugly, Dr. Stanislav Avdoshenko, and Dr. Anindya Majumder. I thank Ortrud Trommer and Axel Mensch for their electron microscopy analysis, Dr. Nora Haufe for the transmission electron microscopy (TEM) analysis, Dr. Michael Thieme and Dr. Christa Blank for kind support and all members of the chair of Functional Materials, of whom I learned much about science and life.

I would like to thank all group members of the collaborating institutes for fruitful discussions and their technicians for support. I am looking forward to publish the scientific results of this collaboration together with all involved persons of the different collaborating institutes and based upon the understanding, mutual confidence, and respect for each other I am glad to perpetuate this scientific collaboration in conjointly implemented projects.

Also, I thank my family who has always supported me, especially my mom Maria Lackner, my sister Michaela Krebs and my "big" brother Andreas Lackner. And thank you for your patience flower.

"Wie mühsam und schwierig diese Umwandlung auch sein mag, welche Hürden und Hindernisse sich ihrer Vollendung auch in den Weg stellen mögen, so verläuft sie doch nicht gegen die Naturgesetze." - Paracelsus

Declaration

Herein, I do declare that this thesis is a product of my own original work without any help from a third party or other aids apart from those the listed. Thoughts, ideas and information taken or used from others or previously published ideas have been correctly cited and acknowledged in the references. Further, all persons who helped me with the sorting and interpretation of material used in this thesis have been clearly acknowledged. Otherwise, no further people were involved in this work. In particular, I neither obtain the help of a Ph.D. consultant nor pay a third party for any work related to the content of this thesis.
This work has never been presented to an Examining Authority in this or any similar form for an award of academic qualification, and it has not been published in this or any similar form anywhere else.
I never presented any other thesis of mine to an Examining Authority in this or any similar form for an award of the academic degree of Doctors Engineer.
I confirm that I accept the doctoral guidelines of the Faculty of Engineering of the University of Duisburg-Essen.

Essen, den 13.12.2012

Gerhard Lackner

ABSTRACT

Organic solar cells have been lately attracting much attention due to Tang's technological breakthrough in organic solar cell construction [1]. In such devices efficiencies of over 8% have been achieved nowadays [2]. Due to such promising efficiencies, organic solar cells are being considered as a potential low-cost alternative to standard inorganic cells. It is expected that with the development of large-scale production methods the production cost benchmark of 1 € per Watt peak will be undercut. In addition, their competitiveness in the solar cell market is strongly enhanced by the use of flexible substrates, which offers a wide range of possible novel applications.
Such substrates can be coated with carbon nanotube (CNT), which are being advocated as materials for interdigitated heterojunctions structure that would make organic solar cells to have high-performance. In view of this, this thesis reports a study that investigated the electrical roles of carbon nanotubes (CNTs) in organic solar cells in a novel inverted interdigitated structure using vertically aligned carbon nanotubes. The basis for use of CNT lies in the basic principle of energy conversion in solar cell devices, which involves the separation of photogenerated charges at an interface between electron donor and acceptor materials. In most cases, this imposes some constraints on the photoactive layer of the cells. Thus, to improve the active layer morphology and cell efficiency, anisotropic nanoparticles, the CNT can be incorporated to facilitate charge transport to the electrodes.
First prototypes of organic solar cells with this inverted interdigitated structure using a vertically aligned carbon nanotube (va-CNT) array have been produced. These devices give the proof of the working principle of this solar cell structure. Other solar cell structures including a blend of donor-acceptor materials and randomly dispersed CNTs have been studied as well. Their performances were characterized and an increase of photocurrent was observed for these devices compared to devices without CNTs.
This thesis is divided into 4 parts: firstly the chapters Introduction and Fundamentals deal with the fundamental functioning and characteristics of organic solar cells and the used materials, as well as the correlation between irradiation, internal charge transfer mechanisms and resulting efficiency. Secondly, the chapters Materials, Solution processed organic solar cells, and Carbon nanotube processing deal with the technological implementation of the pursued cell architectures including all steps of manufacturing. In the third part, the chapters Carbon nanotube solar cells and Vertically aligned carbon

nanotube solar cells deal with the quality and properties of the produced dispersions, layers, semi-finished products and devices in detail. Finally, in the chapter Conclusions the results are discussed, conclusions drawn and an outlook given.

CONTENTS

GLOSSARY

AFM	atomic force microscopy
Al	aluminium
Alq3	Aluminium-tris(8-hydroxychinolin)
AM1.5	air mass 1.5
ATFL	above trap-filled limit
BHJ-SC	bulk-heterojunction solar cell
BHJ	bulk-heterojunction
BPhen	4,7-Diphenyl-1,10-phenanthroline
CA	contact angle
CMC	critical micelle concentration
CNT	carbon nanotube
CNTs	carbon nanotubes
CT	charge transfer
CTAB	cetyl trimethylammonium bromide
CuPc-DMA	Copper(II) 3,10,17,24-tetra-tert-butyl-1,8,15,22-tetrakis (dimethylamino)-29H,31H-phthalocyanine
CuPc-TS	Copper phthalocyanine-3,4',4",4"'-tetrasulfonic acid tetrasodium salt
CuPc	copper(II) phthalocyanine
CV	cyclovoltametry
CVD	chemical vapour deposition
DFT	density functional theory
DMF	dimethylformamide
DOS	density of states
DSSC	dye-sensitized solar cell
EDS	energy dispersive spectroscopy
EDTA	ethylenediaminetetraacetic acid
ESEM	environmental scanning electron microscopy
FE-SEM	field emission scanning electron microscopy
FF	fill factor
FIB	focused ion beam
FT-IR	fourier transform infrared
H_2O_2	hydrogen peroxide
H_2SO_4	sulfuric acid
HCl	hydrochloric acid
HJ	heterojunction
HNO_3	nitric acid
HOMO	highest occupied molecular orbital
HOMO	highest occupied molecule orbital
IKTS	Fraunhofer Institute for Ceramic Systems and Technology
IPCE	incident photon to current conversion efficiency
IPES	inverse photoemission spectroscopy
ITO	indium tin oxide
J-V	current density-voltage
LCAO	linear combination of atomic orbitals
LEDs	light emitting diodes
LiF	Lithium fluoride
LUMO	lowest unoccupied molecule orbital
MIM	metal-insulator-metal
MO	molecular orbital
MPP	maximum power point
MWCNT	multi-walled carbon nanotube

1. INTRODUCTION

1.1 Background

Since the beginning of modern civilization, the mankind has been consuming more and more energy as it tries to improve the quality of life. In recent years, people's attitude towards the environment and conservation has changed. Motivated by this social movement, the German government has defined its policy on energy by the "Energieplan 2050" [3]. This master plan is based upon the improvement of nine areas, namely: investment in renewables, general energy efficiency, nuclear power and fossil fuel, grid infrastructure improvement, energy efficient construction, mobility via electric energy, innovation and technology, international energy supply, as well as acceptance and transparency. Currently, the main used energy resources have a finite lifetime (uranium, fossils and coal), which need to be replaced by renewable sources. Although renewable energy resources cannot compete at the moment with the traditional energy resources in the market because the former still have low efficiency and their production costs are very high [4]. Nevertheless, the situation is changing due to constantly rising fuel costs and demand for the conventional energy resources (see Figures 1.1 and 1.2), on one hand, while on the other hand technology involving renewable resources is rapidly improving. Some authors have predicted that the costs will be

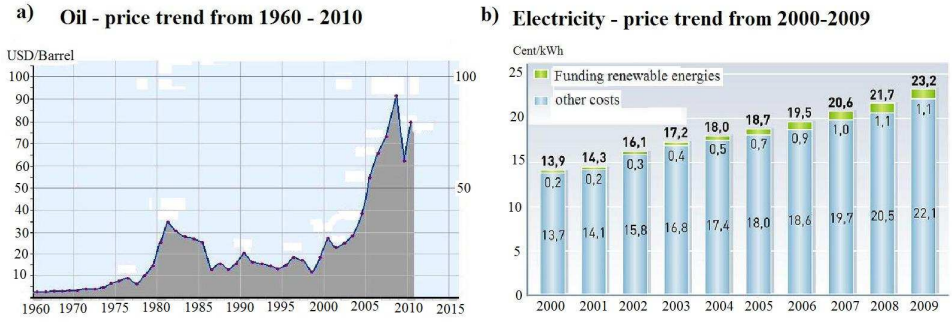

Fig. 1.1: Development of oil price and electricity. Oil price increased significantly. Influence of renewable energy to electricity costs is less. Graphs taken from [5] and [6].

equal within the next two decades, which would allow the renewable energy resources to be competitive in the market (see Table 1.1) [8]. However, there

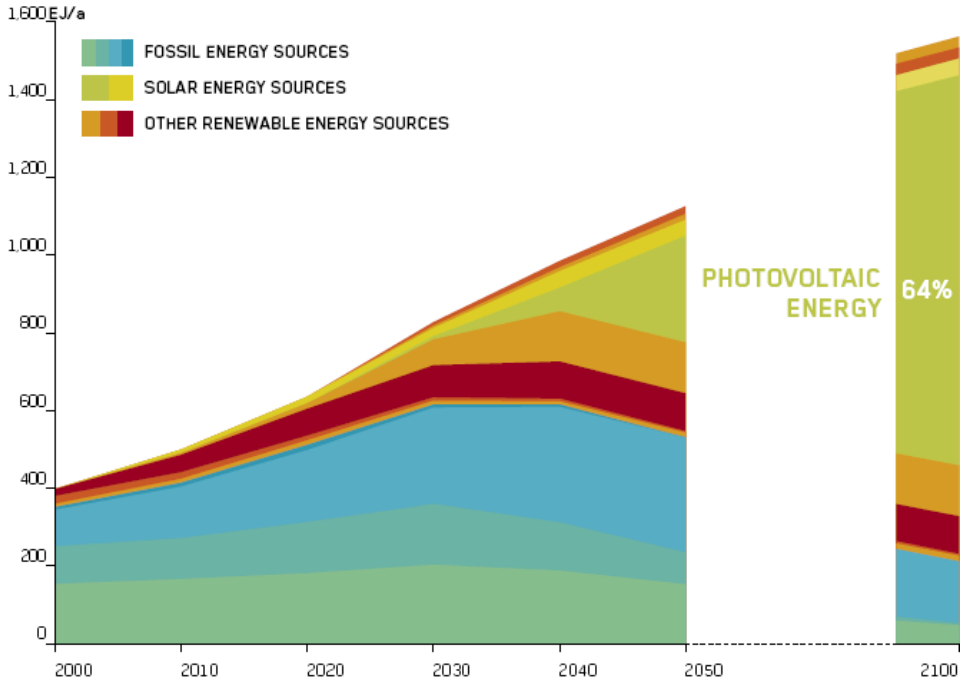

Fig. 1.2: Consumption trend of energy resources in eta joule per year. Image taken from [7].

is still the need to improve the efficiencies of the different renewable energy sources. For instance, if alternative technologies like roll-to-roll production can be applied in the fabrication process of working solar cell devices with reasonable efficiencies a technological breakthrough will be achieved [9]. In order to improve cell efficiency and performance further new materials have to be found and combined in new ways.

1.2 Motivation

Most of the current energy source on earth are limited, whereas sunlight will shine for the next billion years. The energy resources on earth (including sunlight) are visualized in Figure 1.3. It clearly shows that the conversion of sunlight into electric power makes sense because sunlight is the most abundant but least tapped energy by human beings. Thus, it can easily be one of the main basic electrical energy resources in the future [10]. However, the currently used solar energy convertors based on inorganic materials - conventional silicon solar cells - are expensive and not available to use under all conditions. Thus, organic solar cells have more potential compared to conventional silicon solar cells. Their flexibility facilitates low-cost roll-to-roll fabrication and opens new market directions such as the application of organic photovoltaics (OPV) in textiles. However, organic solar cells still

Energy source	Power generation technology	Production Cost Of Energy in US$			Fuel price sensitivity
Natural gas	Gas Turbine	50-60	65-75	70-80	Very high
Oil	Combustion Diesel Engine	100-125	140-165	140-160	Very high
Coal	Pulverised Coal Combustion	40-50	65-80	65-80	Medium
Nuclear	Nuclear Fission	50-85	45-80	45-80	Low
Biomass	Solid Biomass	80-195	85-200	85-205	Medium
	Biogas	55-215	50-200	50-190	Medium
Wind	On-shore	75-110	55-90	50-85	nil
	Off-shore	85-140	65-115	50-95	nil
Hydro	Small	60-185	55-160	50-145	nil
	Large	35-145	30-140	30-130	nil
Solar	Photovoltaic	520-880	270-460	170-300	nil
	Concentrating Solar Power	170-250	110-160	100-140	Low

Tab. 1.1: Prediction of energy costs. Data taken from [8].

lag behind the conventional silicon solar cells in terms of efficiently. It is in view of this, that the work reported in this thesis was motivated. Hence, a possible route for the improvement of organic solar cell devices, in this case, the exceptional properties of CNTs are used to enhance the poor charge carrier transport in the organic layers. The motivation for this work can be summed up as:

1. Energy demand
2. Sun energy untapped
3. Direct energy conversion of sunlight to electrical energy via photovoltaic
4. Improved charge carrier mobility in the organic matrix

The main energy source for the photovoltaic process is the sun. It converts every day $657 \cdot 10^6 t$ of hydrogen by the process of fusion into $653 \cdot 10^6 t$ of helium. This means, that $m = 4 \cdot 10^6 t$ are converted to photonic energy. The total amount of energy generated by the sun per day can be calculated as follows

$$e = m \cdot c^2 = 4 \cdot 10^9 kg \cdot \left(299792458 \frac{m}{s}\right)^2 \approx 3,6 \cdot 10^6 TW, \qquad (1.1)$$

where c is the speed of light. The temperature in the sun, T_i is around $T_i \approx (8 - 40) \cdot 10^6 K$ and at the surface $T_{surf} \approx 6000K$. Figure 1.4 gives

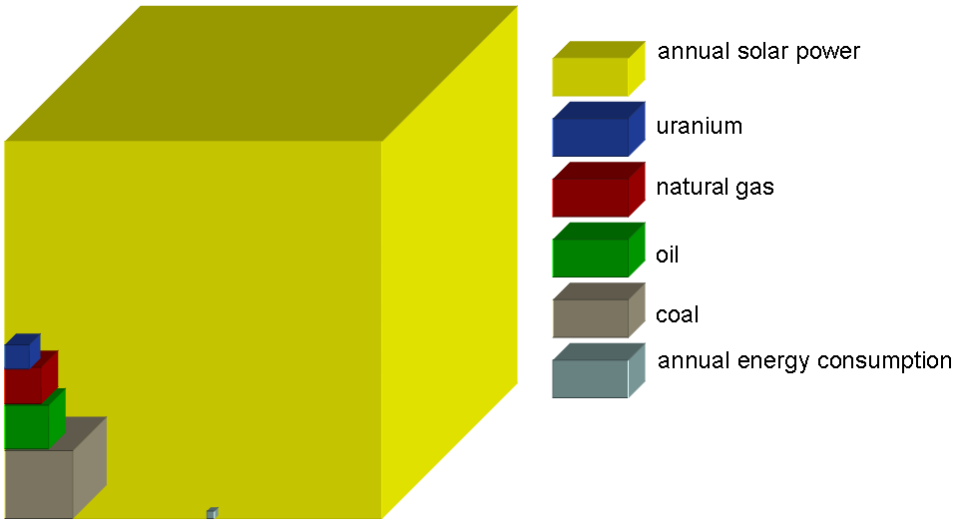

Fig. 1.3: Visualization of energy resources. Image based upon [10].

an impression of the sun's activity. In comparison to the conventional inorganic solar cells the organic solar cells have one major advantage, they can be deposited on flexible substrates. This feature enables new and cheap fabrication process as well as new application fields. For example, jackets and tents could perform their normal task of weather protection and simultaneously be an energy supply (preferably for recharging than as a generator). The demand for such materials and their portable energy supply is expected to increase as people acquire more and more mobile gadgets, which consume electrical energy, such as mobile phones, mp3 players, notebooks etc. The market for such textiles is found in the field of outdoor pursuits (civil sector) with an expected sales volume in 2-3-digit million € range [12].
In the past, several approaches have been investigated in order to enhance device properties and cell life-time. The recently achieved state of the art is given in Figure 1.5. Currently, conventional solar cells are fabricated by using inorganic materials like silicon or Cu(In,Ga)Se_2 (CIGS). No inorganic solar cell can be fabricated on flexible substrates like organic solar cells. Moreover, organic solar cells work with higher efficiency with diffuse light and for higher temperatures than inorganic ones [13]. This yield higher average daily electrical energy output, which make organic solar cells more profitable. However, organic solar cells are in the process of being introduced into the market. The first photo effect in an organic crystal was found in 1906 by Pochettino [14] in anthracene. Anthracene has since then become the most investigated organic molecular material. Modern organic solar cells use fullerenes and their derivatives with a dye serving as the active layer in which radiation is transformed into electric current. Different architectural approaches have been investigated and are introduced in the

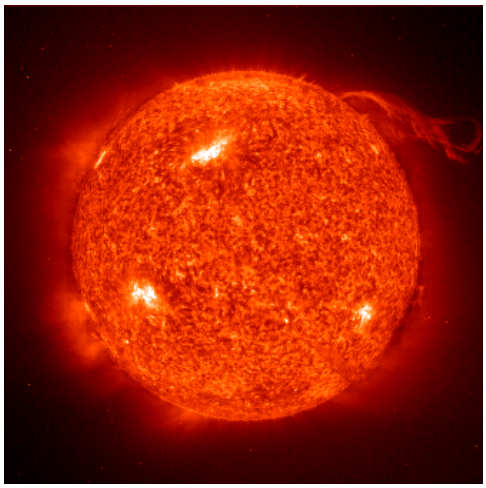

Fig. 1.4: H-alpha image of the sun. Image taken from [11].

following subsection.

1.2.1 Overview of organic solar cell architectures

In order to improve the device efficiency the material combination, layer thicknesses, minimization of surface dipole formation and the architecture itself have attracted much attention [15]. The latter route was considered in order to increase the efficiency of the dissociation process. Motivated to enable exciton dissociation within the whole active matrix a new structure was innovated: the bulk heterojunction [16]. However, the charge carrier mobility is relatively low for organic materials [17]. An ordered bulk heterojunction concept is supposed to solve this problem. Ideally, the ordered structure is built with excellent conductive materials. The studied ordered structure in this thesis is a va-CNT array (see Figure 1.9) synthesized on a conductive substrate. Figure 1.6 gives an overview of the different device types of organic solar cells.

Mono junction (Schottky) solar cell

In this architecture, the exciton dissociation takes place at the metal-organic interface. It was first investigated by [19] in 1979. This architecture is the simplest design with efficiencies around η=0,1%. The organic-metal contact is the active interface where the exciton dissociation occurs. However, exciton quenching also takes place at the metal contact. In order to achieve further improvements the exciton dissociation has to be improved. This was achieved by using a better combination of materials.

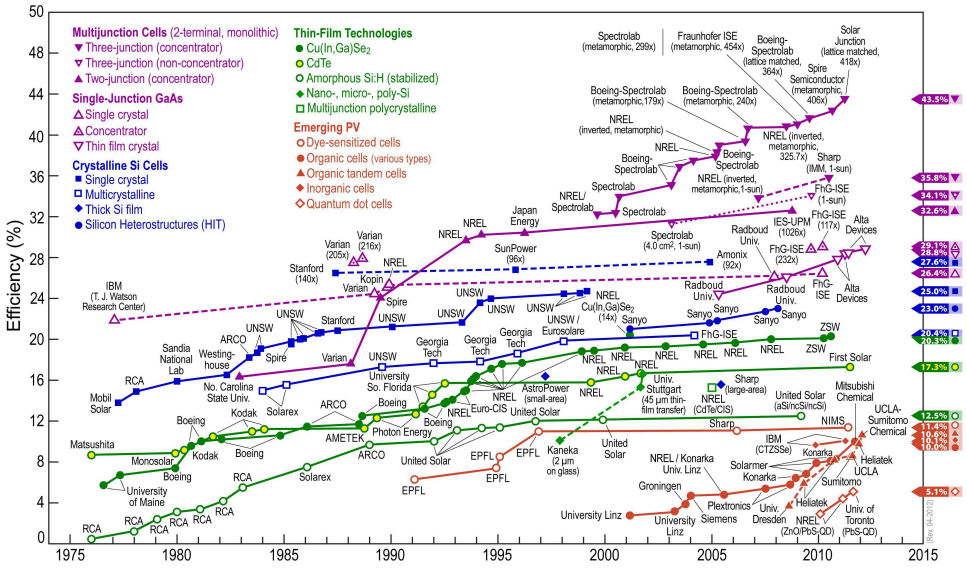

Fig. 1.5: State of the art in photovoltaic research. Image taken from [2].

Bi-layer or heterojunction solar cell

This design consists of two different types of organic materials, a donor and an acceptor. It was first introduced by [1] in 1986. The band shift in such a device occurs at the donor-acceptor interface. If the molecular orbital energies are matched appropriately, the electrochemical potential difference at the interface is responsible for an ultra-fast charge separation process. This was described for the first time in 1994 by [20]. Additionally, the inner electric field superposition at the interface enhances the charge separation there, making the dissociation almost perfect. The efficiency is, however, still limited by the factors of light penetration depth (50nm-200nm) and exciton diffusion length (up to 10nm) [21]. Therefore, the distance between the donor and acceptor should be decreased, in order to decrease exciton recombination, which results in an increase of the incident photon to current conversion efficiency.

Organic p-i-n solar cells

This architecture suppresses exciton quenching in the intrinsic active layer with the help of two doped layers. The intrinsic layer is sandwiched between a p-doped layer on the cathode side and a n-doped layer on the anode side. These doped layers built up an electric field. This field suppresses exciton quenching. In inorganic solar cells minority charge carrier recombination at the outer electrodes are suppressed in the same way with the help of a back-surface-field. A further advantage of such an architecture is the possibility that it can be optical optimised so that the light intensity maximum can be

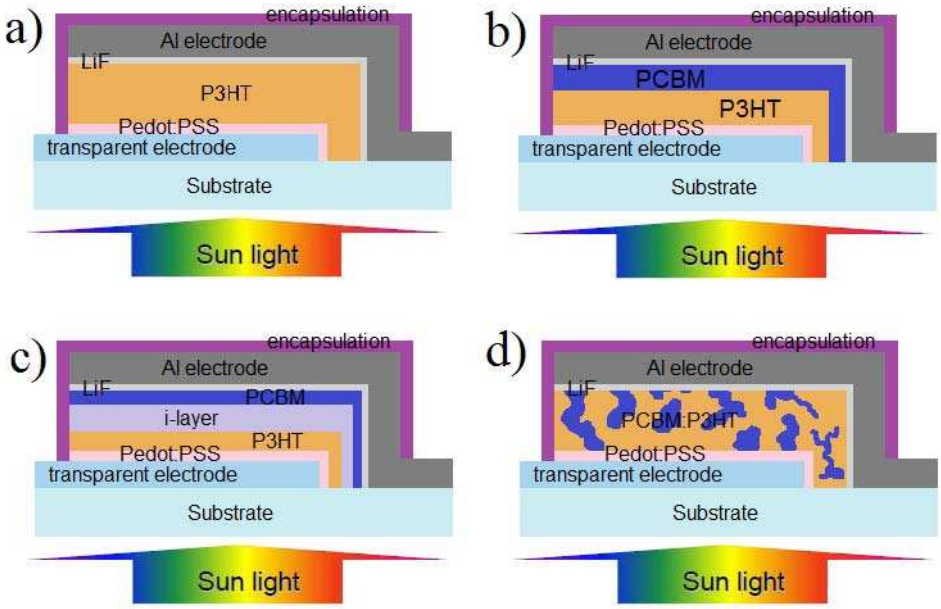

Fig. 1.6: Schemes of the architectures of the four main types of organic solar cells: a) the Schottky solar cells. The exciton dissociation takes place at the interface of dye and metal electrode. b) heterojunction solar cell. The combination of two organic semiconductors as a donor-acceptor material combination enables an ultra-fast charge transfer at their interface, which results in higher efficiencies. c) organic p-i-n solar cell. In between the two different doped materials, an intrinsic dye layer acts as both absorber and optical spacer layer. d) bulk-heterojunction solar cell. The donor and acceptor are mixed together in a blend. The exciton dissociation takes place in the whole organic blend layer, resulting in high device efficiencies. Images taken from and inspired by [18].

placed at the donor-acceptor interface [22].

Bulk-heterojunction (interpenetrating network) solar cell

One of the easiest ways to decrease the distance between donor and acceptor molecules is to mix them within one active layer. This can be done either via thermal evaporation of both at the same time or by dissolving them both in a solvent and, subsequently, spin coating them onto a substrate. Ideally, no exciton diffusion is necessary and the dissociation is complete. The generated charge carriers hop to the outer electrodes through percolation pathways, which is the limiting factor. One of the first devices of this architecture was built in 1995 by [23].

1.3 Objectives of this work

Several approaches to enhance the device efficiency have been presented above, however, the list excluded attempts that were made to realize an optimized bulk-heterojunction solar cell (BHJ-SC). A further optimization step is to bring some organisation to the randomly distributed materials in the interpenetrating network of a bulk-heterojunction (BHJ). This is expected to ensure that every single exciton can be dissociated and the free charge carriers (electrons and holes) can be collected at the outer electrodes. Therefore, a way to control the different distances (firstly the distance of the donor-acceptor interface for excitons and secondly the distance for the free charge carriers to the electrodes) responsible for device efficiency has to be found. The main idea in this work is to keep the distances constant in an active layer consisting of an adequate choice of donor and acceptor material. In addition, this layer structure could be vertically aligned relative to the incident light. Such an approach has been investigated and the pertinent technology developed for the fabrication of the first prototypes of this type.

Donor material

For the donor material, the common materials like copper(II) phthalocyanine (CuPc) (and its derivatives) and regioregular-poly(3-hexylthiophen-2,5-diyl) (P3HT) were chosen. In contrast to P3HT the exposure to oxygen does not degrade CuPc in its β-form but rather acts as a p-dopant, which is advantageous for this application as hole transport is enhanced. P3HT has to be kept under an inert gas in order to protect it against oxidation; therefore, all work with P3HT has been done in a glove box. CuPc is classified as a *small molecule* and P3HT is a polymer; they are shown in Figure 1.7.

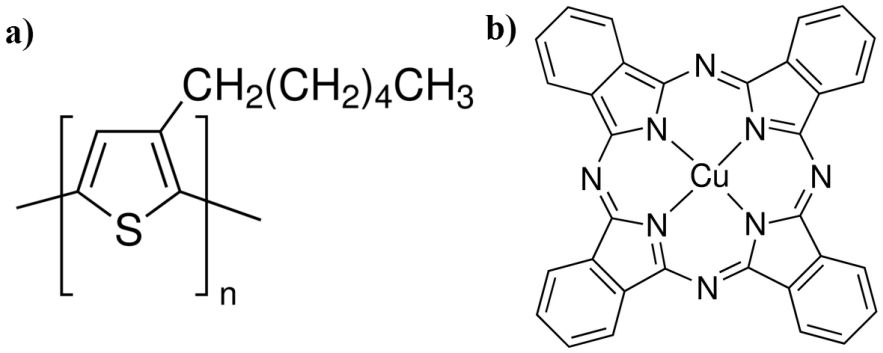

Fig. 1.7: Donor materials used in this study. a) regioregular poly(3-hexylthiophene-2,5-diyl) (P3HT). b) copper phthalocyanine (CuPc). Images taken from [24] and [25].

Acceptor material

CNTs are used as electrode and possible acceptor material due to their exceptional electrical properties, see [26], [27]. They have endured the highest current density ($S = 1 \cdot 10^9 \frac{A}{cm^2}$) ever measured in a material [28]. Moreover, one dimensional ballistic transport takes place in a metallic CNTs (within 10μm-100μm CNT length) [29]. With diameters in the nanometre range and a length of several microns CNTs have a large aspect ratio. The CNT is a molecule formed only from carbon atoms and sp^2-hybrid bonds. This forces the p_z orbital to be perpendicular to the CNT surface. These orbitals overlap with their neighbours, which leads to a conduction path throughout the whole molecule. This is called a π-system. In addition to CNTs, fullerenes like the buckminsterfullerene (C_{60}) and its derivative the phenyl-C61-butyric acid methyl ester (PCBM) have also been used. Fullerenes are the most common acceptor material in organic photovoltaics. Figure 1.8 shows the structure of a carbon nanotube and the fullerenes. The dissoci-

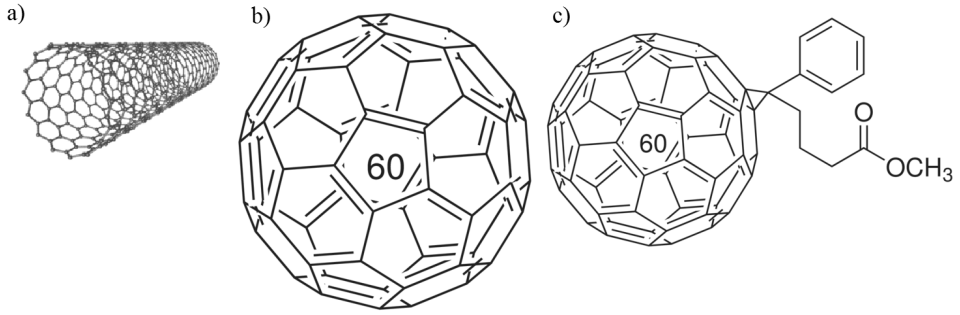

Fig. 1.8: Overview of the different structures of a) CNT, b) C_{60} and c) PCBM. For more details see chapter 3. Images b) and c) taken from [30] and [31].

ated charge carrier can flow to the outer electrode in the π-system of the CNT.

3D solar cell structure

The combination of CNT, dye and the use of a vertically aligned ordered 3D structure leads to the following architecture shown in Figure 1.9. By using this architecture the dissociated charge carriers have the shortest ways to the outer electrodes. Every CNT is directly connected to the titanium nitride (TiN) layer at the bottom. The TiN is metallic and has a conductivity of $\kappa = 5,6 \cdot 10^6 \frac{S}{m}$. This combination forces the CNT to work as the major electrode *and* as the possible acceptor for the ultra-fast charge separation at the donor-acceptor (d-a) interface [20]. The average space between the single nanotubes is approximately 40nm. As the CNT itself works as one electrode, the electric field ends at the CNT sidewalls and caps; this reduces the pathway for an exciton to the d-a interface to around 20nm. This distance is

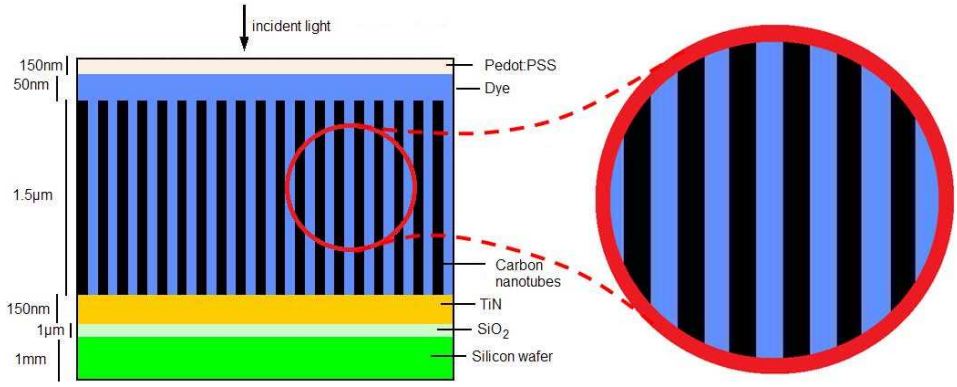

Fig. 1.9: 3D structure of an inverse organic solar cell with vertically aligned carbon nanotubes. The va-CNT array is infiltrated with the dye forming a BHJ. Absorbed light generates excitons, which are possibly dissociated at the dye-CNT interface. Free charge carriers either hop (in the dye) or flow in the *pi*-system of the CNTs to the outer electrodes. Right: magnification of CNT-dye interface.

approximately within the exciton diffusion length. The great challenge is to cover the va-CNT array with a dye layer of homogenously thickness (in nanometre range) over the whole working device area.

2. FUNDAMENTALS

In the following the physical working mechanisms of both organic semiconductors and solar cells are explained.

2.1 Organic semiconductors

Organic semiconductors are made of organic hydrocarbon compounds and their derivatives. Semiconductors are materials, which have a narrow gap between their valence and conduction band, the so-called band gap. This band gap plays an important role in the absorption of incident light, which is necessary for potential solar cell application. A comprehensive introduction to the field of solar cells can be found in [32] and organic electronics are very well explained in [33]. Nevertheless, a full understanding of the fundamental processes involved is still lacking. Neither the precise nature of charge carrier transport [34]; exciton generation [35], dynamics [36], diffusion [37], or heat transport [38] are fully understood - especially for π-conjugated (see later) organic semiconductors. They can be classified according to molecule class and structure:

- molecule classes
  - small molecules (benzene, anthracene, Aluminium-tris(8-hydroxychinolin) (Alq3))
  - polymers (P3HT, Poly(p-phenylene vinylene) (PPV))
- structure
  - crystalline
  - amorphous

The fabrication of thin layers of small molecules is preferably done by evaporation. Polymer layers are normally spin coated. Polymers mainly form amorphous layers, which is almost always the case with spin coating, if no additional posttreatment is applied. Small molecules normally form crystalline layers. The morphology of spin coated polymer thin films can be partly changed from amorphous to nanocrystalline by post thermal annealing. This crystallization process is a consequence of self-assembly forces. If polymers are blended with other materials in the post deposition thin film,

the blended materials will de-mix during the thermal annealing process [39]. This yields percolation pathways for charge carriers in each material. In layers treated in such manner the long chain polymers are normally stacked together in coplanar conjugated segments [40]. The following parts are based upon [41] and [42].

2.1.1 Electronic structure

The electronic structure of the molecules and organic crystals can be divided into the quantum single particle states (electron) and the quantum many-body states (excitons) consideration. The quantum single particle states are designated as orbitals of defined energy which can be occupied by an electron. As every atom interacts with all neighboured atoms, a geometrical equilibrium occurs in form of a crystal or molecule. In order to make electron-structure calculations some fundamental simplifications have to be considered:

- electrons move independently from one another, and
- the potentials of the cores and electrons are known.

As a consequence, a molecular orbital (MO) can be calculated and defined.

Quantum mechanics

The quantum state of a particle and how it behaves is described in quantum mechanics by the wave function Ψ. The linear combination of the wave function of two neighbouring atoms results in two solutions:

$$\Psi_1^{atom} - \Psi_2^{atom} \quad and \quad \Psi_1^{atom} + \Psi_2^{atom}. \tag{2.1}$$

These two solutions differ in their energies. The quantum mechanical combination of neighbouring atoms is described by the linear combination of atomic orbitals (LCAO) model. With the help of the linear combination of the atomic orbitals the molecular orbitals can be calculated in good approximation. These calculations can be expressed as

$$\Psi^{mol} = \sum_n c_n \Psi_n^{atom}, \tag{2.2}$$

where c is a constant [43]. The linear combination of the wave function of two or more neighbouring atoms yields two basic solutions. One is energetically favourable and the second one is energetically non-favourable. Consequently, a bonding and anti-bonding orbital are formed, which can be referred to the ground and excited state, respectively. The more atoms are included the

more manifoldly the linear combinations of the wave functions. This yields various energy levels [43]:

$$E_n = \alpha + 2\beta \cos\left(\frac{2\pi n}{6}\right), \tag{2.3}$$

where α is the on-site energy (Coulomb energy) and β is the off-site energy (exchange energy).
The outer MO can take several discrete energy levels, in general the highest occupied molecule orbital (HOMO) and the lowest unoccupied molecule orbital (LUMO). The HOMO and LUMO are the bonding and anti-bonding molecular orbitals, respectively. For radicals or ions an open-shell ground state exists, which results in a single occupied molecular orbital (SOMO). In order to determine the energy of these orbitals either theoretical calculations, e.g. using density functional theory (DFT), or measurements like cyclovoltametry (CV) or ultraviolet photoemission spectroscopy (UPS) can be done.
From a quantum mechanical point of view a discrete state can be a superposition of several basic states. This is the fundamental background of the hybridized orbitals (two states in superposition). Consequently, as molecular orbitals are spread over the whole molecule, hybridization effects play an essential role with regard to molecular properties. Under certain framework conditions this results in delocalized states along the length of the molecule (the previously mentioned alternating double atom bonds and single atom bonds along the molecule).

2.1.2 Hybridization of carbon

The electronic shell configuration of carbon is: $1s^2, 2s^2, 2p^2$, which means it needs four electrons left to fulfil the octet rule. For example, starting with two carbon atoms, every valence electron will have the same energy level. This means that in order to form a hydro-carbon molecule these two carbon atoms have to covalently bond six other hydrogen atoms. This yields ethane. The bonding orbitals are so-called σ-bonds. If two hydrogen atoms are absent the two carbon atoms will form a π-bond at the same geometric place in addition to their σ-bond. These two types of orbitals are of different symmetries and do not hybridize. For planar organic molecules (like CuPc) as well as in graphene and CNTs this leads to the formation of two different sets of almost independent molecular orbitals, σ-type and π-type. The π-type orbitals are formed from out-of-plane p_z atomic orbitals and have a smaller overlap with one another than the orbitals of the σ-system. Therefore, the π-orbitals are energetically higher than the σ-orbitals. These form the HOMO orbitals in molecules or valence band in periodic systems. π-orbitals are more delocalized than σ-orbitals. Thus, the π-orbitals define electron transport properties of conjugated polymers, graphene and CNTs.

Figure 2.1 gives an overview of the orbitals. The π-system has the following

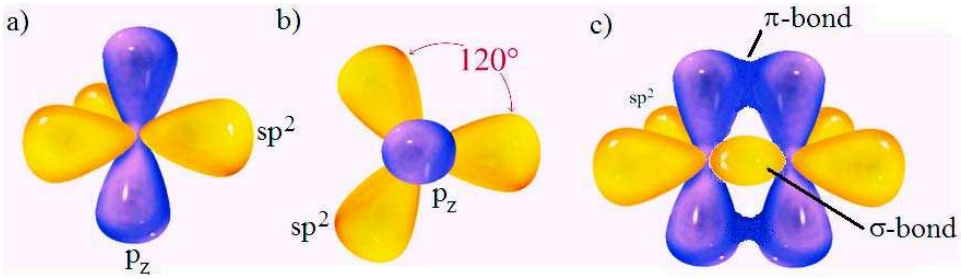

Fig. 2.1: a) side view of a sp^2-hybridized carbon atom. b) top view of a sp^2-hybridized carbon atom. c) hybridization orbitals of ethene.

characteristics and influences on the molecule:

- every electron is completely delocalized over the entire π-system,
- the HOMO-LUMO gap decreases with increasing size of the π-system,
- big π-systems (chlorophyll, etc.) shift the absorption from the ultraviolet to the visible spectra.

2.1.3 Energy levels and excited states

The consideration of energy levels should be divided into two parts - for the single molecule and for the organic crystal. For the latter energy bands are formed due to the system (lattice-) periodicity. However, these bands are quite narrow due to the limited overlap of the molecular orbitals of two neighbouring molecules. The bandwidth of the energy bands in an organic crystal is around $\Delta E \approx 0.2eV \pm 0.1eV$. On the level of a single molecule the excited state is formed by an exciton, which consists of a hole on the HOMO- and an electron on the LUMO-level, also designated as a bound pair. The excitons themselves can be further divided into ones showing triplet and singlet characteristics. The lifetime of a triplet exciton is several orders of magnitude higher than that of a singlet exciton. The exciton energy without electron-hole interaction can be calculated from the Hückel model as follows

$$\Delta E = \varepsilon_r - \varepsilon_a. \tag{2.4}$$

By taking into account the electron-hole interaction, the excitation energy can be calculated for singlet and triplet excitons using the Hartree-Fock model (see [44])

$$\Delta E = \varepsilon_r - \varepsilon_a - J_{a,r} + 2K_{a,r} \tag{2.5}$$

$$\Delta E = \varepsilon_r - \varepsilon_a - J_{a,r}, \tag{2.6}$$

where $J_{a,r}$ is the dispersion relation (parabolic in semi-conductor) and $2K_{a,r}$ is the two-body interaction (exciton). Therefore the optical excitation energy differs from the HOMO-LUMO gap. The excitons in organic crystals have a binding energy of approximately $E_{Exc-bind} \approx 0.5eV$. These "quantum many-body states" can be further divided into Frenkel excitons (located on a single molecule), Wannier-Mott excitons (spread over several molecules) and charge transfer excitons (distance between hole and electron within the range of 10nm - 30nm). The orbitals (HOMO, LUMO) are single particle states whereas the excitons (S0, S1,... and T0, T1,...) are many-body states. The transition from a ground state to an excited one occurs via a transition dipole moment (Franck-Condon principle). This is a vector, which is proportional to the overlap of the wave vectors. Its absolute value is proportional to the probability of transition and its orientation is parallel with the incident light. Figure 2.2 illustrates these correlations. Due to the molecular interac-

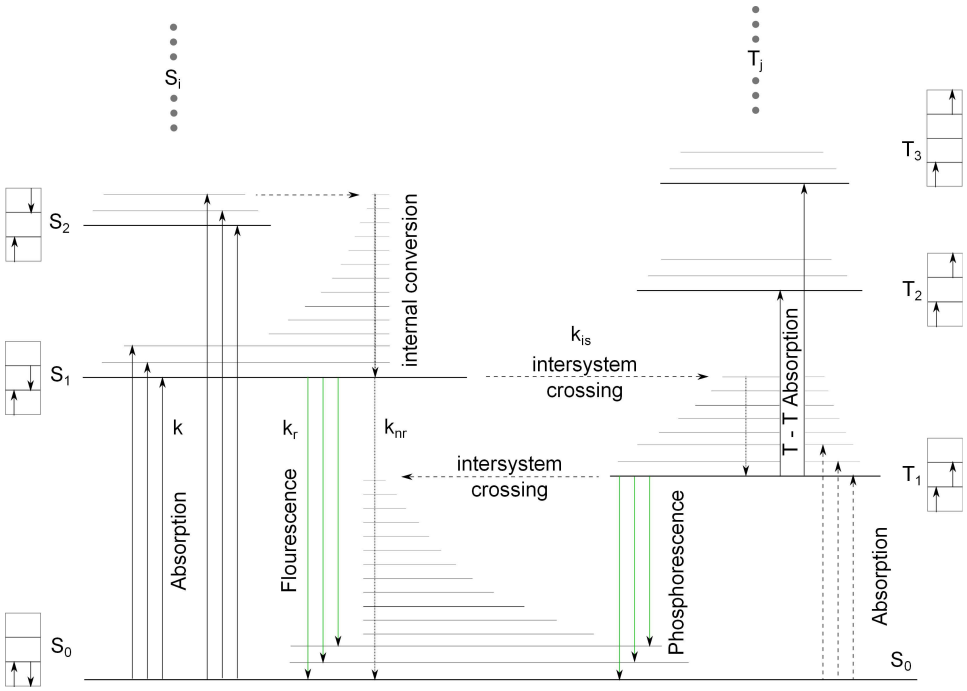

Fig. 2.2: Jablonski diagram. This diagram shows all possible interactions of photons and excitons with the allowed energy levels and states of an organic semiconducting molecule. Image taken from [44].

tion in the solid the energy levels of the molecule change in comparison to the gas phase as shown in Figure 2.3.

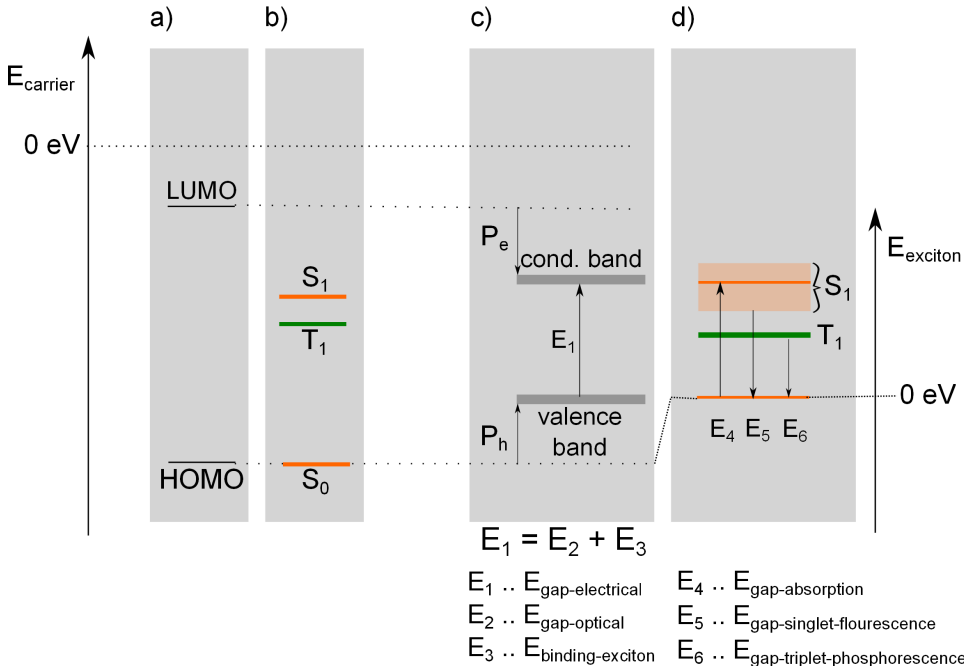

Fig. 2.3: Energy levels in organic materials, where P_e and P_h are the polaron energy shifts, respectively, $E_{gap-abs.}$, $E_{gap-singl.}$ and $E_{gap-tripl.}$ are the values of the band gap, band gap compression by singlet excitons and band gab compression by triplet excitons, respectively. Image inspired by [45].

2.1.4 Charge carrier transport in organic crystals

Strong interatomic interactions in inorganic semiconductor lead to large bands and small lattice constants ($\approx$ 1Å). Contrastingly, the intermolecular forces in an organic semiconductor are weak van der Waals (VdW) forces. Coupled with the weak overlap of atomic orbitals of neighbouring molecules this leads to very narrow bands in the organic semiconductor bulk with a bandwidth of around 0.1eV to 0.4eV (the bandwidth in anorganic semiconductors are in the range of 1eV to 2eV) for ideal crystals [44]. This leads to strongly localized charge carriers, which polarize their neighbourhood. Due to that fact they are named *polarons*. The nature of these charge carriers is explained in detail later. Another influence on the transport mechanics is the orientation of the single molecules in the crystal (with respect to the crystal axes). The overlap between electronic orbitals of the nearest neighbour molecules in crystals is a very important factor in this matter. The packing in molecular crystals strongly influences their intrinsic transport properties. The largest overlap of π-orbitals occurs for flat molecules packed in parallel [44]. A crystal with such a layered structure should have good electronic properties, at least in the plane of the layers. However, the realization of such a layered structure in organic crystals of acenes is not observed [46].

As most of the fundamental work was done by making an investigation of this molecule class, it is worth considering the crystallographic nature of these crystals. These crystals grow in a herringbone structure (see Figure 2.4), forming both monoclinic (naphthalene and anthracene) and triclinic (tetracene and pentacene) crystallographic systems [47]. The inversion cen-

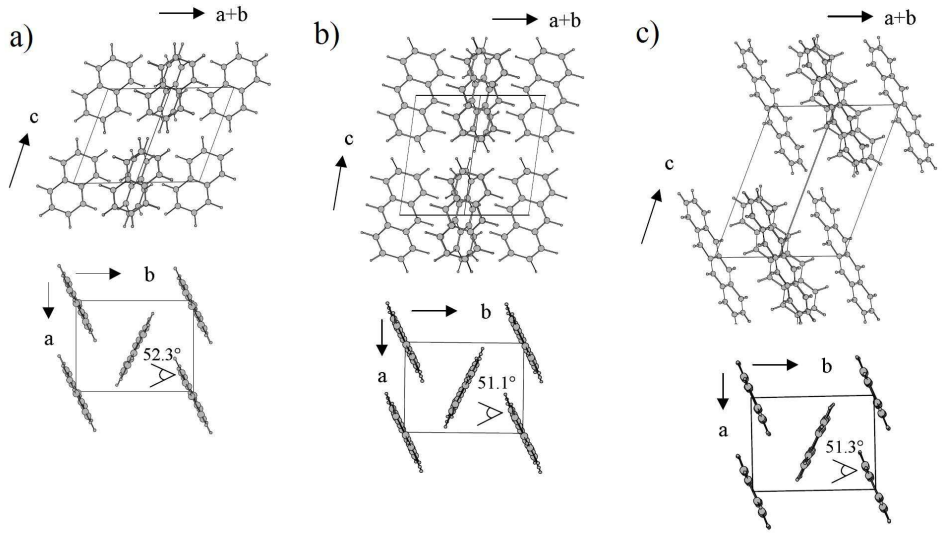

Fig. 2.4: Crystal structure (heringbone) of acene crystals: a) naphthalene, b) anthracene, c) tetracene. A projection on the a+b direction is given in the top of a)-c). The projection along the axes of the molecules is given on the bottom of a)-c). Image taken from [47].

tre of the given molecules is placed in the corners of the unit cell and in the (1/2, 1/2, 0) point. Between molecular planes of non-equivalent molecules an angle occurs. This angle α is in the range of 51.1°-52.3° for the different acenes [48]. Because the angle between the molecular axis and c axes is different for non-equivalent molecules as well. Thus, anisotropy of the charge carrier properties is to be expected. The better the overlap of the electronic orbitals of adjacent molecules the better the conductivity. The mobility of different directions in the plane a-b was measured. The mobility of holes were approximately 2.9, 3.2, 2.3, 2.20 cm^2/Vs for directions forming an angle of 0°, 30°, 60° and 90° in each case with b axis. The anisotropy is clearly determined [48].

Drift

Charge carrier transport is due to the process of directed charge carrier drift under the application of an electric field. The fundamental equations for the drift are [44]:

$$\vec{v} = \mu \vec{F} \tag{2.7}$$

$$\vec{j} = \sigma \vec{F} \tag{2.8}$$

$$\sigma = en\mu_{eff} \tag{2.9}$$

$$\vec{j}_{diff} = -D\left(\vec{\nabla} n\right) \tag{2.10}$$

$$D = \frac{k_B T}{e}\mu, \tag{2.11}$$

where $\vec{v}$ is the drift velocity, μ the mobility, $\vec{F}$ the applied electric field, $\vec{j}$ the current density, σ the conductivity, e the elementary charge, n the charge carrier density, μ_{eff} the effective mobility, j_{diff} the diffusion current, D the diffusion constant, ∇n the concentration gradient, k_B the Boltzmann constant and T the temperature. Equation (2.11) describes the fundamental correlation between drift and diffusion. Excitons do not drift as they are charge neutral but with (2.11) excitons and charge carriers have jointly one quantity: the diffusion constant. This, excitons diffuse. However, literature mostly refers to the mobility μ and not to the diffusion constant.

2.1.5 Covalently bonded crystal

In a covalently bonded crystal the charge carriers stay within a band. This can be modelled using two approximations [44]

- the charge carrier is spatially fully delocalized (Bloch wave) or
- the charge carrier forms spatially limited wave packets spread over several lattice constants.

The electric field accelerates the wave packets, on average after the mean free path has been travelled scattering takes place. Summed over all packets and scattering events results in there being an average drift velocity.
In an organic crystal another transport mechanism, the so-called "hopping transport", can occur. This process exists, when the mean free path is smaller than the lattice constant, which means the band model is not applicable and the wave packets are strongly localized [44]. In this case the strong electron-phonon coupling causes small polaron bands and the gain in energy due to delocalization is very low. Hence, the charge carrier itself (the electron in the LUMO or the hole in the HOMO of a molecule) can be considered due to its small size as a molecule polaron or "small polaron". Hence, a polaron is a charge (electron or hole) plus a polarisation of the neighbourhood of the charge due to coulomb interaction with the bulk [44] (see Figure 2.5). In this mechanism a charge carrier (polaron) "sees" a potential barrier to every neighbouring molecule and hopping is the thermally activated "jump" (tunnelling) of the charge carrier over this barrier. The Boltzmann's law gives the correlation between the rate of passing this barrier and the applied temperature

$$r = r_0 e^{-\frac{\Phi}{k_B T}}, \tag{2.12}$$

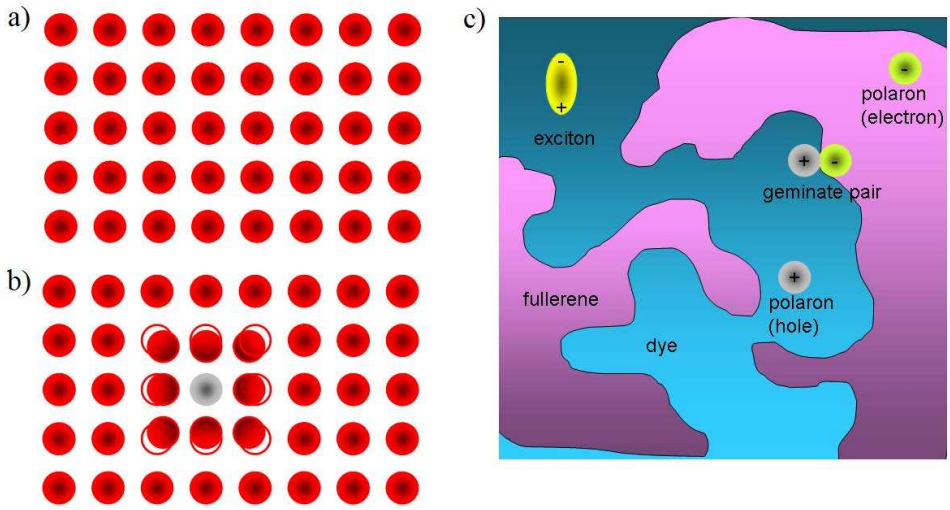

Fig. 2.5: Polarons in organic matrix. a) organic crystal without excitation. b) polaron (hole) attracting the electron cloud of the π-systems of the neighbouring molecules. c) Sketch of polarons in organic matrix. At the donor-acceptor interface (polymer-fullerene) the exciton is dissociated and becomes a geminate pair of polarons (electron and hole polaron). The polarons completely dissociate and "hop" in their respective organic semiconductor towards the outer electrodes.

where r is the actual rate of hopping, r_0 the base rate and Φ is the potential barrier between two neighbouring molecules. The thermal mobility μ of the charge carriers is Arrhenius-like and can be considered as

$$\mu = \mu_0 e^{-\frac{\Phi}{k_B T}}, \tag{2.13}$$

where μ_0 is the initial mobility. If an electric field is applied, the barriers are lower in the direction of the electric field, which enables a directed hopping along the field direction [42]. A realistic mathematical description of the hopping-mobility in an organic semiconductor is hard to obtain as it is a very complex phenomena (influence of traps, lattice disorder, etc.). Further more, the mobility also depends on the applied electric field. Empirically the following relation is found

$$\mu = \mu_0 e^{-\frac{\Phi-\beta\sqrt{F}}{k_B T_{eff}}}, \quad \frac{1}{T_{eff}} = \frac{1}{T} - \frac{1}{T_0}, \quad \beta = \sqrt{\frac{e^3}{\pi e_r \varepsilon_0}},$$

where F is the applied electric field [49]. As equation (2.14) is closely related to the Pool-Frenkel effect [33], then

$$j = j_0 e^{-\frac{\beta\sqrt{F}}{k_B T}}, \tag{2.14}$$

where j is the current density and j_0 a constant. Equation (2.14) is called the Pool-Frenkel mobility.

Another derivation used to define the mobility of charge carriers in organic materials is the Lyons model [50]. In this model the energy needed to form equal quantum states on two neighbouring molecules is estimated to be half of the polaron binding energy

$$\mu \sim \mu_0 \exp(-2\alpha R) \exp\left(-\frac{E_{bin}}{2k_B T}\right), \tag{2.15}$$

where μ is the mobility. According to equation (2.15) the mobility of the charge carriers depends on the temperature. But the mobility increases also at low temperatures. In order to balance theory and experiment the model has to be adjusted with a term related to small exchange energies.
In amorphous layers the single molecules are arranged randomly. This causes a variation in the degree of polarization of each molecule, which also yields a disorder in the energy states. The distribution of these states can be modelled with a gaussian distribution [44].

Space charge limited current

Within an organic layer the electrical conductivity can be limited by a space charge limited current (SCLC) due to different mobilities of electrons and holes, e.g. CuPc. The mobility of charge carriers can be determined by the space charge limited I-V characteristics [33]. The general equation for current I (for unipolar current) caused by an electric field

$$I = \mu \rho_f F - D \frac{d\rho_f}{dx}, \tag{2.16}$$

where $D = \frac{\mu k_B T}{E}$ is the Einstein diffusion coefficient (see 2.11). As Poisson's equation has to be fulfilled

$$\frac{dF}{dx} = \frac{\rho}{\varepsilon \varepsilon_0} \tag{2.17}$$

where ρ is the total charge density. This is the sum of free carriers ρ_f and trapped ρ_t carriers. The free carrier density depends on the total density as well as on position x: $\rho_f = \rho_f(\rho, x)$. The simplest solution of equation 2.16 is given by Mott and Gurney, [51], for the case of no traps and without diffusion as

$$I = \frac{8}{9} \mu \varepsilon \varepsilon_0. \tag{2.18}$$

This solution gives an estimate for the SCLC. The solutions for when different kinds of traps were included were given by Bonham and Jarvis [52]. For shallow traps and exponentially distributed energy the current is correlated to the square of the applied voltage U.

$$I = \frac{8}{9} \mu \varepsilon \varepsilon_0 \Theta \frac{U^2}{L^3}, \tag{2.19}$$

where Θ is the trapping factor and L the travelled length of the charge carrier. The constant trapping factor Θ can be expressed as

$$\Theta = \frac{n_h}{H_t} e^{-\frac{E_t}{k_B T}}, \tag{2.20}$$

where n_h is the density of states, H_t the density of traps and E_t its energy. For a sufficiently large voltage above the trap-filled voltage (above trap-filled limit (ATFL)) the Fermi level is shifted towards the valence band above the trap levels. This liberates the charge carriers from the traps. As a result a rapid increase of the current is observed. Unlike in anorganic semiconductors the conductivity of organic materials decrease with increasing temperature. This is caused by the worsening molecule orbital overlap due to the increasing number and magnitude of lattice vibrations with increasing temperature [44].

2.1.6 Doping and charge carrier generation

The states of charge carriers can be described by their density of states (DOS), either forming bands or localized states. The DOS in a covalently bonded organic semiconductor can be seen in Figure 2.6. According to [44]

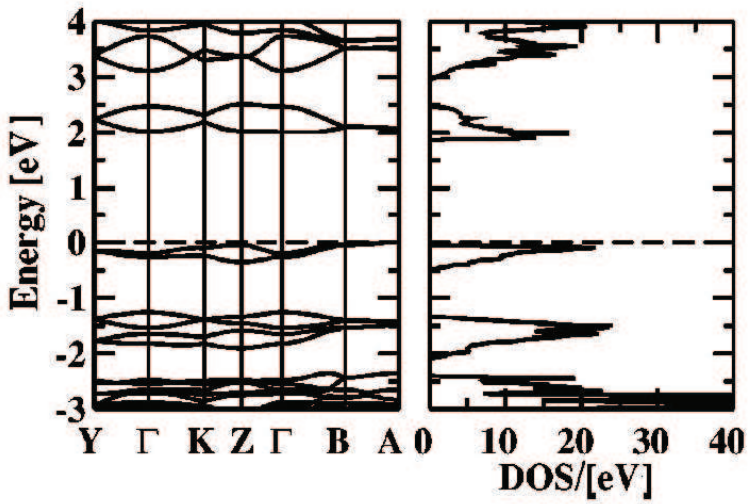

Fig. 2.6: DOS of anthracene at p=0GPa. Image taken from: K. Hummer, P. Puschnig, C. Ambrosch-Draxl, Physical Review B, 67, (2003), 184105. ©(2003) by the American Physical Society, [53].

the electrical conductivity σ is the sum of the concentration of free electrons (n) and holes (p) multiplied with their mobility (μ_e and μ_h respectively).

$$\sigma = e\left(n\mu_e + p\mu_h\right). \tag{2.21}$$

At T=0K the concentrations are equal (n=p=0) and the semiconductor is an insulator. The charge carriers are generated by several mechanisms such as

- thermal generation in an intrinsic semiconductor,
- photogeneration via absorption,
- doping,
- injection at electrodes.

The quantum statistics for a system consisting of N electrons denotes that the highest occupied energy level at T=0 K is the Fermi level, E_F. E_F results from N and the integral of the DOS. The occupation probability for the energy levels is

$$f(E) = 1 \quad for\ E < E_F$$
$$f(E) = 0 \quad for\ E > E_F.$$

In an inorganic semiconductor at finite temperature electrons can be excited into the conduction band thereby also generating holes in the valence band. According to the neutrality condition (n=p) the charge carrier density can be expressed for an intrinsic semiconductor as

$$n_i = p_i = \sqrt{N_c N_v e^{-\frac{E_{gap}}{2 \cdot k_B T}}}, \tag{2.22}$$

where N_c, N_v are the effective density of states of the conducting and valence band, respectively, and E_{gap} is the band gap.
The photogeneration of charge carriers, which is based on the absorption of incident light results in an electron-hole pair. In a covalently bonded semiconductor a direct band-to-band excitation takes place resulting in photoconductivity. In an organic semiconductor the absorption creates a singlet or triplet exciton, which can be dissociated on separation of the electron-hole pair. The dissociation can be described with the Onsager model [44], which contains the following algorithm

- excitation to a higher excited state,
- partial relaxation from state S_N to S_1,
- thermally activated formation of charge-transfer states within a thermalization radius,
- Brownian movement of charge carriers (thermally activated hopping),
- overcoming of the potential barrier thus yielding free charge carriers.

This model is appropriate for single crystals is a bad fit for polycrystals or amorphous layers. The extrinsic charge carrier generation takes place at interfaces, where the generated excitons are dissociated.

Doping

In principle doping is a controlled contamination of a pure semiconductor material [42]. In a covalently bonded semiconductor n-doping is realized with a donor, which donates an electron into the conduction band, and the positive charged donor stays fixed within the material. For p-doping an acceptor creates one hole in the valence band by attracting one electron of the semiconductor bulk and a negative charged acceptor stays fixed in the lattice. In an organic semiconductor the interaction between the dopant and the semiconductor involves the HOMO and LUMO energy levels. For n-doping the HOMO level of the dopant has to be slightly lower than the LUMO of the semiconductor. Consequently, an electron will hop to the LUMO of the semiconductor from HOMO level of the subsequently positively charged dopant. The energetically higher placed orbitals of the donor are susceptible to oxidation. For p-doping the LUMO of the p-dopant (acceptor) has to be slightly higher than the HOMO of the semiconductor. This forces an electron from the HOMO level of the semiconductor to hop to the LUMO of the dopant and , subsequently, the negatively charged acceptor will stay fixed. The deep energy levels of the HOMO and LUMO of the acceptor makes it strongly electronegative [42]. A short overview of the different electronic state configurations of the semiconductor and the dopant is shown in Figure 2.7. Different doping methods such as

- electrochemical doping,
- oxidation with gas, and
- co-evaporation

can be used to dope an organic semiconductor. Electrochemical doping yields high conductivities in the doped layer. However, the dopant diffuses and the doping itself is thermally unstable. The same disadvantages apply in the case of doping due to oxidation with a gas, e.g. oxygen or chlorine. Doping through thermal co-evaporation leads to thermal stability [42]. Organic molecules as well as anorganic materials such as alkali metals (lithium, caesium, iron chloride etc.) can be used as the dopants with this technique. However, alkali metals cause problems related to thermal stability and diffusion. Thermal co-evaporation can also be used to fabricate p-i-n heterostructures [42].

2.2 Semiconductor interfaces

In a semiconductor device several interfaces exist, the most important of these are the metal-semiconductor or p-n interfaces. In order to obtain a better understanding band formation is considered to exist in the organic semiconductor.

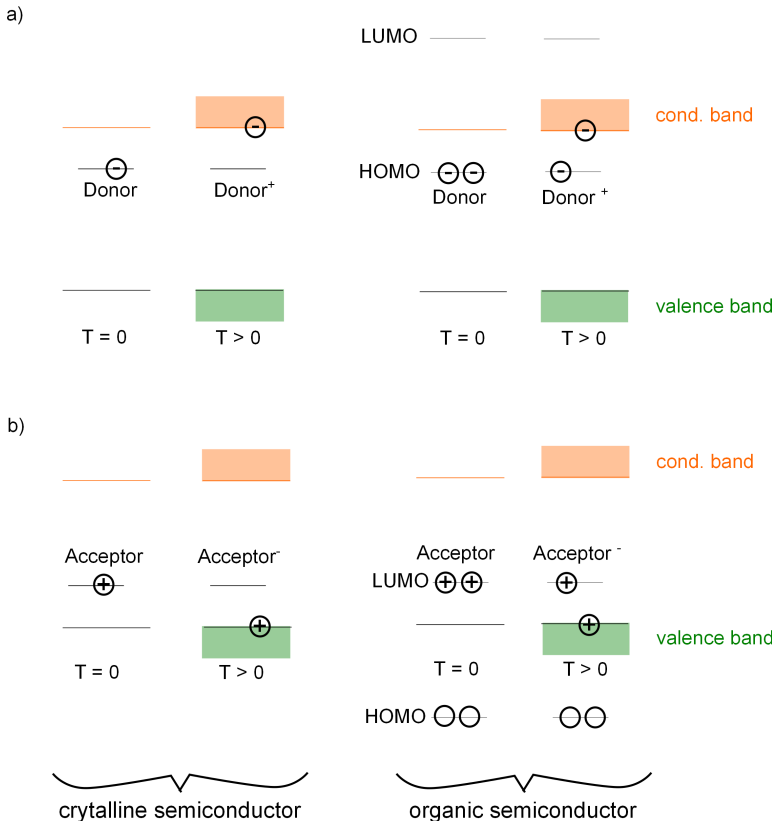

Fig. 2.7: n- and p-doping scheme for an inorganic and organic semiconductor. a) left: n-doping of inorganic semiconductor. Right: n-doping of organic semiconductor. The n-dopant transfers an electron from its HOMO level onto the LUMO level of the organic semiconductor. b) left: p-doping of a covalently bond inorganic semiconductor. Right: p-doping of organic semiconductor. The p-dopant transfers an electron from its LUMO level onto the HOMO level of the organic semiconductor. The temperature has to be significantly higher than 0K or the charge carrier can not change its energy level. Image inspired by [42].

2.2.1 Band scheme and Fermi level

The Fermi level is defined by the Fermi distribution function, which is the population density at a certain energy E,

$$f(E) = \frac{1}{\beta e^{\frac{E-E_F}{k_B T}} + 1}, \tag{2.23}$$

where β is a statistically weighting factor (for band states β=0). The temperature dependency results in a "fusing" or "luting" of the Fermi distribution. The Fermi level is defined to be in the middle of the band gap of an intrinsic semiconductor. In a n-doped semiconductor the Fermi level is shifted upwards towards the conduction band whereas in a p-doped semiconductor the Fermi level is shifted downwards close to the top of the valence band [42]. This behaviour is brought together in Figure 2.8.

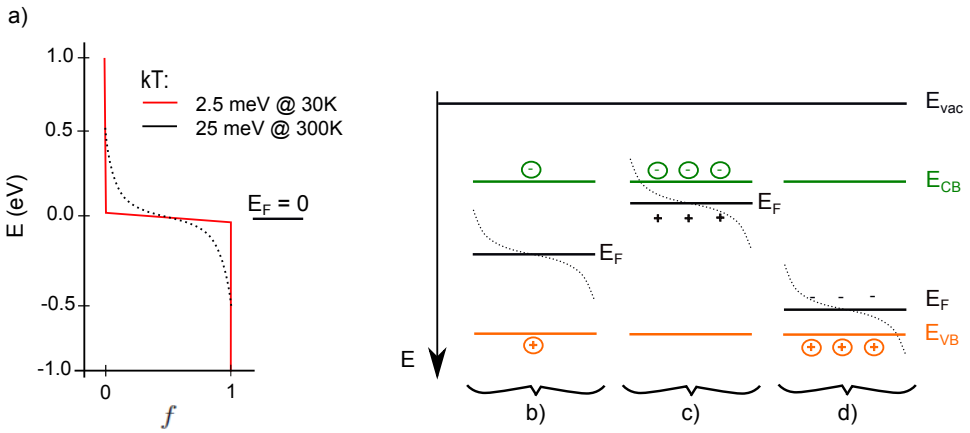

Fig. 2.8: Fermi distribution and Fermi level. a) Fermi distribution for different temperatures. b) Fermi level of an intrinsic semiconductor. c) Fermi level of an n-doped semiconductor. d) Fermi level of a p-doped semiconductor. Image inspired by [42].

2.2.2 Metal-semiconductor junction

Before the two materials are connected together the Fermi energies are not in the same energy level. After the two materials are connected together, the Fermi levels equalize, resulting in a band bending of both the valence and conduction bands in the band diagram. This leads to the formation of a barrier with barrier height Φ_b, which is responsible for the non-ohmic behaviour of this junction, known as a Schottky junction. In the band diagram this barrier is modelled as a bend of the valence and conduction band. The contact voltage Φ_c which occurs in the air gap between the metal and semiconductor before contact, can be measured via a backside contact

of the two materials, the electric field via Kelvin probe. The contact voltage, the electric field and the barrier can be expressed as [42]

$$\Phi_c = \frac{1}{e\left(E_{F,sc} - E_{F,m}\right)} \tag{2.24}$$

$$F = \frac{\Phi_c}{\Delta x} \tag{2.25}$$

$$\Phi_b = \Phi_m - EA = \Phi_c + \Phi_{sc} \approx \Phi_c, \tag{2.26}$$

where $E_{F,sc}$ and $E_{F,m}$ are the Fermi levels of the semiconductor and the metal, Δx the distance, Φ_m and Φ_{sc} the work function of the metal and semiconductor, respectively, and EA is the electron affinity. The band diagrams are shown in Figure 2.9. The I-V behaviour of a Schottky contact is

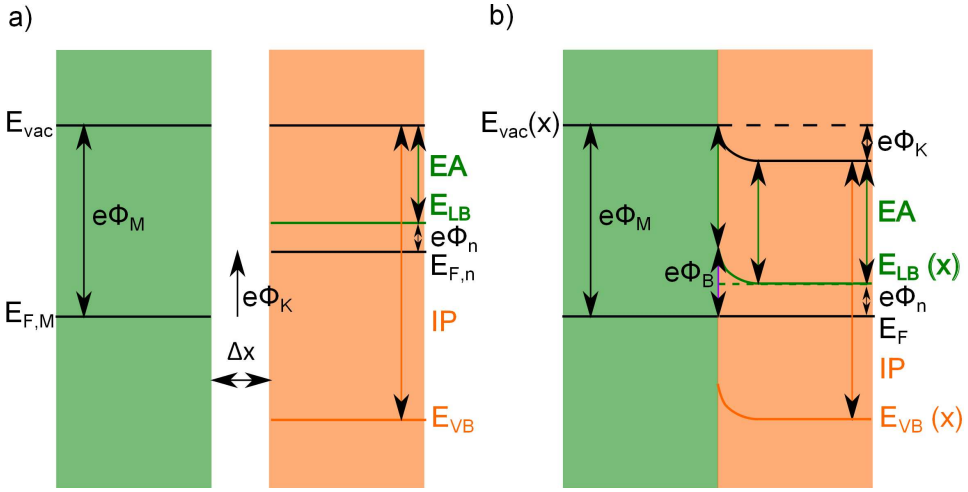

Fig. 2.9: Overview of the semiconductor-metal contact. a) before equilibrium state; metal and semiconductor are not in contact. b) semiconductor and metal are in contact with each other and equilibrium state is reached. c). air gap between metal and semiconductor, although brought in contact electrically by a back side contact. Image inspired by [42].

given by the equation (2.27)

$$j = j_s \left(exp^{\frac{eV}{k_B T}} - 1 \right), \tag{2.27}$$

where j and j_s are the current density and saturation current density. This resembles the behaviour of a diode described by the Shockley equation. The saturation current density equals

$$j_s = \frac{1}{4} e \cdot n \cdot exp^{-\frac{e\Phi_b}{k_B T}}. \tag{2.28}$$

According to the band diagram a Schottky contact is normally formed when the Fermi level before contact of the semiconductor is higher than that of the metal ($E_{F,sc}$>$E_{F,m}$) [42]. If the Fermi level of the semiconductor is lower, then its bands will be bent downwards at the interface and the electrons can "fall" into the metal without "seeing" a barrier. If the Fermi levels cannot be shifted in the desired direction and $E_{F,sc} > E_{F,m}$ is the work function combination of the used materials, then doping can be used in order to form a "quasi-ohmic" contact. At a Schottky contact interface a depletion region occurs on the semiconductor side. Its width can be modelled using the "Schottky approximation" (charge carrier distribution, n(x), is box shaped) so that

$$x_w = \sqrt{\frac{2\varepsilon\varepsilon_0}{eN_D}\Phi_c}, \tag{2.29}$$

where N_D is the donor density in the semiconductor, and ε_0 and ε are the permittivity and relative permittivity, respectively [42]. The width of the depletion region depends on the donor density. If the depletion region is thin enough, tunnelling is the dominant transport mechanism, and from a macroscopic point of view the contact is "ohmic". This junction configuration is thus named "quasi-ohmic" [42].

2.3 Terrestrial solar spectrum

The terrestrial solar spectra is described by a spectra dependent photon flux density spectral dependent photon flux density (n_p(f)). The flux is the amount of photons of a certain wavelength per second and area. This can be used to yield the spectral irradiance [54]

$$b(f) = n_p(f) \cdot h \cdot f. \tag{2.30}$$

By integrating the spectral irradiance over the considered frequency interval the total irradiance can be derived.

$$B = \int_{f_{\min}}^{f_{\max}} b\,(f)\,df = \int_{f_{\min}}^{f_{\max}} n_p\,(f) \cdot h \cdot f \cdot df = \int_{\lambda_{\min}}^{\lambda_{\max}} n_p\left(\frac{c}{\lambda}\right) \cdot \frac{h \cdot c^2}{\lambda^3} \cdot d\lambda \tag{2.31}$$

$$B = \int_{\lambda_{\min}}^{\lambda_{\max}} r\,(\lambda)\,d\lambda \tag{2.32}$$

By taking into account the different distances of the solar irradiation on its way to earth, due to different angles spanned with the zenith, different AMx-standards are established (AM= Air Mass, $x \geq 0$). For this standard AM0 is the extra terrestrial irradiance($\triangleq$ solar constant; AM0=1367$\frac{W}{m^2}$), and AM1 is the irradiance through the earth's atmosphere at zenith (AM1=1042$\frac{W}{m^2}$

including diffuse irradiation) [55]. AM1 corresponds to the shortest possible way to earth. The AMx factor is expressed as follows

$$AMx, \quad wherby \quad x = \frac{1}{\cos\alpha} \quad (0 \leqslant \alpha \leqslant 90°)\,, \tag{2.33}$$

with α the angle between the zenith and the actual angle of incidence. AM1.5 equals the irradiance at european latitude and is AM1.5 $= 1000\frac{W}{m^2}$. This corresponds to the standard IEC 904-3 (1989)part III) (calculation yields $AM1.5 \approx 930\frac{W}{m^2}$ including diffuse radiation), which is a result of an angle to the zenith of 48.2° (see Figure 2.10) [55]. As the irradiation passes through

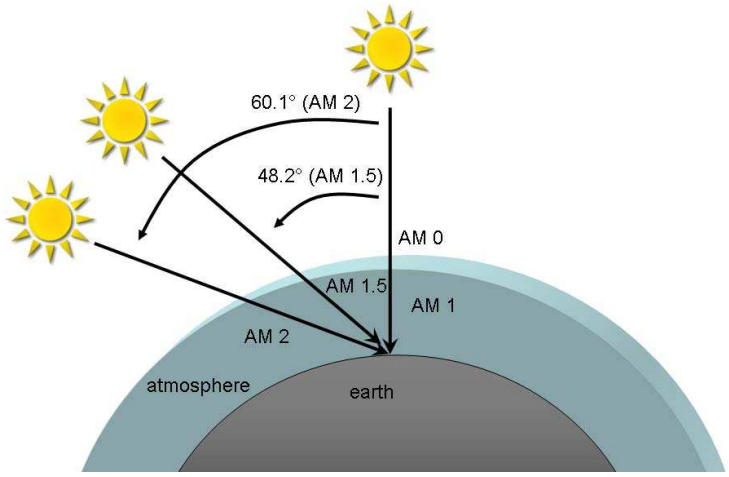

Fig. 2.10: Air mass factors of solar irradiance. The different irradiation levels are AM0, AM1.5, and AM2. Image inspired by [56].

the atmosphere several losses occur such as absorption by water vapour, ozone, oxygen, and carbon dioxide, or scattering by dust particles as well as reflection (e.g. on clouds). This results in the typical absorption bands in the spectra shown in Figure 2.11. For light absorption the photon flux density, which is the amount of photons per second, area and wave length is given by

$$n_p\,(f) = r\,(\lambda)\,\frac{\lambda}{h \cdot c.} \tag{2.34}$$

Equation (2.34) causes a shift of the maximum photon flux towards longer wavelengths (by about $\lambda = 710nm$).
Among the different potential absorber materials the absorption maxima of P3HT do not perfectly fit but this material yields good organic solar cell performance. CuPc with a band gap of 1.8eV passes much better to the solar spectrum. However, polymers show better processing properties in solution based solar cell fabrication (printing) than the small planar molecule CuPc (thermal evaporation). A crucial point is to fit the optical band gap of the absorber material to the photon flux density and to shift the absorption

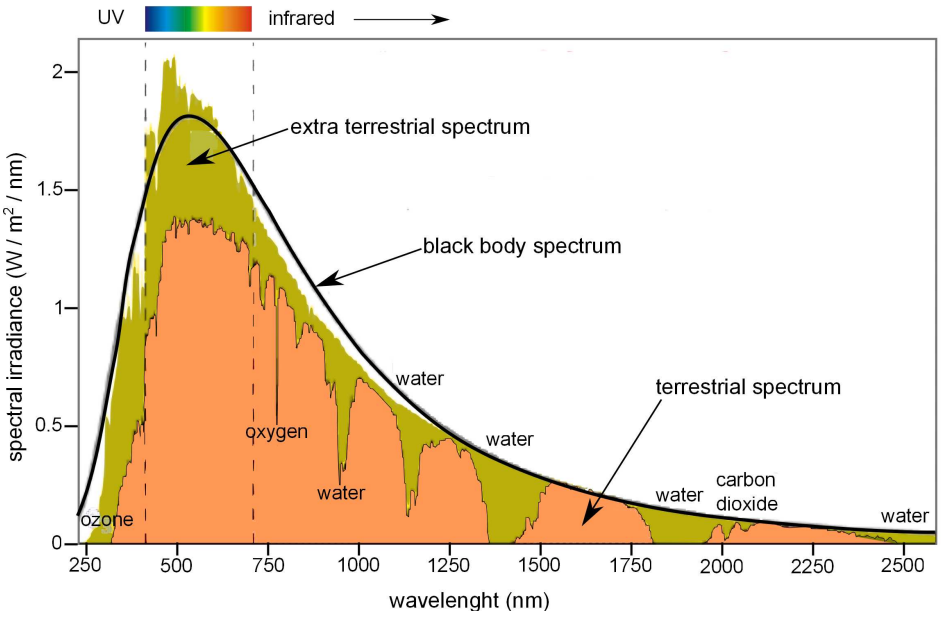

Fig. 2.11: Solar radiation spectrum including black body spectrum, extra terrestrial spectrum, and terrestrial spectrum. Image based upon [57].

range into the near infra red range; e.g. silicon solar cells obtain their large photocurrent because of their ability to absorb in the near infra red [54].

2.4 Solar cell principles

The single junctions can be arranged to form new interactive junctions in form of a heterojunction of donor-acceptor materials. This is the basis for organic solar cells. The solar cell basics will be explained in detail below. Silicon solar cells have been under development for the last six decades; as a consequence they dominate the photovoltaic market. Although these anorganic solar cells differ in many aspects from organic solar cells, they have nevertheless much in common. Therefore, for the sake of completeness, the theory of the silicon solar cells is briefly explained in the following.

2.4.1 Silicon solar cell physics

In a silicon solar cell incident light absorption takes place in the p-doped (boron) region and free charge carriers are generated directly, see Figure 2.12. Diffusion of these charge carriers (electrons and holes) takes place and reflection of the electrons by the back-surface field (highly p-doped region) occurs due to suppressed recombination at the back contact. The drift current, caused by the electric field, transports the charge carriers out of the depletion region resulting in an accumulation of electrons in the n-region and

holes in the p-region. This generates an open circuit voltage (Fermi level not spatially constant, therefore no thermodynamic equilibrium). The solar cell works efficiently, if the minority charge carrier diffusion length is larger than the layer thicknesses and than the light penetration depth (usually around 100μm). Silicon is an indirect semiconductor ($E_{gap} = 1.1eV$), which results in weak absorption. The band diagram of a classical silicon solar cell is shown in Figure 2.12. The p-doped region in a silicon solar cell is around

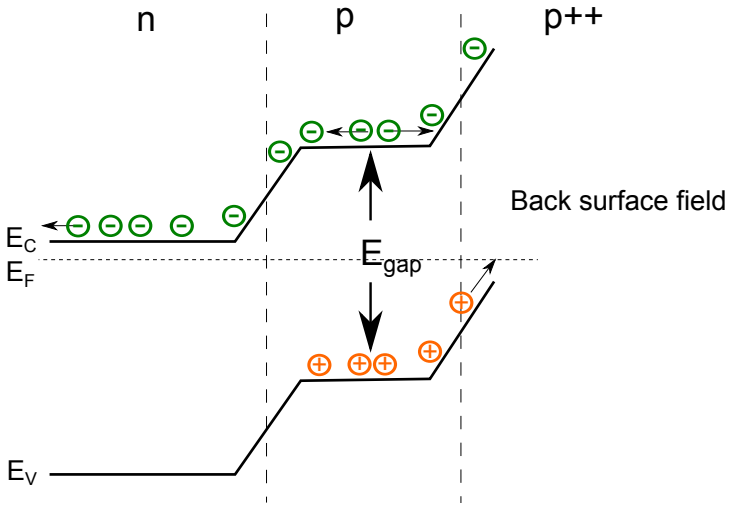

Fig. 2.12: Band diagram of a typical silicon solar cell (dark condition). Image inspired by [42].

200μm - 400μm thick and is covered with a thin (50μm) n-doped layer. The free charge carrier lifetime, τ, is around 50μs and is strongly dependent on the purity of the material. The charge carrier diffusion length, L_D, is a measure of the recombination in the bulk. The larger the diffusion length the less the recombination. It can be expressed as

$$L_D = 2\sqrt{D \cdot \tau}, \tag{2.35}$$

where D is the diffusion constant of the material. The diffusion constant is linked to the carrier mobility, μ, via the Einstein relation

$$D = \frac{k_B T}{q}\mu, \quad \frac{k_B T}{q} = U_T, \tag{2.36}$$

where U_T is the thermal stress. The mobility itself is limited by two influential factors: dispersion by lattice interaction and ionic impurities (dopants). Consequently, the more impurities that are contained in a material the thinner the layers have to be fabricated in order to reduce losses via recombination [42].

Process	Loss mechanism
Incident light	reflection, transmission, scattering
Absorption	weak absorber, spectral mismatch
Exciton diffusion	recombination
Charge separation	energy level mismatch, charge carrier recombination
Charge transport	traps, series resistance, low mobility
Charge carrier extraction	leakage current, energy barrier at electrodes

Tab. 2.1: Overview of physical processes and correlated loss mechanisms.

2.4.2 Organic solar cell physics

The absorbing materials in organic solar cells are organic dyes, which upon the absorption of photons generate Frenkel excitons. These dyes have a high absorption coefficient resulting in light penetration depthes of only 50nm - 200nm. This facilitates the use of very thin layers and cells, which puts low requirements on the layer morphology as structural disorders cause flat traps. Moreover, they can be easy produced on flexible substrates. As discussed previously, organic semiconductors all do have a π-based electronic conduction in a conjugated system due to an alternation of single and double bonds of carbon atoms within the molecule. The $\pi - \pi^*$ molecular orbitals of this π-electron system correspond to the HOMO and acLUMO, respectively, and enable light absorption or light emission from the molecule. In the case of solar cells light will be absorbed and transformed into electrical energy. The basic conversion process and the correlated loss mechanisms in an organic solar cell can be described by a sequential process of steps: The first step is the absorption of incident light with an energy of $e = h \cdot f$, [32], by the absorber and the subsequent formation of an excited state π^* on the molecule. The exciton diffusion towards an interface is a consequence of the overlap of two neighbouring molecular orbitals (one in excited state). The overlap results in the transformation of the neighbouring molecule into an excited state and the return to the ground state of the initial molecule. Excitons can "move" in such a manner by up to 68nm±20nm in CuPc [58]. The second step is discussed in the next subsection.

Exciton generation and diffusion

Under irradiation excitons are generated in the absorber material. This location-dependent process can be expressed by the exciton generation rate $G_e(x)[\frac{1}{m^3 s}]$. The specific exciton generation rate at a specific location x within a layer and for a specific wave length λ of incident light is:

$$\begin{aligned} G_E(\lambda, x) &= \alpha(\lambda) I(\lambda, x) \frac{\lambda}{h \cdot c} = \frac{4\pi}{\lambda} k(\lambda) \frac{1}{2} \varepsilon_0 c n(\lambda) |E(\lambda, x)|^2 \frac{\lambda}{h \cdot c} \\ G_E(\lambda, x) &= 2\pi \frac{\varepsilon_0}{h} k(\lambda) n(\lambda) |E(\lambda, x)|^2, \end{aligned} \tag{2.37}$$

where $\alpha(\lambda)$ is the wavelength dependent absorption coefficient, $I(\lambda, x)$ is intensity of the incident light in the layer, (λ) the wave vector, n is the real share of the complex index of wavelength dependent refraction and k the imaginary share, ε_0 is the vacuum permittivity, c is the speed of light, h is the Planck constant, and E(λ,x) is the location and wavelength dependent absorbed energy in the layer [54]. The intensity of the incident light, $I = \frac{1}{2}\varepsilon_0 cn\,(\lambda)\,|E\,(\lambda, x)|^2$ at a depth x in the irradiated layer forms the basis for (2.37). Because $|E\,(x)|^2 = Pd\,(x)\,|E_0|^2$ with the normalized photon flux density $Pd\,(x)$, equation (2.37) can be written as (using the incident light intensity $I_0 = \frac{1}{2}\varepsilon_0 c\,|E_0|^2$):

$$G_E\,(x) = \frac{4\pi}{h \cdot c} I_0 \cdot k \cdot n \cdot Pd\,(x)\,. \tag{2.38}$$

By using the equation of continuity

$$\frac{\partial \rho}{\partial t} + div\,\mathbf{j} = 0 \tag{2.39}$$

a stationary diffusion equation for excitons (no distinction is made for triplet or singlet excitons) can be found for a fixed wave length λ and a location-dependent exciton generation rate $G_e(x)$ as follows

$$\frac{\partial n_E\,(x,t)}{\partial t} = 0 = G_E\,(x) - \frac{n_E\,(x)}{\tau_E} + D_E \frac{\partial^2 n_E\,(x)}{\partial x^2}, \tag{2.40}$$

where $n_E[\frac{1}{m^3}]$ is the exciton density, $\tau_E[s]$ the exciton life time and the exciton diffusion constant $D_E[\frac{m^2}{s}]$. The exciton diffusion length, L_E, is the root of the multiple of D_E with the exciton lifetime τ_E: $L_E = \sqrt{D_E \cdot \tau_E}$ [54].
In organic solar cells the exciton dissociation at the heterojunction between the donor and acceptor material has to be taken into account for the exciton diffusion equation. This is achieved by adding a dissociation term (physically an electrostatic force occurs at the interface) expressed by $F(x - x_G)$. Furthermore, the dissociation at the metal-semiconductor interface has also to be included. By including all these effects the exciton diffusion equation (for an arbitrary wave length) for steady state conditions and the location-dependent exciton density $n_E(x)$ becomes [54]:

$$0 = \frac{4\pi}{h \cdot c} I_0 \cdot k \cdot n \cdot Pd\,(x) - \frac{n_E\,(x)}{\tau_E} + D_E \frac{\partial^2 n_E\,(x)}{\partial x^2} - F\,(x - x_G)\,n_E\,(x)\,. \tag{2.41}$$

2.4.3 Exciton dissociation

The conventional photon absorption mechanism yields the creation of Frenkel excitons with an exciton binding energy of around ≈ 0.5eV. According to the Onsager model this requires large fields ($\approx 10^6 V/cm$) are required to dissociate these excitons into free charge carriers. These field intensities

cannot be generated by built-in voltages. This binding energy is also much larger than the thermal energy at room temperature ($\approx 25meV$), thereby making thermal dissociation practically impossible. In efficient solar cells performance the dissociation of excitons must be faster then competing recombination processes. These processes are: radiative recombination such as fluorescence, and phosphorescence within ns-μs, or non-radiative recombination via phonons, heat, or photoemission from metal electrode. The latter is a consequence of the surface states of the metal electrode. Therefore, dissociation is induced at a material interface. The donor-acceptor interface forms a heterojunction, which results in a band shift. This shift causes there to be an electro chemical potential difference across the interface, which is strong enough to overcome the exciton binding energy. The dissociation process at the donor-acceptor interface takes place on the fs-scale and is, therefore, 1000-times faster than any other competitive recombination process. The dissociation takes place, if the following relation between the energy states of the excited donor molecule and the acceptor molecule is fulfilled:

$$I_{D^*} - EA_A - E_b < 0, \tag{2.42}$$

where I_{D^*} is the excited donor, EA_A the electron affinity of the acceptor and E_b the exciton binding energy [59]. The driving force at the interface is the difference in the electron affinity, EA, of the donor and acceptor molecule. Hence, for dissociation the EA and the ionization potential, IP, of the acceptor should be higher than those of the donor molecule. In this dissociation process the Frenkel exciton is transformed into a charge transfer (CT) exciton, where the negative charge stays on the LUMO of the acceptor and the positive charge on the HOMO of the donor. This CT exciton (Wannier-Mott exciton) has a much smaller binding energy as it is spread over at least two molecules. Subsequently, the negative and positive charges are considered to be an individual electron and hole. The energy stored within the separated positive and negative charges equals the difference in their electrochemical potentials μ_{elchem} [60]. The binding energy can also overcome with the help of a combination of the built-in voltage and the thermal energy. In this process this CT exciton is thermally dissociated into two polarons. The electron as well as the hole polaron have a strong interaction with the lattice (or in polymers with the polymer chains) which means the polarons have a large effective mass. Due to its interaction it polarizes its neighbourhood yielding its name: polaron. These polarons or CT pairs are stable on the ms-scale [42]. A band structure of a organic solar cell is shown in Figure 2.13. According to the band diagram a charge transfer for electrons can be expected. Whether a photoinduced charge transfer for holes exists for the material combination CNT and the respective dye still has to be investigated. In contrast to inorganic solar cells little space charge exists in organic solar cells, because the intrinsic amount of free charge carriers is

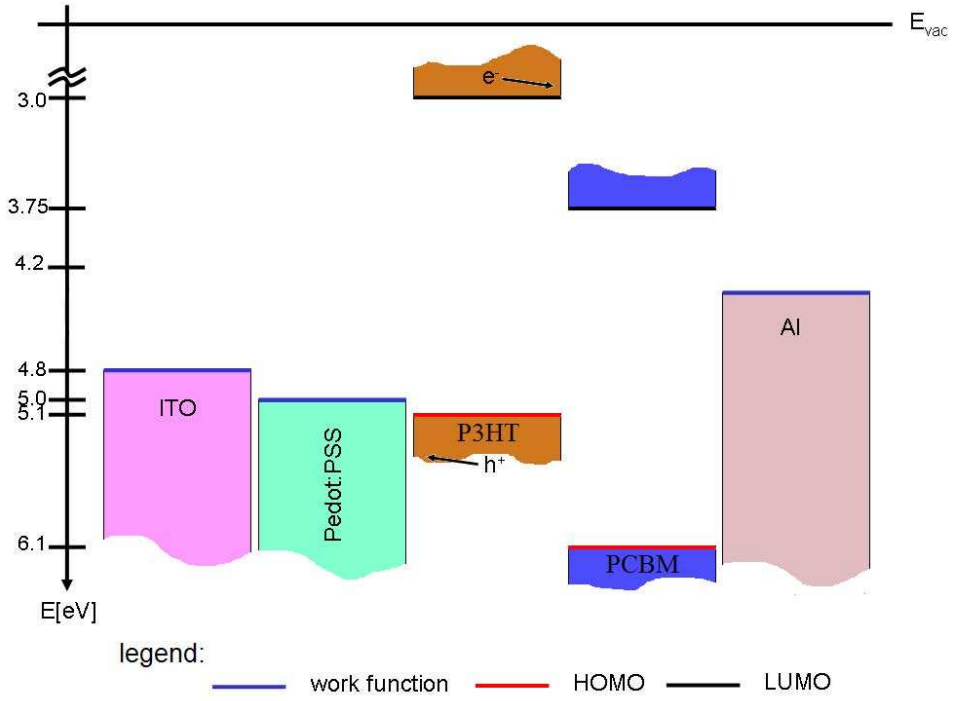

Fig. 2.13: Band diagram of a heterojunction organic solar cell with P3HT and PCBM as donor-acceptor combination.

very low. However, an increase in the space charge can be achieved by doping the organic materials with appropriate dopants (or with high injection or extraction barriers).

2.4.4 Quasi-Fermi levels and open circuit voltage

Under illumination the electron density is larger compared to the electron density without illumination ($n_e > n_e^0$). The same occurs for the hole density ($n_h > n_h^0$). Due to the increase of the electron density the Fermi level moves closer to the conduction band and due to the increased hole density it simultaneously moves closer to the valence band. One solution to this predicament is to split the Fermi level into two quasi-Fermi levels. One for the electrons and the other one for holes. Consequently, the description of non-equilibrium states can be given in terms of these quasi-Fermi levels. The descriptive use of a quasi-Fermi level distribution in the non-equilibrium state (e.g. caused by photogeneration) is enabled by the fact that the equilibrium state adjusts much faster within a band than between different bands (that means for either the negative charge carrier density *or* the positive charge carrier density). As a consequence, the densities can be described using separate Fermi distributions called quasi-Fermi levels (see

Figure 2.14). The band diagram of a solar cell under dark conditions and

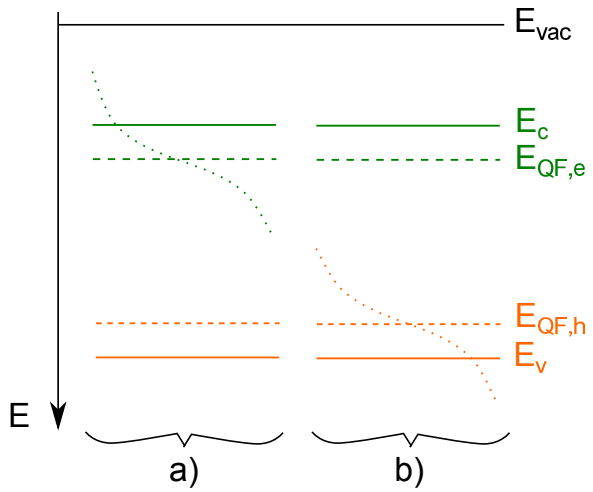

Fig. 2.14: Quasi-Fermi levels. a) Quasi-Fermi level for negative charge carriers and b) Quasi-Fermi level for positive charge carriers of organic solar cells. Image inspired by [42].

illuminated (short circuit and open circuit) is shown in Figure 2.15. It is

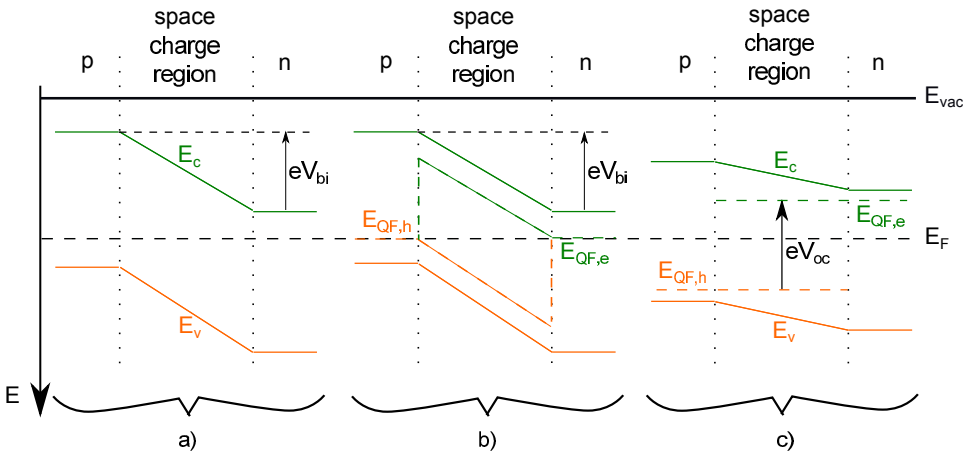

Fig. 2.15: Band diagrams of a solar cell under a) dark conditions and b) illuminated and short circuit condition c) illuminated and open circuit condition. Image inspired by [42].

assumed that the anode and the valence band of the active material as well as the cathode and the conduction band form ohmic contacts. Under illumination the Fermi level splits into two quasi-Fermi levels and the gradient of these levels yields short circuit current. Under open circuit condition and illumination the splitting of the Fermi level is due to the photogeneration of charge carriers [42]. As soon as the bands become flat, no more transport of

electrons and holes towards the outer electrodes is possible. The resulting open circuit voltage can be expressed as

$$V_{oc} = E_{QF,e} - E_{QF,h} < V_{bi}, \tag{2.43}$$

where $E_{QF,e}$ and $E_{QF,h}$ are the quasi-Fermi levels of electrons and holes, respectively, and V_{bi} is the built-in voltage, [61]. This voltage will remain intact under the conditions of high temperature or weak illumination. The temperature dependence at the maximum generation rate can be derived from the difference of the two quasi-Fermi levels equation (2.43) and from the photogenerated charge carrier density given by

$$n \cong N_c e^{-\frac{E_c - E_{QF,e}}{k_B T}} \tag{2.44}$$

for negative charge carrier density and by

$$p \cong N_v e^{\frac{E_v - E_{QF,h}}{k_B T}} \tag{2.45}$$

for positive charge carrier density [42]. By inserting equation 2.44 and 2.45 into equation 2.43 the temperature dependence of the open circuit voltage is obtained, where

$$V_{oc} = (eE_c - eE_v) - k_B T \left(\ln \frac{N_v}{p} + \ln \frac{N_c}{n} \right) \tag{2.46}$$

$$V_{oc} = eE_{gap} - k_B T \ln \left(\frac{N_v N_c}{pn} \right). \tag{2.47}$$

2.4.5 Solar cell parameters

The main solar cell parameters are introduced below.

Unilluminated I-V curve

The I-V behaviour under dark conditions is the same as the I-V curve of a common pn-diode, which can be expressed by the Shockley equation

$$I_D = I_S \left(e^{\frac{U}{n \cdot U_T} - 1} \right). \tag{2.48}$$

Short circuit current density: J_{sc}

Under illumination a photocurrent is generated. This photocurrent moves the diode I-V curve down the I axis in accordance with equation (2.48). For the application of no external voltage, the short circuit current I_{sc} is obtained. As this parameter depends on the device size, usually the short circuit current density, J_{sc}, is usually used, which is independent of device size.

The current-voltage dependence is dependent on the wavelength of the incident radiation. The spectra are called photo current spectra. These spectra show the efficiency of the wavelength dependent charge carrier generation and transport [42].

Open circuit voltage: V_{oc}

The voltage level where the current becomes zero is called the open circuit voltage, V_{oc}. It is correlated with various materials properties such as the HOMO-LUMO level of the organic semiconductors and the work function of the electrode materials. Furthermore, the open circuit voltage depends on temperature and other effects, such as charge carrier mobilities (Dember-voltages) [42].

Fill factor: FF

Under illumination the I-V curve crosses the fourth quadrant, which means the product of current and voltage is negative. In this region the solar cell is working as an active device. Consequently, power is generated and fed into the circuit. The point of the I-V curve, where the maximum power is generated, is called the maximum power point (MPP). This is used as the operating point of the device. As shown in Figure 2.19 the short circuit current density, J_{sc}, and the open circuit voltage, U_{oc}, define the theoretical maximum power generated by the cell. The real achievable MPP is the product of the maximum values of the measured current density and voltage. The corresponding J, U values are J_{mpp} and U_{mpp}, respectively. If J_{sc}, U_{oc} and J_{mpp}, U_{mpp} span a rectangular area in the I-V-diagram two areas of different size are created. The correlation of these is the fillfactor defined by

$$FF = \frac{P_{\max}}{V_{oc} \cdot I_{sc}} = \frac{V_{MPP} \cdot I_{MPP}}{V_{oc} \cdot I_{sc}} \tag{2.49}$$

The fill factor is mainly influenced by the series resistance of the device, [62]. The fill factor decreases for larger series resistance. It is used to characterize the quality of device performance. The fill factor for anorganic cells is within the range of $FF = 0.75 - 0.85$ and in the range of $FF = 0.5 - 0.6$ for organics. Calculating the fill factor from the integral of the I-V curve under illumination yields bigger values and is not comparable with the fill factor determined by equation (2.49). The fill factor is visualized in Figure 2.16.

External quantum efficiency: EQE

Another important parameter is the incident photon to current conversion efficiency (IPCE), which gives the wavelength-dependent effectiveness of the cell to convert photons (of a specific wavelength) into charge carriers. This conversion happens at the first step at the donor/acceptor interface, where

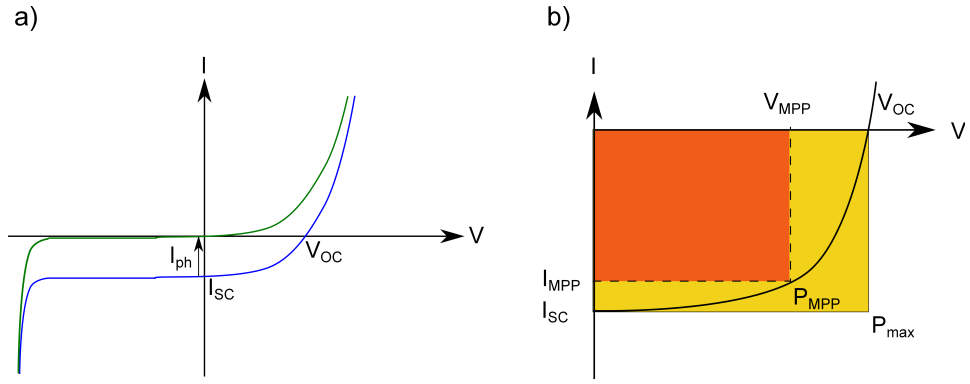

Fig. 2.16: a) I-V curve of a solar cell under dark condition and illuminated. The I-V curve is downshifted under illumination due to the photocurrent. The device is working as current source. b) visualization of the fill factor. Theoretically the maximum power is determined by $P_{maxtheor} = I_{sc} \cdot V_{oc}$. The measured power differs from this value. The fill factor is expressed as the ratio of the measured value and $P_{maxtheor}$.

Frenkel excitons are dissociated into CT excitons with an efficiency of nearly 100 %. However, during the dissociation of these CT excitons have to be fully dissociated by thermal activation into polarons, losses occur. The incident quantum efficiency gives the overall efficiency of the conversion process of photons to charge carriers, as it includes all dissociation and transport losses [33]. The IPCE can be expressed as

$$IPCE = \frac{hc}{e} \cdot \frac{J_{sc}}{\lambda \cdot I_0}, \tag{2.50}$$

where h is the Planck constant, c is the speed of light, λ the wavelength of the incident photon and I_0 the radiation intensity (I_0=100mW/cm^2 at AMG 1,5). Furthermore, it gives a spectra according to each specific wave length and can be expressed using the short circuit current density and the incident light intensity, which transforms equation 2.50 to:

$$IPCE\,[\%] = \frac{J_{sc}\left[\frac{\mu A}{cm^2}\right]}{I_0\left[\frac{mW}{cm^2}\right]} \cdot \frac{124}{\lambda\,[nm]}. \tag{2.51}$$

This gives the IPCE as a percentage and represents the correlation of incident photon to photocurrent more conveniently [63]. The photo current density is proportional to the incident light intensity

$$J_{sc} \propto I_0, \tag{2.52}$$

which means that the photo current spectra can be normalized and the influence of e.g. layer thicknesses can be studied.

Efficiency

The proportion of converted electrical power (P_{MPP}) relative to the incident light power (P_L) defines the efficiency, η. It is expressed as:

$$\eta = \frac{P_{MPP}}{P_L} = \frac{V_{MPP} \cdot I_{MPP}}{P_L} = FF \cdot \frac{V_{oc} \cdot I_{sc}}{P_L}. \tag{2.53}$$

The equation (2.53) implies that for good device performance three parameters have to be as large as possible. These are the fill factor, the short circuit current and the open circuit voltage. Hence, tuning just one parameter is not enough to obtain a large efficiency [33].

Equivalent circuit of a solar cells

Illumination of the solar cell induces the formation of an electron-hole pair. This is followed by a charge separation process at the interface of the donor and acceptor, called dissociation. The basic architecture of a heterojunction solar cell with such an interface is shown in Figure 2.17. The dark condition

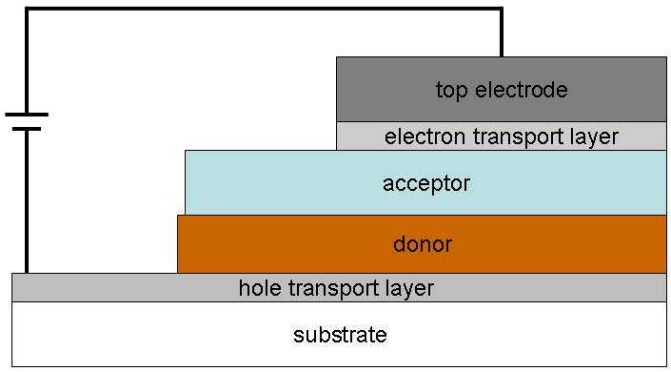

Fig. 2.17: Design of a typical heterojunction solar cell. The heterojunction is formed at the donor and acceptor interface.

properties of such a junction are the same as those of a diode. The current of a diode is given by the thermionic injection model, [64]:

$$I = -I_D = -I_s exp^{\left(\frac{eU}{k_B T} - 1\right)}, \tag{2.54}$$

where I_s is the saturation current under reverse bias, e the elementary charge and U is the bias voltage. Under illumination it works as a current source and can be modelled as a current source in parallel with a diode. From 2.54 we get under illumination

$$I = I_{ph} - I_D = I_{ph} - I_s exp^{\left(\frac{eU}{k_B T} - 1\right)}, \tag{2.55}$$

where I_{ph} is the photo current. A real cell has two additional resistances, the shunt resistance R_{sh}, related to shorts and the series resistance R_s, representing the contact and bulk semiconductor resistances. The equivalent circuit is shown in Figure 2.18. By taking into account the two resistances

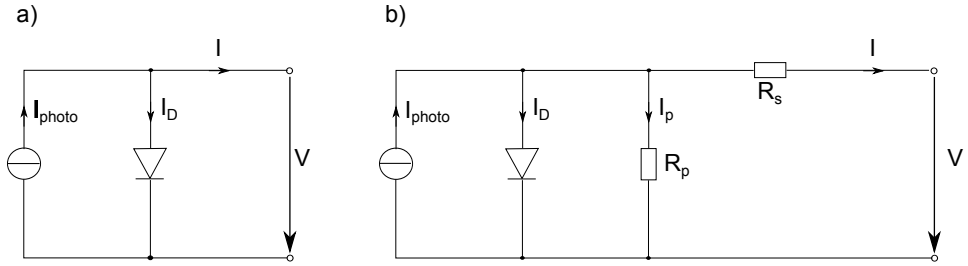

Fig. 2.18: Equivalent circuit of an ideal (left) and real (right) solar cell.

and an ideality factor b (b=1 for an ideal diode) equation 2.55 extends to

$$I = I_{ph} - I_D - \frac{U_{R_{sh}}}{R_{sh}} = I_{ph} - I_s exp^{\left(\frac{U+R_s \cdot I}{b \cdot k_B T} - 1\right)} - \frac{U + R_s \cdot I}{R_{sh}}. \qquad (2.56)$$

The influence of R_s and R_{sh} on the I-V behaviour in comparison to an ideal cell is shown in Figure 2.19.

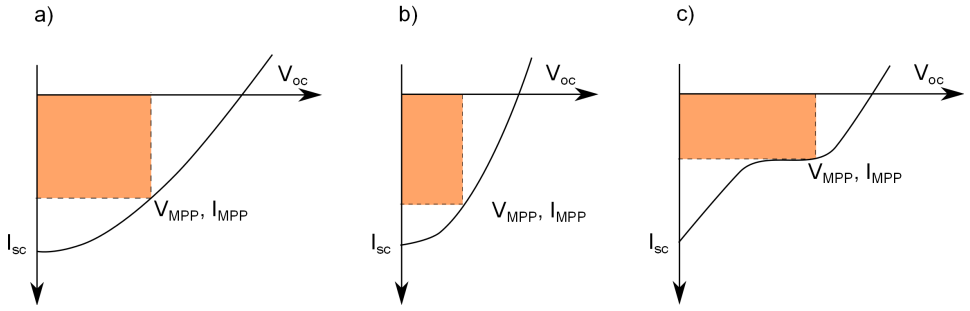

Fig. 2.19: I-U characteristic under illumination. a) $R_{sh} = \infty$ b) R_{sh} is small c) R_s is large. Image inspired by [65].

2.4.6 Current source versus battery

In ideal current sources the current is completely independent of the applied voltage. In real current sources the current drops either linearly with increasing applied voltage or nonlinearly (like in solar cells). From inside the device the electrons are ejected to the anode. The counter electrode, to where holes are ejected from inside the component, is called the cathode. The anode and cathode are not correlated with the energy level of the electrodes of the component. The difference in the energy levels of the electrodes, which yields a voltage, is determined by the positive and negative

terminal. The positive terminal denotes the electrode with the higher energy level and the negative terminal is the electrode with the lower energy level. This description determines the direction of voltage drop. In a zinc-lead car battery an oxidation reaction takes place at the zinc electrode. Electrons are generated at the zinc electrode (anode - positive terminal), which reach the lead electrode (cathode - negative terminal) with through the outer circuit. If the car battery is charged, the polarity is reversed. For electroplating processes the positive terminal is the anode and the negative terminal the cathode.
In organic solar cells the indium tin oxide (ITO) electrode (if ITO is used) acts as the cathode as it collects the holes from within the cell or in the outside circuit. The counter electrode (mostly metal) is the anode. The anode material has a low work-function which means it is energetically at a higher level than the cathode, which is made from a high work-function material. The positive terminal is the anode (usually metal contact) and the negative terminal is the cathode (usually the transparent conductive oxide (TCO)). The current flow in Figure 2.20 is marked with an arrow.

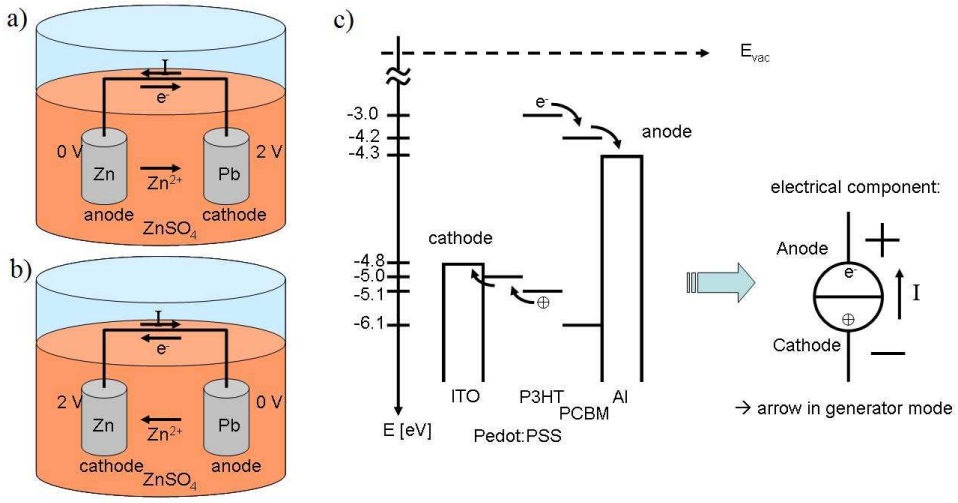

Fig. 2.20: Comparison of current source as galvanic component and current source as solar cell component. a) battery in generator mode. b) battery in recharge mode. c) organic solar cell.

2.5 Summary

In this chapter an introduction of the physics of solar cells was given. The basic working mechanisms in the context of irradiation from the sun, absorption properties of the absorber, and the process of free charge carrier generation as well as charge carrier transport properties and collection at the outer electrodes have been discussed.

3. MATERIALS

In the following the materials used in this work are introduced and the most common methods of analysis are described. All materials, which are introduced in the following, are organic semiconductors. Hence, they can absorb radiation due to their band gab. The relative energetic position of HOMO and LUMO to the vacuum energy level (and in some cases additional the energetic position of the Fermi-level in the band gap) defines, whether the material is a donor or an acceptor. These materials are categorised in a donor-acceptor combination for organic solar cell application.

3.1 Acceptor materials

An acceptor is a molecule that receives an electron from an excited molecule due to the match of energy levels at the interface of these two molecules.

3.1.1 Buckminsterfullerene (C_{60})

The fullerene consists of sixty carbon atoms formed in twelve pentagon and twenty hexagon rings of $sp^2 - hybridised$ carbon atoms. It is an aromatic alkene. It is the most commonly used acceptor molecule in organic photovoltaic devices, together with its various derivatives such as C_{71} or PCBM. On the basis of its major impact in research it is explained in detail. Its derivative PCBM is also discussed. In order to form a closed cage out of pentagons and hexagons all fullerenes fit the formula

$$Fullerene \in C_{20+m}, m \in \mathbb{N}. \tag{3.1}$$

The structure of a C_{60} is a "truncated icosahedron" [66]. The truncated icosahedron is derived from an icosahedron. Each of the twelve vertices are truncated and replaced by pentagons. This process converts each of the twenty former triangular faces into hexagons, resulting in a soccerball-shaped structure (see Figures a)-b) in Figure 3.1). The absorption spectrum is given in Figure 3.3. There are many other possible hollow cage structures for the fullerenes amongst other things resulting in different absorption behaviour (e.g. the C_{71}, which has a larger absorption in the visible range than the C_{60}). A common feature of all closed fullerene structures is that they consist of twelve pentagons and with a variable number of hexagons.
The synthesis of fullerene was first described by Krätschmer et al. [69]. The

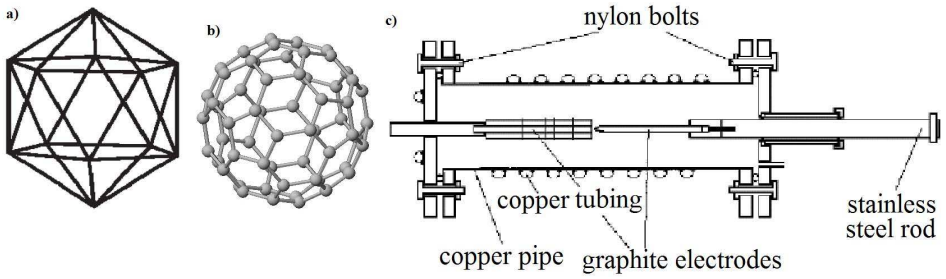

Fig. 3.1: Fullerenes. a) icosahedron. b) truncated icosahedron (Fullerene). c) synthesis chamber for C_{60}. Images taken from [67] and [68].

process reached 100% efficiency in 2008 in the work of $Gomez - Lor$ and $Martin - Gago$ [70]. Krätschmer used a process chamber with a 13,3kPa helium inert gas atmosphere in which a graphite electrode (rod) was evaporated by resistive heating (see Figure c) in Figure 3.1). This technique produces a condensate containing amorphous carbon, C_{60} and other fullerenes. The C_{60} and the other fullerenes can be extracted from the condensate by using an organic solvent (toluene, benzene) to dissolve it; the rest being insoluble. Drying the supernatant yields a dark brown to black residue consisting of C_{60} and other fullerenes. Fullerenes with encaged atoms inside are called "endohedral fullerenes". These enable for example the electrical engineering of the bulk material [71]. The density of C_{60} is $1.65\frac{g}{cm^3}$, the cage diameter is 7.11Å, the ionisation potential is $7.6 \pm 0,2eV$, the electron affinity is $2.6eV$, the bandgap is 1.8eV, it forms a face-centred cubic lattice structure and the absorption coefficient is $6.07 \cdot 10^{-5}\frac{1}{cm}$ at a wavelength of 220nm [72]. All collected data from literature agree with the given values. Another notable feature of the buckminsterfullerene (C_{60}, also called buckyball) is its reversible uptake of up to six single electrons [73].

3.1.2 Phenyl-C_{61}-butyric acid methyl ester (PCBM)

Due to the poor solubility of C_{60} in organic solvents (less than 6mg/mL), it has been chemically functionalized. An important example is the phenyl-C61-butyric acid methyl ester (PCBM) (CAS number 160848-22-6) (see Figure 3.3). The butyric acid methyl esther group attached to the surface of the C_{60} yields a much better solubility in organic solvents (up to 100mg/mL in dichlorobenzene). This makes PCBM one of the most commonly used acceptor materials for solution processed organic photovoltaic devices. The mobility of electrons in spin cast PCBM films is around $2 \cdot 10^{-3}\ cm^2/Vs$ (in single crystals up to $0.5cm^2/Vs$) and the density is $1.5g/cm^3$ [74]. The absorption spectra of PCBM and C_{60} are shown in Figure 3.3. The band diagram is shown in Figure 3.2.

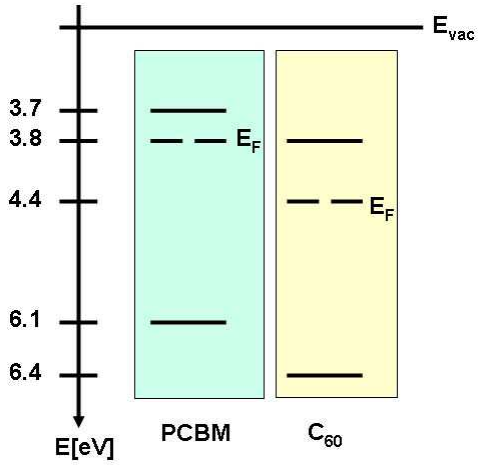

Fig. 3.2: Band diagram of PCBM (left) and C_{60} (right), where E_{vac} is the vacuum energy, E the energy in eV, and E_F is the Fermi level. Values taken from [75], [76], and [77].

3.2 Donor materials

The used donor materials will be introduced in the following.

3.2.1 Copper(II)phthalocyanine (CuPc)

Phthalocyanines are organic macrocyclic molecular semiconductors, which are easy and cheap to synthesize. They show excellent resistance towards UV irradiation. This makes them a popular material for application. The CuPc (CAS number 147-14-8) consists of isoindol components which are imino-bridged for the aza-function to its neighbouring isoindol component (see Figure 3.6). In its centre the ionized metallic atom, copper, is bound with two nitrogen atoms and complexed with the other two free valence electrons from the other two nitrogen atoms. Its absorption coefficient is about $1.5 \cdot 10^5 cm^{-1}$ in the visible range [79]. The UV-vis spectra and molecular structure are shown in Figure 3.6. These molecules are usually deposited using thermal evaporation. The resulting layer morphology is poly crystalline at room temperature [80]. In a crystal the molecules are stacked with a slight offset between each other and with a separation of about 3.4Å [81]. The electrical conductivity is space charge limited and reaches values of $1 \cdot 10^{-6} \frac{S}{cm}$ [82]. It is also strongly anisotropic [83]. Upon doping with acceptor gas the conductivity rises up to $1 \cdot 10^{-2} \frac{S}{cm}$ but the dopants are unstable [84]. Phthalocyanines can be synthesized by using different methods, in which the metal (e.g. copper) can be added either before or after cyclization. For an overview see Figure 3.4. CuPc is known to be a p-type semiconductor with a hole mobility of $\mu_h = 0,1 - 1 \frac{cm^2}{Vs}$. In order to dissolve this molecule

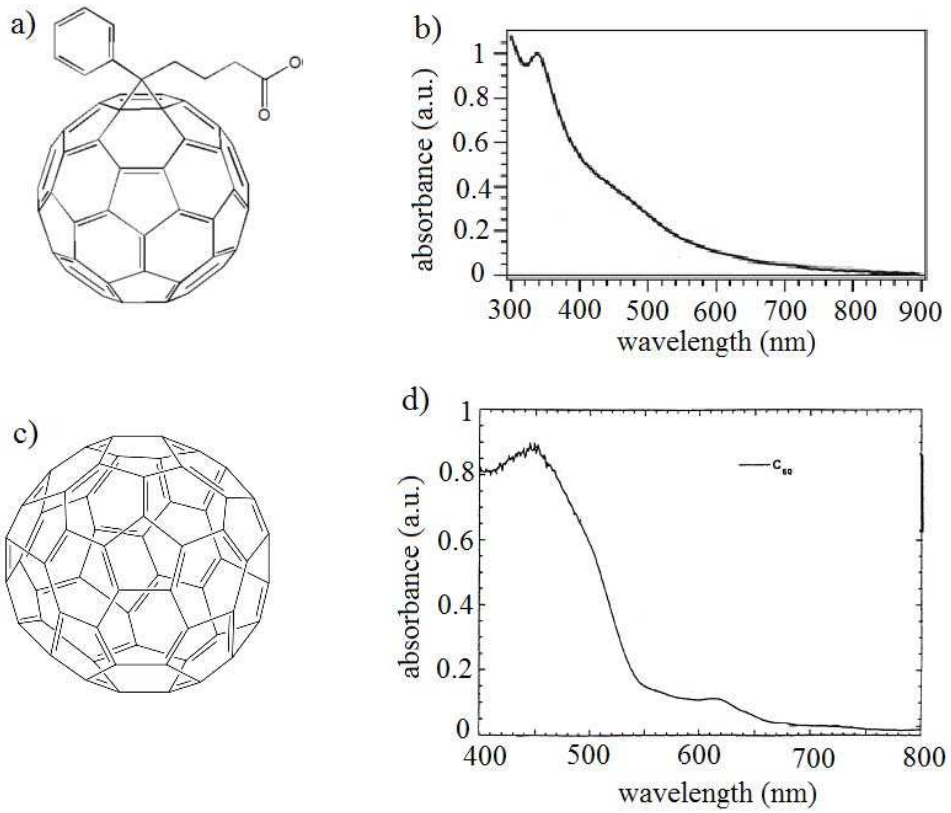

Fig. 3.3: Structures and UV-vis spectra of C_{60} and PCBM. Left: structures of a) PCBM, and c) C_{60}. Right: UV-vis spectra of b) PCBM and d) C_{60}. Images a) and b) taken from [78] (reprinted from Publication Chemical Physics Letters, Vol. 445, issues 4-6, S. Cook, H. Ohkita, Y. Kim, J. J. Benson-Smith, D. D.C. Bradley, J. R. Durrant, A photophysical study of PCBM thin films , 276, ©(2007), with permission from Elsevier), c) and d) taken from [30].

covalently bonded functionalising groups have to be added. This peripheral substitution is done at the benzo group with e.g. a sulfuric group. These sulfuric groups cause, however, aggregation of the dye in the solvent [86]. This process is additionally caused by the metal atom in the middle of the phthalocyanine (copper in this case) [87]. All phthalocyanines have two absorption bands: one in the visible region of 500nm-700nm (Q-band) and another one in the near UV at 300nm-400nm (Soret band). The absorption of a photon causes the $\pi \rightarrow \pi^*$ transition, which generates an excited state. This results in a charge transfer of an electron from the outer benzene rings into the inner macrocyclic ring [88] and [89].
CuPc shows high polymorphism. The polymorphism occurs due to the relatively weak intermolecular forces. This also has an influence on the conductivity as well. At least five different polymorphs are known for CuPc:

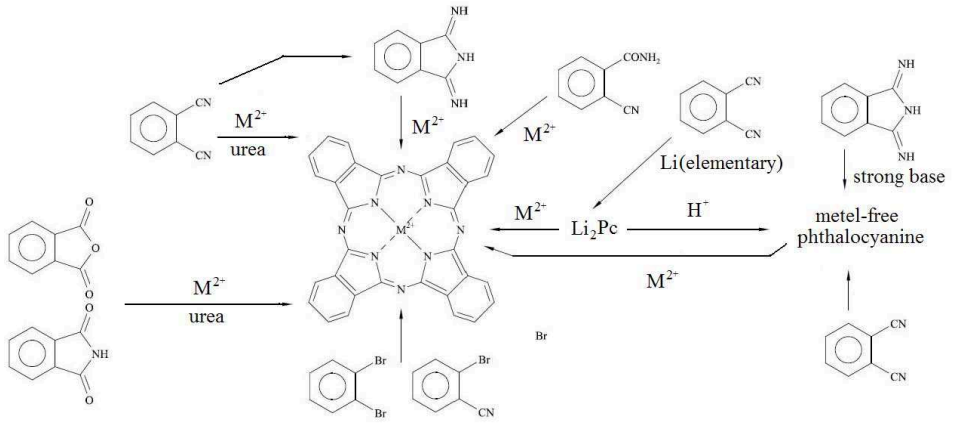

Fig. 3.4: Overview of the phthalocyanine synthesis when using different reactants. Image inspired by [85].

$\alpha, \beta, \gamma, \delta$ and ϵ. However, only the β-CuPc turns out to be stable, whereas the others are metastable. It has already been used successfully in organic solar cells [90].

3.2.2 Copper phthalocyanine-3,4',4",4"'-tetrasulfonic acid tetrasodium salt (CuPc-TS)

Copper phthalocyanine-3,4',4",4"'-tetrasulfonic acid tetrasodium salt (CuPc-TS) (CAS number: 123439-80-5) is the water soluble anion derivative of CuPc (see Figure 3.6). CuPc-TS is synthesized by using a process of sulphonation. A sulphuric group (HSO_3) is introduced to the aromatic ring with a covalent carbon-nitrogen bond. The corresponding sulphuric acids are $R-SO_2OH$ (see Figure 3.5). The attached sulphuric acid groups deactivate

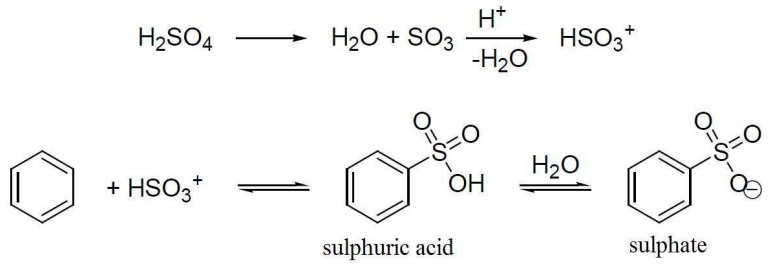

Fig. 3.5: Sulphonation scheme for aromatic rings. Image inspired by [85].

the aromatic ring. CuPc-TS solar cells with titanium dioxide nanoparticles produced using a layer-by-layer technique have been investigated by [91]. It has been reported that CuPc-TS forms ring-stacked aggregates in solution, which is in contrast to non-substituted CuPc [92]. These aggregates were

suggested to be responsible for the high open circuit voltage of solar cells with CuPc-TS fabricated by common spin coating, and with C_{60} as acceptor [93]. The absorption spectrum is shown in Figure 3.6.

3.2.3 Copper(II)3,10,17,24-tetra-tert-butyl-1,8,15,22-tetrakis (dimethylamino)-29H,31H-phthalocyanine (CuPc-DMA)

The Copper(II) 3,10,17,24-tetra-tert-butyl-1,8,15,22-tetrakis (dimethylamino)-29H,31H-phthalocyanine (CuPc-DMA) (CAS number: 61113-98-2) is a butyl and amino functionalized CuPc derivative (shown in Figure 3.6). It has been used for non covalent sidewall functionalization of hydrophilized multi-walled carbon nanotube (MWCNT) [94]. Chemos GmbH (Germany) supplies a closely related derivative, the 4,4',4",4'-tetra-tert-Butyl copper phthalocyanine (CAS: 61113-98-2), is Chemos GmbH in germany.

3.2.4 Regioregular poly(3-hexylthiophen-2,5-diyl) (rr-P3HT)

In recent years, regioregular poly(3-hexylthiophen-2,5-diyl) (rr-P3HT) (CAS number: 156074-98-5) has supplanted many other polymers of the Poly(p-phenylene vinylene) (PPV) series as the donor material of choice. The polymer rr-P3HT has a lower band gap (1.9eV) and higher hole mobility (μ_h) [98]. Devices containing rr-P3HT achieved power conversion efficiencies of η>5% [99]. However, rr-P3HT has become one of the most important polymer donor materials, although it has several problems related to its synthesis (e.g. complex procedures under cryogenic conditions [100]), purification, and intrinsic electronic properties. The regio-regularity, molecular weight, and polydispersity of P3HT have major influence on the device performance of BHJ solar cells [101]. In addition, the reproducibility of results is much affected by the commercial source. This implies that the purity and structural control of the synthesized P3HT varies between suppliers. Another disadvantage of this material is its small absorption band (FWHM=150nm), which yields in combination with its band gap a theoretical absorption of only 30% of the solar spectrum. The UV-vis spectra and the structure is shown in Figure 3.8. Additionally the relatively high lying HOMO limits the open circuit voltage to 0.6V - 0.7V, and the cells show instability under atmospheric conditions.
Postprocess thermal annealing tremendously improves the morphology of the bi-continuous phase and the crystallinity of the P3HT [102]. The quasi one-dimensional, linear π-conjugated system of rr-P3HT causes an anisotropic charge transport. This transport has its maximum conductivity along the stacking direction of the chains. Thermal annealing also yields randomly orientated nanocrystalline domains [35]. The anisotropic structure yields different transport directions for charge carriers (see Figure 3.7).

3.3 Combined acceptor and electrode materials

The function of the electrode material in solar cells is to level off or to reduce the injection and ejection barrier between the semiconductor material and the outer electrical circuit. CNTs have been reported as electrode materials by several authors [105], [106], [107], [108]. CNT electrodes can be purchased from a commercial source [109]. In addition, several authors have used them as an acceptor material for an organic solar cell in combination with either P3HT, or poly(3-octylthiophene) (P3OT) [110], [111], [112] and [113], or with polythiophene and PPV [114], or as improvement of the conductivity of holes in the donor layer [115], or with C_{60} were attached to the CNTsidewall and mixed with P3HT [116]. Others have covalently bonded protonated porphyrin are covalently bond to the CNT sidewall [117]. One author has used them to improve the conduction of holes in the donor layer, [115]. In another approach the donor was attached covalently to the CNT leading to monochromatic IPCE, of up to 4.2% have been achieved for a bilayer cell and 8.5% for a multilayer cell, [118], [119]. The location of the CNT in the solar cell is also important, [120]. Barazzouk et al showed that by using the CNT as an acceptor in a dye-sensitized solar cell (DSSC) it was photoactive [121]. A good overview about CNT in organic solar cells is given by [122].
Donor and acceptor states in pure single single-walled carbon nanotube (SWCNT) have been observed using scanning tunneling microscopy (STM) and scanning tunneling spectroscopy (STS) due to the influence of heptagons (which will donate one electron) and pentagons (which will accept one electron) within the hexagonal lattice structure, [123]. But these states are not applicable to the donor-acceptor interface model, which is applied to explain the exciton dissociation at their interface.
In this work vertically aligned carbon nanotubes (va-CNTs) are used as the acceptor material in a 3D-organic solar cell architecture. In the following the properties of a CNT is explained in detail and a band diagram of the cell given.

3.3.1 Carbon nanotubes

In general, carbon nanostructures appear in several forms, e. g. bamboo-like CNT, SWCNT, or MWCNT and lots more. CNT) were discovered in 1991 by Iijima [124]. Much work has been done since to study the exceptional and unique chemical, mechanical and electrical properties of the CNT. CNT have diameters in the range of 0.4nm - 100nm and a length of up to several centimeters. Hence, CNT have a large aspect ratio and can be considered as a one dimensional material [125]. Due to their alternating sp^1- and sp^2-

hybridized carbon bonds, they are almost chemically inert, mechanically extremely sturdy and stiff in the axial direction. In the form of powders SWCNT have a low density of 1.3-1.4$\frac{g}{cm^3}$ and MWCNT have a density of 1.8$\frac{g}{cm^3}$.

Structure and properties of CNT

The atomic structure of CNT can be easily described by by using graphene layers, which consists of sp^2-hybridised carbon. In graphene, atoms all lie in a plane. The unit cell contains two carbon atoms forming a honeycomb-like lattice. The angle between the three covalent σ-bonds of each single carbon atom is 120°. Three of the four valence electrons form these bonds. The fourth valence electron occupies an out-of-plane P_z atomic orbital which overlaps with that of the neighbouring carbon atom and forms π-type molecular orbitals (see Figure 2.1). This overlap enables the movement of electrons in π-orbitals over the whole system. This feature is mainly responsible for the conduction properties of graphene as well as of the CNTs.
A CNT is a long hollow cylinder formed from a rolled-up graphene sheet whilst still conserving its periodic lattice structure. The diameter of the CNT are related to the nanotube circumference vector $\overrightarrow{C}$ (called chirality vector), which for an unrolled nanotube can be expressed in terms of the primitive lattice vectors of graphene $\overrightarrow{a_1}$ and $\overrightarrow{a_2}$ as

$$\overrightarrow{C} = n \cdot \overrightarrow{a}_1 + m \cdot \overrightarrow{a}_2, \tag{3.2}$$

where n, m $\in \mathbb{N}^+$. The components n and m are the chiral indices of $\overrightarrow{C}$. They are used to define a CNT: the convention is: $n \geq m$, which means all existing CNT are denoted $[(n,0),...,(n,n)]$.
Carbon nanotubes are classified as single-walled, double-walled (two SWCNT put inside each other) and multi-walled nanotubes (several SWCNT put inside each other) as shown in Figure 3.9.
SWCNT have several possible symmetric structures: zigzag, armchair and chiral types (see Figure b) in Figure 3.10). The structure observed is dependent on the direction of winding, the so-called chirality. In zigzag tubes m=0 and in armchair tubes n=m. In general when

$$n - m = 3q \tag{3.3}$$

(where q is an integer), (n,m) nanotubes have metallic properties. This is used to explain why one third of all CNT produced are metallic and the others semiconducting. Whether the CNT are metallic or semiconducting depends on their diameter and chirality; the band gap in the semiconducting tubes is inversely proportional to the nanotubes's diameters $E_g \propto \frac{1}{d}$ (that means tubes with a large diameter can be assumed to be metallic). All armchair nanotubes and about one third of zigzag nanotubes are metallic.

The peaks in the nanotube DOS have singularities in accordance with the single quantum subband model. These singularities are important for the interpretation of the experimental data of scanning tunnelling spectroscopy and resonant Raman spectra.
In the following the electrical, mechanical, chemical, and thermal properties of carbon nanotubes are described.

Electrical properties

CNT can be considered to be a one-dimensional very small solid strongly influenced by molecule quantum state properties such as excitons and polarons. With regard to their electronic properties, solids are classified in accordance to their band structure as metals, semiconductors or insulators depending on their band structure. As electrons and holes are Fermions, the Pauli-principle can be applied, which means every electronic state can be occupied by only two electrons (each with different spin) and the temperature dependent occupation of the electronic states can be modelled by the Fermi-Dirac distribution function

$$f\left(E,T\right)=\frac{1}{e^{\frac{E-E_F}{k_BT}}+1}. \tag{3.4}$$

At 0 K every state which is lower than the Fermi-level is occupied and all other states are empty. If this level is within an electronic band charge carriers can be easily (low energy input) excited into an energetically higher unoccupied state. Upon application of an external electric field these charge carriers form a current. Such materials are called metals. Materials with the Fermi-level placed within a bandgap are called semiconductors or insulators depending on the width of the bandgap. In some materials the E_F lies at energy level where two bands meet. These materials are called semimetals (see Figure a) in Figure 3.10). In order to explain the electrical band structure of CNT, it is very helpful to describe the electronic structure of graphene first. The sp^2-hybridised σ-type orbitals form σ-bands (occupied σ and unoccupied σ^*) which are energetically far away from one another. In comparison to these, the two π-bands (π and π^*) are much closer energetically and even touch at the K-points of the Brioullin-zone. The number of states per π-band is half as many as the number of atoms within the graphene layer. Therefore, the π-band is fully occupied with electrons and the π^* is completely empty. These are the valence and conduction band respectively. As these two bands touch each other at the K-points, graphene is semi-metallic. The calculated band structure of graphene is shown in Figure a) of Figure 3.11.
The electronic structures of CNT differ from that of graphene mainly because of two reasons:

- The transformation of the two-dimensional band structure of graphene into bands limited by the circumference of the CNT in one direction

and in the other having an infinite extension along the CNT axis. Consequently, a one-dimensional band structure is formed (main impact).

- The bending of the nanotube walls to a cylinder, leading to a shift of the subbands (especially important for CNT with small diameters).

The small circumference of the CNT causes a quantization of the electronic states, which results in the splitting of bands into several subbands which were formerly single bands in graphene. The quantization criterion for all electrons, whose wave vectors $\overrightarrow{k} = \frac{2\pi}{\lambda_e} \cdot \overrightarrow{e}$ are not parallel with the CNT axis is

$$\overrightarrow{k} = \frac{2\pi}{\overrightarrow{C}} \cdot i \quad (i \in) \,. \tag{3.5}$$

The number of subbands depends on the diameter of the CNT. The subbands occur as electric states along lines in the Brioullin-zone of graphene. As can be seen from equation 3.5 the lines obtain their orientation from the chirality vector $\overrightarrow{C}$. This results in a fixed orientation of these subbands in the graphene Brioullin-zone. Only if the K-points are connected with these lines is the CNT metallic (see Figure d) of Figure 3.11). For any other case the SWCNT is semiconducting. Consequently, all armchair SWCNT are metallic. According to equation 3.3 all SWCNT with

$$\frac{n-m}{3} \in \mathbb{N} \tag{3.6}$$

are metallic as their subbands meet the K-points, [128]. One exception to this are SWCNT with very small diameters, which have small band gaps caused by bending, [129]. However, small diameter SWCNT have enough free charge carriers at room temperature to assume that one third of all SWCNT are metallic.

Density of states

The amount of electronic states (N) per energy interval (E) is known as the density of states ($\frac{dN}{dE}$). In one dimensional electronic systems it is typical to find van-Hoove-Singularity (vHS); these form pairs of singularites, which are energetically symmetric to the SWCNT Fermi level. For metallic SWCNT a constant density of states exists between the first pair of vHS due to the bands linearly crossing the K-points. The density of states have been calculated and verified by scanning tunnelling spectroscopy [130]. These singularities define the electronic transport mechanisms to a large extent and also define the optical properties. The distance between the first pair of vHS corresponds to the band gap of semiconducting SWCNT.

Ballistic conduction

On the basis of the quasi one dimensional structure and the strong chemical bonds, only a weak interaction between electrons and phonons is possible. Hence, charge carriers can cover long distances, up to $100\mu m$ before phonon scattering takes place. The maximum conductivity (ballistic limit case) calculated by [131] is

$$2G_0 = \frac{h}{4e^2} \tag{3.7}$$

per channel. In most real applications a diffuse conduction mechanism can be assumed. In this case the charge carrier is first accelerated by an electric field and then scattered after a certain distance. This distance is the mean free path. The mean free path divided by the travelled time yields the mean drift velocity. In order to investigate their electronic properties Frank et al. in 1998 dipped CNT into liquid mercury as a way of aiding the measurement of the conductivity with Scanning Probing Microscopy [132]. It was reported that the CNT showed quantum mechanical behaviours and had ballistic conductance. Sanvito et al. observed a reduction of quantum mechanical conductive channel in the inside of MWCNT and a rearrangement of electron flow of each carbon nanotube by interwall interactions.

Current density

The resistivity of rope shaped metallic SWCNT is about $\rho = 1 \cdot 10^{-4}\Omega/cm$ at 300 K. Frank et al. observed that the maximum stable current densities are $10^7\ A/cm^2$ for SWCNT and $10^13\ A/cm^2$ for MWCNT. Field emission experiments have driven currents of up to $I = 2\mu A$ through single SWCNT, which corresponds to current densities of up to $1 \cdot 10^8 A/cm^2$ [133].

Optical transitions

The optical transitions only occur within one pair of vHS and are usually investigated by UV-vis measurements (see Figure 3.12). The absorption spectra shows several peaks. In order to identify whether a metallic or semiconducting SWCNT has caused a peak in the absorption spectra the peaks are marked with the letter S or M, respectively. Furthermore, the transitions are marked with an index to the letter, either 11 or 22, which correspond to the first or second vHS, respectively. Recombination processes also take place in CNT; either radiatively through the process of fluorescence, or non-radiatively by defects, [134]. The measurement of the dependence of the fluorescence spectra on excitation wave length can be used to determine the chirality of the CNT within the sample. Metallic CNT do not show any fluorescence.

Raman modes, mechanical and thermal properties of CNT

One of the most important Raman modes is the radial breathing mode (RBM), which is specific to CNT as no other carbon material has these modes in that specific wave length interval. By using this method metallic CNT can be detected in contrast to fluorescence spectroscopy. The exact Raman shift of this oscillation depends on the CNT diameter. The Raman modes of a CNT are increased, when the excitation wave length of the laser corresponds to an optical transition. A two dimensional mapping, where the intensity is laid to both the Raman shift and the excitation energy was done by [135]. The highly energetic G-band is different for semi-conducting and metallic CNT; this facilitates the quantitative determination of the proportion of semi-conducting and metallic CNT within a sample. A further important observation obtained from Raman modus is the shift of the G-band caused by lattice defects. This can give evidence of the disorder of the lattice. It is therefore called D-bands (see Figure 3.13).

Synthesis of CNT

Arc-discharge, laser ablation, chemical vapour deposition (CVD), CNT and pyrolysis methods have been used for the synthesis of CNT. CNT synthesised using the CNT method show very good dispersion properties. After synthesis, the tubes have to be purified to remove catalysts, carbon and graphene impurities. It is still not possible to synthesise CNT of a specific chirality, conducting behaviour, diameter or length specifically. The SWCNT in the form of a bundle (powder) used in this work were synthesised by arc-discharge, have an average length of 5μm and an average diameter of 2 nm. In the method of arc discharge CNT are synthesised by nearing two electrodes together under a low helium gas pressure (at least one is of high purity graphite) and creating an arc between them (50-100A), which has a temperature around 3000-4000°C (see Figure 3.14). In the arc CNT are formed. Another production method involves laser ablation. In a furnace, which is heated up to 1200°C, a pulsed laser is used to ablate material from a target. The target consists of carbon and metal acting as a growth catalyst. In the argon flow the CNT are transported to a cooled collector, see left image in Figure 3.15. In comparison to the two previously described methods the plasma enhanced chemical vapour deposition (pe-CVD) operates at low temperature around 700°C and below. It uses a high frequency field (13,56MHz to 2,47GHz) to generate the plasma. The substrate is placed on the bottom electrode and the process gas flows from above. The substrate is heated up to synthesis temperature and the plasma is then ignited, see right image in Figure 3.15. The process gases used for CNT synthesis are methane (CH_4), ethane (C_2H_2) and hydrogen (H_2). By using CVD it is possible to synthesise va-CNTs, see Figure 3.16. These have many applica-

tions. In this work they play a key role within the solar cell structure. In contrast to pe-CVD the vapour phase growth (VPG) method uses another gas to support synthesis with metal catalyst for CNT growth. This synthesis process is constantly supported with synthesis material for CNT growth. Hence, very long process times can be achieved resulting in large scale CNT production. In the VPG method the metal catalyst boat and reaction gas injection are placed on opposite sides. This ensures that the vaporized metal can be cooled down to form nanosized particles in the furnace and serve then as growth catalysts in combination with the process gas for CNT synthesis. With both the pe-CVD and VPG methods CNT of high crystallinity can be synthesized.

3.4 Band diagram of va-CNT solar cell

The efficiency of organic solar cells is strongly limited by their insufficient absorption in the near infra red spectral range and by their low charge carrier mobilities. The latter handicap can be overcome by using CNT. In addition, the CNT are expected to act as an acceptor, see [138], [139], [140]. From a certain perspective CNT can be considered to be the longest fullerenes, which are a very common acceptor material. The band diagram of the va-CNTsolar cell is explained in the following. The values for the diagram are taken from literature [141]. As previously discussed in chapter 2, the working principle of organic solar cells is based on the alignment of the molecular orbitals of the donor and acceptor. This enables ultra-fast interfacial charge transfer. A good overview of the band scheme of a CNT-dye solar cell can be found in [142]. A general view of the band diagram is shown in Figure 3.17. The work-function of pristine CNT are in the range of 3.7eV-4.8eV [144], [133], and [145]. The used CNT-dye blends are considered to form an interpenetrating network. This means that to a good approximation all CNT are in electrical contact with each other and the Fermi-levels align with all other CNT. Consequently, as the metallic tubes constitute one third of all the tubes they dominate the electrical behaviour of the CNT blend. Therefore, it is possible to model this layer with metallic tubes in the band diagram, where the Fermi-level equals the work-function. The polymer P3HT can be assumed to behave as a p-type semiconductor as its hole mobility is much higher than its electron mobility. Therefore, the junction of the P3HT-CNT blend can be considered to be a semiconductor-metal junction [142]. If these two materials are brought into contact with each other, the differences in the electrochemical potentials initiate a charge transfer process until these potentials are in equilibrium. As the Fermi level of the polymer is energetically lower than the Fermi-level of the CNT, electrons flow from the CNT to the polymer. As a consequence of this flow both materials lose their charge neutrality with the polymer being negatively- and the CNT positive-charged. The accumulated charges change the position of

the Fermi-level of the polymer, which becomes more negative. As the available states per unit energy in the nanotube (metal) far exceeds the available states per unit energy in the polymer, the excess of holes on the CNT do not influence the Fermi-level of the CNT and it stays at its initial level. This means that when both materials are brought in contact, the Fermi-levels equalize to the initial level of the CNT. The accumulated negative charges on the polymer change its charge carrier concentration. As a consequence the Fermi-level is shifted upwards to the negative [142].
The charge transfer process (for equilibration of the different electrochemical potentials) creates an electric field at the polymer-nanotube interface. This built-in field ($q\Phi_b$) can help to split up excitons, if this field is bigger than the exciton binding energy (based on the coulomb interaction of the hole in the HOMO and the electron in the LUMO).
The thickness of a depletion layer can be expressed as (for a one-sided abrupt junction) [64]:

$$W = 2L_D\sqrt{2\left(\beta V_{bi} - 2\right)}, \tag{3.8}$$

where $\beta = q/k_BT$, q is the electronic charge, k_B is the Boltzmann constant, T the temperature, V_{bi} is the interface band bending where

$$V_{bi} = E_{F,P} - E_{F,n} = 4.8 - 4.5 = 0.3$$

and L_D is the Debye length. The Debye length is a characteristic length for semiconductors and can be expressed as:

$$L_D = \sqrt{\frac{\varepsilon\varepsilon_0 k_B T}{q^2 N}} = \sqrt{\frac{\varepsilon\varepsilon_0}{qN\beta}}, \tag{3.9}$$

where ε is the dielectric constant of the dye, ε_0 is the vacuum dielectric permittivity and N is the carrier concentration. The depletion layer width can be calculated to be:

$$\begin{aligned} W &= 2L_D\sqrt{2\left(\beta V_0 - 2\right)} \\ W &= 2L_D\sqrt{2\left(38.68 \cdot 1.3 - 2\right)} \\ W &= 2L_D\sqrt{2 \cdot 48.29} \\ W &= 2L_D \cdot 9.83 \\ W &\approx 20L_D. \end{aligned}$$

The Debye length is proportional to the carrier concentration as

$$L_D \propto \frac{1}{\sqrt{N}}.$$

Therefore, the Debye length drops by a factor of 2.82 per decade of the doping concentration. For a carrier concentration of around $2 \cdot 10^{16} cm^{-3}$

and a dielectric constant of 6.5 [146] the Debye length can be calculated to be:

$$L_D = \sqrt{\frac{1.44 \cdot 10^{-12} m}{1.602 \cdot 10^{-3}}}$$
$$L_D \approx 10nm.$$

This yields a depletion width of 200nm. The thickness of a CNT-dye solar cell device is in the range of 100nm - 200nm. As the band bending and depletion zone width is smaller than the layer thickness the physical properties of this structure can be approximated as a charged capacitor [147], as the band bending and depletion zone is smaller than the layer thickness. The CNT-polymer junction can be assumed to be an insulator-metal junction. In this model the built-in voltage (Φ_{bi}) equals the difference of the valence band of the polymer and the Fermi-level of the metal (CNT). This is also equal to the barrier height (Φ_b) at the insulator-metal interface and can be expressed as:

$$\Phi_b = \frac{\Phi_{CNT} - HOMO_{Dye}}{q}. \tag{3.10}$$

For the CNT-P3HT combination equation (3.10) becomes:

$$\Phi_b = \frac{4.5\,eV - 5.1\,eV}{1\,eV} = 0.6\,eV,$$

which is 0.1eV ... 0.3eV larger than the reported exciton binding energy for P3HT (E_{exc} 0.3eV ... 0.5eV [148]). Consequently, charge transfer (after exciton separation) at the CNT-dye interface can be assumed to occur. The use of a va-CNT array ensures that at least one CNT of the array is placed within the exciton diffusion length of any point of the polymer as the average distance between two CNT is around 15nm (so every exciton has to diffuse 7.5nm within the polymer to reach the polymer-nanotube interface). If an electron is accepted on the CNT it can tunnel, with the presence of an external field of:

$$E_{junc} > \frac{E_{exc}}{q \cdot r_{exc}},$$

where r_{exc} is the diffusion length of the exciton (usually around 10nm). This means that with the application of an electric field, excitons can be dissociated several The band diagram of the va-CNT solar cell is shown in Figure 3.18. Catalyst material (iron) from bottom growth of va-CNTs are included in the band diagram.

3.5 Summary

In this chapter the donor and acceptor materials where introduced, which were intensively studied in this study. Some common analysis methods of the specific materials were explained. The band structure of the 3-dimensional

solar cell using vertically aligned carbon nanotubes was given. The fabrication of such a (prototype) device is the main objective of this study.

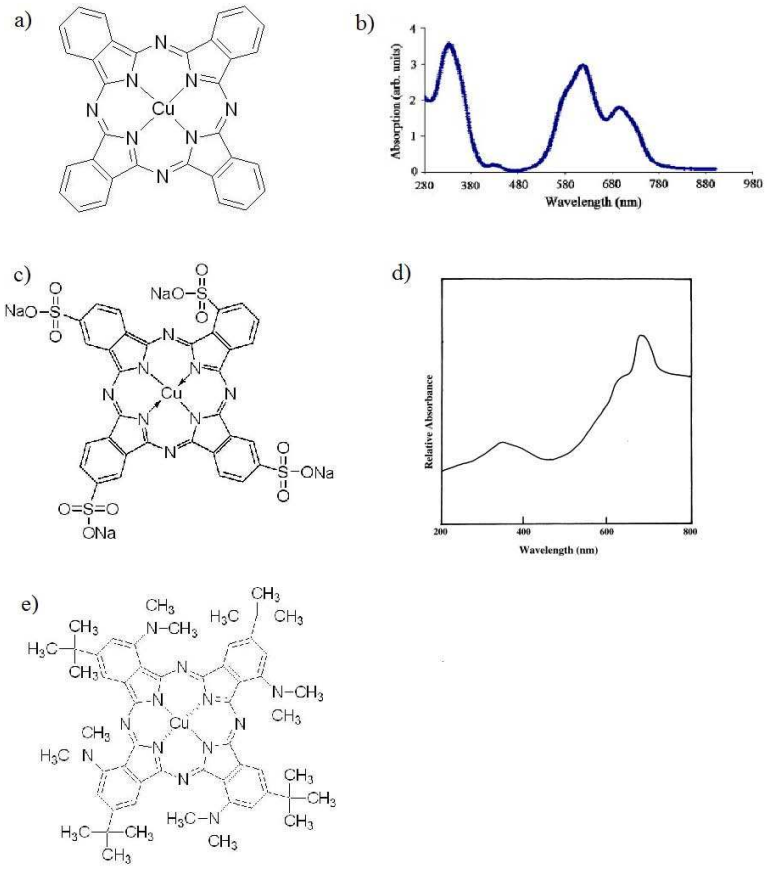

Fig. 3.6: Structure and UV-vis spectra of the different copper phthalocyanines. Left: structures of a) CuPc, c) CuPc-TS, and e) CuPc-DMA. Right: UV-vis spectra of b) CuPc, and d) CuPc-TS (images a) and b)taken from [95] (reprinted from Publication Solar Energy Materials and Solar Cells, Vol. 93, Issue 1, S. Rajaputra, G. Sagi, V. P. Singh, Schottky diode solar cells on electrodeposited copper phthalocyanine films, 60, ©(2009), with permission from Elsevier), images c) and d) taken from [96] (reprinted from Publication Journal of Molecular Catalysis A: Chemical, Vol. 267, Issues 1-2, K. M. Parida, N. Baliarsingh, B. S. Patra, J. Das, Copperphthalocyanine immobilized Zn/Al LDH as photocatalyst under solar radiation for decolorization of methylene blue, 202-208, ©(2007), with permission from Elsevier), image e) taken from [97]).

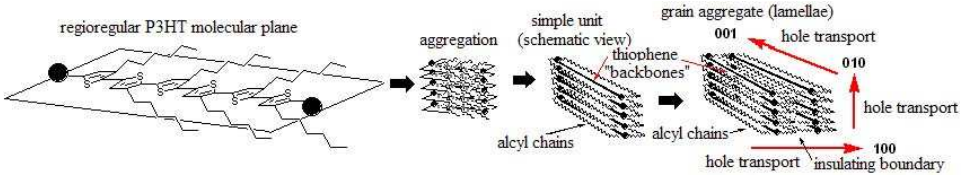

Fig. 3.7: Possible route of the for morphology forming process (image taken from [103]). **100, 010, 001** are hole transport directions along molecular planes.

Fig. 3.8: Structure and UV-vis spectrum of rr-P3HT. Left: structure (image taken from [25]), right: UV-vis spectra, image taken from [104] (reprinted from Publication Thin Solid Films, Vol. 483, Issues 1-2, A. Watanabe, A. Kasuya, Effect of atmospheres on the open-circuit photovoltage of nanoporous TiO2/poly(3-hexylthiophene) heterojunction solar cell, 358-366, ©(2005), with permission from Elsevier).

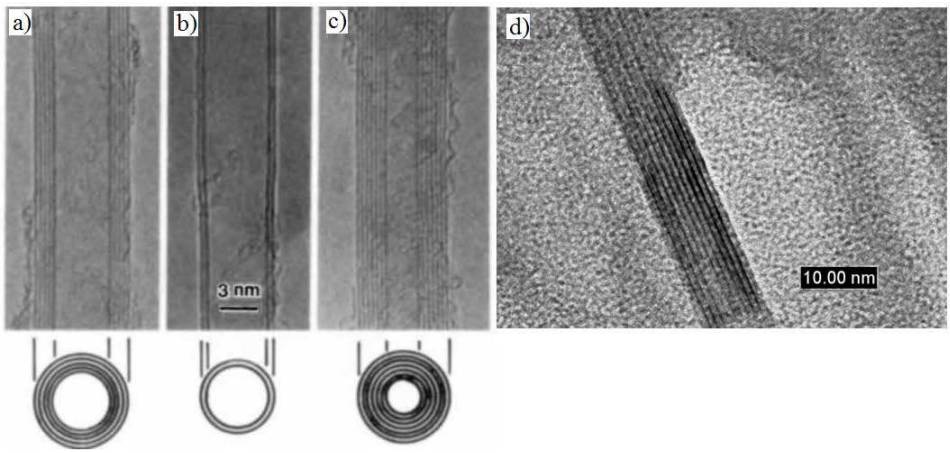

Fig. 3.9: TEM images of the described possible shapes of CNT described in the text. a) multi-walled CNT, b) single-walled CNT c) multi-walled CNT, and d) multi-walled CNT. Images a)-c) taken from [124] (reprinted by permission from Macmillan Publishers Ltd: [Nature] (Vol. 354, Issue 6348, S. Iijima, Helical microtubules of graphitic carbon, 56 - 58), ©(1991) by the Macmillan Publishers Ltd, image d) taken from [126].

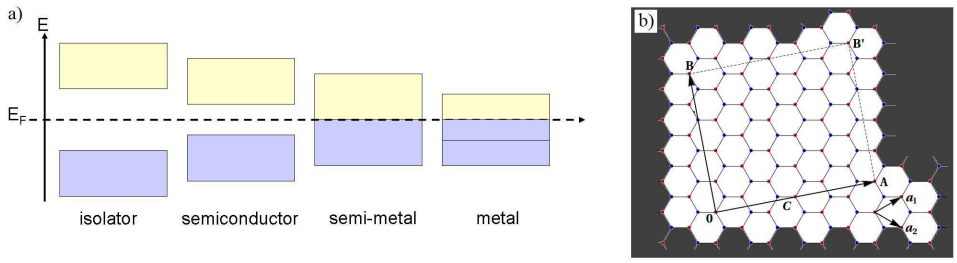

Fig. 3.10: Band structures and chirality. a) scheme of the band structure for metals, semi-metals, semiconductors and insulators. b) chirality of a CNT. The rectangle 0AB'B defines the unity cell of a (4,2) CNT.

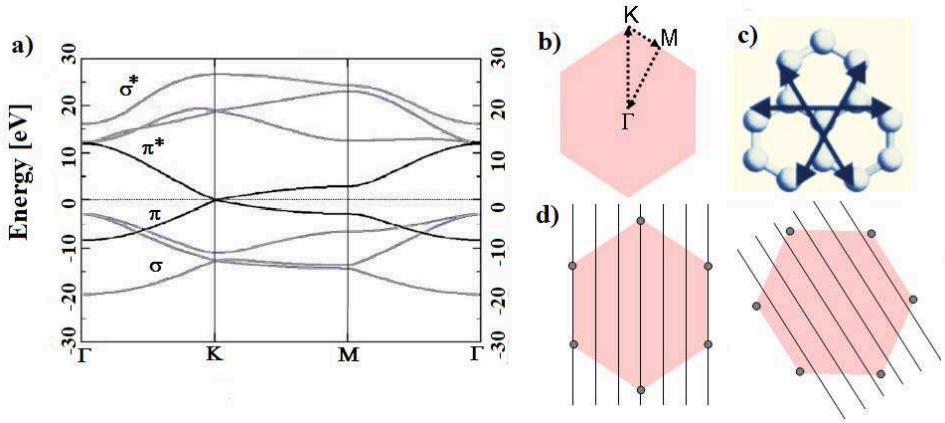

Fig. 3.11: a) Calculated band structure of graphene, image taken from [127] (Y. J. Dappe, R. Oszwaldowski, P. Pou, J. Ortega, R. Perez, and F. Flores, Physical Review B, 73, Issue 23, 2006. ©(2006) by the American Physical Society). b) Brillouin-zone indexed with K, M and Γ points. c) directions of metallic conductivity (for calculated band structure of a)). d) Brillouin-zone of a (4,4) CNT (left) and of a (4,0) CNT (right).

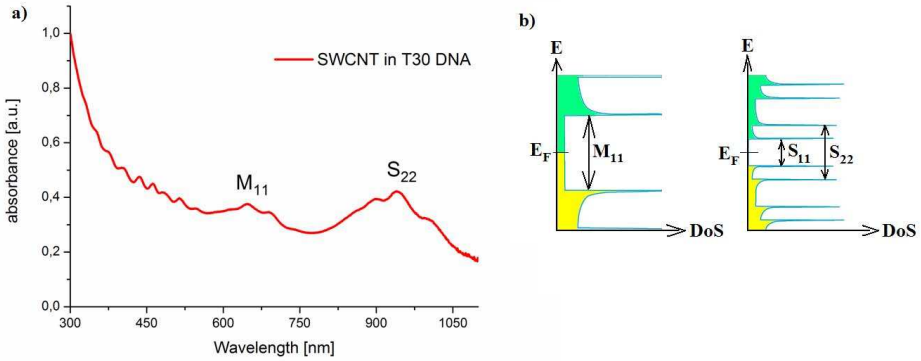

Fig. 3.12: Left: absorption spectra of a SWCNT dispersion with the help of T30DNA. The M or S peak corresponds to metallic or semi-conducting SWCNT. The transition itself is indexed with 11 or 22 corresponding to the first or second vHS. Right: corresponding DOS.

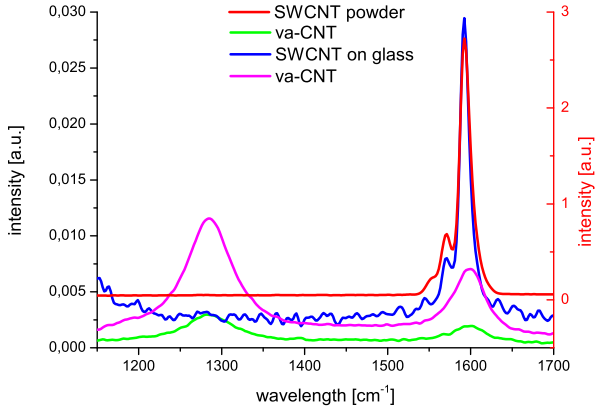

Fig. 3.13: Raman spectra of several CNT samples. The red spectra corresponds to the right axis (also red), all other spectra correspond to the left axis. D and G bands clearly determine CNT.

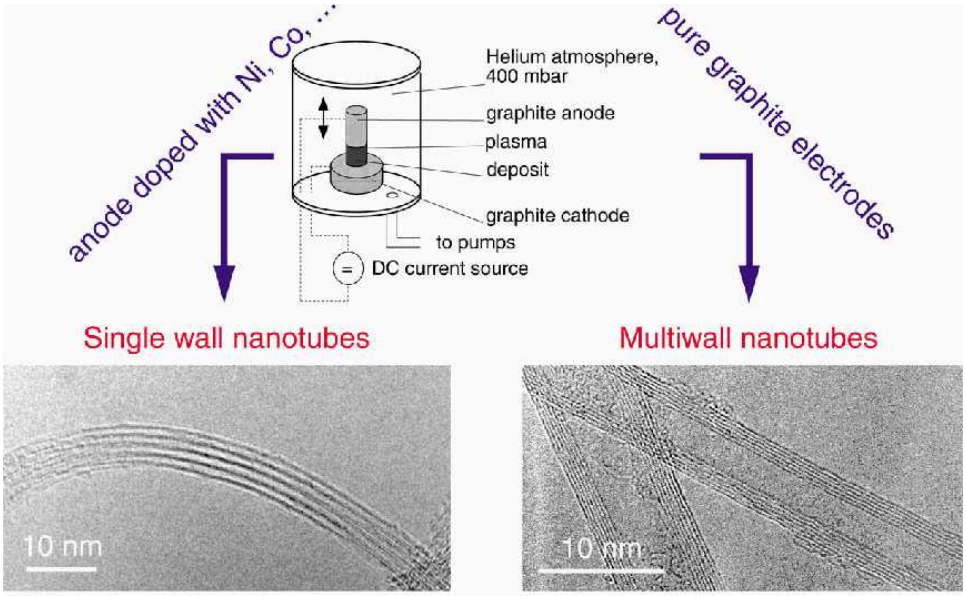

Fig. 3.14: Arc discharge synthesis of SWCNT and MWCNT shown at the top, below images of single- and multi-wall nanotubes. Image taken from [136].

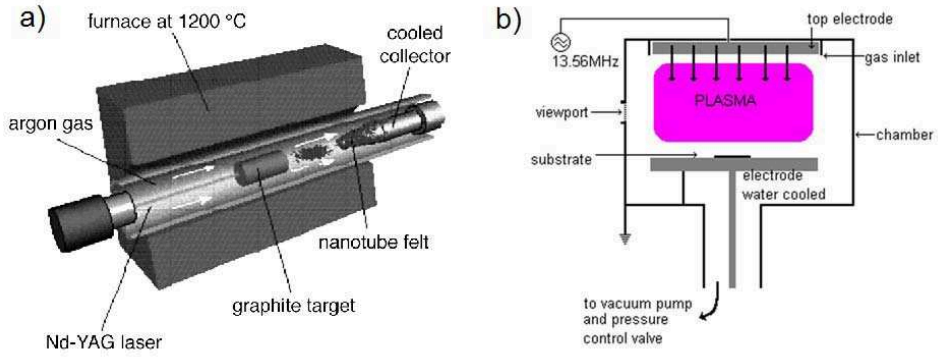

Fig. 3.15: Two different synthesis methods. a) Scheme of synthesis of SWCNT and MWCNT using laser ablation. b) pe-CVD synthesis of SWCNT and MWCNT. Image a) taken from [136], image b) taken from [137].

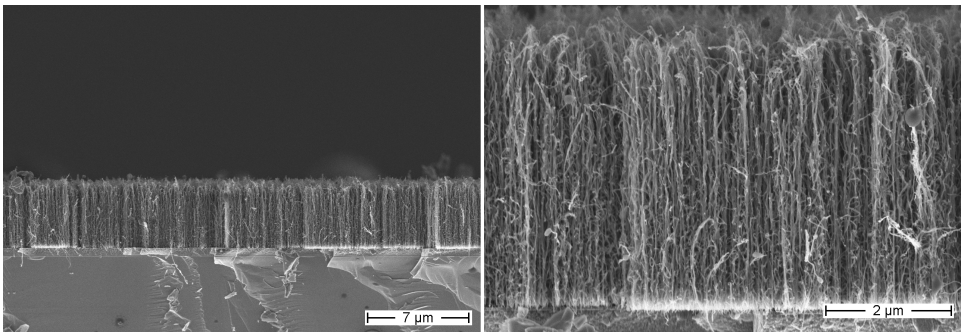

Fig. 3.16: Image of a va-CNT forrest. Left: overview. Right: magnification of the overview.

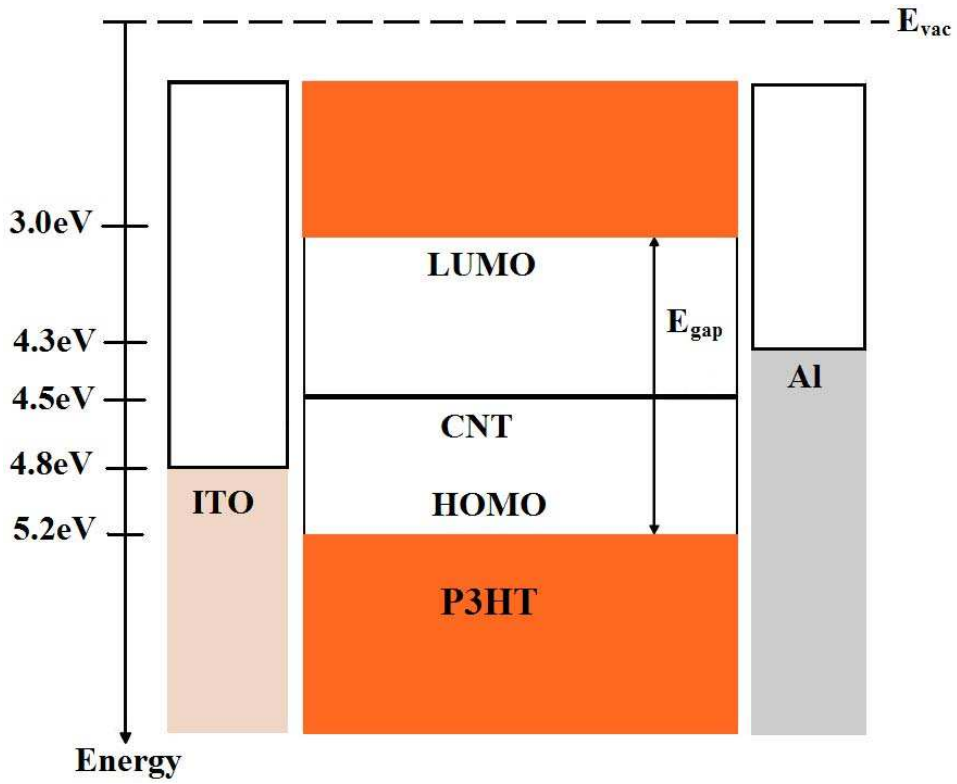

Fig. 3.17: This scheme illustrates the band diagram of a polymer-CNT solar cell. Image inspired by [143].

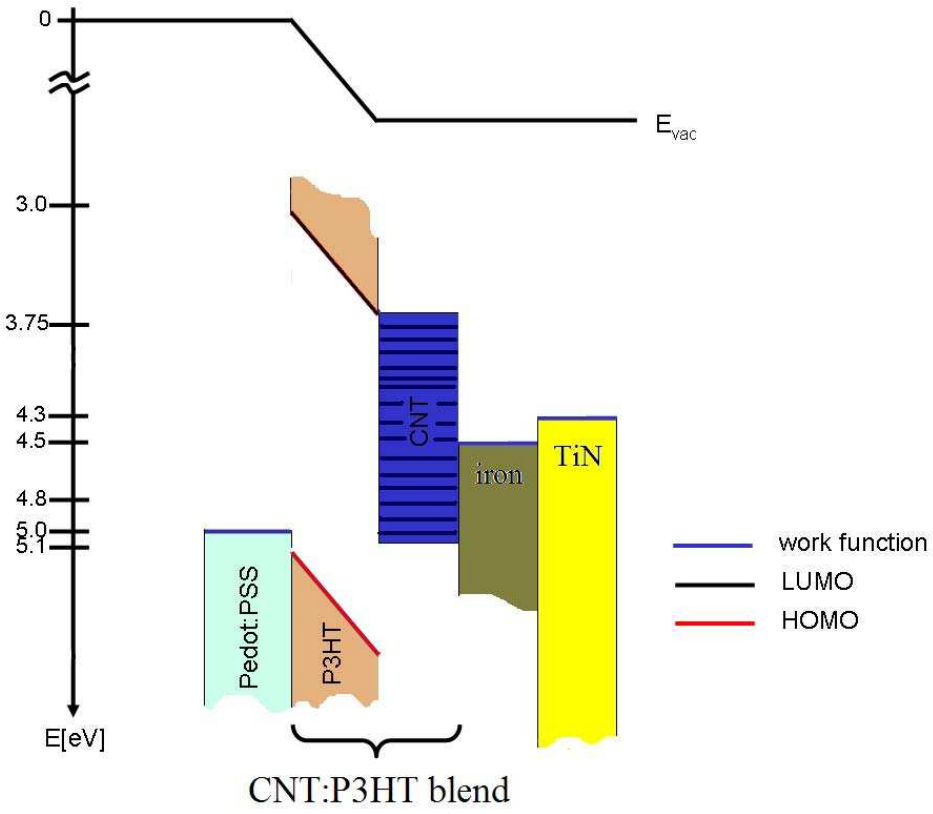

Fig. 3.18: Scheme of the band diagram of the va-CNT solar cell. The work function of the CNTs is assumed to vary in the range reported by literature.

4. SOLUTION PROCESSED ORGANIC SOLAR CELLS

Solution processed organic solar cells offer a large advantage with their applicability to roll-to-roll fabrication. This offers the opportunity for the easy low-cost manufacture of large scale photovoltaics (PV) devices using a printing technique. However, for this to be effective the wetting properties have to be studied in order to ensure adhesion of the solution on the appropriate flexible substrate.

4.1 Solvent based coating

The following sections dealing with the theory of wetting base upon [149].

4.1.1 Wetting

In order to enlarge the surface of a material by an amount dA, a specific amount of work, dw, has to be done:

$$dw = \gamma \cdot dA, \tag{4.1}$$

where γ is called the surface energy (for solids) or the surface tension (for liquids). The work needed to create the surface also contributes to the free energy, dF, of the system:

$$dF = -S \cdot dT - p \cdot dV + \gamma dA, \tag{4.2}$$

where S is the entropy of the system, T the temperature, p the pressure and V its volume. According to the laws of thermodynamics, every system maximizes its entropy under certain boundary conditions. This translates to a minimum of the Gibb's free enthalpy G. If the surface area decreases at constant temperature and volume, the free energy, dF, decreases. Liquids always try to get the smallest possible surface area for that reason and e.g. form droplets. The surface energy of a material determines the energy expenditure needed to decrease its surface area. As the surface energy is physically based on the interaction of the surface molecules, it is determined by the intermolecular forces of these surface molecules. The surface energy is not measured directly but via an analysis of the contact angle of specific liquids on the surfaces [149]. Properties like polarity, hydrophilicity and surface impurity can be determined. At the three phase point of liquid,

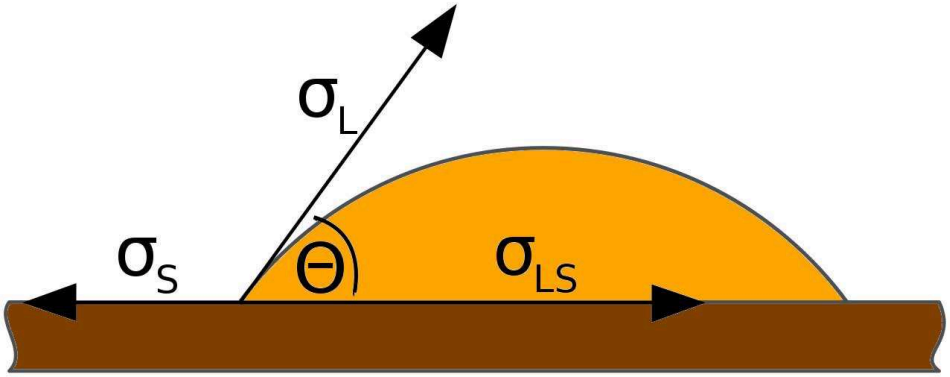

Fig. 4.1: Wetting of a surface determined by the contact angle θ, σ_S is the surface energy of the substrate, σ_L is the surface tension of the liquid, and σ_{LS} is the interfacial energy. Image taken from [150].

solid and gas the equilibrium of forces determines the contact angle (CA), θ, as shown in Figure 4.1. Generally, θ decreases with increasing surface energy for the same liquid as the interfacial energy decreases. The relation between CA and surface energy is given by Young's equation:

$$\gamma_s = \gamma_{sl} + \gamma_l \cos\theta, \tag{4.3}$$

where γ_s is the surface energy of the solid, γ_{sl} is the interfacial energy and γ_l is the surface tension of the liquid. Equation (4.3) determines the surface energy in vacuum. However, the difference between the surface energy in vacuum to that at atmosphere pressures ($\pi = \gamma_s - \gamma_{sv}$) can be neglected. The energy needed to remove a droplet from a surface is called the adhesive work, W_a and is expressed according to Dupre as:

$$W_a = \gamma_s + \gamma_l - \gamma_{sl}. \tag{4.4}$$

Adhesive forces can also be calculated by measuring the CA, when equation (7.1) and (4.4) are combined:

$$W_a = \gamma_l \left(1 + \cos\theta\right). \tag{4.5}$$

Hence, the surface tension of the liquid has to be known in order to calculate the adhesive forces [149]. The adhesive forces occurring at the interface are mainly due to either be permanent or induced dipoles. These dipoles generate electrostatic fields around the molecule which are the cause of the electrostatic forces. Permanent dipoles exist due to the difference in the electronegativity of the single atoms of the molecule, which in many cases involve hydrogen bridge linkages. Induced dipoles can either be generated by interaction with an outer molecule or be based on the time dependent charge distribution within the electron cloud of the molecule. These induced dipoles

interact with their neighbouring molecules and induce dipoles in them. The interaction forces are called London forces and are a dispersive interaction. On the basis of the different interaction forces, the adhesive force can be divided into its polar and dispersive fraction [149]:

$$W_a = W_a^d + W_d^p. \tag{4.6}$$

The dispersive term W_a^d comprises the London forces. They occur at every phase interface. The polar fraction only appears when polar molecules exist at the interface. In a similar manner to the adhesive forces, the interfacial energies occurring at the interface, γ_i, can be divided into their dispersive and polar fractions [149]:

$$\gamma_i = \gamma_i^d + \gamma_i^p, \tag{4.7}$$

where γ_i^d and γ_i^p are the dispersive and polar fractions, respectively. By assuming that the adhesive energy can be divided into its specific fractions the interfacial energies yields [149]:

$$W_a = f\left(\gamma_1^d, \gamma_2^d\right) + f\left(\gamma_1^p, \gamma_2^p\right). \tag{4.8}$$

A good overview of all the theories used to describe the various expressions linked to the interfacial energies is given by [151]. According to Fowkes [152] only the dispersive parts of the surface energy influence the adhesion at the interface and the adhesive work, W_a, can be expressed using the geometric mean as:

$$W_a = 2\sqrt{\gamma_s^d, \gamma_l^d}. \tag{4.9}$$

In order to improve the wetting behaviour surfaces are often treated using chemicals or plasma. In these cases a polar interaction at the surface takes place and the approach by Fowkes is no longer applicable. The approach by Owens, Wendt, Rabel and Kälbe (OWRK) fits these cases much better, because it distinguishes between the polar and dispersive fractions. The adhesive work is then expressed as:

$$W_a = 2\sqrt{\gamma_s^d \cdot \gamma_l^d} + 2\sqrt{\gamma_s^p \cdot \gamma_l^p}. \tag{4.10}$$

Combining equations (4.10) and (4.5) yields:

$$\gamma_l\left(1 + \cos\theta\right) = 2\sqrt{\gamma_s^d, \gamma_l^d} + 2\sqrt{\gamma_s^p, \gamma_l^p}. \tag{4.11}$$

Equation (4.11) can be transposed by dividing with $2 \cdot \sqrt{\gamma_l^d}$ in order to get a linear equation of the following form:

$$\frac{\gamma_l}{\sqrt{\gamma_l^d}} \cdot \frac{1 + \cos\theta}{2} = \sqrt{\gamma_s^p}\sqrt{\frac{\gamma_l^p}{\gamma_l^d}} + \sqrt{\gamma_s^d}. \tag{4.12}$$

By using equation (4.12) it is possible to calculate the polar fraction of the surface energy γ_s^p from the slope of the curve and the dispersive fraction of the surface energy, γ_s^d from the axis intercept of the same curve, if the two values are known:

1. the surface tension of the two different liquids, and
2. the CA of these two liquids on the surface.

The chosen method for the CA studies in this work is the OWRK method.

4.1.2 Spin coating

Spin coating first received scientific interest at the same time as the anorganic semiconductor industry developed in the mid 1950's. Many factors contribute to the spin coating process, of which some are coupled [153]. The main parameters can be placed into four groups [153]:

- Fluid: density, viscosity, polarity, dye, dye concentration, and surface tension,
- Spin process: speed, acceleration, and ramp control sequence,
- Atmosphere: composition (solvent - air), temperature, humidity and relative speed in comparison with the chuck (coupled-motion), and
- Substrate: surface roughness, substrate temperature, surface energy, and substrate size.

The spinning speed has the strongest impact on the control of the spin coating process. The speed of the substrate (measured in revolutions per minute (rpm)) is correlated with the size of the radial force, the velocity and the turbulence of the atmosphere above the fluid. In particular, the best layer deposition can be achieved if the air in the deposition chamber rotates along with the chuck. In this case, there is no relative velocity of the atmosphere above the wetted substrate which can generate turbulence. The highest used speed step of the spin process mainly defines the film thickness. A variation of ±50rpm yields a 10% film thickness variation [153]. The ratio between the rotation speed (causing the radial force) and the drying rate of the fluid also influences the layer thickness. The latter affects the viscosity of the remaining fluid on the substrate. After a specific process time, the viscosity and the radial force equilibrate so that the layer thickness will not decrease significantly with an increased spinning time. The acceleration of the rotational speed provides the fluid with a twisted force which improves the dispersal of the fluid on the surface. Keeping the spin atmosphere saturated by the chosen solvent yields a slower drying rate. This improves the film thickness homogeneity on the substrate [153].

Spin coating theory

For the application of a theory to the spin coating process the three following approximations are often made [154]:

- horizontal rotating plane,
- gravitational homogeneity of the liquid layer, and
- no Coriolis force.

The first assumption ensures that no radial gravitational component influences the process. The second point means that the liquid layer is so thin during the coating process that gravitational differences have no influence. The last point means that the radial velocity must be small enough to neglect Coriolis forces. In addition, further approximations are used in order to simplify the problem even more: the liquid layer is radially symmetric and the fluid itself is Newtonian, the rotating plane is infinite large; the surface is completely wetted by the liquid and the shear resistance is only appreciable in the horizontal plane [154]. As solvent evaporation during the coating process cannot be neglected it is introduced by starting with the case of there being no evaporation in the process followed by extending this approach with an increasing level of evaporation.

No evaporation

The basic physics explaining spin coating in the case when evaporation is ignored was considered by [155]. Figure 4.2 shows the scheme of spin coating. On the basis of the previous assumptions and that the variable z, which is

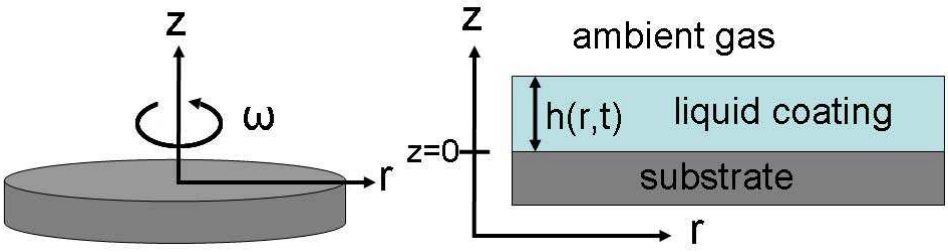

Fig. 4.2: Spin coating scheme, image taken from [154].

at right angles to the substrate, is set to zero at the substrate surface the following is obtained

$$-\eta\frac{\partial^2 v(r)}{dz^2} = \rho\omega^2 r, \tag{4.13}$$

where η is the viscosity, ρ the density of the liquid, ω the rotational speed, r the radius of the substrate and v the radial velocity. By substituting the quotient $\frac{\eta}{\rho} = \beta$, where β represents the kinematic viscosity, into (4.13) then

[154]:

$$-\beta\frac{\partial^2 v(r)}{dz^2} = \omega^2 r. \tag{4.14}$$

Integration of equation (4.14) by taking into account the boundary conditions of v=0, z=0 and $\frac{dv}{dz} = 0$ (at the free surface, where no shearing force occur), gives

$$v = \frac{1}{\beta}\left(-\frac{1}{2}\omega^2 r z^2 + \omega^2 r h z\right), \tag{4.15}$$

where h is the actual liquid layer thickness. The radial flow of the fluid over the substrate, q, can be determined by integration over z. Combining this with the continuity equation given by

$$r\frac{\partial h}{\partial t} = -\frac{\partial\left(rq\right)}{\partial r} \tag{4.16}$$

yields the following differential equation for the thickness of the liquid film on the substrate as a function of time as [154]:

$$\frac{\partial h}{\partial t} = -K\frac{1}{r}\frac{\partial}{\partial r}\left(r^2 h^3\right), \quad K = \frac{\omega^2}{3\beta}. \tag{4.17}$$

Equation (4.17) implies that a thick layer of liquid thins faster than a thin layer upon rotation, which results in uniformity for non-uniform initial films. By using the total derivative for equation (4.17)

$$\begin{aligned} &\frac{dh}{dt} = \frac{\partial h}{\partial t} + \frac{\partial h}{\partial r}\cdot\frac{dr}{dt} \\ &yields \\ &\frac{dh}{dt} = -2Kh^3,\ \frac{dr}{dt} = 3Krh^2 \end{aligned} \tag{4.18}$$

with the specific solutions:

$$h = \frac{h_0}{\left(1 + 4Kh_0^2 t\right)^{\frac{1}{2}}}, \quad r = r_0\left(1 + 4Kh_0^2 t\right)^{\frac{3}{4}}, \tag{4.19}$$

where h_0 and r_0 are the initial layer thickness and coordinate on the substrate, respectively [154]. Equation (4.19) gives the values of the parameters r and h at any point on the substrate. Further analysis of this issue shows that by considering the time and radius dependence of different fluid distributions, the film homogeneity increases for increasing spin time, [155].

Constant evaporation

As the solution evaporates it causes the precipitation of the dissolved material due to supersaturation, subsequently a homogenous film is formed in the spin coating method. The evaporation of solvent yields an increase in the time dependent concentration, c(t), of the dissolved material. As the liquid layer thickness, h, is independent of the radius, r, the increase in concentration is also uniform for uniform films across all of the substrate. This allows for the application of the following additional approximations [154]:

- concentration, c(t), is independent of h,
- volume of liquid solution equals volume of solvent plus dissolved material, and
- evaporation rate correlates only with rotation.

Two definitions can be created from these approximations: firstly by using a volume per unit area of liquid, L, and of solid, S, the time dependent concentration, c(t), becomes $c(t) = \frac{S}{S+L}$ and, secondly, the time dependent layer thickness of the liquid, h(t), becomes $h(t) = S + L$ [154]. On the basis of the constant evaporation the initial film thickness reduces uniformly but the thinning rate differs according to a new variable, the evaporation rate, e, [156]. By using this rate, the change of L and S can be expressed as [156]

$$\begin{aligned} \frac{dS}{dt} &= -c\frac{1}{r}\frac{\partial\left(rq\right)}{\partial r} = -2Kh^3c \\ \frac{dL}{dt} &= -2Kh^3\left(1-c\right) - e. \end{aligned} \tag{4.20}$$

In principle, this system of equation can be integrated, which means the integration of the rates from the initial film thickness and concentration values until $L = 0$ (when only the solid film remains on the substrate). These equations were solved numerically by Meyerhofer (as they cannot be solved analytically), with the help of empiric values and relationships for the viscosity and concentration so that:

$$\beta = \beta_{solvent} + \beta_{solids} \cdot c^{\gamma}, \tag{4.21}$$

where γ is assumed to be 2.5 for photoresists [156]. Meyerhofer further determined that for high spinning speeds the final layer thickness depends only on the spinning speed. This allows the division of the spin process into two parts, where in the first viscous forces dominate the film thickness, and in the second fluid flow stops and solvent evaporation dominates. When the point evaporation and viscous flow rate are equal the film gels on the substrate. This can be expressed as [156]

$$\left(1-c\right) = \frac{2\omega^2h^3}{3\beta} = e, \tag{4.22}$$

where $c \approx c_0$ and $\beta \approx \beta_0$ as the concentration of the solution is constant up to this point. Beyond this point the liquid flowing off the substrate is negligibly small and the layer thickness is given by [156]

$$h_f = S_f \approx c_0 h_{\frac{1}{2}} \approx \left(\frac{3\beta_0 e}{2\omega^2\left(1-c_0\right)}\right)^{\frac{1}{3}} c_0. \tag{4.23}$$

The evaporation rate, e, is proportional to the air flow rate above the substrate, which is proportional to the square root of the spin speed [157]. Therefore,:

$$h_f = k_{spincoater} c_0 \left(1 - c_0\right)^{-\frac{1}{3}} \omega^{-\frac{1}{2}} \beta_0^{\frac{1}{3}}, \tag{4.24}$$

where $k_{spincoater}$ is a constant that has to be measured for every spin coater. The dependence of the final layer thickness on the inverse of the square root of the spinning speed is in good agreement with experimental results [158]. A modification of this analysis was made by [158] in order to eliminate the empiric constants in the equations. This was done by setting the rate of evaporation to

$$e = k_{mass} \left(x_A^0 - x_A^\infty\right), \tag{4.25}$$

where k is the mass transfer coefficient, x_A^0 is the initial concentration of solvent in the fluid and x_A^∞ is the mass fraction of solvent in the coating liquid that is in equilibrium with the mass fraction of solvent in the bulk gas. Consequently, the thickness of the liquid film, h_{wet} is given by

$$h_{wet} = \left[\left(\frac{3\beta_0}{2\omega^2}\right) k_{mass} \left(x_A^0 - x_A^\infty\right)\right]^{\frac{1}{3}} \tag{4.26}$$

and the thickness of the dry layer can be calculated as

$$\begin{aligned} h_f = h_{wet}\left(1 - x_A^0\right) &= \left[\left(\frac{3\beta_0}{2\omega^2}\right) \tilde{k}_{mass} \left(x_A^0 - x_A^\infty\right)\right]^{\frac{1}{3}} \omega^{-\frac{1}{2}} \\ k_{mass} = \tilde{k}_{mass}\omega^{\frac{1}{2}}, \quad \tilde{k}_{mass} &= \left(\frac{cD_g}{\beta_g^{\frac{1}{2}}\rho}\right)\left(\frac{p_A^* M_A}{RT}\right), \end{aligned} \tag{4.27}$$

where D_g is the binary diffusivity of the solvent in the ambient gas, p_A^* is the vapour pressure of the pure solvent at temperature T, β_g is the kinematic viscosity of the ambient gas and M_A is the molecular weight of the solvent [158]. The dependence upon ω in this equation is explicit. Equation (4.27) was derived from the mass transfer coefficient for the transport from the surface of an infinite spinning disk to the surface of an infinite spinning disk to the surface of semi-infinite fluid in laminar flow above it. This relation has been coupled with the relation between vapour pressure and mole fraction in an ideal solution, [159] [160] and [161]. These results have been experimentally proven. The theoretical results are in good agreement with experiment [162].

Spin coating troubleshooting

Several spin-coating related defects of the layer can occur, see Figure 4.3. The examples shown were collected by [163]. Such defects were also present relatively frequently in this work when using a new dye, sample preparation

route, concentration of dye, or solvent. Some examples of these and possible causes are [163]:

- air bubbles on the substrate surface (Figure a) in 4.3)
  - air bubbles in the dispensed fluid (resin)
  - dispenser tip manufacturing fault
- comets, streaks or flares (Figure b) in 4.3)
  - fluid velocity (dispensing rate) too high
  - spin bowl exhaust rate too high
  - fluid dispensed too early
  - speed and acceleration too high
  - particles on substrate surface
  - fluid not dispensed at centre
- swirl pattern (Figure c) in 4.3)
  - fluid striking substrate surface off centre
  - spin bowl exhaust rate too high
  - speed and acceleration too high
  - exposure time of liquid on the substrate too short
- centre circle (Figure d) in 4.3)
  - incorrect chuck
- uncoated areas (Figure e) in 4.3)
  - insufficient dispense volume
- pinholes (Figure f) in 4.3)
  - air bubbles
  - particles in fluid
  - particles on substrate

If the spin coating parameters are chosen appropriately the layer deposition process works well and homogeneous layers are formed, as shown the example in Figure 4.4.

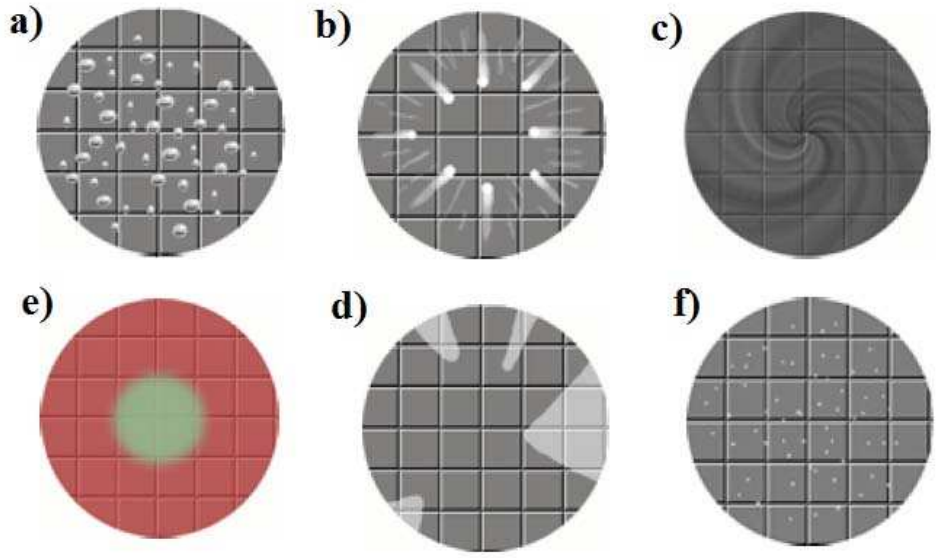

Fig. 4.3: Faulty spin coatings. Images taken from [163].

4.1.3 Layer thickness determination via spectroscopic ellipsometry

The layer thicknesses were measured by spectroscopic ellipsometry, which is based on the change of polarization of a defined polarized radiation upon transmission or reflection from an optically homogenous and isotropic layer. The interaction of the radiation with the layer to be characterized is correlated with its material properties such as: thickness, complex refractive index (n), or dielectric function tensor ($\varepsilon(\omega)$) [164]. Usually, this method can be applied to layer thicknesses of less than one nanometre up to several micrometers. In the reflective experimental setup (typically) the emitted light is first linearly polarized by a polarizer before meeting the sample after which it is reflected. This reflected radiation passes through a second polarizer before hitting the detector. Both, the incident and the reflected beam forms the plane of incidence by its polarization state, which is composed of the s- and p-component. The first oscillates perpendicular and the latter oscillates parallel to the plane of incidence. What is measured by ellipsometry is the complex reflectance ratio, ρ, which can be expressed by the amplitude, Ψ, and its correlated phase difference ϕ. The amplitudes of the components s and p are denoted by r_s and r_p respectively, when normalized to their initial value after reflection. In ellipsometry the ratio of these two values is measured which yields the complex reflectance ratio [164]:

$$\rho = \frac{r_p}{r_s} = \tan(\Psi)\, e^{i\varphi}. \tag{4.28}$$

$tan(\Psi)$ is the amplitude ratio upon reflection, and Φ is the phase shift, or in other words the difference in the phase of the light before and after hitting

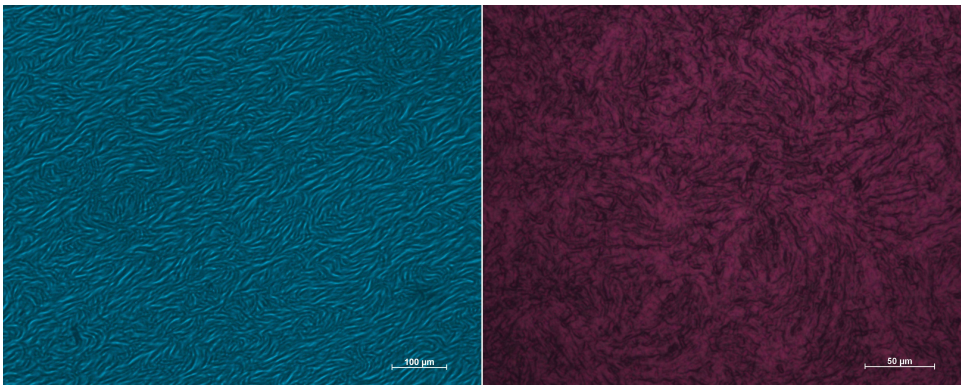

Fig. 4.4: Images of different organic layers on ITO substrate. The images were taken with a light microscope. Left: CuPc-TS layer. The thickness is 60nm. Right: P3HT layer of 70nm thickness.

the sample. Nevertheless, as only the thickness of the simplest sample can be measured directly with this method, a layer model has to be applied which includes all the individual layers in the correct sequence. The layer thickness is then obtained by a mathematical fit of the model to the measured results [164]. A scheme of the ellipsometry setup is shown in Figure 4.5.

4.2 Sample preparation

Patterning:
The fabrication of the different types of organic solar cells by spin coating is explained in the following. All substrates were prepared under clean room conditions. The ITO substrates were purchased from Thin Film Devices Inc. or from Flabeg GmbH. Substrates from Thin Film Devices Inc. are delivered already patterned. The other substrates had to be patterned before cleaning. (The patterns of all ITO substrates can be seen in Figure 4.6). The surface roughness parameters of the ITO substrates are $R_a = 1.43nm$, $R_{ms} = 1.73nm$, average height equals 7.18nm, and the maximum height equals 13.6nm. atomic force microscopy (AFM) images show a domain-grain structure. The crystal size is 15-20nm (see Figure 4.6). In order to texture a substrate in the desired way with the help of acid, as ITO dissolves in hydrochloric acid (HCl) [166], a multi-step procedure had to be applied. Firstly, the substrate had to be cleaned in a concentrated sulphuric acid bath for 3 minutes at room temperature (150mL for 50 substrates of $2.5cm^2$). Subsequently, the substrates were thoroughly rinsed with distilled water. Positive photoresist (AR-P 5350) was then either dip coated or spin coated onto the substrates. Dip coating involved the substrate being manually dipped into the photoresist. Layer deposition via spin coating was done at 3500rpm for 30 seconds at a constant rotation rate of 500rpm/s. Afterwards, all samples

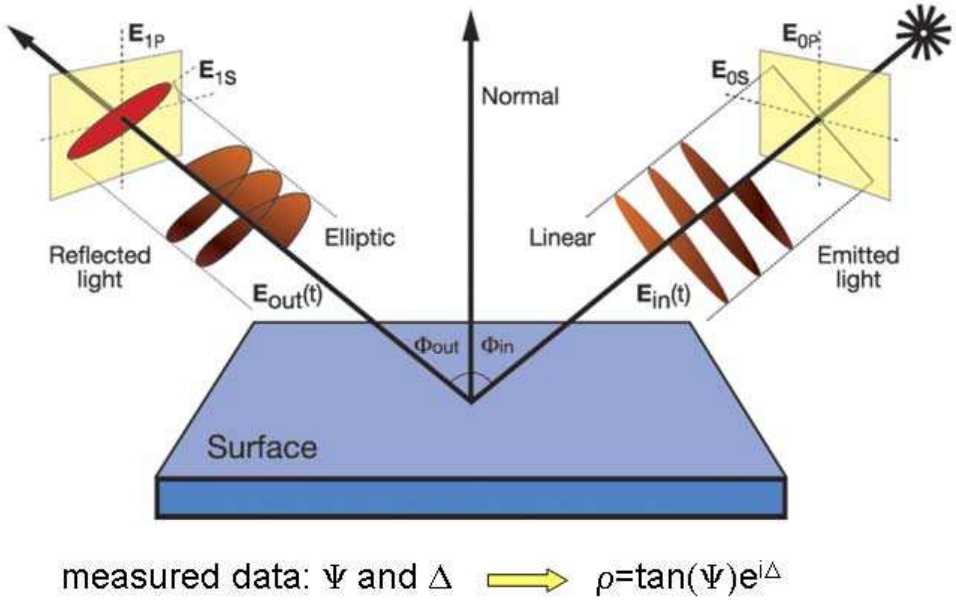

Fig. 4.5: Scheme of spectroscopic ellipsometry. Image taken from [165]. Light which is polarized parallel to the plane of incidence is called p-polarized and light polarized perpendicular to the plane of incidence is called s-polarized.

were annealed for 4 minutes at 105°C on a hotplate. The dip coated samples were only partly coated with photoresist, where the coated area depended on the immersion depth. Consequently, only one part of the ITO layer on the sample was protected with photoresist. The substrates were put into the HCl acid bath for 8 minutes (150mL for 20 substrates), after which the uncovered ITO on the substrate was completely dissolved away. Following the treatment of 20 samples in the 150mL HCl acid bath, the bath was replaced with fresh HCl. The photoresist was washed away with acetone, thus yielding a patterned ITO substrate. The pattern in this case was very simple due to the simple process used. Much more detailed patterns were produced with the spin coated samples. After deposition of the resist by spin coating the substrates were illuminated for 5 seconds with UV light through a shadow mask. Subsequently, the substrates were put in a developing bath for 10 seconds. The developing bath (150mL) consists of a mixture of distilled water and AR-300-35 developer in the ratio of [2:1]vol% (150mL for 30 samples). The samples were removed from the developing bath after 50 seconds. The developing bath was freshly prepared after 30 samples had been processed. This bath dissolves the illuminated parts of the positive photoresist. After the development the samples were rinsed with distilled water and dried in order to remove any water residues. Subsequently, they were put into the HCl acid bath for 8 minutes in order to dissolve the exposed ITO. This was followed by a rinsing step with distilled water and the

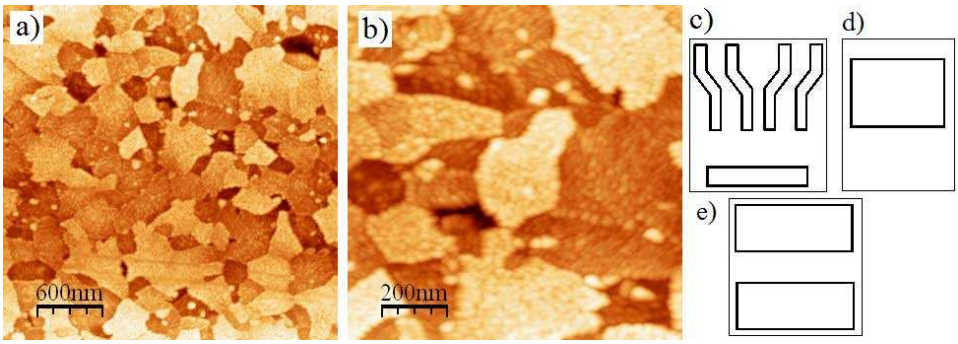

Fig. 4.6: AFM measurements and pattering of the ITO substrates. a) and b) AFM images of ITO substrate. The domain-grain structure is clearly visible. c), d), and e) pattering of the ITO substrate. It is necessary to suppress shorts.

removal of the photoresist in an acetone bath. After a thorough clean the substrates were ready to be used in the spin coating process of the organic solar cell fabrication.

Cleaning:

The cleaning procedure, which removes most of the impurities including adsorbates, enhances the wetting properties and improves the electrical behaviour of the ITO-poly(3,4-ethylenedioxythiophene) poly(styrenesulfonate) (Pedot:PSS) interface. These impurities create interfacial states, e.g. surface dipoles, which affect the electrical properties of the junction and hinder the current flow though this interface. The manually patterned and the already patterned purchased samples were cleaned in the same way before the spin coating process. The established cleaning techniques involve:

- plasma-cleaning,
- ozonizing, and
- wet cleaning.

The solutions used for wet-cleaning employed in this work are of VLSI quality. The substrates were cleaned using the following routine (inspired from [167]):

- removal of adhering glass-particles with the help of acetone and a lint free tissue (glass-particles remain from a previous cutting step),
- placement of 15 samples vertically in a teflon sample holder,
- ultrasonic bath for 10 minutes at 60 °C in a 3 vol.% mixture of deionized water and Mucasol©,
- thorough rinse with deionized water,

- ultrasonic bath in a mixture of 1:1 vol.% ethanol and methanol for 10 minutes,
- thorough rinse with deionized water,
- ultrasonic bath in acetone for 5 minutes at 40°C,
- thorough rinse with deionized water, and
- drying of the samples under nitrogen flow.

There are many variants of this wet-cleaning procedure. In some cases they include a plasma cleaning step. In my case, 15 substrates were placed vertically into a teflon© sample holder and sonicated for 15 minutes in a 3% aqueous solution of Mucasol© (an industrial glass detergent) at 40°C. Subsequently, they were rinsed thoroughly with distilled water and sonicated in an acetone bath for 10 minutes at 40°C. Following this they were rinsed with distilled water and sonicated in an isopropanol bath for 10 minutes at 40°C. Finally, the substrates were rinsed with distilled water and dried under a nitrogen flow. After the wet-process the samples were placed in a plasma chamber in order to purify the samples with an oxygen plasma. As the chamber is designed for 300mm silicon wafers the reported plasma treatment procedures had to be modified. A suitable plasma treatment was achieved for an applied power of 400W (He=15sccm, O_2=50sccm, p=$1 \cdot 10^{-5}$ bar) and a 10W reflected power for 600 seconds (sccm=standard cubic centimetres). The plasma treatment affects the electronic properties of the ITO layer. The plasma treatment can cause unbalanced charge carrier mobilities, injection barriers, traps or unwanted doping in the ITO layer, which would yield a decrease in the current flow through this interface.

Pedot:PSS

At the present time almost every electrode made of a TCO is covered with a Pedot:PSS layer when used in an organic solar cell. The Pedot:PSS forms a favourable quasi-ohmic contact with the TCO, which establishes a low-resistance path for the positive charge carriers from the organic material to the anorganic TCO. The company H.C. Starck supplies several special grades of Pedot:PSS. Each is optimized for its particular field of application. The grade CLEVIOS^{TM} HTL SOLAR is especially developed as a buffer layer for organic solar cells. In this work the electronic-grade CLEVIOS^{TM} P VP AI 4083 was used as a hole-collection layer and for anode planarization due to its high work function. An additional benefit of the buffer layer is the associated reduction in the number of electrical shorts. Before the Pedot:PSS is deposited onto an ITO surface filtering of the dispersion is necessary. The filtering procedure removes residual agglomerates and particles. Good filtration results were obtained by using a syringe equipped

with a 0.45μ Millex 25 polyvinylidene fluoride (PVDF) filter. A hydrophobic filter membrane like polytetrafluorethylen (PTFE) is more or less useless for this purpose as the Pedot:PSS is in an aqueous solution. The plasma assisted cleaned samples showed much better wetting properties than the samples which were cleaned only with liquids. The Pedot:PSS solution was sonicated in an ultrasonic bath for 40 minutes at room temperature prior to spin coating. This pretreatment prevents comets (or flares or rather streaks) on the spin coated layer. On the cleaned ITO substrate Pedot:PSS was usually spin coated at 4000rpm for 120 seconds and dried on a hotplate for 10 minutes at 110°C. The Pedot:PSS layer thickness varied in the range of 60nm-100nm. Due to the Pedot:PSS films being hygroscopic, the samples were either quickly processed further or handled in a moisture-free atmosphere for further layer deposition.

4.3 Polymer solar cells

As discussed in Chapter 2, the exciton binding energies are in the range of 0.1eV to 2eV based upon strong phonon coupling [60], [168], and[169]. Or in other words: an electric field in the range of 10^6V/cm is sufficient to cause exciton separation. For geminate pair separation 10^5V/cm is required [170]. Charge generation and separation is mandatory for organic photovoltaic devices [171]. The material combination of the polymer P3HT, and acceptors such as C_{60} and PCBM meets these requirements. The layer thickness of the Pedot:PSS layer was 100nm. Also the layer thicknesses of the P3HT layer and of the P3HT:PCBM blend layer were 100nm. The aluminium layer was 150nm thick. The layer thicknesses of these layers stood unchanged for all presented polymer solar cells.

4.3.1 Photoconductivity

The photoconductivity of various samples has been measured. The measured values differ from those reported in literature due to contamination by air and impurities during the lab-to-lab transportion of the semi-finished samples.

4.3.2 P3HT:PCBM

Frequently, organic solar cells are fabricated with the donor-acceptor material combination P3HT and PCBM, respectively. Such a combination was tested in order to form a comparison with previous studies, a base line for this work and to develop the methods needed for new cell architectures.
The P3HT:PCBM solar cell was spun-on patterned ITO substrates covered with a Pedot:PSS layer and deposited with an aluminium or silver top electrode. In order to improve the wetting properties every ITO substrate was

sample	voltage	current	
		dark	illuminated
Au-SWCNT-Ag	1V	4.12mA	
	2V	8.4mA	
Au-CuPcTS-Ag	10V	4pA	6pA
	20V	15pA	15pA
Au-CuPcTS-Ag	5V	60nA	60.5nA
Au-Pedot:PSS-CNT	5V	50μA	50μA
Au-Pedot:PSS-CNT-Ag	5V	9.2mA	9.2mA
Au-Pedot:PSS-Ag	5V	5.7μA	5.9μA
Au-CNT:CuPc-Ag	5V	30nA	30nA
	0V	200pA	175pA

Tab. 4.1: Photoconductivities of various samples.

plasma treated in a plasma chamber. The electrical properties of solar cell devices have been reported to be very sensitive to oxygen doping or plasma treatments of the ITO substrate, [172], [173], [174], [175], and [176]. These treatments can cause unbalanced charge carrier mobilities, injection barriers, traps or unwanted doping which would yield a s-shaped J-V dependency in dark-conditions, see Figure 4.7. Under illumination diodic behaviour is found. The obtained current under illumination is two orders of magnitude larger than obtained under the dark condition. Many charge carriers are within the bulk. Space charge accumulation is expected to be enhanced by any unbalanced charge carrier transport properties, or barriers at interfaces yielding field weakening causing a drop in the photo current. Although the dependency should be more s-shaped under illumination, the opposite happens. This implies that the photo induced charge carriers bypass the barrier during the extraction or injection of charge carriers. According to [172] a long oxygen plasma treatment causes the elimination of the photo current in the J-V dependency. If the device has just this defect, the measured J-V behaviour should be that of a good diode. Such a J-V behaviour is shown in Figure 4.7.
The sample preparation conditions had an unpredictable impact on the manufactured devices. Each prepared sample had to be transferred between two institutes for the deposition of the metal top electrode. This lead to an alteration and contamination of the device. In particular, the surface of the active layer was crucially exposed and contaminated. The top electrode was deposited onto this surface in the next step of fabrication which yielded unpredictable surface states. In addition, these surface states (oxidized organic, impurities, dipoles) cause energy mismatch or barriers at the interface to the electrode layer. This results in a variation of the efficiency on the same substrate (up to 50 single solar cells were deposited on one ITO glass substrate).

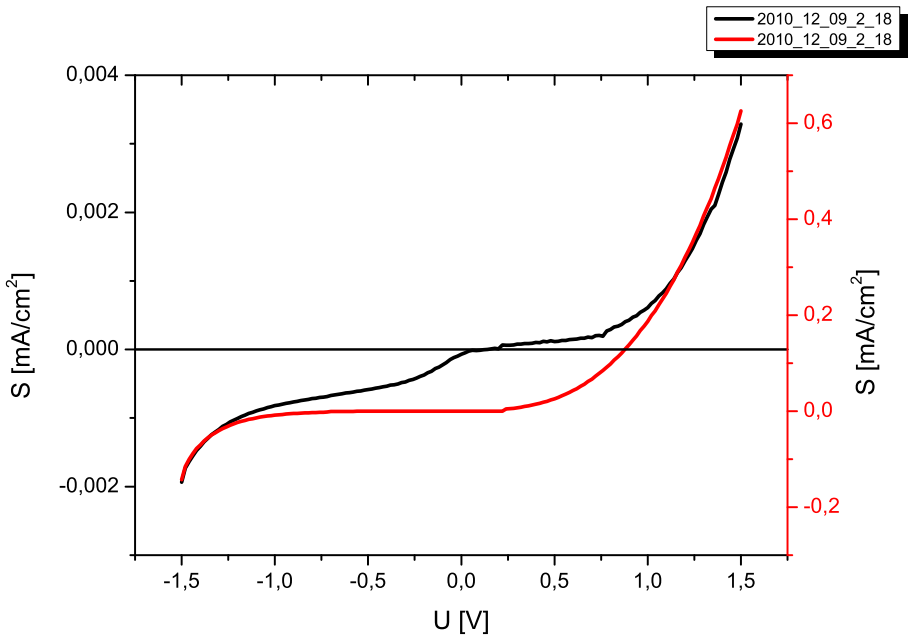

Fig. 4.7: P3HT:PCBM Diode. Under dark conditions a s-shape curve occurs. Under illumination diodic behaviour still exists but with much larger current densities.

The metal top electrode was directly deposited onto the organic active layer. However, a buffer layer has to be deposited in between these two layers. This layer can consist of 4,7-Diphenyl-1,10-phenanthroline (BPhen), Lithium fluoride (LiF), or Alq3 with a thickness of several nanometres. In this study BPhen was used for some samples.
In order to obtain more parameters from the measured J-V curves, mathematical operations were applied. The J-V curve was fitted with a transcendental equation based on a single diode model of the solar cell under illumination. This transcendental equation has no explicit analytical solution. Mathematical approximation methods have been used to address this issue, [177], or the application of the prior knowledge of some parameters like series resistance identifying the missing model parameters [178].

Theory of Lambert W function for solar cells

In order to get an explicit analytical solution, the Lambert W function has to be applied:

$$z = W(z)\, exp^{W(z)}, \quad z \in \mathcal{C}. \tag{4.29}$$

One limitation of using the Lambert W function is the influence of the noise in the measurements, which reduces the precision of the extracted data, [179]. Polynomial curve fits (smoothing spline) to the measured J-V curves have been used to smooth the curve. A filter of the noise was made by applying a low degree polynomial fit, which avoided the Runge-Effect. Acquiring the appropriate fit is crucial to obtaining good parameters. The current-voltage behaviour for a single diode model of solar cells can be expressed as:

$$I = I_{ph} - I_0 \left[\exp\left(\frac{V + I \cdot R_s}{n \cdot V_{th}}\right) - 1\right] - \frac{V + I \cdot R_s}{R_{sh}}, \tag{4.30}$$

where I and V are the current and voltage, respectively, I_{ph} and I_0 are the photo and saturation current, respectively, R_s and R_{sh} are the series and shunt resistance, respectively, n the diode ideality factor, and $V_{th} = k_b \cdot T/q$ is the thermal voltage (see Chapter 2.4). The solution of equation (4.30) derived using the Lambert W function is, [180]:

$$I = \frac{R_{sh}\left(I_{ph} + I_0\right) - V}{R_s + R_{sh}} - \frac{nV_{th}}{R_s} W\left\{\frac{R_s R_{sh} I_0}{nV_{th}\left(R_s + R_{sh}\right)} \exp\left(\frac{R_{sh}\left(R_s I_{ph} + R_s I_0 + V\right)}{n \cdot V_{th}\left(R_s + R_{sh}\right)}\right)\right\}, \tag{4.31}$$

where W denotes the short-hand notation of the Lambert W function. According to [181] the differential dV/dI can be expressed as:

$$\frac{dV}{dI} = -A - \frac{B}{-V - C \cdot I + D}, \tag{4.32}$$

where the parameters can be defined as:

$$\begin{aligned} &A = R_s, \quad B = nV_{th}R_{sh}, \quad C = R_s + R_{sh}, \\ &D = nV_{th} + R_{sh}\left(I_{ph} + I_0\right). \end{aligned} \tag{4.33}$$

The first derivative dI/dV of the measured I-V curve can be expressed with the help of equation (4.33) as:

$$\frac{dI}{dV} = f'\left(V, I\right) \frac{V + C \cdot I - D}{V \cdot A + A \cdot C \cdot I - A \cdot D}. \tag{4.34}$$

In equation (4.33) four parameters A to D are defined in terms of the single diode model. When the measured and calculated data (current at applied voltage and the first derivative of the I-V curve) are fed into equation (4.33), then the parameters A to D can be calculated. After the transposition of the equation (4.32) the solar cell parameters expressed in terms of the variables A to D are:

$$I_{ph} + I_0 = \frac{\frac{D-B}{R_{sh}}}{R_{sh}} = Z. \tag{4.35}$$

Equations (4.30) and (4.35) form two equations and two variables (I_0, I_ph). These yield:

$$I_{ph} = \left[\frac{(V + C \cdot I)}{R_{sh}} - Z\right] \cdot \exp\left(-\frac{V + I \cdot R_s}{n \cdot V_{th}}\right) + Z, \quad I_0 = Z - I_{ph}. \tag{4.36}$$

This method was applied in this work to obtain the solar cell parameters from the measured J-V dependencies.

Software implementation

The software implementation of this analysis was made using Matlab. This is briefly discussed in the following. The fit function "lsqnonlin" solves nonlinear least- squares problems including nonlinear data-fitting problems. By using this approach the fitting of data with heteroskedasticity or homoskedasticity can be supported with the addition of a weighting factor. This makes the function even more suitable for the application. The function "lsqnonlin" yields good results, if the starting points are appropriately chosen. Practically, a high value for C yields good fits, whereas setting the starting points for A yields bad fits.
A possible explanation is that the dynamic of this nonlinear system is more dominated by the parameter C.
Parameter A accumulates relatively many residues in its neighbourhood. These residues yield a bad fit for the whole function.
In order to prove whether the calculated fits were in good agreement with the measured data, the fitted curves were integrated using a trapezoidal function. The integrated curve was then compared with the measured I-V curve. The results obtained from such a comparison are shown in Figure 4.8. The band diagram of the following solar cells are shown in Figure 4.9. The P3HT:PCBM devices have initial series resistances of 150Ω-250Ω. The shunt resistances are one or two orders of magnitude larger than the series resistance. The diode factor, n, is larger than 2 for the fabricated devices, which can be related to occurrence of recombination centres within the active layer. The J-V curves for such a device are shown in Figure 4.10 a). A relatively small series resistance is observed, because the energy levels are well aligned at the different interfaces. This also leads to the observed short circuit current. In many cases the shunt resistance is larger than $1k\Omega$. The large value here is due to good device properties. Low shunt resistances are caused by highly conductive areas at the interfaces in the device leading to a large leakage current. In these sample only the diode ideality factor n is out of the range needed to obtain good solar cells. Normally, the diode ideality factor varies from 1 to 2 ([182], [183], [184], and [185]). It is reported in the literature that large values for n are due to recombination centres caused by defects in the space charge layer [186]. Other groups have reported that large values for n can originate from the shunt resistance, [187]. Another explanation is that the value of n correlates with the recombination mechanism, [188]. If recombination in the active area (depletion region) becomes more dominant than the recombination in the charge carrier transport layers (neutral regions, $n \approx 1$) the value of n increases. In this case a large value of n would indicate an increase of recombination centres in the depletion

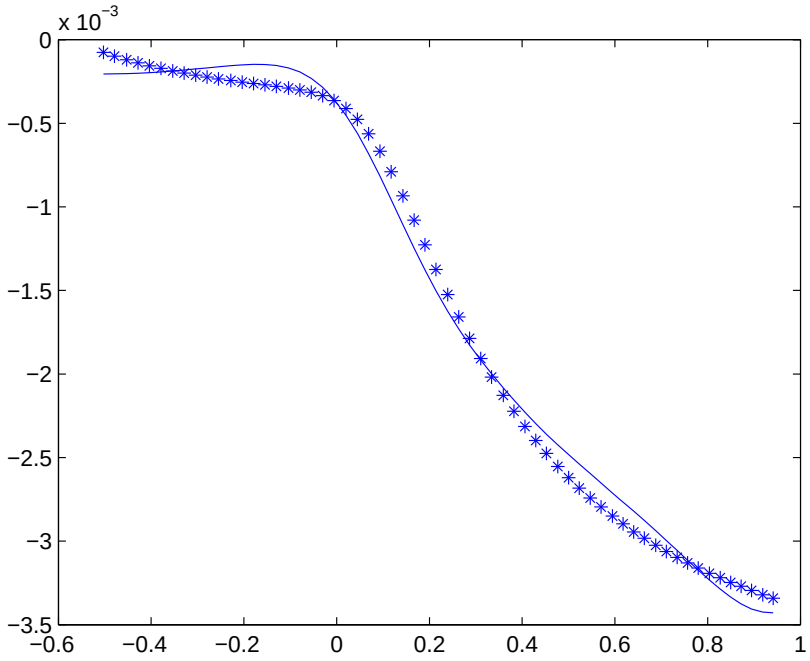

Fig. 4.8: The fit of the first derivative with the Lambert W function (solid line). This was implemented in Matlab with the help of "lsqnonlin" and "fitfun".

region caused by shunts. Such a shunt can be formed during the fabrication of the organic solar cell device. If the thermal annealing procedure was done under a nitrogen atmosphere for 30 minutes at 150°C the open circuit voltage increased from 62mV to 184mV, for the sample shown in Figure 4.10 b). Figure 4.10 b) also shows an increase of all the resistances after a thermal annealing treatment. In addition, the diode ideality factor increases. Such degradation of all device parameters due to the thermal process indicates that the device itself degrades. The same changes in the device parameters occurs for all samples of this series, as can be seen in Figures 4.10 c) and 4.11. The device parameters of this series before and after a thermal annealing treatment are summarized in Table 4.2. In the next series of experiments the top electrode was evaporated after transport from one lab to another. Although the samples were treated very carefully, the devices showed low photo currents. Nevertheless, the photocurrent is clearly detectable in the electrical measurements under the condition of illumination (see Figure 4.12).

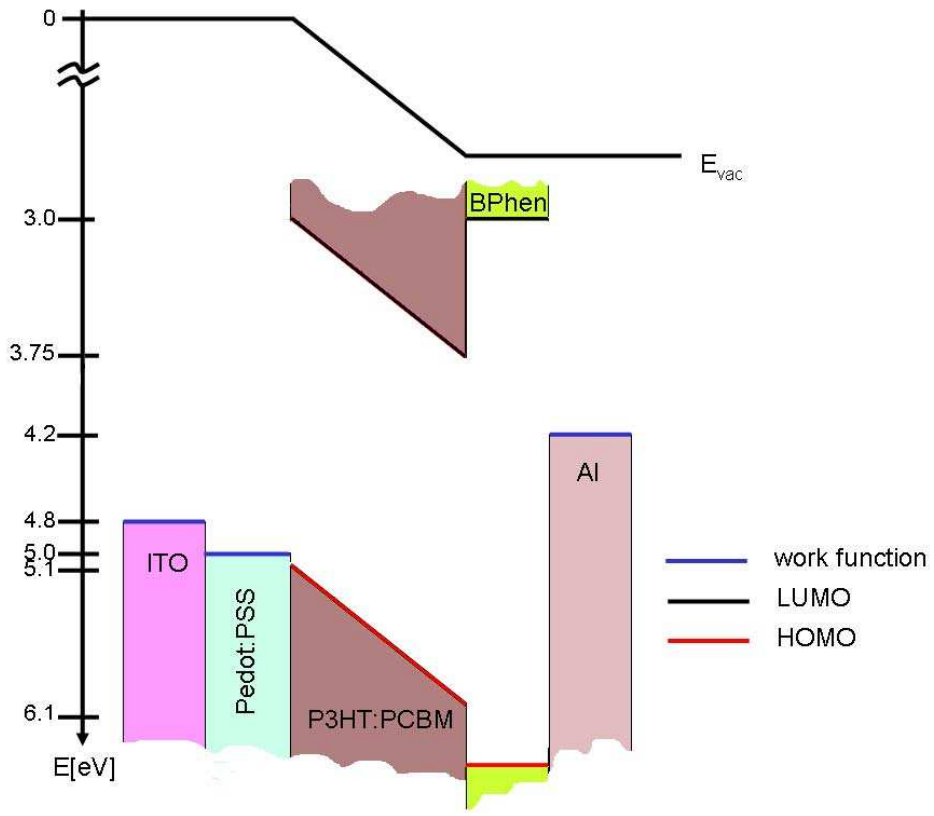

Fig. 4.9: Band diagram of the studied solar cells. The sample architecture consisted of ITO-Pedot:PSS-P3HT:PCBM-BPhen-Al. The P3HT:PCBM blend is the active matrix.

4.3.3 P3HT:PCBM and evaporated C_{60}

A combination of spin coating and thermal evaporation was used for layer depositions in another series of experiments. The polymer Pedot:PSS, and a polymer-PCBM layer were spin coated onto various ITO substrates. The sample architecture consisted of ITO-Pedot:PSS-P3HT:PCBM. A C_{60} layer was deposited onto the top layer of these samples. The C_{60} layer was 30nm thick. The top electrode was subsequently deposited in the same thermal evaporator. It consisted of a buffer layer (6nm BPhen) with a 100nm thick aluminium metal layer on top. The thin layer of BPhen was deposited on the active layer as a hole buffer layer. The band diagram of the following solar cells are shown in Figure 4.13. The cell efficiencies varied from η=0.12% to η=1% and the FF stays around FF≈0.3. The main difference to the samples only fabricated by spin coating was the increased photocurrent in this series of samples. This is probably caused by the use of better deposition conditions. The spin coated samples had to be transferred to another laboratory for the deposition of the top electrode. Contrastingly,

sample		R_s [Ω]	R_{sh}[kΩ]	n	fill factor (FF)	J_{sc} [mA/cm^2]	V_{oc}[V]	η[%]
$G2_1$	as-is	246	77.89	4.04	0.29	-0.91	0.062	0.016
	annealed	250	7.78	4.08	0.24	-1.21	0.184	0.053
$G2_2$	as-is	172	9.42	3.22	0.29	-0.98	0.061	0.017
	annealed	767	12.17	3.93	0.24	-1.31	0.188	0.06
$G2_3$	as-is	176	4.08	3.24	0.29	-0.98	0.06	0.017
	annealed	856	9.27	4.28	0.23	-1.20	0.191	0.054
$G2_4$	as-is	188	5.66	3.35	0.29	-0.99	0.063	0.018
	annealed	1360	17.9	3.55	0.24	-1.01	0.229	0.057

Tab. 4.2: Overview of the characteristic values of the ITO-Pedot:PSS-P3HT:PCBM-BPhen-Al samples.

the deposition of the top electrode can be done directly after the layer deposition for the samples in which the organic layers are partly fabricated by thermal evaporation. Hence, contamination of the organic top layer due to air exposure during transportation and the handling of the sample can be excluded. The J-V dependence of such a sample is shown in Figure 4.15 b). An increase in the photocurrent was the major difference between these samples and those that were transported between labs for the deposition of different layers. The short circuit current density is $2.6mA/cm^2$, which is more than two orders of magnitude larger than the purely spin coated samples. The open circuit voltage is 141mV , which is 2 to 4 times less than the spin coated case. The samples were annealed for 30 minutes at 150°C under a nitrogen atmosphere in this series of experiments. This additional process yields an even higher photocurrent. This is most likely to be caused by a phase transition and the segregation of the organic blend, as determined by [189]. The phase transition causes nano crystallisation in the layer. The segregation process yields percolation pathways for the respective charge carriers. Both changes enhance the charge transport in the organic blend. In particular, the short circuit photocurrent density of the sample decreases from $J = 5.97mA/cm^2$ to $J = 5.03mA/cm^2$. This is accompanied by an open circuit voltage increase from 0.12V to 0.53V. The thermal annealing processes causes a 3 times increase in the open circuit voltage. The corresponding J-V dependency is shown in Figure 4.15 b). The annealing treatment leads to the roughening of the top electrode. Furthermore, the C_{60} deposition appears yellow as shown in Figure 4.14. The impact of thermal annealing to efficiencies and fill factor is shown in Figure 4.16. The device performance is significantly improved by thermal annealing, if the solar cells contain a C_{60} layer.

sample		R_s [Ω]	R_{sh}[kΩ]	n	FF	J_{sc} $[mA/cm^2]$	V_{oc}[V]	η[%]
$G1_1$	as-is	179	10.23	2.61	0.32	-2.86	0.108	0.08
	annealed	222	13.381	3.56	0.44	-3.67	0.511	0.84
$G1_2$	as-is	188	5.66	3.35	0.33	-2.32	0.530	0.08
	annealed	1360	17.898	3.55	0.43	-3.58	0.530	0.82
$G1_3$	as-is	150	9.96	3.29	0.32	-2.82	0.107	0.09
	annealed	1786	16.27	3.39	0.39	-3.18	0.544	0.68

Tab. 4.3: Overview of the characteristic values of the ITO-Pedot:PSS-P3HT:PCBM-C_{60}-BPhen-Al samples. The thickness of the C_{60} layer is 30nm.

4.4 Small molecule solar cells

Small molecules are the other class of organic materials that can be used for organic solar cells. The layer thickness of the Pedot:PSS layer was 100nm. Also the layer thickness of the CuPc-TS layer was 100nm. The aluminium layer was 150nm thick. The layer thicknesses of these layers stood unchanged for all presented polymer solar cells.

4.4.1 CuPc

One intensively studied small molecule is CuPc. Its band gap of 1.9eV, [190], is ideally suited to its use as a solar cell absorber material. According to the Shockley-Queisser limit the ideal band gap should be around 1.7eV, [186]. Consequently, as in many previous studies this molecule and its derivatives were chosen also for this study. The robustness of CuPc to weather, irradiation, and absorption in the visible spectra makes it an almost ideal material for OPV. The easiest way to fabricate a CuPc based solar cell is to deposit it onto a transparent electrode with a work function close to that of the energetic level of the HOMO of the CuPc followed by the deposition of another metal electrode on top of the CuPc layer. Although exciton quenching occurs at the organic semiconductor-metal interface, there is also exciton dissociation at a much lower rate at the same interface. The latter process generates the photo current in this device so that it can work as an organic solar cell (OSC). The first device with this structure (also known as the Schottky-junction solar cell) was fabricated in 1981 by [191]. In this study a water soluble functionalized derivative was used, CuPc-TS, instead of the CuPc used by [191]. The architecture of the device in the work of [191] is shown in Figure 4.17. CuPc-TS only. The band diagram of the following solar cells are shown in Figure 4.18. The device performances of the first four samples were the same. Their parameters did not differ much. The four Figures 4.19 and 4.20 show the J-V dependency of the fabricated devices under 1.5AM illumination. Not every sample acts as an OSC. Many of the prepared samples simply work as diodes as shown in an exemplarily fashion

sample		R_s [Ω]	R_{sh}[kΩ]	n	FF	J_{sc} $[mA/cm^2]$	V_{oc}[V]	η[%]
$D3_1$	as-is	680	27.60	2.93	0.13	-0.076	0.324	0.003
$D3_2$	as-is	719	32.50	2.81	0.13	-0.065	0.333	0.002
$D3_3$	as-is	904	21.10	2.32	0.15	-0.055	0.284	0.002
$D3_4$	as-is	560	26.85	2.84	0.16	-0.04	0.107	0.002

Tab. 4.4: Overview of the characteristic values of ITO-Pedot:PSS-CuPc-TS-Al samples. Tempering destroys the samples.

sample		R_s [Ω]	R_{sh}[kΩ]	n	FF	J_{sc} $[mA/cm^2]$	V_{oc}[V]	η[%]
$D2_1$	as-is	82	58.33	2.33	0.27	-0.46	0.038	0.005
$D2_2$	as-is	86	53.07	2.17	0.27	-0.43	0.028	0.003
$D2_3$	as-is	92	50.57	2.61	0.26	-0.27	0.021	0.001
$D2_4$	as-is	560	26.85	2.84	0.16	-0.04	0.107	0.002
	annealed	292	24.28	4.12	0.36	-0.007	0.041	0.0001

Tab. 4.5: Overview of the characteristic values of ITO-Pedot:PSS-CuPc-TS-C_{60}-BPhen-Al samples. The C_{60} layer is 30nm thick. Tempering destroys most of the samples.

in Figure 4.21. This particular device dependency can be interpreted in terms of a two diode device. The energy level mismatch between the layers results in barrier formation at every electrode interface. These barriers form a Schottky-diode at the electrode-CuPc-TS interfaces. Unfortunately, these barriers work against each other, which leads to the complete suppression of the photocurrent as one of the two diodes always blocks the generated photo current.

4.4.2 CuPc-TS and C60

This series of samples combined CuPc-TS and C_{60}. The next four had a 30nm thick C_{60} layer. All showed similar properties to the previous ones, although the current densities were smaller. The band diagram of the following solar cells are shown in Figure 4.22. Almost all these samples show bad performance after tempering for 30 minutes at 150°C. This is probably caused by degradation processes of water residues in the CuPc-TS layer interacting with the aluminium top electrode.
The following series of samples combine CuPc-TS and a 60nm thick C_{60} layer.

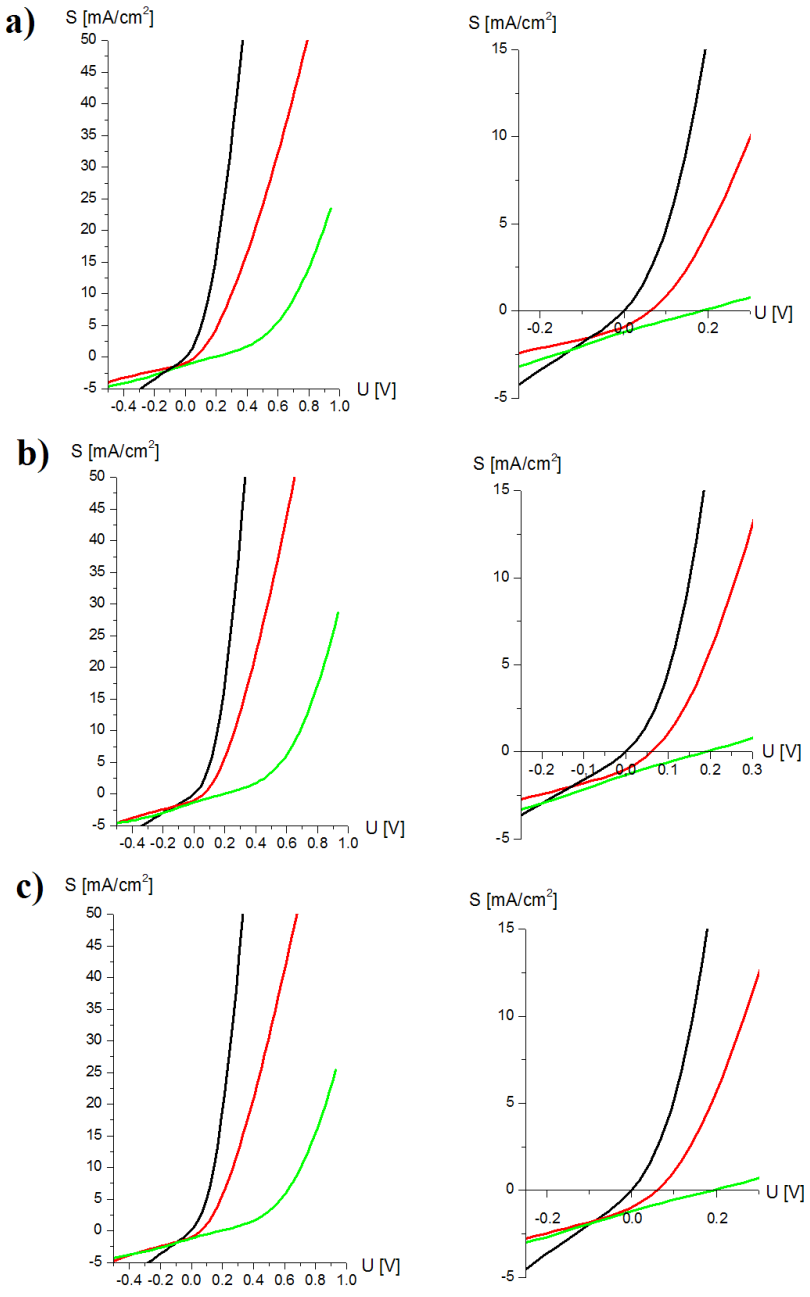

Fig. 4.10: J-V curves of the fabricated organic solar cells. The device architecture is ITO-Pedot:PSS-P3HT:PCBM-BPhen-Al. a)-c) Left: full graph of J-V characteristics, where black corresponds to dark condition, red represents under illumination and green corresponds to illumination after thermal annealing. Right: magnification around the origin. The characteristic values are summarized in table 4.2.

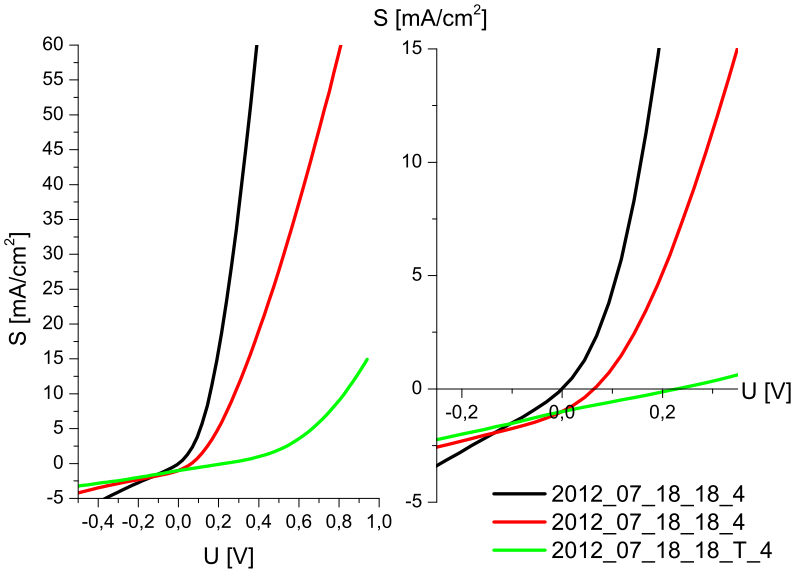

Fig. 4.11: J-V curves of the last organic solar cell of this series of experiments. The device architecture is ITO-Pedot:PSS-P3HT:PCBM-BPhen-Al. Left: full graph of J-V characteristics, where black corresponds to dark condition, red represents under illumination and green corresponds to illumination after thermal annealing. Right: magnification around the origin. The characteristic values are summarized in table 4.2.

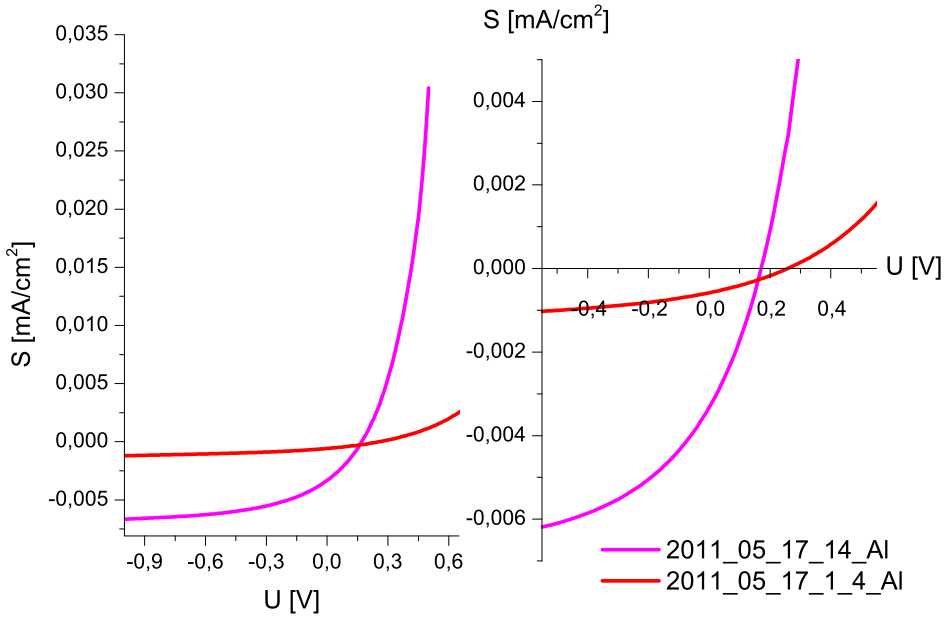

Fig. 4.12: Left: J-V characteristics of two ITO-Pedot:PSS-P3HT:PCBM-Al samples under illumination. The efficiency varies from $4.5 \cdot 10^{-5}\%$ to $1.73 \cdot 10^{-4}\%$, the open circuit voltages are: $V_{oc} = 0.170V$ and $V_{oc} = 0.25V$, the short circuit current densities are: $J_{sc} = 0.003mA/cm^2$ and $J_{sc} = 0.00058mA/cm^2$. Right: zoom around the origin. Fill factor around 0.30 are typically for these J-V curve shapes.

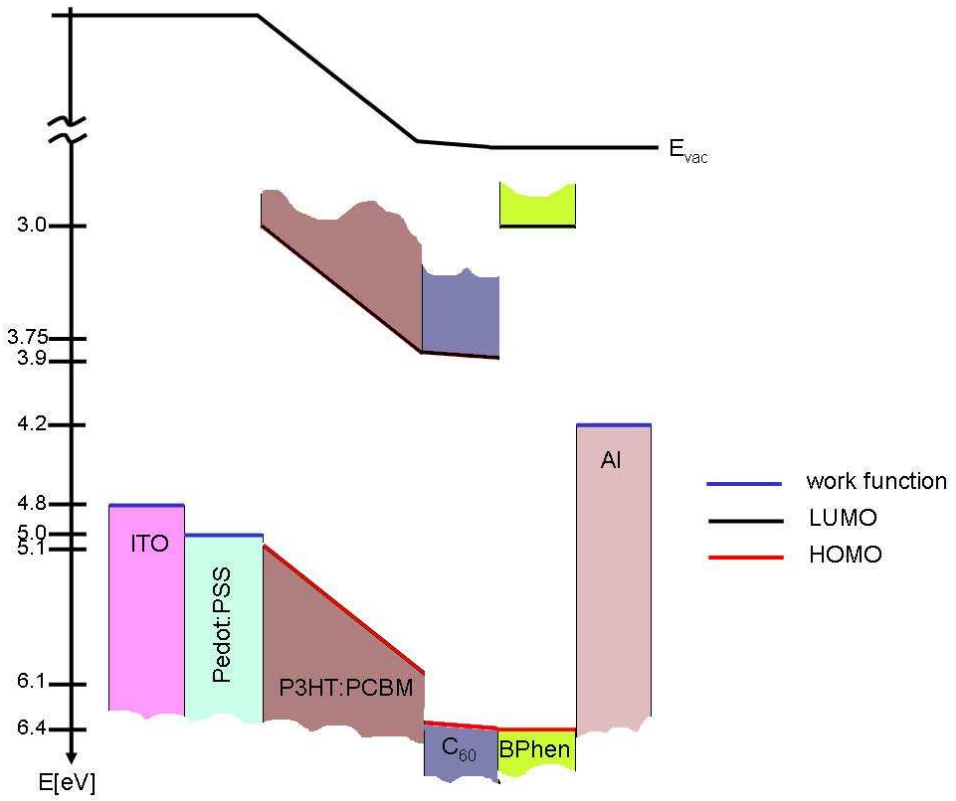

Fig. 4.13: Band diagram of the studied solar cells. The sample architecture consisted of ITO-Pedot:PSS-P3HT:PCBM-C_{60}-BPhen-Al. The P3HT:PCBM blend covered with a 30nm thick C_{60} layer is the active matrix.

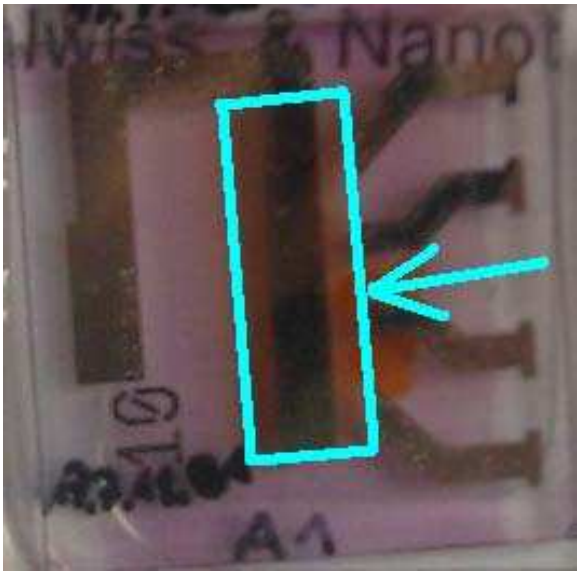

Fig. 4.14: Visible effects of thermal annealing on the sample.

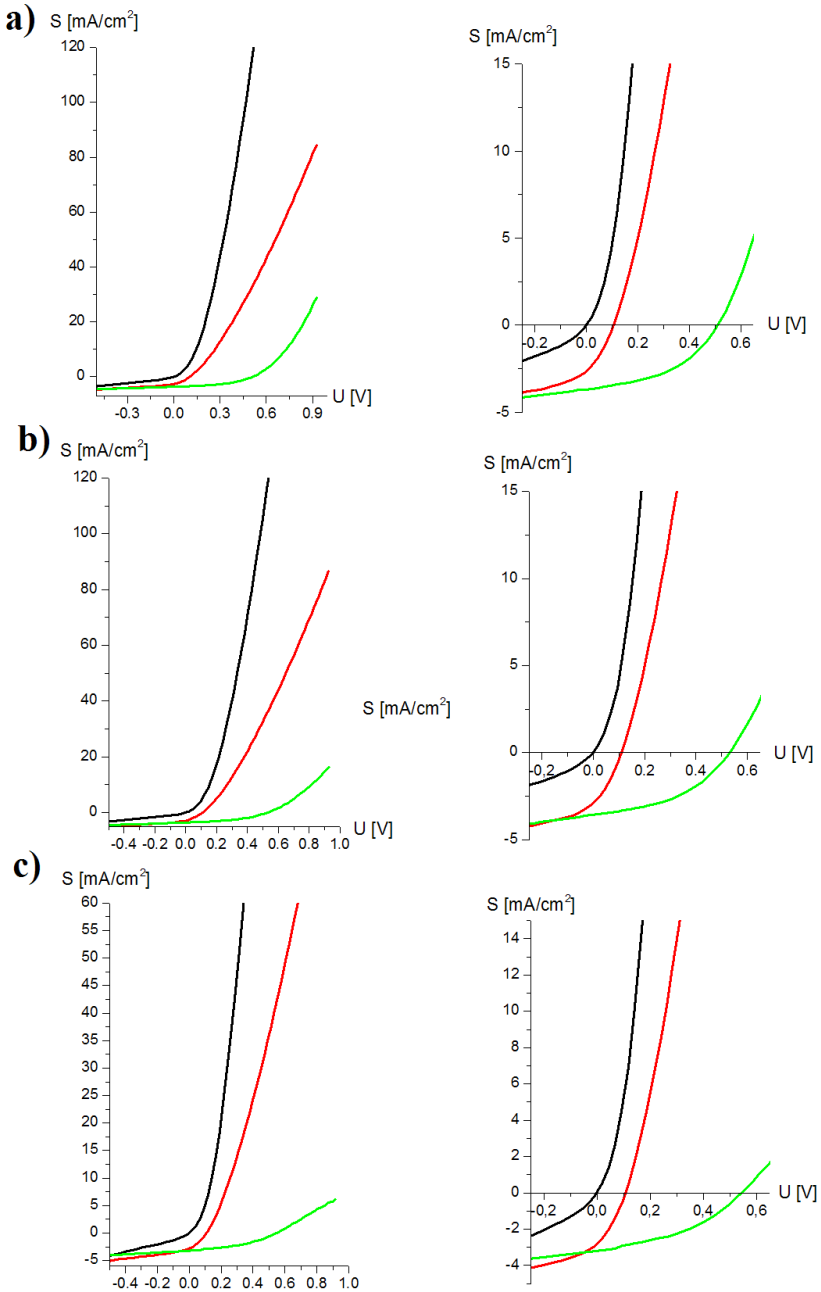

Fig. 4.15: J-V curves of the organic solar cells of this series of experiments. The device architecture is ITO-Pedot:PSS-P3HT:PCBM-C_{60}-BPhen-Al. The thickness of the C_{60} layer is 30nm. The devices form a BHJ-HJ structure. Left: full graph of J-V characteristics, where black corresponds to dark condition, red represents under illumination and green corresponds to illumination after thermal annealing. Right: magnification around the origin. The characteristic values are summarized in table 4.3.

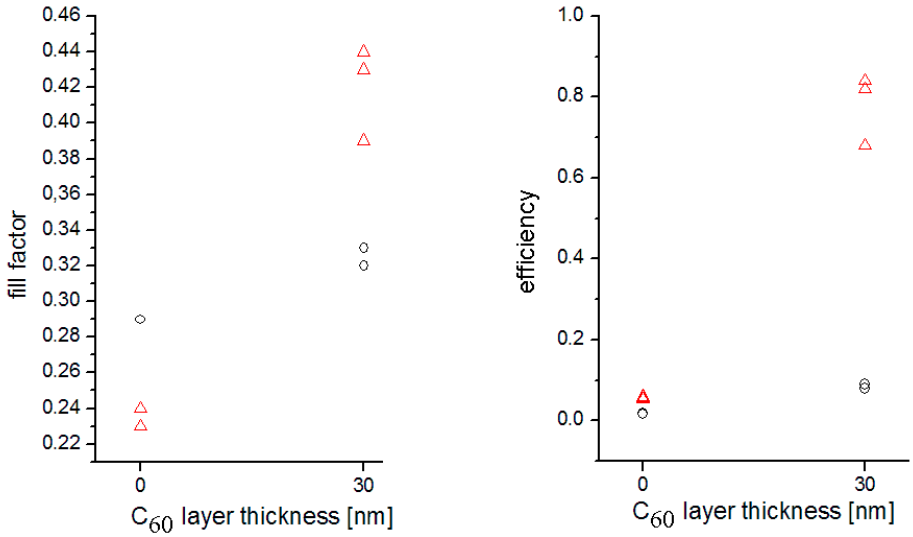

Fig. 4.16: Efficiencies and fill factors of P3HT:PCBM and P3HT:PCBM-C_{60} solar cells before and after thermal annealing. Thermal annealing significantly improved the device performance, if the solar cell contains a C_{60} layer.

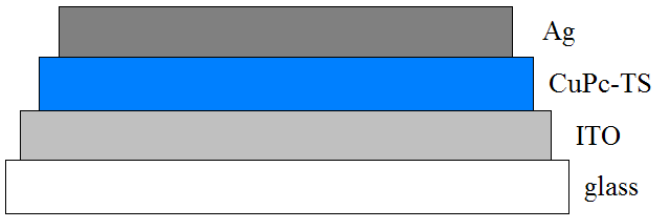

Fig. 4.17: Scheme of the organic solar cell made with CuPc-TS and an aluminium top electrode.

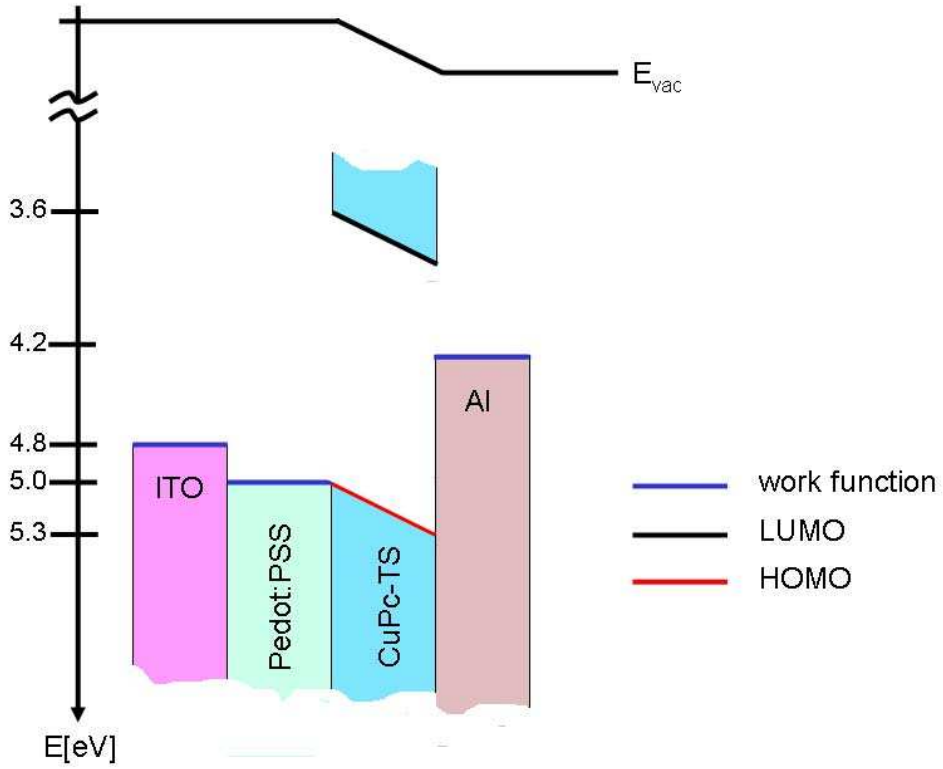

Fig. 4.18: Band diagram of the studied solar cells. The sample architecture consisted of ITO-Pedot:PSS-CuPc-TS-Al. The interface of CuPc-TS and aluminium is the active matrix.

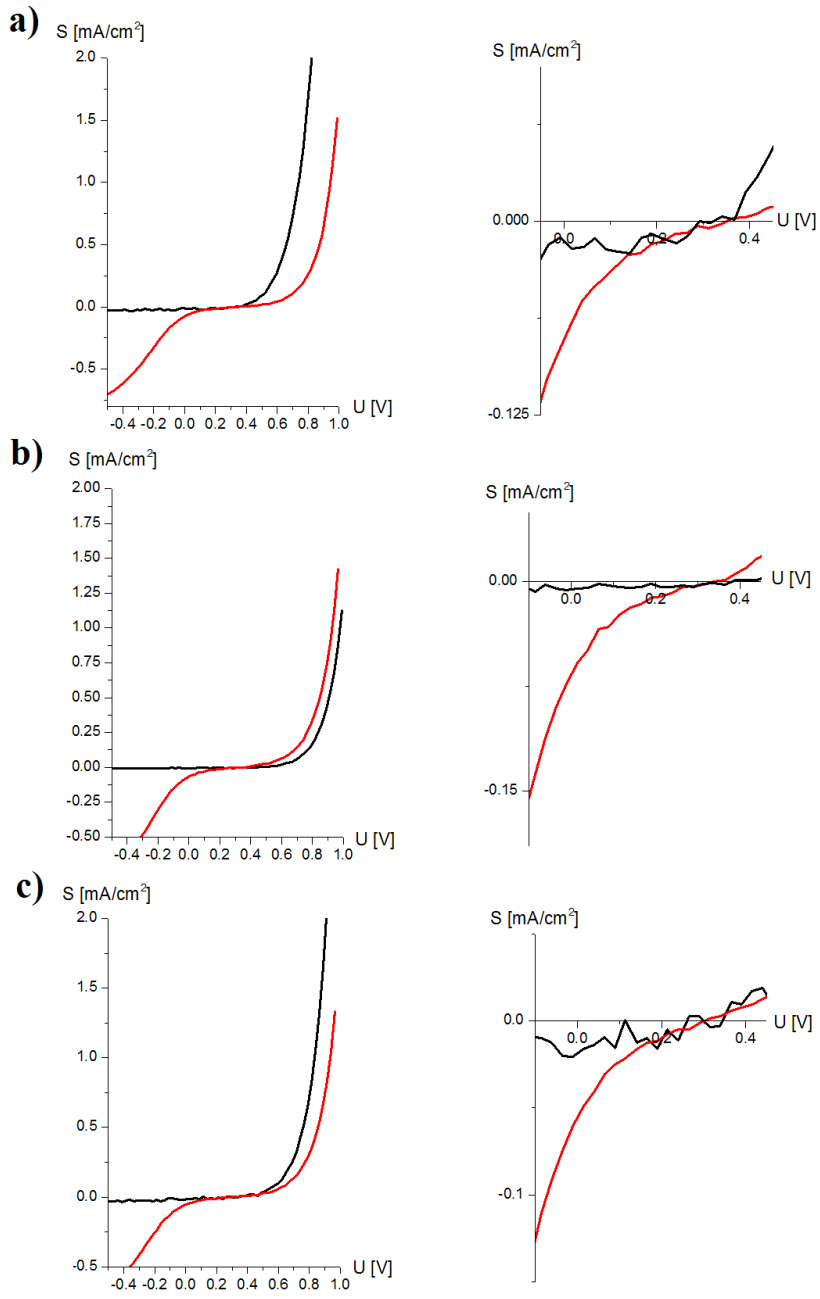

Fig. 4.19: J-V curves of CuPc-TS solar cells. The device architecture is ITO-Pedot:PSS-CuPc-TS-Al. Left: full graph of J-V characteristics, where black corresponds to dark condition, and red represents under illumination. Right: magnification around the origin. The characteristic values are summarized in table 4.4. Tempering destroys the devices.

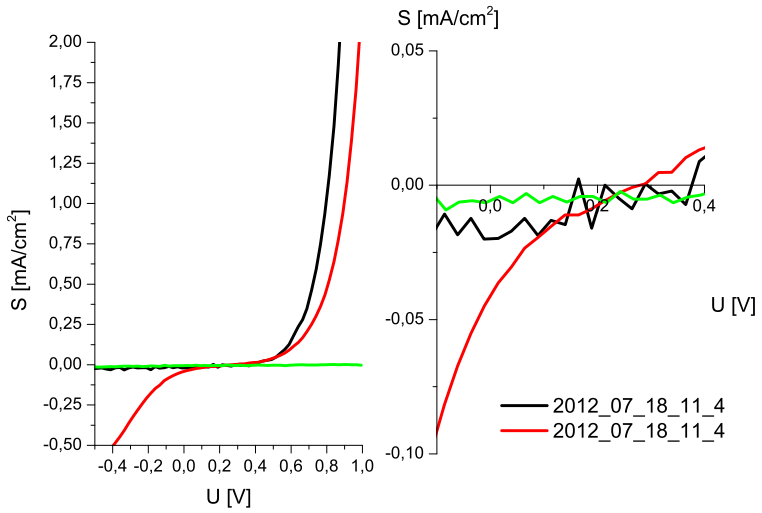

Fig. 4.20: J-V curves of a CuPc-TS solar cell. The device architecture is ITO-Pedot:PSS-CuPc-TS-Al. Left: full graph of J-V characteristics, where black corresponds to dark condition, red represents under illumination and green corresponds to illumination after thermal annealing. Right: magnification around the origin. The characteristic values are summarized in table 4.4. Tempering destroys the device.

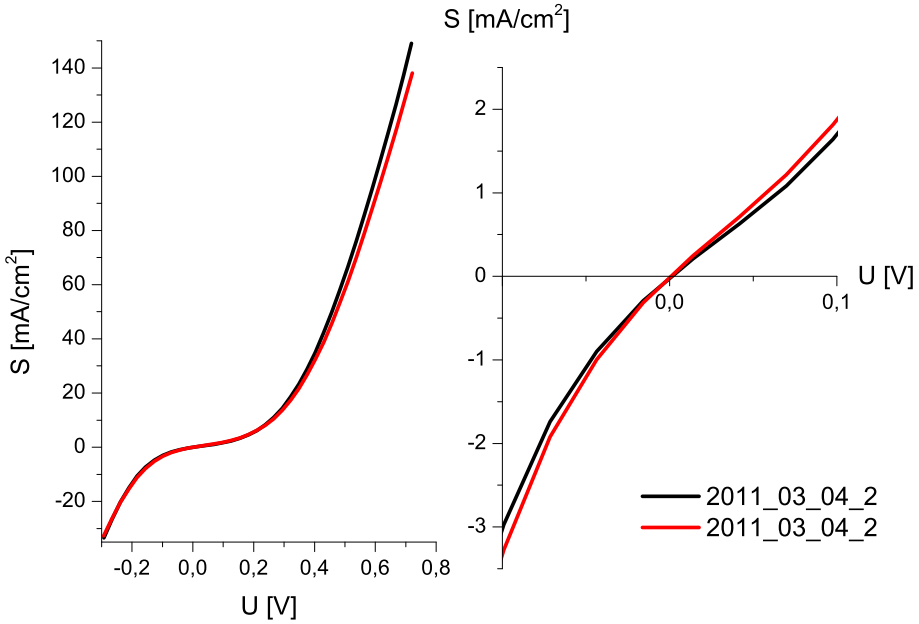

Fig. 4.21: CuPc-TS diode. The mismatch of the energy levels at the two outer electrodes yield the formation of two energy barriers and the device works as double diode. R_s=149Ω, R_sh=1569Ω, n=4.42.

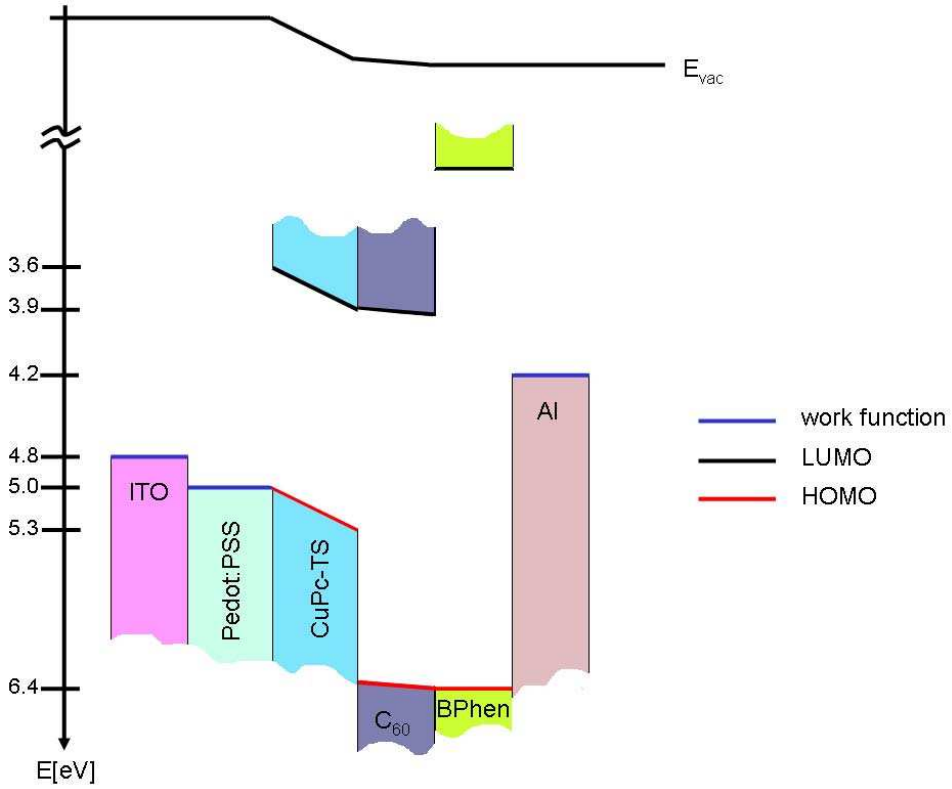

Fig. 4.22: Band diagram of the studied solar cells. The sample architecture consisted of ITO-Pedot:PSS-CuPc-TS-C_{60}-BPhen-Al. The interface of CuPc-TS and C_{60} is the active matrix. The C_{60} layer is either 30nm or 60nm thick.

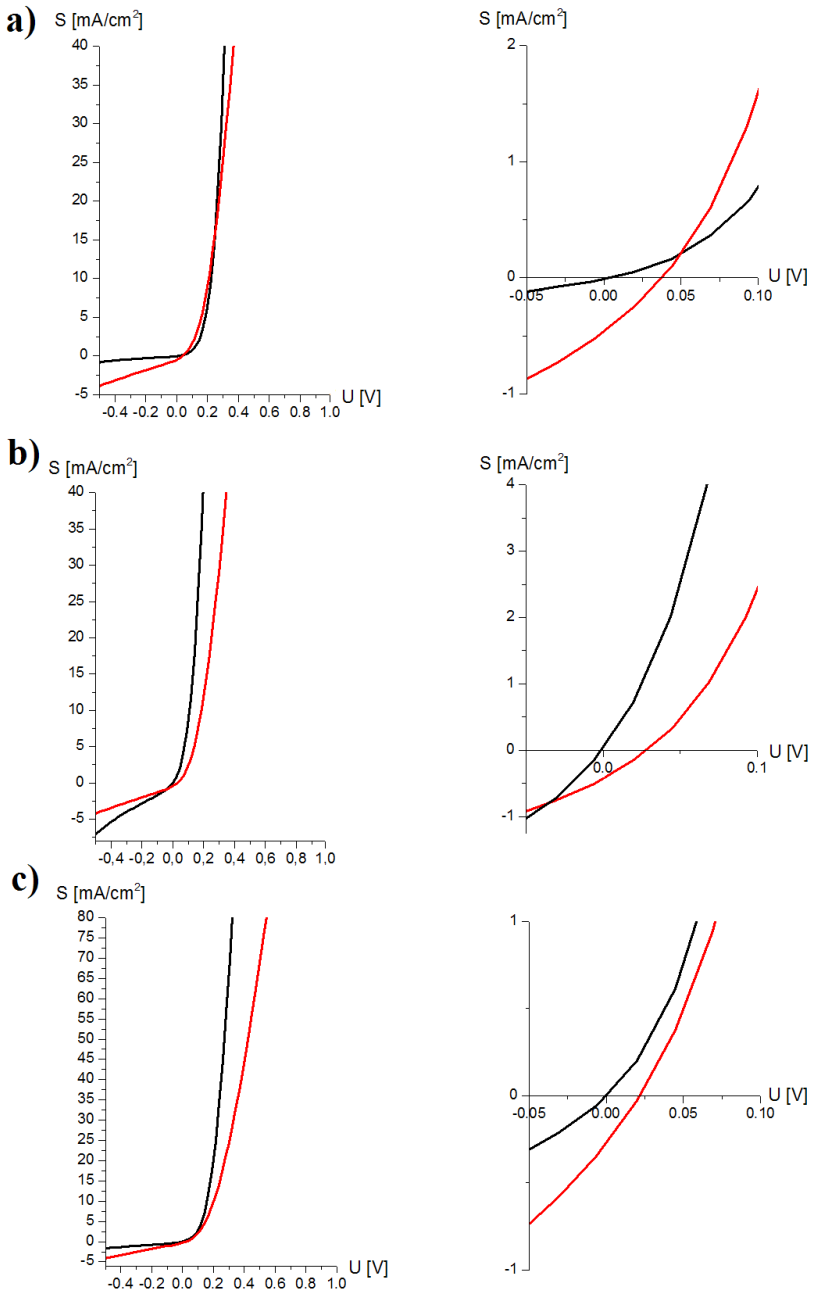

Fig. 4.23: J-V curves of a CuPc-TS solar cell containing a C_{60} acceptor layer. The C_{60} layer is 30nm thick. The device architecture is ITO-Pedot:PSS-CuPc-TS-C_{60}-BPhen-Al. Left: full graph of J-V characteristics, where black corresponds to dark condition, and red represents under illumination. Right: magnification around the origin. The characteristic values are summarized in table 4.5. Tempering destroys the device.

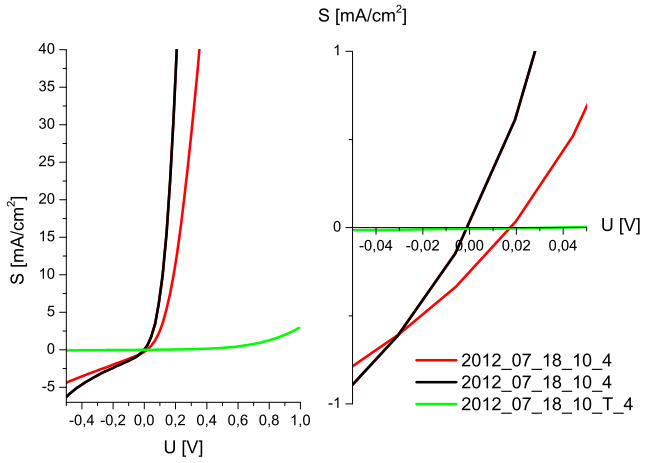

Fig. 4.24: CuPc-TS solar cell. The C_{60} acceptor layer is 30nm thick. The device architecture is ITO-Pedot:PSS-CuPc-TS-C_{60}-BPhen-Al. Left: full graph of J-V characteristics, where black corresponds to dark condition, red represents under illumination and green corresponds to illumination after thermal annealing. Right: magnification around the origin. The characteristic values are summarized in table 4.5. Tempering badly stresses the device.

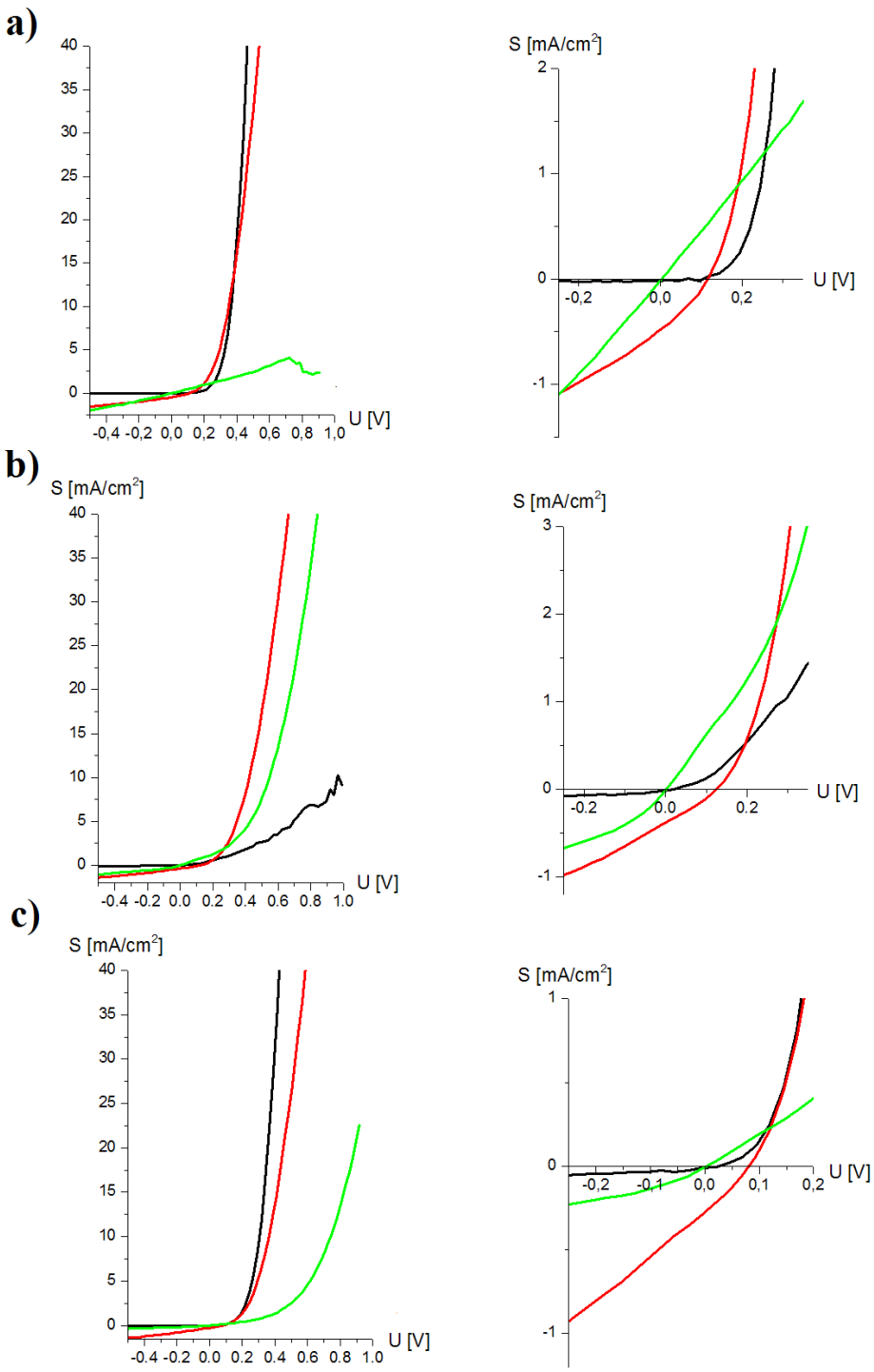

Fig. 4.25: CuPc-TS solar cell. The C_{60} acceptor layer is 60nm thick. The device architecture is ITO-Pedot:PSS-CuPc-TS-C_{60}-BPhen-Al. Left: full graph of J-V characteristics, where black corresponds to dark condition, red represents under illumination and green corresponds to illumination after thermal annealing. Right: magnification around the origin. The characteristic values are: V_{OC} =0.059V, $J_{SC} = -0.16 mA/cm^2$, FF=0.27, η = 0.002%, R_s=133Ω, R_sh=20700Ω, n=2.90. Tempering destroys the device.

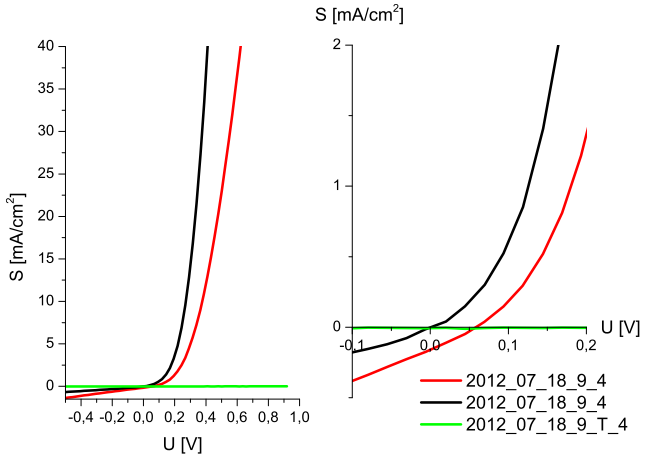

Fig. 4.26: CuPc-TS solar cell. The C_{60} acceptor layer is 60nm thick. The device architecture is ITO-Pedot:PSS-CuPc-TS-C_{60}-BPhen-Al. Left: full graph of J-V characteristics, where black corresponds to dark condition, red represents under illumination and green corresponds to illumination after thermal annealing. Right: magnification around the origin. The characteristic values are: $V_{OC} = 0.059V$, $J_{SC} = -0.16mA/cm^2$, FF=0.27, $\eta = 0.002\%$, R_s=133Ω, R_sh=20700Ω, n=2.90. Tempering destroys the device.

The device performances of the first four samples equal each other. Their parameters do not differ much.
The impact of thermal annealing to efficiencies and fill factor is shown in Figure 4.27. The device performance is absolutely not improved by thermal annealing.

4.5 Summary

In this chapter wetting was discussed and the theory of spin coating was given. Solution processed organic solar cells made of polymers, such as P3HT, and small molecules, such as CuPc-TS were fabricated and characterized. The device architectures studied were Schottky-junction, heterojunction, and bulk-heterojunction as well as a combination of the latter both (e.g., P3HT and PCBM blend (forming the bulk-heterojunction) covered with a layer of C_{60} (forming the heterojunction) yield the BHJ-HJ architecture). The C_{60} layer was deposited by thermal evaporation. Efficiencies of $0.001 < \eta < 1\%$ were achieved. Solar cell parameters were calculated with Matlab by J-V curve fitting using the Lambert W function. The achieved efficiencies and fill factors were summarized.

sample		R_s [Ω]	R_{sh}[kΩ]	n	FF	J_{sc} [mA/cm^2]	V_{oc}[V]	η[%]
$D1_1$	as-is	98	14.37	2.18	0.30	-0.48	0.116	0.01
	annealed	502	71.20	4.20	0.23	-0.012	0.002	0.000008
$D1_2$	as-is	128	13.92	2.40	0.28	-0.38	0.125	0.01
	annealed	137	13.41	3.82	0.24	-0.012	0.002	0.000006
$D1_3$	as-is	126	14.13	2.32	0.29	-0.27	0.082	0.006
	annealed	171	30.95	4.71	0.23	-0.005	0.002	0.000003
$D1_4$	as-is	133	20.70	2.90	0.27	-0.16	0.059	0.002

Tab. 4.6: Overview of the characteristic values of ITO-Pedot:PSS-CuPc-TS-C_{60}-BPhen-Al samples. The C_{60} layer is 60nm thick. Tempering destroyed one of the samples.

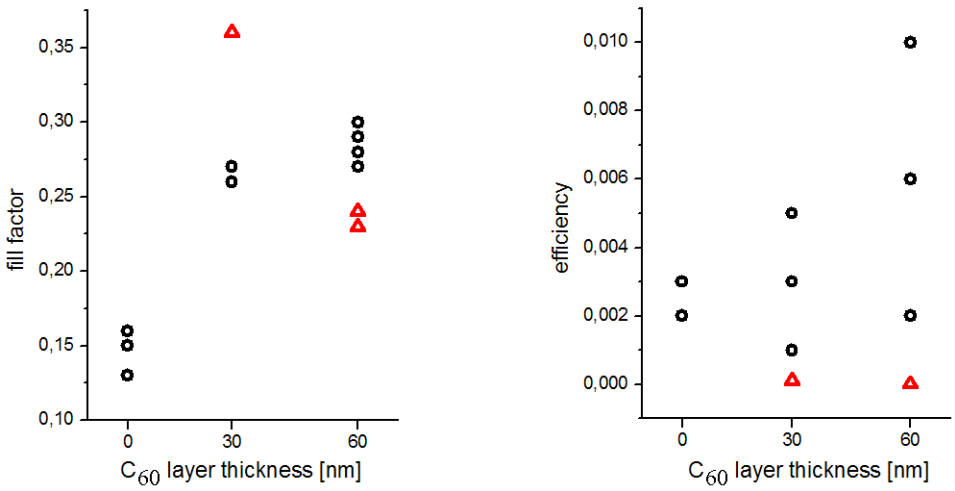

Fig. 4.27: Efficiencies and fill factors before and after thermal annealing. Thermal annealing worsened the device performance.

5. CARBON NANOTUBE PROCESSING

The handling of CNTs is still a challenging problem, as e.g. even nowadays the microscopic properties of single CNT cannot be fully applied at the macroscopic scale in most fabricated devices. Furthermore, purchasable CNT powders always consist of a mixture of different kinds of CNTs: single walled, multi walled, and tubes of various chiralities. Strictly speaking this implies that using CNT powder means different materials with different properties have to be handled. Consequently, clear conclusions from experimental data with these CNT are difficult to make. The most important first step in CNT processing, after their synthesis, is always their purification.

5.1 Purification

A precise understanding of the impurities and their concentration have a major impact on the purification process used for the specific material. In particular, the properties of organic materials show a high sensitivity to impurities. Therefore, the purification process of gradient sublimation is used (often several times consecutively) whenever it is applicable as CNTs cannot be sublimated at all. The choice of the best purification method is dependent on the expected impurity. The most common impurities contained in synthesised CNT powders are: various types of carbon like graphitic nanoparticles, amorphous carbon, fullerenes, polyaromatic hydrocarbons on the product site and particles containing (transition) metal or catalyst support material (CVD) on the synthesis site. For arc discharge prepared samples unvaporized graphitic particles are particularly prevalent, as graphitic rods are the carbon source in arc discharge and particles are sometimes ejected from the surface in the discharge process. Graphitic polyhedrons with enclosed metal particles also coexist with CNTs synthesized by arc discharge (see Figure 5.1). In addition, the concentration of the impurities often increases with a decrease of the obtained CNT diameter, [192]. The choice of the applied purification method also depends on the reactivity of the impurity and the stability of the CNT to the chemical, physical or combined applied purification method. In the last few years, considerable progress in the purification of CNT powders has been achieved and numerous methods of purification including chemical oxidation, physical separation, and combinations of chemical and physical techniques have been developed for obtaining CNT powders with the desired purity. A good overview of the

methods is given by [192] and [193]]. Some information from these reviews is included in the following subchapters

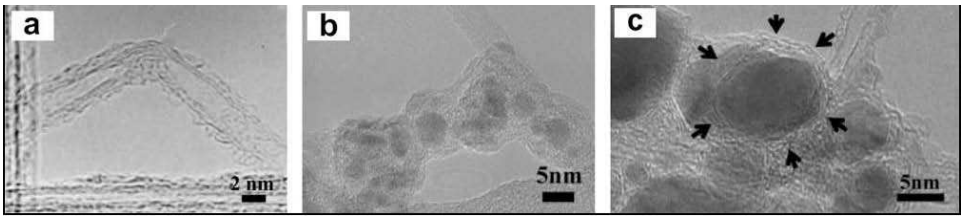

Fig. 5.1: TEM images of (a) amorphous carbon and fullerene molecules on the surface of CNTs. Image taken from [194]. (b) metal nanoparticles covered by amorphous carbon layer, and (c) metal nanoparticles covered by graphitic carbon multi-layer, (reprinted from Publication Chemical Physics Letters, 359, Issues 3-4, W. Ren, F. Li, J. Chen, S. Bai, H.-M. Cheng, Morphology, diameter distribution and Raman scattering measurements of double-walled carbon nanotubes synthesized by catalytic decomposition of methane, 196–202, ©(2002), with permission from Elsevier) [192].

5.1.1 Assessment of CNT purity

In order to evaluate the purity of CNT powders both the efficiency of the chosen purification method as well as the resulting rate of defect generation in the CNTs due to the purification process are required. In general three different objectives have to be analyzed: metal catalyst, carbonaceous impurity and structural changes of the CNT like defects, functional groups, open ends,...). Structural changes (defects, open caps) can be optically observed using TEM, however, it cannot give a quantitative evaluation of the purity of the CNT powders [195]. The metal impurity content can be precisely evaluated by using thermogravimetric analysis (TGA). The differences obtained between the TGA, oxidation temperature and metal content obtained in separated TGA runs evaluate the homogeneity of the CNT sample [196]. Carbonaceous impurities can be analyzed by using Raman spectroscopy. The quantification of the relative fraction of the D/G bands of Raman resonant scattering under a fixed laser power density gives information about the diameters and electronic structures [197]. The ultra violet to visible spectroscopy near infrared (UV-vis NIR) methods deliver estimates about the relative purity of single-walled carbon nanotubes (SWCNTs) on the basis of the integrated intensity of $S_2 2$ transition compared with that of a reference SWCNTs sample (representing, 100% purity), [198]. In addition, this method can be used to determine the concentration of CNT dispersions, once the extinction coefficient is known, [199]. It is also possible to evaluate, with the knowledge of the van-Hove singularities ($S_1 1$, $S_2 2$, $M_1 1$), the electrical behaviour and the chirality of the CNT by this technique [200]. A significant drawback of this method lies in the difficulties to prepare stan-

dardized dispersions and concentrations, which makes it difficult to obtain a quantitative analysis. As no absolute values of the purity of CNT exist due to there being no 100% pure CNT reference sample the extinction coefficient could not be measured for the CNTs. In order to characterize the functional groups on the CNT sidewall fourier transform infrared (FT-IR) spectroscopy is used. For a measurement of the trace amounts of metal impurity energy dispersive spectroscopy (EDS) can be applied, [201] and [202].

5.1.2 Chemical treatment

Fullerenes are easily removed, due to their solubility in different organic solvents. The process of acid oxidation takes advantage of selective oxidation caused by different oxidation rates. The high reactivity of the carbonaceous nanoparticles can be attributed to their large curvature and pentagonal carbon rings, [203]. Consequently, carbonaceous impurities and free metal impurities can be oxidized or dissolved faster than the CNTs. Therefore, liquid phase oxidation removes both amorphous carbon and metal catalysts. A limitation of the process is, however, that catalysts encaged in polyhedral graphitic particles stay untouched. Further more, carbonaceous and metal impurities have very wide particle size distributions. Also the amount of defects or curvature varies depending on synthesis conditions. This has so far made it impossible to develop a unified purification method for the obtainment of reproducibly high-purity CNT materials. As the CNT are well dispersed in the rinsing solution the oxidative ions and acid ions can evenly interact with the CNTs, which allows fine tuning of process parameters for oxidation reaction to obtain high-purity CNT. Some commonly used oxidants for liquid phase oxidation are: nitric acid (HNO_3) [204], hydrogen peroxide (H_2O_2) or a mixture of H_2O_2 and HCl [205]. However, all these oxidants have been shown to either destroy the CNT structure (including opening and catting of the CNTs) or add functional groups. Nitric acid is a commonly used reagent for SWCNT purification due to its mild oxidizing strength that selectively removes amorphous carbon. It is also inexpensive, nontoxic, capable of removing metal catalysts and no secondary impurities are introduced by this acid. The CNTs synthesized by arc discharge were purified in accordance with the procedure published by [204]. Hu was the first to evaluate the relationship between purification yield and grade, with systematic and quantitative measurements based on near infrared (NIR) spectroscopy. The applied purification procedure was: 1g of the as-prepared SWCNT sample was refluxed in 150mL 7M HNO_3 for 6h. The weight percent of each component for several concentrations and reaction times were calculated from TGA measurements. These were combined with the NIR spectra are taken from [204] and plotted in Figure 5.2. A comparative study of the H_2SO_4/HNO_3 (3:1) and 6M HNO_3 treatments with regard to their purification effectiveness was made by [206]. Other authors found

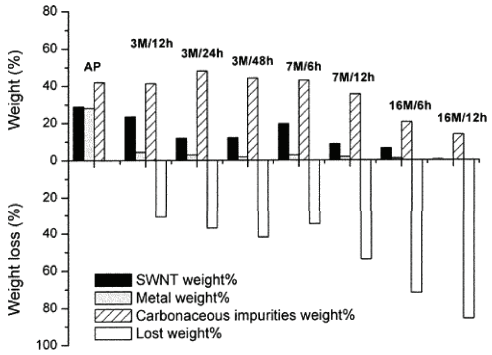

Fig. 5.2: "Mass balance of the normalized weight percentages of all components including the SWCNTs, metals, carbonaceous impurities, and weight loss of the SWCNT samples." [204] "reprinted (adapted) with permission from (H. Hu, B. Zhao, M. E. Itkis, and R. C. Haddon, Nitric acid purification of single-walled carbon nanotubes, Journal of Physical Chemistry B, 107(50):13838–13842). ©(2003) American Chemical Society."

that by using that mixture as the oxidant yields carbonaceous impurities, [207]. TEM images of SWCNTs purified with different treatment conditions are shown in Figure 5.3. The images show that concentrated sulfuric acid $(H_2SO_4)/HNO_3$ (3:1) is more effective than nitric acid in removing impurities. Furthermore, by using the best purification conditions SWCNT purities of up to 98% could be achieved with a yield of $40wt\%$ within 2h. Reports have been made in which there was no decrease in the number of small diameter nanotubes despite the use of a 3h reflux process involving a concentrated H_2SO_4/HNO_3 mixture (3:1). This method was used to ad functionalized groups on the CNT sidewalls in this work.
Another approach to remove the metal compounds involved a multi-stage gas phase-electrochemical treatment. This had three steps: firstly the removal of the metal catalysts, secondly the removal of the carbonaceous impurities followed, lastly, by a gentle annealing step in order to heal the damage to the CNTs. An extensive understanding of the role of metals in oxidizing carbons was achieved by [208]. They found that metal particles randomly catalyze the oxidation of carbons. As a consequence, SWCNTs are destroyed in the presence of oxygen and other oxidizing gases during a thermal annealing treatment. Firstly the encapsulation of the metal catalysts has to be cracked. This can be done by wet air oxidation. The physical process of breaking the carbonaceous encapsulation by wet air oxidation is based on the different densities of iron ($\rho = 7.86\frac{g}{cm^3}$) and rust ($\rho = 5.18\frac{g}{cm^3}$). As the mass of the metal catalysts itself stays constant during the oxidation process, an increase of the volume is the result. This expansion breaks the carbonaceous encapsulation. For the oxidation process the samples were heated to 225°C for 18hr in wet air. Subsequently, the exposed metal cat-

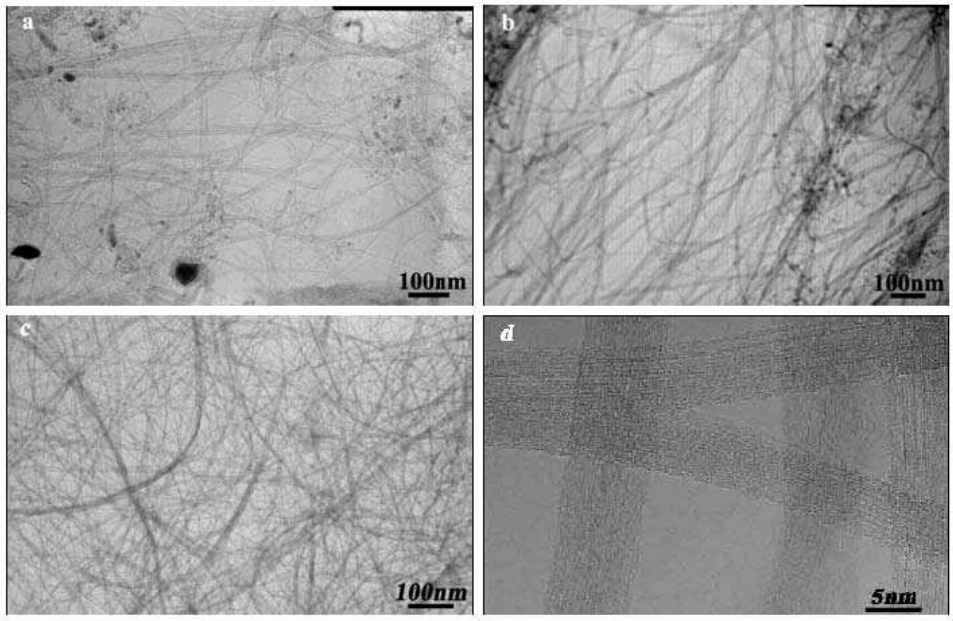

Fig. 5.3: TEM images of purified SWCNTs. (a) After sonication in 6M HNO_3 for 4h, (b) after refluxing in 6M HNO_3 at 120°C for 4h, (c) after refluxing in concentrated H_2SO_4/HNO_3 mixture (3:1) at 120°C for 2h, and (d) after refluxing in concentrated H_2SO_4/HNO_3 mixture at 120°C for 4h. Image taken from [206].

alysts was dissolved by an acid (HCl) or gas (carbonylation). The wet air oxidation can then repeated e.g. at 325°C followed again by an acid or or gas treatment. This multi-stage approach with wet air and acid was validated also by another group[209]. It appears that if electrochemical oxidation is done in neutral or basic aqueous solutions, no significant tip opening occurs. However, aqueous solutions of common strong or medium strength acids (5% H_2SO_4, 5% HNO_3, or 25% HNO_3 + 25% H_2SO_4, 5% H_3SO_4**!** (H_3SO_4**!**), and 5% CH_3COOH) remove both amorphous carbon and metal catalysts.

CNT shortening

CNTs of various lengths can be shorted using acids, for example, purified CNTs can be shorted by sonication in the presence of a mixture of concentrated sulfuric and nitric acids (in ratio 3:1 or in wt%, 98% and 70%, respectively) at $40°C$, [207]. Sonication is efficient due to the formation of microscopic high temperature domains (12) when the cavitation bubbles collapse, which induce localized sonochemistry. Sonochemistry means the application of ultrasonics in chemical reactions and processes. Cavitation itself is the formation, the growth and the implosive collapse of bubbles in a liquid. The cavitation collapse causes a local high temperature ($\approx 5000K$), high

pressure ($\approx 1000atm$), enormous heating and cooling rate ($> 10^9 K/sec$), and liquid jets ($\approx 400km/h$) [210]. This sonochemistry is strong enough to generate an open hole in the tube sidewall [207]. If an oxidizing acid is present the etching process at the point of damage is enhanced. This leads to the tube being completely cut through at the initial point of damage caused by the sonochemistry process. Subsequently, the oxidation process shortens the CNT further. In addition, the mixture of 3:1 wt% concentrated H_2SO_4:HNO_3 is known to intercalate and exfoliate graphite. Therefore, the length distribution of the treated CNT controllably shortens with exposure time to the acid. Depending on the respective acid treatment shortening rates of roughly 130nm/hour to 200nm / hour can be achieved [207]. After the shortening process the tubes have to be annealed at $700°C$ - $1100°C$ under vacuum in order to heal the CNT of the damage caused by the prior treatments.

5.2 Functionalisation

Liquid phase oxidation often leads to surface modifications. These modifications usually takes place on the sidewall of a CNT. They change the CNT macromolecule from being super hydrophobic to more hydrophilic. This modification enables their dispersion in aqueous solution without any surfactants. A process of surface modification also has the potential for specific engineering of the physical and chemical properties of the CNT. This is desirable if CNTs have to be "tuned" for specific applications, e.g., mechanically reinforced composites, or for scanning probe microscopy tips. In addition, the fabrication of nanotube derivatives with altered electronic structures and properties (organic solar cells) is possible with this approach [211], [212], [213]. CNTs can also be cut into short fragments and oxygen functional groups added. Both, the small size and the oxygen functional groups, increase their dispersibility. This improves their ability to be applied in practical applications.

5.2.1 Liquid phase (carboxylic groups)

The influence of the functionalisation on the CNT can be of quite a different nature depending on the relative energy levels. Over all three different levels of influence can be assumed (see Figure 5.4):

- Fermi level shifting with respect to the vacuum energy,
- in- or decrease of the band gap, and
- band gap shifting with respect to the vacuum energy.

In order to investigate these three possible impacts of functionalisation on the CNT it has to be characterised using photoemission spectroscopy (PES)

to determine the first, by using ultra violet to UV-vis spectroscopy for the second and by inverse photoemission spectroscopy (IPES) for the last. However, before an analysis can be carried out some aspects have to be considered: firstly the CNT powders are still a mixture of semiconducting, metallic and semi-metal tubes. Although much progress has been made by optimizing the synthesis parameters, a typical increase of semiconducting tube content in the CNT powders from 66% to 80% has been achieved. Worldwide only one company is able to provide SWCNT powders with a semiconducting tube content of 99%, Nanointegris, 1mg of these semiconducting, however, SWCNT costs $799 US\$$. Secondly, the chemically inert behaviour of the CNTs indicates that not all tubes are functionalised. Therefore, the characterisation will always give information about the whole mixture of CNTs within the sample. Exactly defined samples of only one kind of CNT can not be prepared experimentally. Attaching carboxylic groups to the CNT

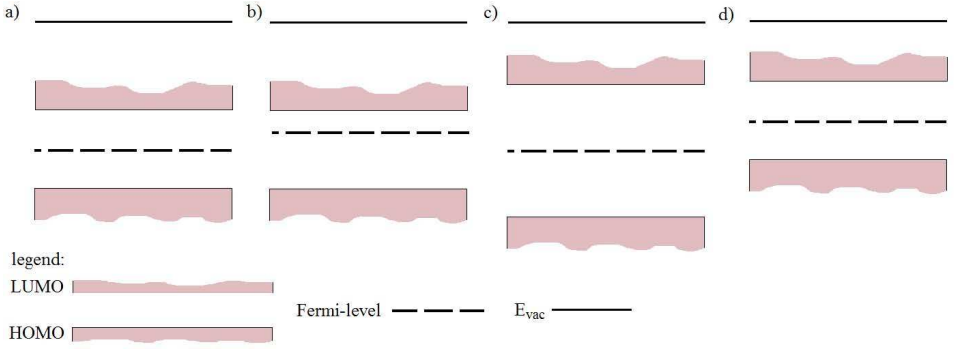

Fig. 5.4: Influence of functionalisation on the energy levels of CNTs. a) before functionalization. b) Fermi-level is shifted upwards due to functionalization. c) The band gap is increased upon functionalization. d) The ionization potential is shifted upwards to vacuum energy level.

sidewall or open ends can be done using sulphuric acid and nitric acid. For such a process several recipes are described in the literature [214], and [215]. Figure 5.5 is a schematic of the addition of carboxylic groups at the CNT sidewall via oxidation. In this work just a few of the published recipes by other groups were investigated. These are introduced in the following.
Figure 5.6 shows the Raman spectra of pristine SWCNTs and SWCNTs functionalized with carboxylic groups. Recipe A used 3M sulphuric acid and 1M nitric acid in a ratio of [3:1] *vol.*%.
Acids of different molar concentrations are used for CNT functionalization. In order to prepare a x molar acid from a y molar initial acid the following protocol was applied. For the preparation from a 14M nitric acid (concentrated nitric acid) of a 1M acid 13mL of distilled water has to be mixed with 1mL of the concentrated nitric acid. As a chemical equation this is written

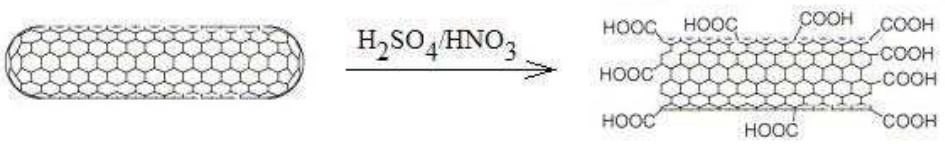

Fig. 5.5: Scheme of the CNT oxidation and formation of carboxylic groups on the CNT sidewall (reprinted from Current Opinion in Chemical Biology, 9, Issue 6, A. Bianco, K. Kostarelos, M. Prato, Applications of carbon nanotubes in drug delivery, 674–679, ©(2005), with permission from Elsevier) Figures taken from [216]

as:

$$13\,mL\,H_2O + 1\,mL\,14\,M\,HNO_3 \rightarrow 14\,mL\,1\,M\,HNO_3 \tag{5.1}$$

In order to prepare a 3M sulphuric acid from a concentrated one (9.8 M), 3mL of sulphuric acid has to be mixed with 1mL of distilled water. As an equation the chemical reaction is written as:

$$2.3\,mL\,H_2O + 1\,mL\,9.8\,M\,H_2SO_4 \rightarrow 3\,mL\,3\,M\,H_2SO_4 \tag{5.2}$$

In 10mL of this mixture 5mg of the CNT (SWCNT or MWCNT) powder was added and sonicated for 1h. After the sonication process the container stood for 11h at room temperature. Subsequently, the mixture was vacuum filtered through a $0.2\mu m$ PVDF filter membrane. The CNT retentate on the filter was scrapped off and put in a beaker filled with distilled water. This was sonicated for 2h in a normal sonication bath. This procedure resulted in a metastable CNT dispersion (stable for two days). The carboxylic groups attached to the CNT sidewall and the open ends made the CNTs hydrophilic.
Recipe B differs slightly from the previous one. Concentrated sulphuric acid (98%) and concentrated nitric acid (65%) are mixed together in the ratio of [3:1]$vol.\%$. Subsequently, 5mg of CNTs were added to 10mL of the acid mixture and sonicated for 1h in a sonication bath. The CNT acid mixture then stood untouched for 1h at room temperature. After this, it was vacuum filtered through a $0.2\mu m$ PVDF filter membrane and rinsed thoroughly with deionized water until ph 7 was reached. In the same way as in recipe A the retentate was sonicated in distilled water. This yielded a metastable (stable for 3 days) dispersion due to the carboxylic group attachment.
Recipe C is made by mixing 1M sulphuric acid with 3M nitric acid in a ratio of [3:1] at room temperature. Subsequently, 5mg of the CNTs were added to 10mL of this acid mixture and sonicated for 2h. Vacuum filtration through a $0.2\mu m$ PVDF filter membrane resulted in a layer of the CNTs on the membrane. The CNTs were scrapped off the filter and put in a beaker. The CNTs were then infused with 5M hydrochloric acid. This mixture was boiled for 6h at 120°C under reflux, followed by a filtration process. The filter was rinsed thoroughly with deionized water until pH 7 was reached.

Recipe D was made by preparing 10mL of a mixture of 1M sulphuric acid and 3M nitric acid in a ratio of [3:1] *vol.*%. 5mg of CNTs were then added and the mixture was sonicated in a sonication bath for 12h at 60°C under reflux. Subsequently, it was vacuum filtered through a 0.2 μm PVDF filter membrane. After this the filter was rinsed with deionized water until ph 7 was reached. The retentate was sonicated in distilled water, which yielded a metastable dispersion (stable for 3 days).

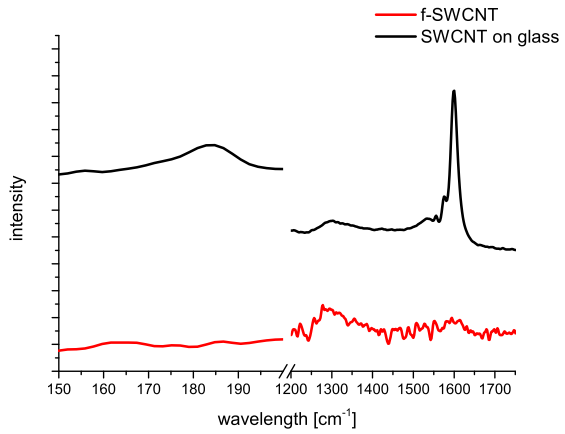

Fig. 5.6: Raman spectra of pristine and functionalized SWCNT. The almost completely missing G-band indicate that the CNTs were heavily stressed during the acid functionalization.

5.2.2 Gas phase

Fluorination of the CNTs can be achieved using either elementary fluorine or fluorine compounds such as nitrogen trifluoride (NF_3).

If elementary fluorine is chosen the fluoridation becomes effective by simply heating the CNTs in the gas to temperatures above $t > 150°C$. If the thermal annealing is done in the temperature range of 150°C to 190°C the resistance of CNT resistor device will increase. This occurs because the covalently bonded fluorine atoms in the CNT lattice either reduce the conductivity mechanisms of the tube or increase the band gap. At temperatures >250°C the CNTs become insulators. In order ro fluorinate the CNTs with elementary fluorine a furnace with a constant gas flow during the whole reaction time (6h) has to be used. A mixture of 20sccm of helium with 2sccm fluorine yields the best results according to [217]. The process is as follows: firstly, the furnace is heated up to the reaction temperature and kept constant (150°C-190°C). Secondly, the gas flow is started. After the annealing step the furnace is cooled down to room temperature, whilst a constant helium flow of 20sccm and no fluorine gas flows through it.

sample	t[s]	power[W]	Ar flow[sccm]	NF_3 flow[sccm]	R [Ω]
$SWCNT$	0	0	0	0	0.016
	0	0	0	0	0.053
$f-SWCNT_1$	60	100	5	16	0.016
	60	100	5	16	0.053
$f-SWCNT_2$	120	100	5	16	0.017
	120	100	5	16	0.06
$f-SWCNT_3$	60	150	5	16	0.017
	60	150	5	16	0.054
$f-SWCNT_4$	120	150	5	16	0.018
	120	150	5	16	0.057

Tab. 5.1: Overview of the NF_3-plasma treatments. EDS measurements proved the existence of fluorine in the va-CNT samples.

As the use of elementary fluorine requires very significant safety obligations it is always worth considering whether another approach can be applicable for the gas phase functionalisation of the CNT array. Indeed, NF_3-plasma can act as a source for elementary fluorine as well as singularly and poly ionized ions when introduced into a plasma (also known to be the fourth aggregate state). In such a plasma nitrogen ions and ionized NF_3 coexist within the plasma. In comparison to the thermal treatment route the plasma produces species that are much more reactive, even without any heating of the sample. In this work the fluorination was made in a plasma chamber to with a NF_3-plasma. The adjustment according to the epitaxy of the fluorination of CNT is done by controlling the power in Watt of the plasma. An overview of these experiments is given by table 5.1. The Raman measurements of the processed CNTs clearly identified fluorine and nitrogen. The electrical measurements of these CNTs showed an increase of the resistance which could be correlated with an increase of the CNT band gap and also with an increase of the amount of insulating CNTs in the array. The electrical measurements were made using both macroscopic and microscopic methods. The microscopic method involved conductive AFM measurements, whereas the macroscopic measurements were done by contacting the CNTs with a copper electrode of $3mm^2$ in size. A scheme of the fluorination of CNT is given in Figure 5.7.

5.3 Dispersion of CNTs

The dispersion of CNTs is still a challenging task. Generally, if the surface area of a particle increases the attractive forces of these particles to each other also increases. With regard to the CNTs the high aspect ratio and strong $\pi-\pi$-interaction of the tubes induce large attractive VdW forces.

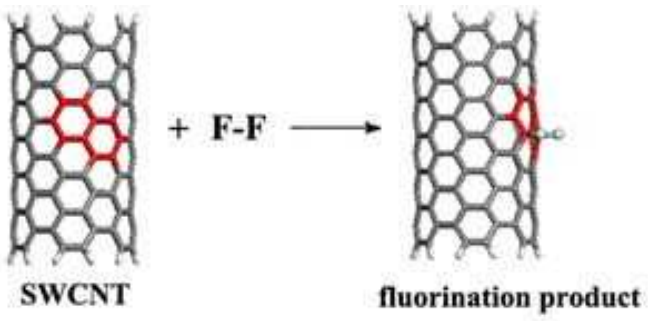

Fig. 5.7: Scheme of the fluorination of a CNT with molecular fluorine. Image taken from [218].

These forces, in combination with the high flexibility of the CNT, leads to significant entanglement and also a high packing density of the CNTs [219], and [220]. The suppression of these forces will result in good and stable CNT dispersions. Several approaches can be used to master this challenge:

- covalent side-wall functionalisation,
- non covalent side-wall functionalisation.

Covalent side-wall functionalisation can lead to an irreversible alteration of the electronic properties of the functionalized CNTs. Non-covalent functionalisation using surfactants (usually tensides with a hydrophobic and hydrophilic part) will in most cases preserve the initially electronic properties. For this reason the latter route is often used in many applications. However, a disadvantage of this method is that the additives will remain in the particular device or application. In the field of organic photovoltaics every impurity - however small - has a big influence on the solar cell performance. Therefore, this method cannot be applied for this reason in OSC. In addition the term dispersion has to be specified first.

Classification of dispersions

The definition of "Dispersion" in chemistry, relates to a system in which particles of one kind are intermixed in a continuous phase of another composition or state, [221]. The continuous phase is a liquid one and the dispersion can be - in general - described in several ways depending on the relative size of the particles in the continuous and dispersed phase. If the particles in the dispersed phase are also dissolved in the continuous phase, a "true solution" is formed and the particles are called solutes (normally these particles are tens of angstroms in size). If the dispersed domains are several nanometres and/or micrometre in size, the solution is called a "colloidal solution". This kind of solution can be subdivided into suspensions (as in the case of

CNT) and emulsions (in the case of liquids). Only additives like surfactants or emulsifiers can stabilize the dispersed phase. In 2005 the dispersions of CNT were classified into two categories. In the case of dispersed CNT bundles the dispersion is called a "macrodispersion". If individual non bundled CNTs are dispersed it is called a "nanodispersion", [222]. Theoretically, the nanoscale dispersion can be classified by a dimensionless parameter, X, which will be explained in the following subsection.

Nanodispersion

The dimensionless parameter X can be defined in three different ways: as X1, the fraction of unbundled CNTs, as X2, the reciprocal of the average number of CNTs per bundle, and as X3, the fraction of unbundled CNTs, [222]. The mathematical definitions of these parameters expressing the degree of a nanodispersion, X, are

$$\begin{aligned} X_1 &= \sum p(z)\,\delta(z-1) = p(1), \\ X_2 &= \frac{1}{\sum p(z)\,z} = \frac{1}{avg(z)}, \\ X_3 &= \frac{\sum p(z)\,\delta(z-1)}{\sum p(z)\,z} = \frac{p(1)}{avg(z)}, \end{aligned} \tag{5.3}$$

where p(z) is the probability that a dispersed entity will have z CNTs (e.g. p(1) indicates the fraction of bundles consisting of just one single CNT), d is a delta function, and avg(z) is the average number of CNTs per bundle [222]. According to the definition, in a nanodispersion of CNT all values of X tend to 1.

5.3.1 Wetting

For the CNT nanodispersions a wetting study is necessary in order to get the data for the correct choice of solvent. The contact angle of a CNT varies from $80° < \theta < 105°$ according to [223], and [224]. A good overview about the dispersion of CNTs is given by [225] and [226]. As CNTs show poor solubility in water and organic solvents, lots of work has done to try to overcome this matter. Contact angle measurements were experimentally made by AFM force measurements by [227]. An environmental scanning electron microscopy (ESEM) picture from [227] of a MWCNT wetted by an organic liquid is shown in Figure 5.8. A plot based on the Owens-Wendt equation is shown in Figure 5.9, where the linearity supports the validity of the applied Owens-Wendt model [228]. Due to the linearity of the graph, the determination of the polar and dispersive fraction of the total surface energy of a single MWCNT can be calculated: $\gamma_{CNT} = 27.8\,mJ/m^2$, $\gamma^d_{CNT} = 17.6\,mJ/m^2, and$ $\gamma^p_{CNT} = 10.2\,mJ/m^2$. The total surface energy of the CNT is quite similar to that of an untreated

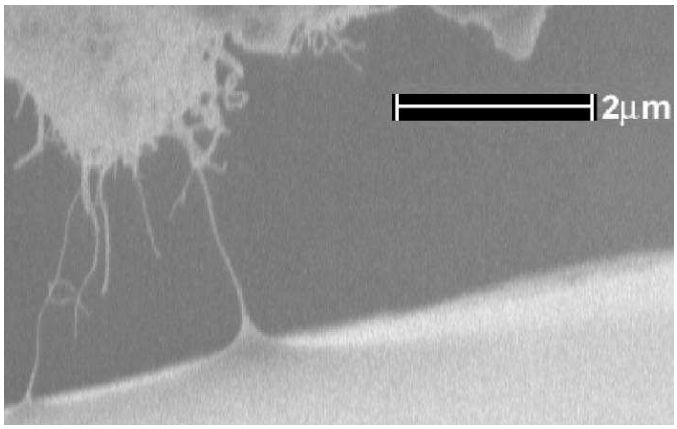

Fig. 5.8: ESEM picture of MWCNTs wetted by an organic solvent. The meniscus is good visible (A. H. Barber, S. R. Cohen, and H. D. Wagner, Physical Review B, 71, Issue 11, 2005, 5443. ©(2005) by the American Physical Society) [227].

graphite, although the polar fraction of graphite is almost twice as much as that of the CNT [228], and [229]. This increase in the polar interactions is expected to be related to curvature effects. This could explain why CNTs are wetted better than planar graphite by water [230]. The contact angle of a single CNT was also obtained by infiltration studies of va-CNTs (cf. chapter 7). At certain locations on the dye-infiltrated va-CNT the stiffened meniscus of the precipitated dye becomes visible around single CNTs. By assuming a roughly perpendicular incidence of the electron beam on the sample in the electron microscope, the contact angle of a single CNT with CuPc-DMA dissolved in 1-decanole was determined to be θ=32°. The original contact angle can be assumed to be larger than the observed 32°. This is, because drying can reduce the value of the angle due to settlement of the surface. Generally, surface tension can be split into a dispersive and polar part, [231], as expressed by the equation

$$\gamma_l = \gamma_l^d \gamma_l^p \tag{5.4}$$

where: γ_l^d is the dispersive and γ_l^p is the polar fraction of the surface tension. 1-decanole has a surface tension of 28.5 mN/m. Its polarity equals $p = \gamma_p/\gamma_d = 0.28$, which yields a dispersive fraction of $\gamma_d = 22.3$ mN/m. The polar fraction can be calculated to be $\gamma_p = 6.3$ mN/m. According to [152], the energy of adhesion is generated by the dispersive parts of the surface tension of the solvent and the surface energy of the substrate. The dispersive fraction of the surface energy of a single CNT in the array can be calculated as:

$$W_A = \gamma_l \left(1 + \cos\theta, \right) \tag{5.5}$$

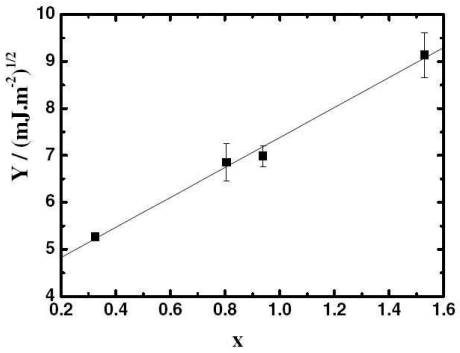

Fig. 5.9: "Owens and Wendt plot for single MWCNTs. On the y-axis $[Y = \gamma_l\,(1+\cos\theta)]\left(2\sqrt{\gamma_l^d}\right)^{-1}$, and on the x-axis value X is $\left(\frac{\sqrt{\gamma_l^p}}{\sqrt{\gamma_l^d}}\right)$. Each point is an average of at least five measurements, the error bar being the σ of each set of points." (A. H. Barber, S. R. Cohen, and H. D. Wagner., Physical Review Letters, 92, Issue 18, 2004, 6103. ©(2004) by the American Physical Society) [228].

where γ_l is the surface tension of the solvent. According to the approach described in [152] equation (5.5) becomes

$$\mathrm{W_a} = 2\sqrt{(\gamma_s^d \cdot \gamma_l^d,)} \tag{5.6}$$

where γ_s^d and γ_l^d are the dispersive fractions of the respective surface energy or tension, respectively. By using

$$W_A^2 = 4\gamma_s^d \cdot \gamma_l^d$$

equation (5.6) can be expressed as

$$\gamma_s^d = W_A^2/4\gamma_l^d, \tag{5.7}$$

which yields a dispersive surface energy fraction

$$\gamma_s^d = \left(\gamma_l^d\,(1+\cos\theta)\right)^2/4\gamma_l^d \approx 19mN/m$$

. Fowkes states that only dispersive forces cause the force of adhesion. By using equation (5.7), the polar fractions yields

$$\gamma_s^p = \left(\gamma_l^p\,(1+\cos\theta)\right)^2/4\gamma_l^p \tag{5.8}$$

and the polar surface energy equals γ_s^p=5.4 mN/m. The surface energy of a single CNT can be determined to be γ_{CNT}=24.4 mN/m, with a polarity of p=0.22. Figure 5.10 shows a field emission scanning electron microscopy (FE-SEM) image of the conserved contact angle of precipitated dye on a

va-CNT. The surface energy calculated by the contact angle "freezed" by the precipitated dye (see Figure 5.10) fits well with that of graphite. It is not possible to determine whether it is a SWCNT or a MWCNT. The contact angle for a MWCNT is shown in Figure 5.8. Differences in contact angles for SWCNT and MWCNT can be assumed to appear, because the diameters of SWCNT and MWCNT differ from each other. However, as SWCNT have a smaller diameter, the surface energy of a SWCNT should differ more from that of graphite due to bending of the graphene structure. The calculated values prove the opposite. This is either due to the contact angle observed by the precipitated dye containing errors or the surface energy of CNT is closely related to that of graphite.

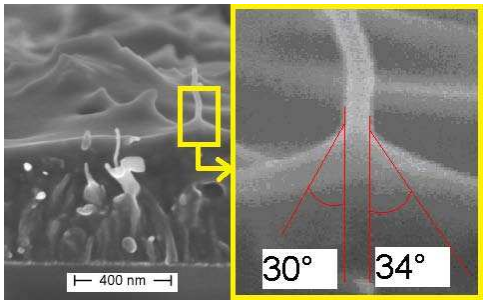

Fig. 5.10: "Contact angle of CuPc-DMA on a va-CNT array. A contact angle of θ=32° is found on a single SWCNT. However, it is expected that the actual contact angle θ is larger than the arithmetic middle of 32°." [143]

5.3.2 Organic solvents

In addition to the common wetting approach with the help of goniometric measurements, dispersion studies of SWCNT in terms of Hansen solubility parameters ($\delta_t^2 = \delta_d^2 + \delta_p^2 + \delta_h^2$) have been reported. Investigations were made for SWCNTs dispersed in several solvents including toluene, chloroform, and acetone. It was concluded that SWCNTs are well dispersed in solvents with dispersive component δ_d^2 between 17-18 $MPa^{1/2}$, [232]. SWCNTs precipitate in solvents with higher polar and hydrogen-bonding (δ_p^2, δ_h^2) components. However, the state of the dispersion had no dependency on the total solubility parameter δ_t^2. Unexpectedly, highly polar solvents (e.g. dimethylformamide (DMF)) have been shown to effectively wet SWCNTs, [233]. A brief overview of the dispersion study from [232] is given in Figure 5.11.

1,2-Dichlorobenzene

Different dispersion procedures have been evaluated for each solvent. For a dispersion in dichlorobenzene a UP200S sonication device with a 5mm sonotrode was used. The sonotrode was put directly in the solvent. 1mg

Table 1
Dispersion of nanotubes in various solvents with different values of Hansen parameters of the solvents

Organic solvents	δ_d[a] ($MPa^{1/2}$)	δ_p[a] ($MPa^{1/2}$)	δ_h[a] ($MPa^{1/2}$)	δ_t[b] ($MPa^{1/2}$)	Molecular weight (g/mol)	Structure	Dispersion state
N,*N*′-Dimethylformamide	17.4	13.7	11.3	24.8	73.10	$HCON(CH_3)_2$	Dispersed
Chloroform	17.8	3.1	5.7	19.0	119.38	$CHCl_3$	Dispersed
1-Methyl-2-pyrrolidone	18.0	12.3	7.2	22.9	99.13	$HN((CH_2)_3CO)$, cyclo	Dispersed
2-Propyl alcohol	15.8	6.1	16.4	23.5	60.10	$(CH_3)_2CHOH$	Swollen
1-Pentyl alcohol	16.0	4.5	13.9	21.7	88.15	$CH_3(CH_2)_4OH$	Swollen
Tetrahydrofuran	16.8	5.7	8.0	19.4	72.11	$(CH_2)_4O$, cyclo	Swollen
Toluene	18.0	1.4	2.0	18.2	92.14	$C_6H_5CH_3$	Swollen
o-Methoxyphenol	18.0	8.2	13.3	23.8	124.14	$2\text{-}(CH_3O)C_6H_4OH$	Swollen
Dichloromethane	18.2	6.3	6.1	20.3	84.93	CH_2Cl_2	Swollen
Benzene	18.4	0.0	2.0	18.6	78.11	C_6H_6	Swollen
Dimethyl sulfoxide	18.4	16.4	10.2	26.7	78.13	$(CH_3)_2SO$	Swollen
Styrene	18.6	1.0	4.1	19.0	104.15	$C_6H_5CH{=}CH_2$	Swollen
Methyl methacrylate	13.7	9.8	6.1	17.9	100.12	$H_2C{=}C(CH_3)CO_2CH_3$	Sedimented
Methanol	15.1	12.3	22.3	29.6	32.04	CH_3OH	Sedimented
Hexane	15.3	0.0	0.0	15.3	86.18	$CH_3(CH_2)_4CH_3$	Sedimented
Acetone	15.5	10.4	7.0	20.0	58.08	CH_3COCH_3	Sedimented
Water	15.6	16.0	42.3	47.8	18.02	H_2O	Sedimented
Ethanol	15.8	8.8	19.4	26.5	46.07	C_2H_5OH	Sedimented
Acrylonitrile	16.4	17.4	6.8	24.8	53.06	$H_2C{=}CHCN$	Sedimented

[a] A.F.M. Barton, CRC Handbook of Solubility Parameters and Other Cohesion Parameters, CRC Press, Boca Raton, FL, 1991 [30].
[b] $\delta_t^2 = \delta_d^2 + \delta_p^2 + \delta_h^2$, where δ_t is total Hildebrand solubility parameter, δ_d is dispersion component, δ_p is polar component, δ_h is hydrogen bonding component of Hansen solubility parameters.

Fig. 5.11: Overview of the dispersion study made by Ham (H. T. Ham, Y. S. Choi, and I. J. Chung, Journal of Colloid and Interface Science, 286, Issue 1, 2005, 216-223. ©(2004) with permission from Elsevier) [232].

of SWCNT was added in 1mL of solvent. The beaker with the solvent was placed inside a second beaker filled with ice in order to cool the mixture during the sonication process. This mixture was sonicated with a pulsation duration of 2 seconds followed by a 8 seconds pause at an amplitude of 10% of maximum power. This process was cycled for 2h. Afterwards the dispersion was centrifuged with a Optima Max ultra centrifuge at 50.000G for 30 minutes. The supernatant, which is the final CNT dispersion, was removed from the centrifuge. In the UV-Vis spectra shown in Figure 5.12 the S_{22} and M_{11} transitions can clearly be identified. This quantifies the dispersion in the macroscopic way. These can be used to quantify the dispersion. Instead of using the Optima Max ultra centrifuge a desktop centrifuge was also used for centrifugation, for example, in a Biofuge stratos the CNT dispersions were centrifuged for 30 minutes at 10.000rpm. The rotor was a 24 x 1.5/2ml (45°) fixed angle rotor - the standard rotor. Good results were also obtained with this device. The AFM image shown in Figure 5.19 shows how individual tubes are dispersed in the organic solvent.

5.3.3 Surfactants

Due to the hydrophobicity of CNTs a aqueous dispersion is difficult to prepare. In order to obtain a dispersion either the CNTs have to be modified in their nature through covalent functionalisation or surfactants have to be used. The molecular structure of a surfactant is constructed of essentially two different parts: the head and the tail. This is the origin of the duality of a surfactant, because the head can be hydrophilic (or polar) and the tail

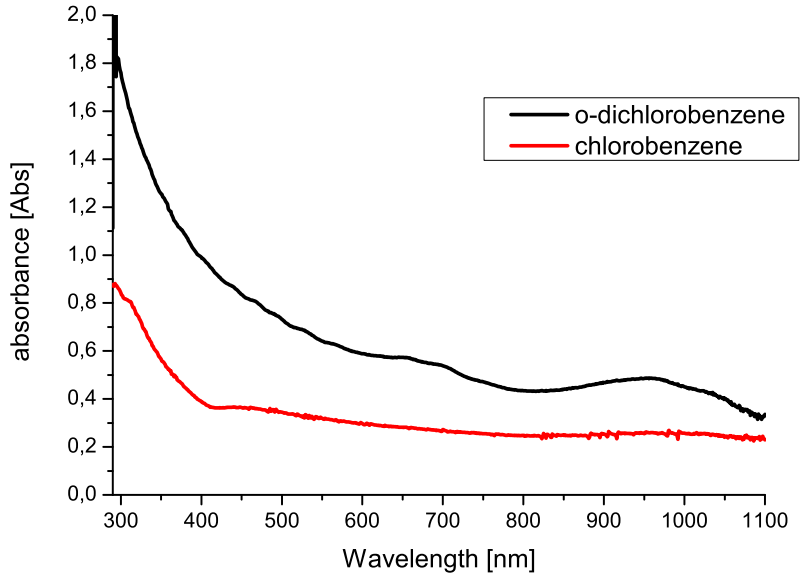

Fig. 5.12: UV-vis spectrum of CNTs dispersed in dichlorobenzene. The baseline correction has been already included. The resulting line attests to the presence of CNTs in the dispersion.

hydrophobic (or non polar). The surfactants are classified according to the charge on their head group, which can be either cationic, anionic, nonionic or zwitterionic. If the adsorption of a surfactant molecule is established, self-organization of the surfactant molecules into micelles (aggregative structures of surfactants) takes place, if the concentration of surfactants is high enough. That means the critical micelle concentration (CMC) has to be reached. A good overview of the CNT surfactant interaction is given by [234], from which the scheme in Figure 5.13 is taken.

Cetyl trimethylammonium bromide

Dispersions were made with the assistance of cetyl trimethylammonium bromide (CTAB). The concentration of CTAB in distilled water was 0.05 wt.%. 10mg CNT were added to 10mL of of the prepared distilled water mixture with CTAB and sonicated for 30 minutes. Afterwards, it was subsequently centrifuged for 30 minutes in a Biofuge stratos centrifuge at 10.000rpm in the standard rotor. The supernatant was, afterwards, removed and used for further processes.

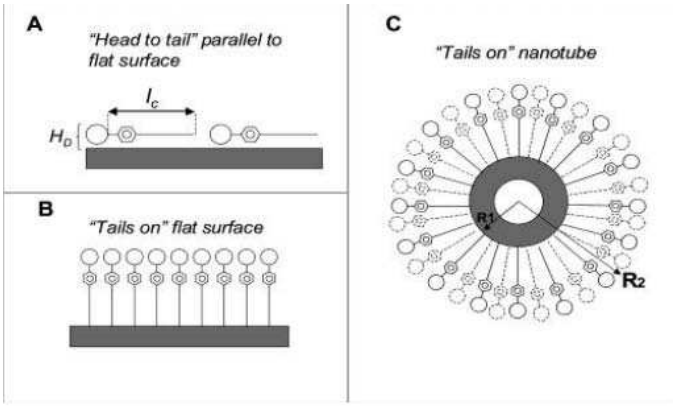

Fig. 5.13: Scheme of CNT surfactant interaction on basis of CNT and NaDDBS. "Reprinted (adapted) with permission from (O. Matarredona, H. Rhoads, Z. R. Li, J. H. Harwell, L. Balzano, and D. E. Resasco, NDispersion of single-walled carbon nanotubes in aqueous solutions of the anionic surfactant naddbs, Journal of Physical Chemistry B, 107(48):13357–13367). ©(2003) American Chemical Society." [234].

Sodium dodecyl sulfate

Dispersions were also made with sodium dodecyl sulfate (SDS) as the surfactant. For this a solution of SDS and distilled water was prepared by adding 1g SDS to 100mL distilled water: $100\% = \frac{1}{100}\left[\frac{g}{mL}\right]$. For CNT dispersion a solution of 1%w/v of SDS in distilled water was used. 1mg of CNTs were subsequently added to 1mL of the dispersion mixture. The mixture was sonicated for 30 minutes at room temperature. Subsequently, it was centrifuged for 30 minutes in a Biofuge stratos centrifuge with the standard rotor. Only the supernatant was used in further processes.

Sodium taurodeoxycholate hydrate

The surfactant sodium sodium taurodeoxycholate hydrate (TDOC) was used as follows. In 1mL of double distilled water 0.03mg of TDOC was dissolved, which yielded a concentration of c=0.03mg/mL. This solution was mixed with 1mg of CNTs. Afterwards, the mixture was sonicated with the UP200S for 10 minutes with a pulsation duration of 3 seconds followed by a 1 second pause at an amplitude of 10% of maximum power (if longer CNTs were desired, the amplitude was held at 8%). The subsequent centrifugation step was done in an Optima Max ultra centrifuge at 45.000rpm, which equals 100.000G, for 1 hour. The supernatant formed the final CNT dispersion.

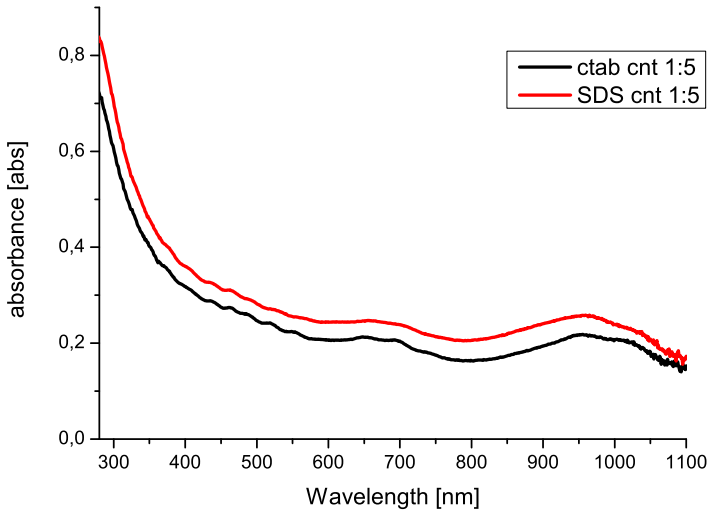

Fig. 5.14: UV-vis spectra of CNTs dispersed in CTAB and SDS. Due to the high concentration of CNTs in the dispersion it was diluted to a ratio of 1:5%vol. with the dispersion agent. The baseline correction has been already included. The corrected line shows the presence of CNTs in the dispersion.

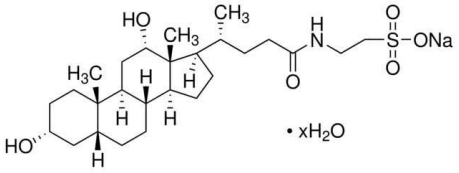

Fig. 5.15: Structure of TDOC. Image taken from [235].

DNA

The basic principle of this approach involves the wrapping of a double-active polymer around the CNT. This polymer consists along its backbone of both a hydrophobic and hydrophilic side. The hydrophobic side wraps around the CNT and the hydrophilic side interacts with the water molecules. This yields a very stable dispersion. For the polymer salmon RNA was used. In order to dissolve the RNA in water a buffer was needed. The TE-buffer used in this study was prepared by mixing 10mM **tris!** (**tris!**) and 1mM ethylenediaminetetraacetic acid (EDTA) with double distilled water. This solution was adjusted to pH-value 9 by adding hydrochloric acid. 0.025mg of salmon RNA and 0.5mg of CNTs were added to 0.475mL of the TE-buffer. The mixture was cooled with ice water and sonicated with the Optima Max

ultra centrifuge for 10 minutes with a pulse duration of 3 seconds followed by a 1 second pause. Afterwards, the mixture was centrifuged for 1h at 45.000rpm (100.000 G) and the supernatant was later removed.
Instead of salmon RNA also T30DNA was used to disperse the CNTs. The procedure used with this differs slightly from the one mentioned above. In detail it was as follows: 0.5mg of the CNTs, 0.495mL of the TE-buffer and 5mg of the T30DNA were mixed together and, subsequently, sonicated and centrifuged in the same way as mentioned above. This method yields the same results as obtained for the salmon DNA. However, the T30DNA is cheaper than the salmon RNA. In Figure 5.16, the absorption peaks around 650nm and 950nm are assigned to the first pair of singularities of the metallic nanotubes and to the second pair of singularities of semiconducting CNTs, respectively. An overview of surfactants for water based dispersions, in

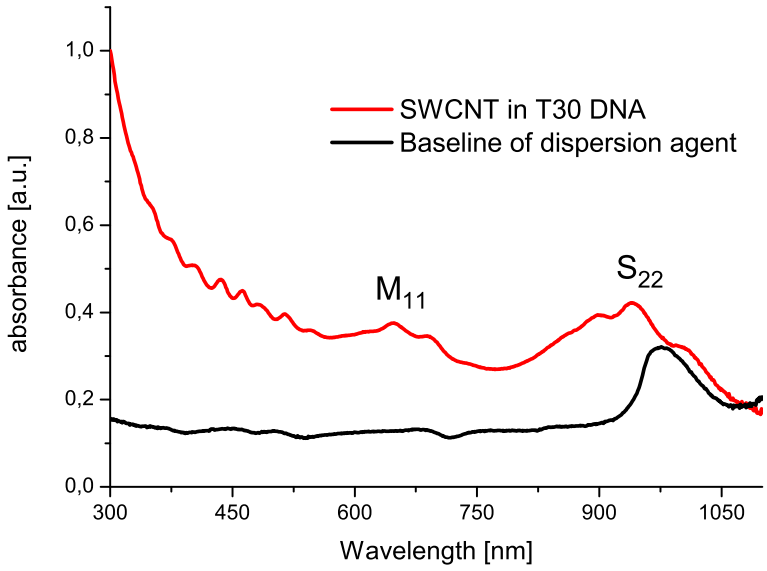

Fig. 5.16: UV-vis spectra of CNTs dispersed in T30DNA. The baseline correction has been already included. The corrected data attests to the presence of CNT in the dispersion. In addition the baseline of the dispersion agent is given.

terms of the Hansen parameters, is given in Figure 5.17. The work with Hansen parameters was taken from literature and given here just to give a wide-spread overview. The according Hansen parameters are listed in the Figure 5.18. All the surfactants used in this work and mentioned in this subsection do not evaporate. Consequently, they stay wrapped around the CNTs and appear as impurities. They can bind charge carriers flowing in

Table 2
Dispersion of nanotubes in aqueous surfactant solutions and the molecular structures, the types, and the HLB values of the surfactants

Surfactants	Structures	HLB numbers[a]	Surfactant type	Dispersion state
Dodecyl sulfate, sodium salt	$CH_3(CH_2)_{11}SO_4^-Na^+$	40.0	Anionic	Dispersed
Decylamine	$CH_3(CH_2)_9NH_2$	11.7	Cationic	Dispersed
Dodecylamine	$CH_3(CH_2)_{11}NH_2$	10.7	Cationic	Dispersed
Hexadecylamine	$CH_3(CH_2)_{15}NH_2$	8.8	Cationic	Dispersed
Triethylamine	$(CH_3CH_2)_3N$	13.6	Cationic	Swollen
Octylsulfate, sodium salt	$CH_3(CH_2)_7SO_4^-Na^+$	41.9	Anionic	Swollen
Dodecylbenzene sulfonic acid, sodium salt	$CH_3(CH_2)_{11}C_6H_4SO_3^-Na^+$	9.5	Anionic	Swollen
Octanoic acid, sodium salt	$CH_3(CH_2)_6COO^-Na^+$	22.8	Anionic	Sedimented
1-Pentanol	$CH_3(CH_2)_4OH$	6.5	Nonionic	Sedimented
1-Octanol	$CH_3(CH_2)_7OH$	5.1	Nonionic	Sedimented
Hexylamine	$CH_3(CH_2)_5NH_2$	13.6	Cationic	Sedimented
Octadecylamine[b]	$CH_3(CH_2)_{17}NH_2$	7.9	Cationic	–
Octadecylsulfate, sodium salt[b]	$CH_3(CH_2)_{17}SO_4^-Na^+$	37.2	Anionic	–

[a] HLB number was calculated by the equation of Davies in accordance with their structures [35]. HLB = ∑(hydrophilic group numbers) + ∑(hydrophobic group numbers) + 7. HLB group numbers were listed on other papers [35–37]. Amine functionality (–NH_2) was looked on as tertiary amine [38].
[b] In case of ODA and SODS, the viscosity of their aqueous solution was too high and formed gel during sonication.

Fig. 5.17: Overview of dispersion study. (H. T. Ham, Y. S. Choi, and I. J. Chung, Journal of Colloid and Interface Science, 286, Issue 1, 2005, 216-223. ©(2004) with permission from Elsevier) [232].

the matrix and can possibly act as traps in worst case. From this point of view the application of dispersions with surfactants are of disadvantageous.

5.3.4 Quality of the dispersion

The quality of a dispersion is usually determined by AFM measurements. Dispersed CNTs are deposited onto a silicon wafer using spin coating. The dispersion was spin coated at 2000rpm for 60 seconds. The dispersion was deposited onto a rotating substrate. The coated silicon wafer was analyzed by AFM. An AFM image is shown in Figure 5.19. The height profiles clearly show that CNTs lie next to each other forming a small band. The band has a height of 1.2nm and a width of 150nm. The height indicate that single CNTs lie next to each other. This is an identification for a CNT dispersion of high quality.

5.3.5 CNT concentration

All production routes have to be calibrated, as no knowledge of the CNT quantity in the dispersion can be made, as only the supernatant was taken after centrifugation. Having once determined the extinction coefficient, the CNT concentration of the dispersion can be ascertained via UV-vis analysis. The extinction coefficient was reported by several groups, [236], and [237].The concentration of CNTs in a dispersion can be calculated from the absorbance peak at 500nm. This wavelength is virtually unaffected by the ambient conditions of theCNTs, [238], and [233]. By using the specific extinction coefficient at 500nm (ε_{500}=28.6 $\cdot$ cm^2mg^{-1}) ([239]) it is possible to calculate the concentration of the CNT dispersions. This calculation uses

Table 3
Hansen parameters and molar volumes of the lipophilic groups of surfactants

Lipophilie	Formula	V (cm^3/mol)	δ ($MPa^{1/2}$)		
			δ_d	δ_p	δ_h
Methyl[b]	CH_3-	34.1	12.6	0.0	0.0
Ethyl[a]	CH_3CH_2-	50.3	14.3	0.0	0.0
Propyl[b]	$CH_3(CH_2)_2-$	66.5	15.1	0.0	0.0
Butyl[b]	$CH_3(CH_2)_3-$	82.6	15.6	0.0	0.0
Pentyl[b]	$CH_3(CH_2)_4-$	98.8	15.9	0.0	0.0
Hexyl[b]	$CH_3(CH_2)_5-$	114.9	16.1	0.0	0.0
Octyl[b]	$CH_3(CH_2)_7-$	147.2	16.4	0.0	0.0
Decyl[b]	$CH_3(CH_2)_9-$	179.5	16.5	0.0	0.0
Dodecyl (lauryl)[a]	$CH_3(CH_2)_{11}-$	211.3	16.7	0.0	0.0
Pentadecyl (palmitate)[a]	$CH_3(CH_2)_{14}-$	260.2	16.8	0.0	0.0
Hexadecyl[a]	$CH_3(CH_2)_{15}-$	275.7	16.8	0.0	0.0
Heptadecyl (stearate)[a]	$CH_3(CH_2)_{16}-$	293.2	16.8	0.0	0.0
Octadecyl (stearyl)[b]	$CH_3(CH_2)_{17}-$	308.8	16.9	0.0	0.0
Nonadecyl[b]	$CH_3(CH_2)_{18}-$	325.0	16.9	0.0	0.0

[a] A.F.M. Barton, CRC Handbook of Solubility Parameters and Other Cohesion Parameters, second ed., CRC Press, Boca Raton, FL, 1991 [31].
[b] Calculated by the equation of Hansen and Hildebrand in accordance with the molar volume and cohesive energy of methyl and ethyl groups [39,40], $\delta_t^2 = \delta_d^2 + \delta_p^2 + \delta_h^2$, $\delta = (-E/V)^{1/2}$.

Fig. 5.18: Overview of Hansen parameters for the several solvents, including those used in this study. (H. T. Ham, Y. S. Choi, and I. J. Chung, Journal of Colloid and Interface Science, 286, Issue 1, 2005, 216-223. ©(2004) with permission from Elsevier) [232].

the Lambert-Beer-Law as follows:

$$A = \epsilon_{\lambda=500} \cdot c \cdot d \tag{5.9}$$

$$\Rightarrow c = \frac{A}{\varepsilon_{\lambda=500} \cdot d}, \quad d = 1mm \tag{5.10}$$

where A is the absorbance, $\varepsilon_{\lambda=500}$ is the specific extinction coefficient at 500nm and d the travel distance travelled by the light through the dispersion. The specific extinction coefficient, $\varepsilon_{\lambda=500}$, was determined in the work of [239]. For this they prepared a CNT dispersion and evaporated 100mL of the dispersion. Subsequently, the retantate was weighed and correlated with the absorption spectra according to equation (5.9).

5.4 Buckypaper fabrication

A buckypaper of CNTs consists of a felt composed of CNTs. There are several ways to fabricate a buckypaper but one of the easiest ways to do this is to firstly prepare a CNT dispersion, ideally of a defined concentration, followed by a vacuum filtration step. The retantate on the filter paper obtained after the filtration process is the fabricated buckypaper. The best filter material has been found to be PVDF with a pore size of $0.45\mu m$. If the smaller pore size of $0.2\mu m$ is chosen, the filter blocks too quickly during the processing. But if fine adjustment of buckypaper thickness is needed, this small pore size filter shows better experimental properties. Because the drainage of the CNT dispersion gives the visible real-time feedback to the

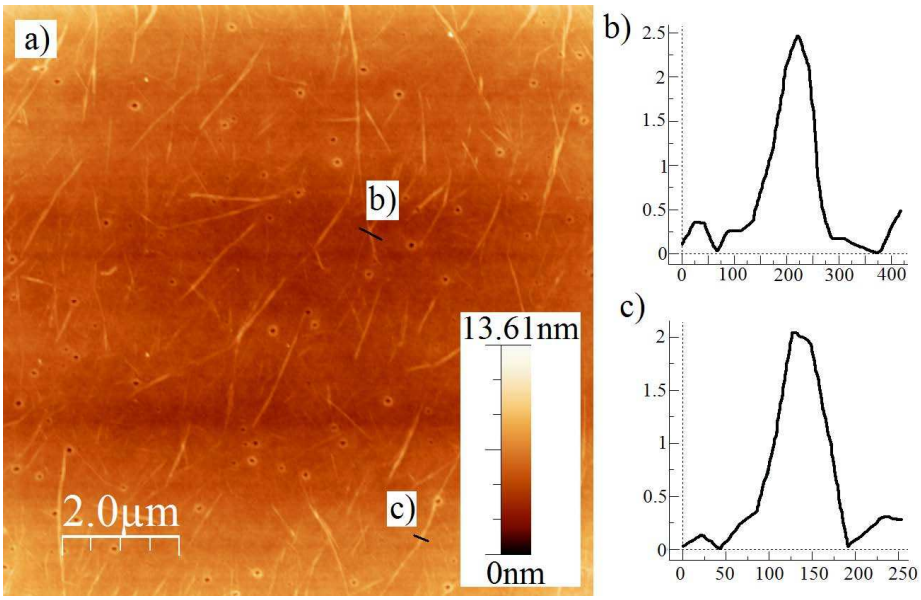

Fig. 5.19: AFM analysis. a) AFM image of a spin coated CNT dispersion. b) and c) corresponding height profile of the indicated lines in a).

experimenter. If the concentration of CNTs and the flow rate trough the filter are known in advanced, the buckypaper thickness can be accurately controlled. The colour of the CNT felt changes from grey, to brown, to black in accordance with the felt thickness. After filtration the wet filter is placed and fixed in a switched on exhaust hood. In the accompanying process a metal mesh grid is placed 2cm above the filter. The upward air draft draws the pure CNT buckypaper from the wet filter onto the metal mesh grid. This buckypaper can be additionally rinsed with distilled or deionized water in order to clean or neutralize it, respectively.
By using this preparation route the buckypaper is not fixed on a substrate and stays flexible. For the electrical analysis of this buckypaper it has to be deposited on an electrical isolating substrate in order to give the paper the necessary mechanical stiffness. An important challenge for this analysis is to fix the buckypaper on the substrate with only adhesive forces. This can be achieved by wetting it with toluene and followed by a thermal annealing treatment. If ethanol, tetrahydrofuran (THF) or another organic solvent is used as adherence agent the attachment of the buckypaper on the substrate is not achieved. The detailed process for the attachment was as follows: firstly, the buckypaper was put on the substrate, secondly, a droplet of toluene was put onto the buckypaper and, thirdly, it was covered with a microscope slide weighted down with a 100g weight. Subsequently, the whole prepared sandwich was placed on a hotplate and annealed for 10 minutes at 140°C.

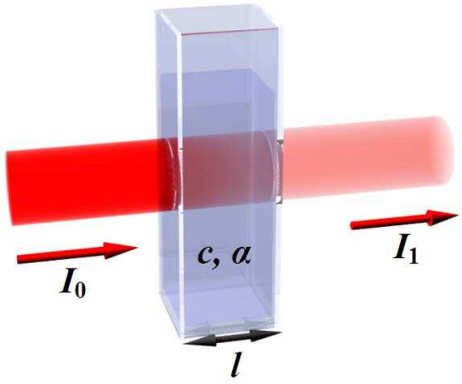

Fig. 5.20: Scheme of the incident light (I_0), concentration depended absorption (c, α) and transmitted light (I_1). Image taken from [240].

Another route to form buckypaper involves the use of a filter made of cellulose mixed ester. The retantate on the filter can be separated from the filter by simply dissolving the filter. Cellulose mixed ester is soluble in different organic solvents, including acetone. This dissolving process has to be done very carefully as the CNTs also interact with the solvent, which can lead to a tear in the buckypaper. The major advantage of this approach is that the buckypaper can be deposited direct onto different substrates. The processing is as follows: the CNT-filter combination is laid with the CNT-side on the substrate and then wetted with acetone. Afterwards, the main part of the filter is transparent and swollen but still as solid. The filter can be washed off the substrate-CNT layer by using an acetone jet. The rest of the filter can be washed off by using a burette placed above the substrate covered with the buckypaper. Afterwards the burette is filled with an acetone and ethanol mixture of [1:1] *vol*% and the substrate is cleaned drop-wise. The substrate itself is tilted in order to allow the acetone filter mixture to drain off the substrate. This completely frees the buckypaper from the filter so that it can be used for further studies.

5.5 Summary

In this chapter the purification, functionalisation, and dispersion of CNT is explained. Different methods of purification and functionalisation (covalent and non-covalent) have been investigated. Non-covalent functionalisation such as wrapping (polymer wrapped around CNT), or surfactants such as tensides yields good CNT dispersion. These materials will remain in further CNT processing. Covalent functionalisation, such as adding carboxylic groups or fluorination, changes the work function of the CNT and enlarge their band gap due to disturbance of the initial lattice of alternating sp^1-

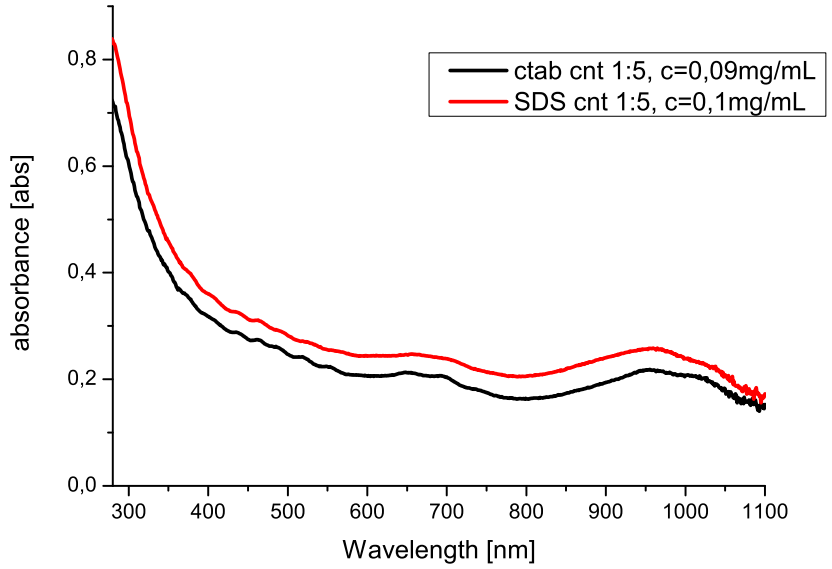

Fig. 5.21: The UV-vis spectra of Figure 5.14. The concentration of SWCNT within the dispersions are $c_{SWCNTinCTAB}$=0.09mg/mL and $c_{SWCNTinSDS}$=0.1mg/mL.

and sp^2-hybridized carbon bonds. The CNT dispersion was analyzed by AFM measurements and UV-vis spectroscopy. The CNT concentration was determined.

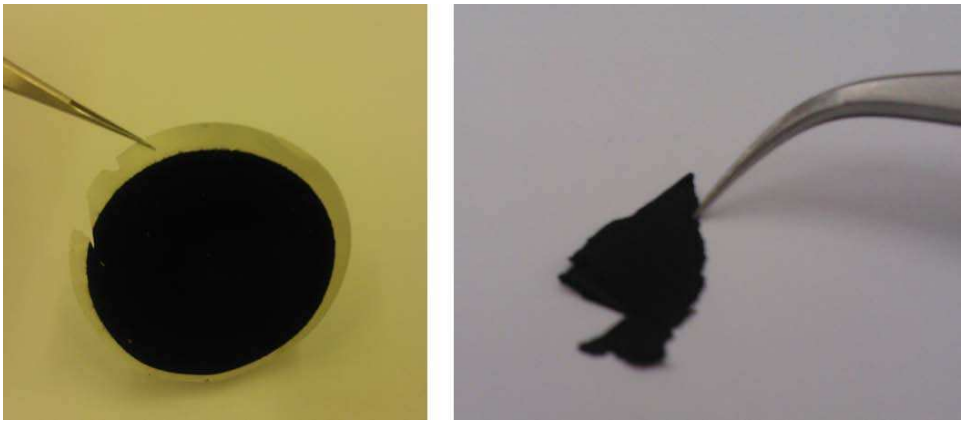

Fig. 5.22: CNT buckypaper. Left: filter with vacuum filtrated CNTs on top. Right: buckypaper after removal from the filter.

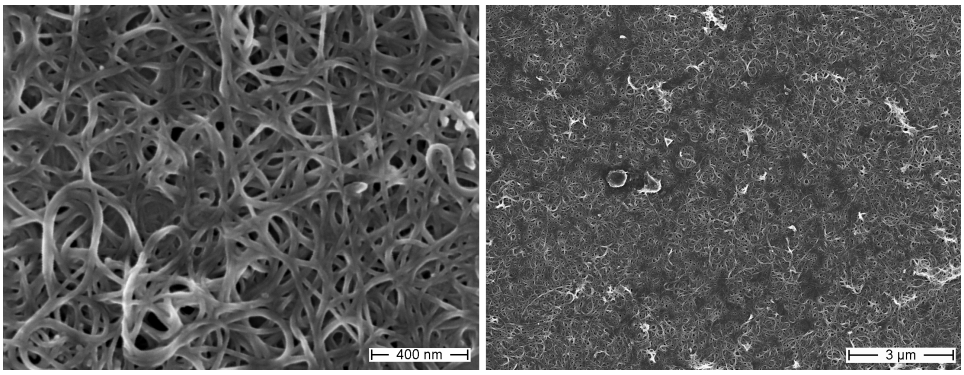

Fig. 5.23: SEM images of a buckypaper. Left: magnification of the images shown in right. Right: CNT buckypaper.

6. CARBON NANOTUBE SOLAR CELLS

The best organic solar cell based on CNTs (according to device efficiency) reported so far was made by [139]. This reached power conversion efficiencies of up to 4.9%. In most cases, solar cells with blended donor and acceptor molecules in the active matrix are based on the so-called donor-acceptor BHJ concept. Such a device consists of a three-dimensional interpenetrating network usually containing conjugated polymers and fullerene derivatives. The exciton diffusion length of about 10nm (reported values vary and have been as large as 62nm) provides an effective limit to the active layer thickness. A thin layer thicknesses is also required to reduce the recombination losses, which are a result of the short carrier drift length $L_d = \mu\tau E$, where, μ is the carrier mobility, τ is the carrier recombination time, and E is the electric field. Post thermal annealing improves device morphology and therefore device performance [99].
Alternatively, CNTs can be added to the matrix. These act as conductive channels with high carrier mobilities for charge carriers and exciton dissociation centres for holes, [115], or electrons, [112]. Up to now, CNT have been used successfully as a TCO replacement in the anode layer. For such hole collecting electrode devices, efficiencies of 2.5% have been achieved, [241]. In the following section organic solar cells, which contain CNTs are presented.

6.1 CNT in polymer solar cells

As the first step of production, the CNTs were dispersed as described in chapter 5. Following on from this the solution of dye with the specific solvent was prepared. Subsequently, the supernatant of the CNT dispersion was mixed together with the dissolved dye to a particular concentration of each. This mixture was spin coated onto a cleaned ITO substrate, which was prepared before hand with a Pedot:PSS layer in accordance with the fabrication process described in chapter 4. The layer thickness of the Pedot:PSS layer was 100nm. Also the layer thickness of the P3HT layer as well as the thickness of the P3HT:CNT blend layer, and the thickness of the P3HT:CNT:PCBM blend layer were 100nm. The aluminium layer was 150nm thick. The layer thicknesses of these layers stood unchanged for all presented polymer solar cells. The CNT concentration was c=0.1mg/mL.

6.1.1 CNT:P3HT

For the first produced sample the active matrix consisted of a P3HT-CNT blend. This was used to investigate the performance of purely polymer-CNT organic solar cells. The band diagram of the following solar cells are shown in Figure 6.1. The Fill factor of these solar cells were in the range of

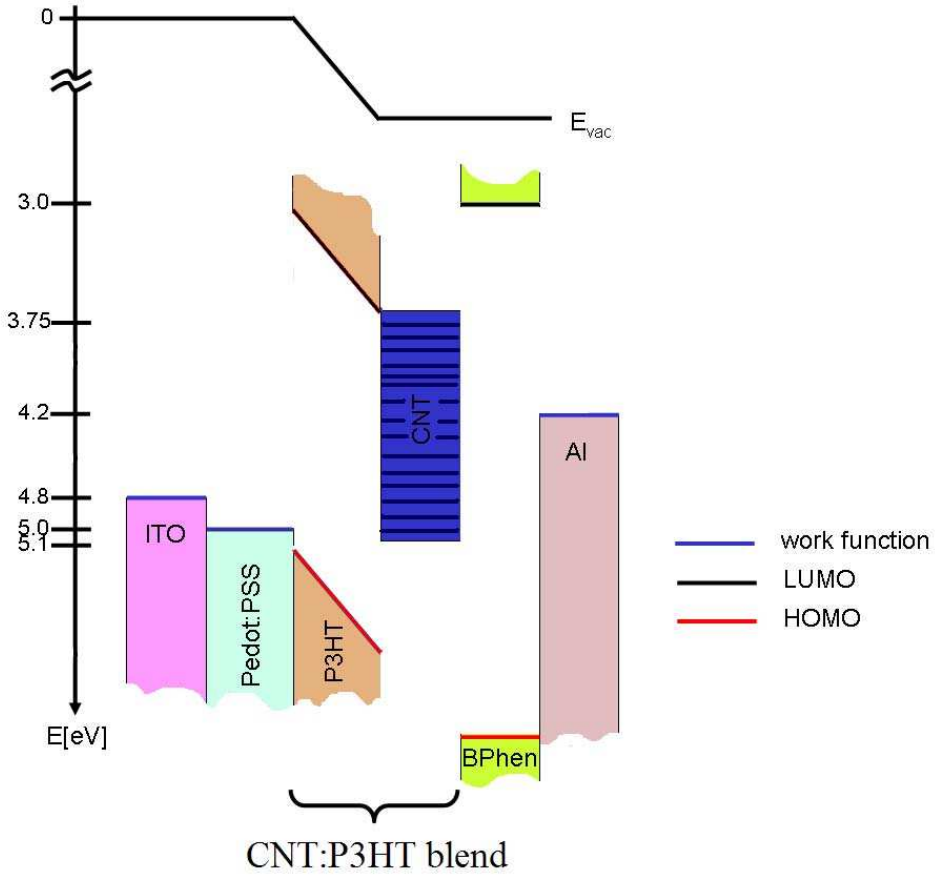

Fig. 6.1: Band diagram of the studied solar cells. The sample architecture consisted of ITO-Pedot:PSS-P3HT:CNT-BPhen-Al. The work function of the CNTs is in the range from 3.75eV-4.8eV as reported by literature. The different energy levels of their work function are indicated by solid lines within the blue rectangle. The P3HT:CNT blend is the active matrix.

0.28<FF<0.33. Thermal annealing treatments were made on these devices. However, the obtained J-V dependency showed poor device performance as.the devices became highly resistive and lost their diodic properties. It is expected that such behaviour is due to oxygen adsorption during device analysis under an ambient atmosphere. Furthermore, they were stored over night under nitrogen before further experiments (thermal annealing) and characterization measurements were made. However, the boxes turned out

sample		R_s [Ω]	R_{sh}[kΩ]	n	FF	J_{sc} $[mA/cm^2]$	V_{oc}[V]	η[%]
$B3_1$	as-is	268	12.05	3.27	0.32	-0.79	0.1	0.025
$B3_2$	as-is	67	16.10	5.97	0.28	-0.75	0.118	0.028
$B3_3$	as-is	214	13.11	3.37	0.33	-0.8	0.021	0.028
$B3_4$	as-is	201	14.91	3.46	0.32	-0.78	0.107	0.026

Tab. 6.1: Overview of the characteristic values of ITO-Pedot:PSS-P3HT:CNT-BPhen-Al samples. Tempering destroys most of the samples.

not to be very gas proof. The diode ideality factor, n, varied for these devices in the range of 3.27<n<5.97 with a mode value of $n \approx 3.4$. Factors above n=2 indicate the occurrence of enhanced recombination processes in the bulk. The open circuit voltage stays relatively stable at around $V_{oc} \approx 0.1V$. According to the metal-insulator-metal model, this implies that much of the built-in voltage (V_{bi}) formed by the difference in the work-functions of the two electrodes (ITO: $\Phi_{ITO} = 4.8eV$ and aluminium: $\Phi_{Al} = 4.3eV$) $V_{bi} = \Phi_{ITO} - \Phi_{Al} = 4.8 - 4.3 = 0.5V$is lost in the device. In addition, the short circuit current density stays relatively constant at $J_{SC} = -0.75mA/cm^2$. This indicates, that CNTs from the Fraunhofer Institute IWS Dresden in combination with P3HT yields devices with comparable and reproducible properties. The efficiencies of these devices are small and in the range of $0.025 < \eta < 0.028$. A post thermal annealing treatment of the device used for the measurements shown in Figure 6.3 caused a significant change in the J-V dependency. This treatment "killed" the photo current, as well as the open circuit voltage. As a consequence, the device no longer functioned as a solar cell. Device performances were enhanced by the addition of acceptor materials like fullerenes. The effect of a thin layer of C_{60} (either 30nm or 60nm thick) is discussed in the next subsection.

6.1.2 CNT:P3HT-C60

On top of the P3HT:CNT layer a 30nm or 60nm C_{60}layer was deposited by thermal evaporation. Due to this process a sharp heterojunction at the interface of the P3HT:CNT and C_{60} was formed. This leads to additional exciton dissociation. The band diagram of the following solar cells are shown in Figure 6.4. The main difference between the samples with the two thicknesses of the C_{60} was observed after the thermal annealing treatment. The samples with a 30nm C_{60}-layer do not show an improvement of their characteristics due to the annealing process. Contrastingly, the samples with a 60nm C_{60}-layer show much improved characteristics. The difference was interpreted as being due to small differences in the experimental conditions. The variation in the series resistance was $203\Omega < R_s < 470\Omega$. Although the lowest series resistances were $R_s < 100\Omega$, values of $R_s \approx 200\Omega$ quite good. The value of 470Ω was observed only for one sample. In Figure 6.5 the I-V

sample		R_s [Ω]	R_{sh}[kΩ]	n	FF	J_{sc} $[mA/cm^2]$	V_{oc}[V]	η[%]
$B2_1$	as-is	203	11.10	2.95	0.34	-3.3	0.172	0.19
$B2_2$	as-is	207	25.96	3.23	0.34	-2.64	0.164	0.19
$B2_3$	as-is	252	23.48	3.7	0.33	-2.33	0.170	0.13
$B2_4$	as-is	470	31.02	4.44	0.31	-2.00	0.171	0.1

Tab. 6.2: Overview of the characteristic values of ITO-Pedot:PSS-P3HT:CNT-C_{60}-BPhen-Al samples. Tempering destroyed the samples.

dependency of the sample shown in Figure 6.7 is fitted using the method described in chapter 5. Since the misfit is quite small ($\Delta < 2 \cdot 10^{-4}$) the input values used in the fit can be assumed to well describe the device. The lowest fill factor of FF=0.31 was calculated for the results shown in Figure 6.7. This cannot be in all cases attributed automatically to be a result of the series resistance, but in this case the higher contact resistance influences the fill factor. The diode ideality factor of n=4.44 for this sample indicates that a high recombination rate occurs in the bulk, which also decreases the fill factor. The C_{60} layer was then increased to 60nm. The doubling in the thickness of this layer yielded good device improvement after the thermal annealing process. Due to this process both the open circuit voltage and the short circuit current increased. The fill factor was unchanged or increased. For the measurements shown in Figure 6.8 a) the series resistance of the sample increased from $R_s = 43\Omega$ to $R_s = 176\Omega$ due to the thermal annealing treatment. However, it would be expected that the series resistance should decrease due to the resulting improved layer morphology of the active layer after the thermal annealing treatment. In addition, the contact resistance between the organic semi-conductor and metal should have also improved. Consequently, the resistance increase of this particular sample was attributed to the formation of an oxidation layer on the aluminium electrode. Contrastingly, the other samples of the series did not show such a significant resistance change despite them undergoing the same treatments. For the other samples the open circuit voltage almost doubles after the annealing treatment. The short circuit current density also doubles. This enhanced performance of the devices can be attributed to improvements in the layer morphology and at the contact interfaces. The fill factor increases slightly but increases as well after annealing. These samples show efficiencies of around $\eta = 0.5\%$ - $\eta = 0.75\%$.

6.1.3 P3HT:CNT:PCBM-C60

The architecture of the samples discussed in this section differ from the previous ones by the addition of PCBM in the P3HT:CNT blend. The layer thickness of the active matrix formed by P3HT:CNT:PCBM was 100nm for all samples. Additionally, a layer of C_{60} was deposited on top of the

sample		R_s [Ω]	R_{sh}[kΩ]	n	FF	J_{sc} $[mA/cm^2]$	V_{oc}[V]	η[%]
$B1_1$	as-is	178	20.02	2.83	0.34	-2.36	0.168	0.13
	annealed	158	20.20	3.7	0.37	-6.61	0.310	0.75
$B1_2$	as-is	43	11.81	3.92	0.35	-3.01	0.164	0.17
	annealed	176	22.42	3.94	0.35	-6.29	0.306	0.67
$B1_3$	as-is	182	41.57	3.85	0.34	-2.38	0.155	0.12
	annealed	159	22.03	4.19	0.35	-5.86	0.290	0.59
$B1_4$	as-is	183	16.72	3.26	0.35	-2.34	0.156	0.13
	annealed	189	19.55	3.90	0.36	-4.78	0.298	0.51

Tab. 6.3: Overview of the characteristic values of ITO-Pedot:PSS-P3HT:CNT-C_{60}-BPhen-Al samples. Tempering destroyed most of the samples.

P3HT:CNT:PCBM layer. This layer was deposited by thermal evaporation in a high vacuum system. The thickness of the C_{60} layer was 30nm. The band diagram of the following solar cells are shown in Figure 6.11. The Fill factors of these samples are relatively stable in the range of $0.32 < \text{FF} < 0.33$ for the as-produced samples. After the annealing process FF=0.34, which means the fill factor was improved by 3-6% due to this step. The open circuit voltage is very much improved for all the samples due to this annealing process, where a rise from around 100mV to values around 500mV was observed. The latter value corresponds well with the difference of the work functions of the two electrodes (ITO: $\Phi_{ITO} = 4.8eV$ and aluminium: $\Phi_{Al} = 4.3eV$). According to the metal-insulator-metal (MIM)-model (see section 2.4) the open circuit voltage can be calculated as:

$$V_{bi} = \Phi_{ITO} - \Phi_{Al} = 4.8 - 4.3eV = 0.5V. \tag{6.1}$$

As the open circuit voltage is in good agreement with the calculated value of the difference of the two electrode work functions, the 500% increase can be attributed to significantly improved contact properties of the metal-semiconductor interface. The increase in short circuit current density is also significant upon annealing. However, in contrast to the increase of the diode ideality factor, this improvement is mainly based on the optimization of the layer morphology. This fact indicates also that the annealing improves the contact of the metal semiconductor interface. Nevertheless, the series resistance approximately doubles due to the annealing process. This series resistance increase can be due to either a bad fit of the data or the resistance within the active matrix genuinely increases. The diode ideality factor before annealing was in the range of $2.92 < n < 3.40$ and afterwards was in the range of $4.51 < n < 5.40$. This can be explained by the increase in the series resistance, which deforms the J-V dependency of the diode. Four samples were produced with a 60nm thick C_{60} layer on top of the P3HT:CNT:PCBM layer. The mobility of negative charge carriers in the C_{60} layer this effect

sample		R_s [Ω]	R_{sh}[kΩ]	n	FF	J_{sc} $[mA/cm^2]$	V_{oc}[V]	η[%]
$C2_1$	as-is	163	17.06	3.34	0.33	-2.76	0.104	0.09
	annealed	549	19.94	4.51	0.34	-4.17	0.525	0.74
$C2_2$	as-is	160	14.54	3.33	0.33	-2.98	0.105	0.1
	annealed	335	17.31	5.06	0.34	-5.13	0.521	0.91
$C2_3$	as-is	200	18.18	3.40	0.32	-2.75	0.105	0.09
	annealed	348	18.68	5.04	0.34	-4.29	0.520	0.76
$C2_4$	as-is	185	14.46	2.92	0.32	-2.61	0.103	0.08
	annealed	350	20.43	5.40	0.34	-4.09	0.511	0.7

Tab. 6.4: Overview of the characteristic values of ITO-Pedot:PSS-P3HT:CNT:PCBM-C_{60}-BPhen-Al samples. Tempering increased the device performance.

has a larger influence such that it causes smaller or comparable short circuit current densities compared with the devices with a 30nm C_{60}. The efficiency was about ten times larger after annealing. This was mainly due to the tremendous increase of the open circuit voltage, on average from 100mV to 500mV. Three of the four samples showed a decrease of the series resistance after the annealing treatment. This can be interpreted as being due to an improvement of the metal semiconductor contact, as also the diode ideality factor increases to values near to n=5. In addition, the shunt resistance increases more or less significantly in three of the four samples. The shunt resistance is known to be an indicator for the quality of the pn-junction in anorganic devices. For the organic system it gives an indication of the quality of the layer homogeneity. In other words the blended CNTs do not break through the single layers and cause shunts.

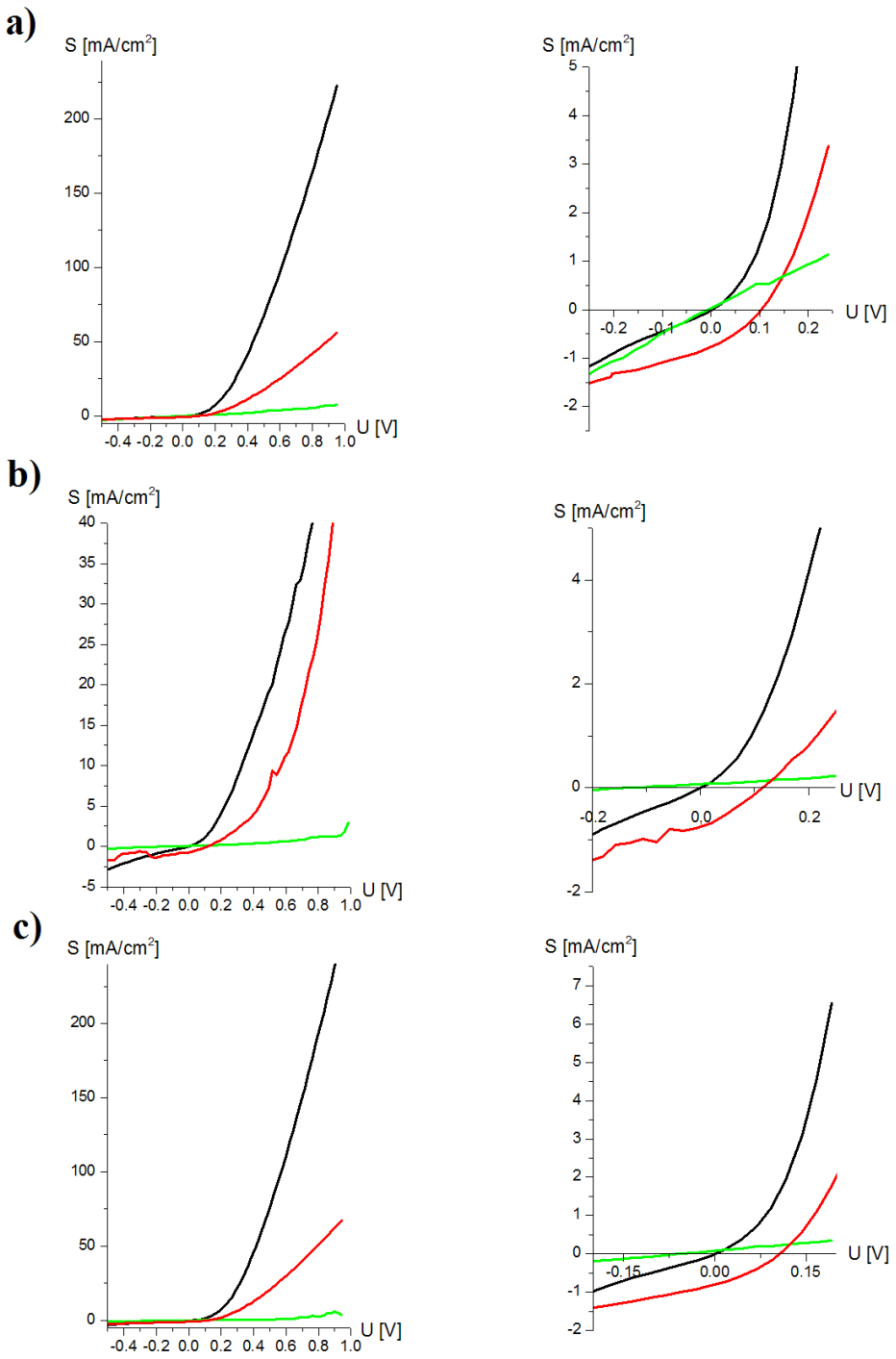

Fig. 6.2: P3HT:CNT solar cells. CNT are blended in the P3HT layer. The device architecture is ITO-Pedot:PSS-P3HT:CNT-BPhen-Al. Left: full graph of J-V characteristics, where black corresponds to dark condition, red represents under illumination, and green corresponds to illumination after thermal annealing. Right: magnification around the origin. The characteristic values are summarized in table 6.1.

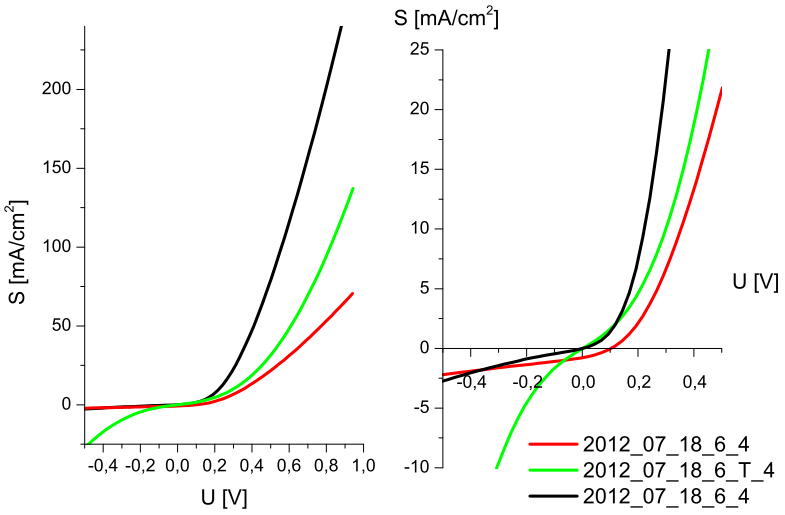

Fig. 6.3: P3HT:CNT solar cell. The device architecture is ITO-Pedot:PSS-P3HT:CNT-BPhen-Al. Left: full graph of J-V characteristics, where black corresponds to dark, red represents under illumination and green corresponds to illumination after thermal annealing. Right: magnification around the origin. The characteristic values are: $V_{OC} = 0.104V$, $J_{SC} = -0.78mA/cm^2$, FF=0.32, $\eta = 0.026\%$, $R_s = 201\Omega$, $R_{sh} = 14915\Omega$, n=3.46.

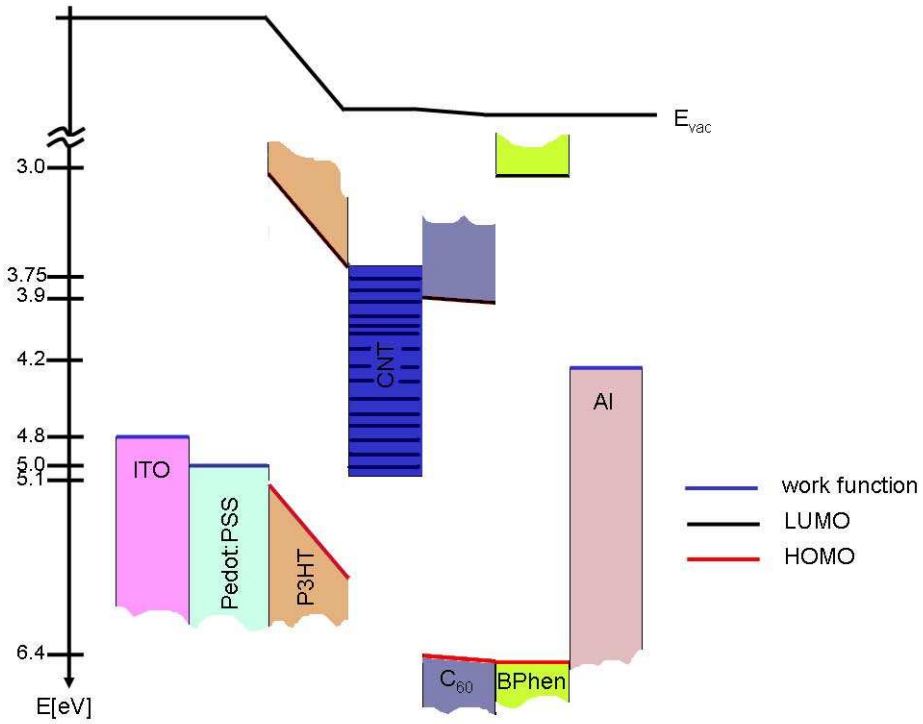

Fig. 6.4: Band diagram of the studied solar cells. The sample architecture consisted of ITO-Pedot:PSS-P3HT:CNT-C_{60}-BPhen-Al. The work function of the CNTs is in the range from 3.75eV-4.8eV as reported by literature. The different energy levels of their work function are indicated by solid lines within the blue rectangle. The P3HT:CNT blend covered with the C_{60} layer is the active matrix.

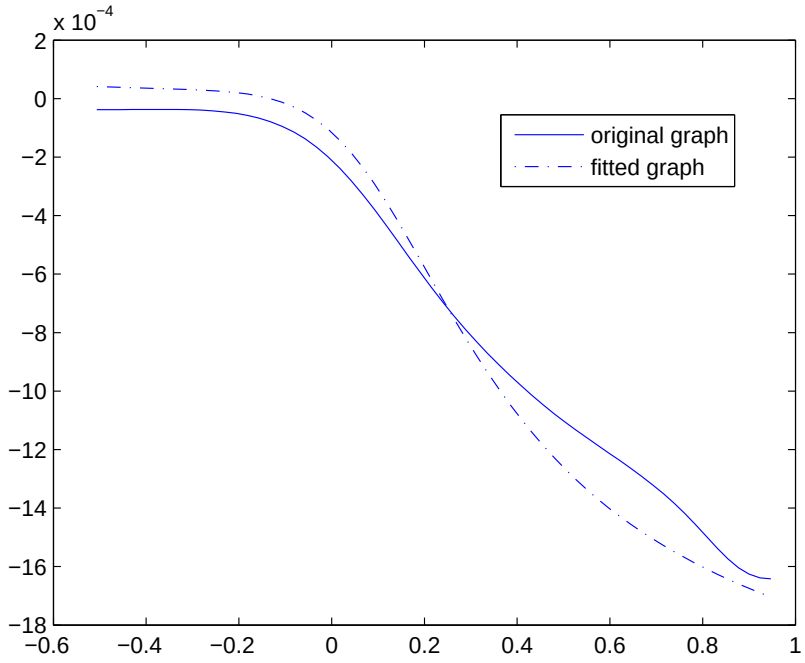

Fig. 6.5: Fit of I-V curve in Matlab (sample:$B2_4$). The match is good.

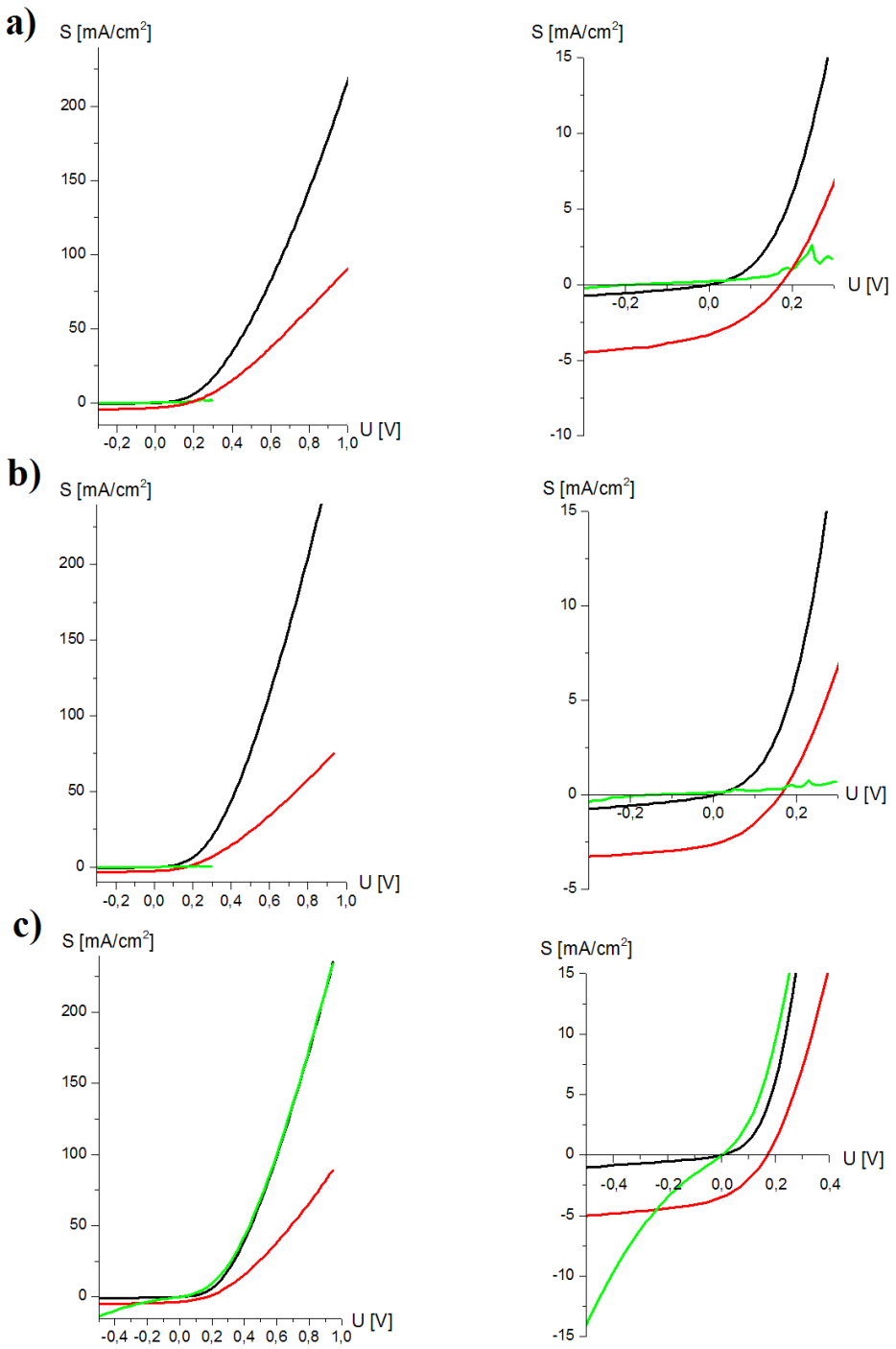

Fig. 6.6: P3HT:CNT-C_{60} solar cells. CNTs are blended in the P3HT layer. The device architecture is ITO-Pedot:PSS-P3HT:CNT-C_{60}-BPhen-Al. The thickness of the C_{60} layer is 30nm. Left: full graph of J-V characteristics, where black corresponds to dark condition, red represents under illumination, and green corresponds to illumination after thermal annealing. Right: magnification around the origin. The characteristic values are summarized in table 6.2.

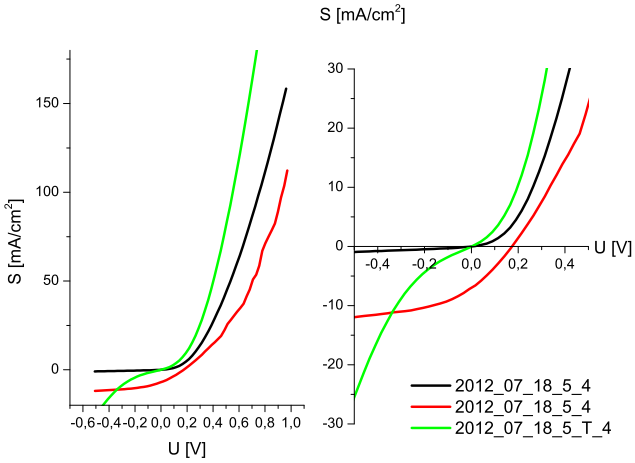

Fig. 6.7: P3HT:CNT-C_{60} solar cell. The device architecture is ITO-Pedot:PSS-P3HT:CNT-C_{60}-BPhen-Al. The thickness of the C_{60} layer is 30nm. The thickness of the C_{60} layer is 30nm. Left: full graph of J-V characteristics, where black corresponds to dark, red represents under illumination and green corresponds to illumination after thermal annealing. Right: magnification around the origin. The characteristic values are: $V_{OC} = 0.171V$, $J_{SC} = -2.00mA/cm^2$, FF=0.31, $\eta = 0.1\%$, $R_s = 470\Omega$, $R_{sh} = 31023\Omega$, n=4.44.

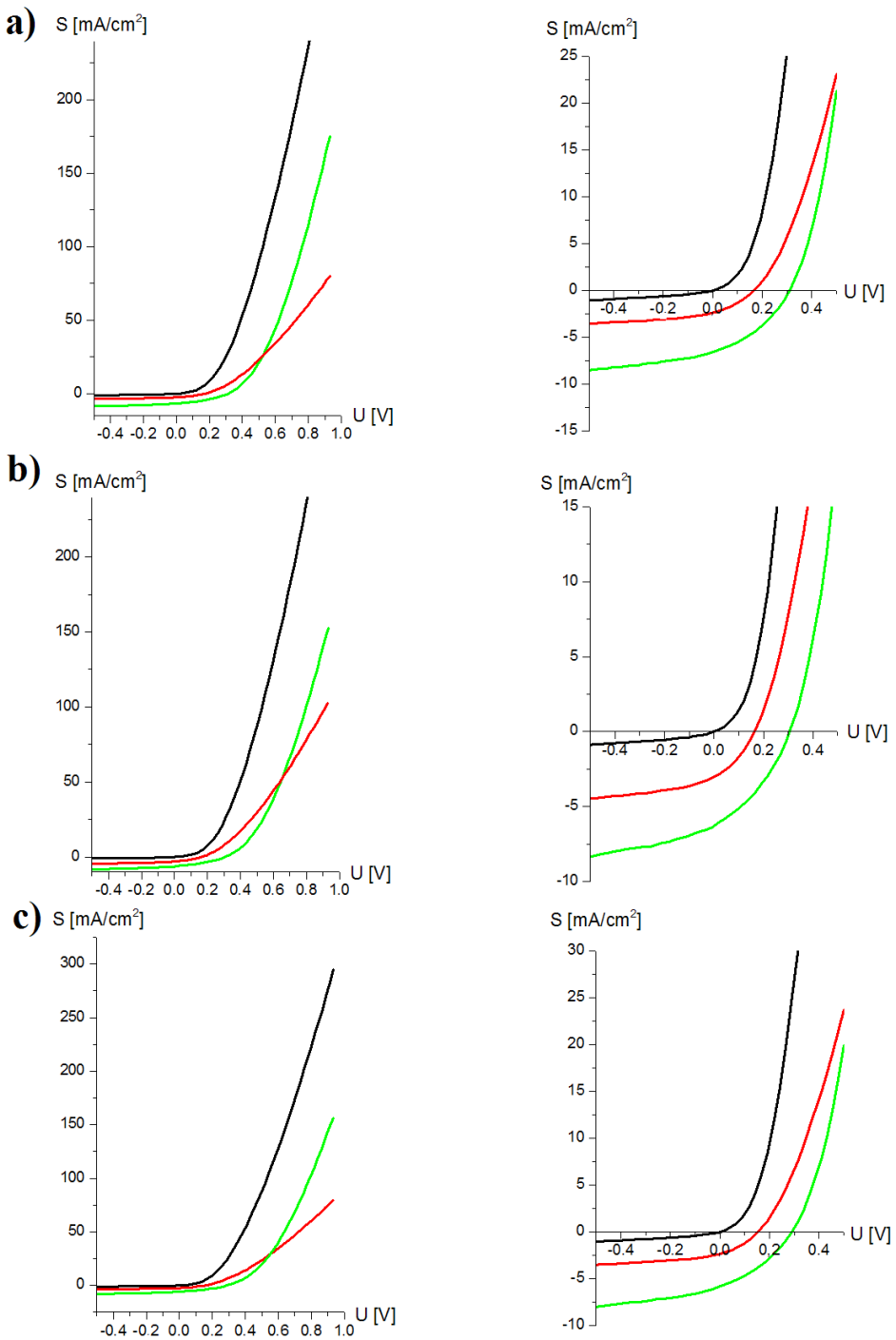

Fig. 6.8: P3HT:CNT-C_{60} solar cells. CNTs are blended in the P3HT layer. The device architecture is ITO-Pedot:PSS-P3HT:CNT-C_{60}-BPhen-Al. The thickness of the C_{60} layer is 60nm. Left: full graph of J-V characteristics, where black corresponds to dark condition, red represents under illumination, and green corresponds to illumination after thermal annealing. Right: magnification around the origin. The characteristic values are summarized in table 6.3.

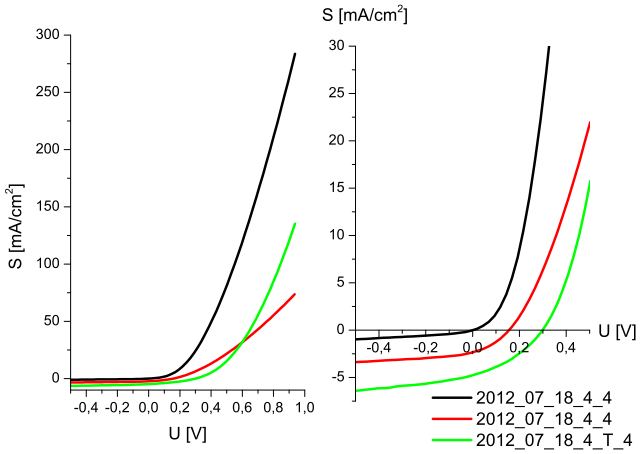

Fig. 6.9: P3HT:CNT-C_{60} solar cell. The device architecture is ITO-Pedot:PSS-P3HT:CNT-C_{60}-BPhen-Al. The thickness of the C_{60} layer is 60nm. Left: full graph of J-V characteristics, where black corresponds to dark, red represents under illumination and green corresponds to illumination after thermal annealing. Right: magnification around the origin. The characteristic values are: $V_{OC} = 0.156V$, $J_{SC} = -2.34mA/cm^2$, FF=0.35, $\eta = 0.13\%$, $R_s = 183\Omega$, $R_{sh} = 16720\Omega$, n=3.26. After thermal annealing the values are: $V_{OC} = 0.298V$, $J_{SC} = -4.78mA/cm^2$, FF=0.36, $\eta = 0.51\%$, $R_s = 189\Omega$, $R_{sh} = 19552\Omega$, n=3.90.

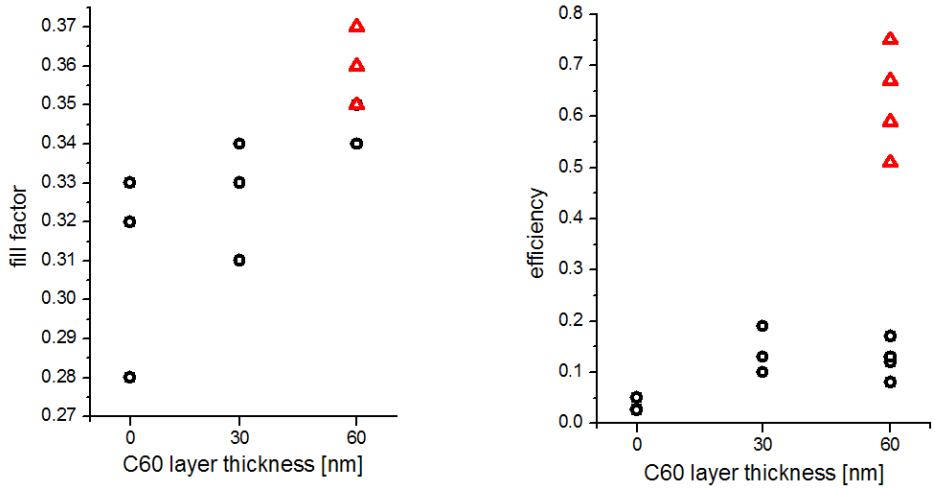

Fig. 6.10: Efficiencies and fill factors before and after thermal annealing of P3HT:CNT and P3HT:CNT-C_{60} solar cells. Thermal annealing significantly improves the device performance, if the solar cell contains a C_{60} layer.

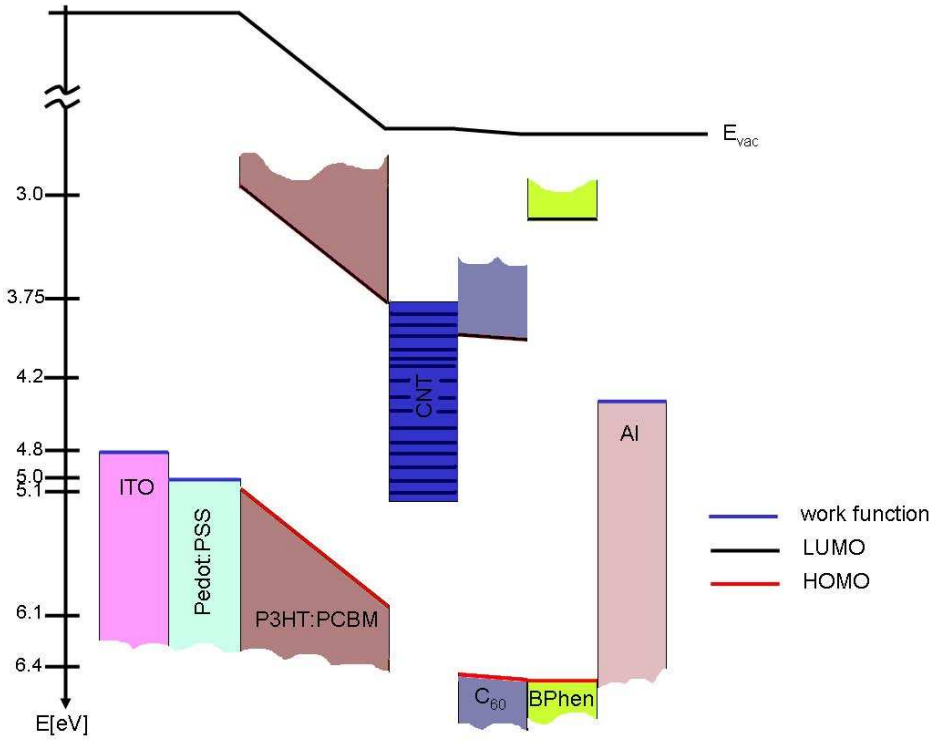

Fig. 6.11: Band diagram of the studied solar cells. The sample architecture consisted of ITO-Pedot:PSS-P3HT:CNT:PCBM-C_{60}-BPhen-Al. The work function of the :CNTs is in the range from 3.75eV-4.8eV as reported by literature. The different energy levels of their work function are indicated by solid lines within the blue rectangle. The P3HT:CNT:PCBM blend covered with the C_{60} layer is the active matrix.

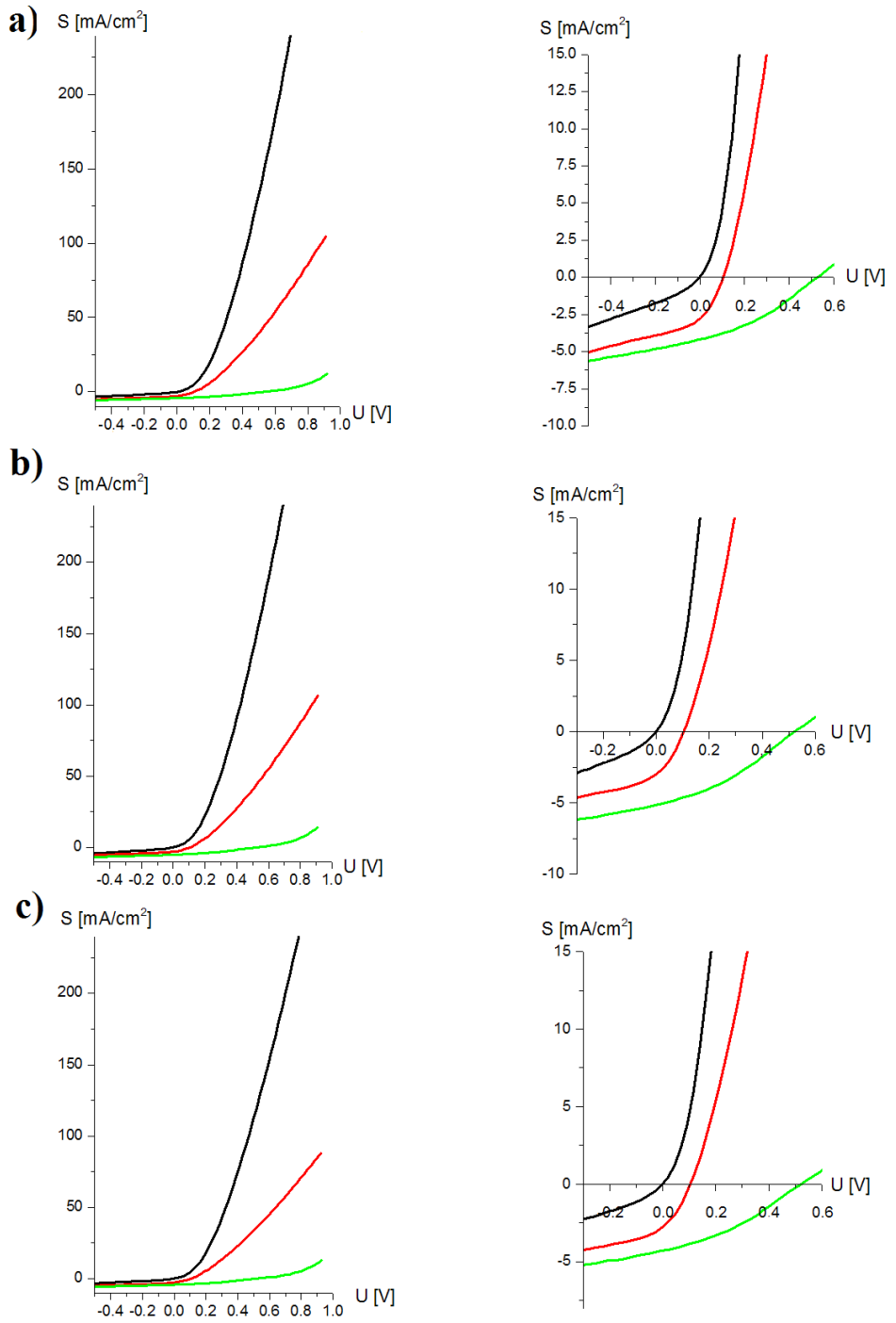

Fig. 6.12: P3HT:CNT:PCBM-C_{60} solar cells. CNTs are blended in the P3HT:PCBM composite layer layer. The device architecture is ITO-Pedot:PSS-P3HT:CNT:PCBM-C_{60}-BPhen-Al. The thickness of the C_{60} layer is 30nm. Left: full graph of J-V characteristics, where black corresponds to dark condition, red represents under illumination, and green corresponds to illumination after thermal annealing. Right: magnification around the origin. The characteristic values are summarized in table 6.4.

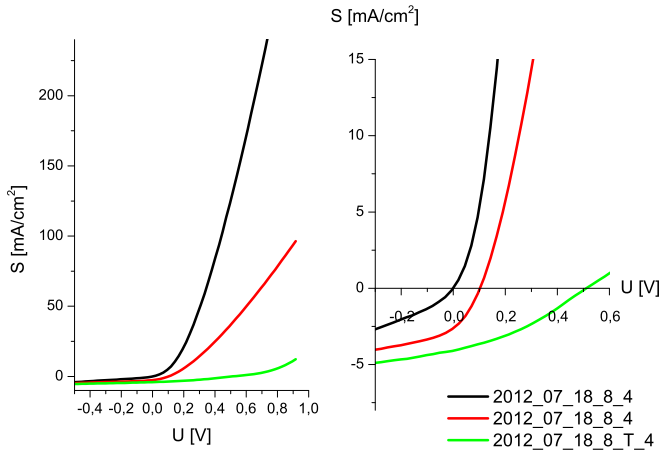

Fig. 6.13: P3HT:CNT:PCBM-C_{60} solar cell. The device architecture is ITO-Pedot:PSS-P3HT:CNT:PCBM-C_{60}-BPhen-Al. The thickness of the C_{60} layer is 30nm. Left: full graph of J-V characteristics, where black corresponds to dark, red represents under illumination and green corresponds to illumination after thermal annealing. Right: magnification around the origin. The characteristic values are: $V_{OC} = 0.103V$, $J_{SC} = -2.61mA/cm^2$, FF=0.32, $\eta = 0.08\%$, $R_s = 185\Omega$, $R_{sh} = 14462\Omega$, n=2.92. After thermal annealing the values are: $V_{OC} = 0.511V$, $J_{SC} = -4.09mA/cm^2$, FF=0.34, $\eta = 0.70\%$, $R_s = 350\Omega$, $R_{sh} = 20430\Omega$, n=5.40.

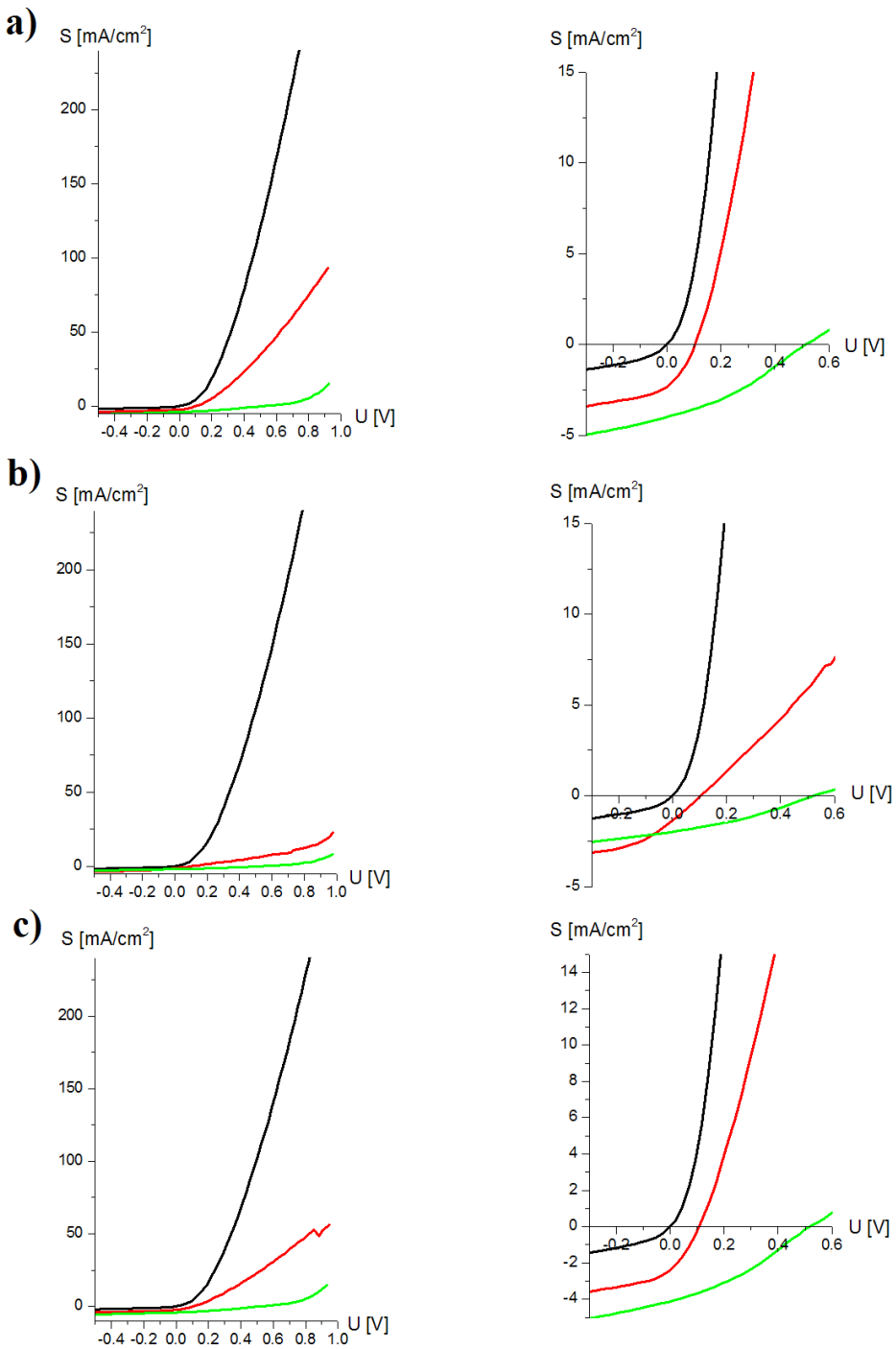

Fig. 6.14: P3HT:CNT:PCBM-C_{60} solar cells. CNT are blended in the P3HT:PCBM composite layer layer. The device architecture is ITO-Pedot:PSS-P3HT:CNT:PCBM-C_{60}-BPhen-Al. The thickness of the C_{60} layer is 60nm. Left: full graph of J-V characteristics, where black corresponds to dark condition, red represents under illumination, and green corresponds to illumination after thermal annealing. Right: magnification around the origin. The characteristic values are summarized in table 6.5.

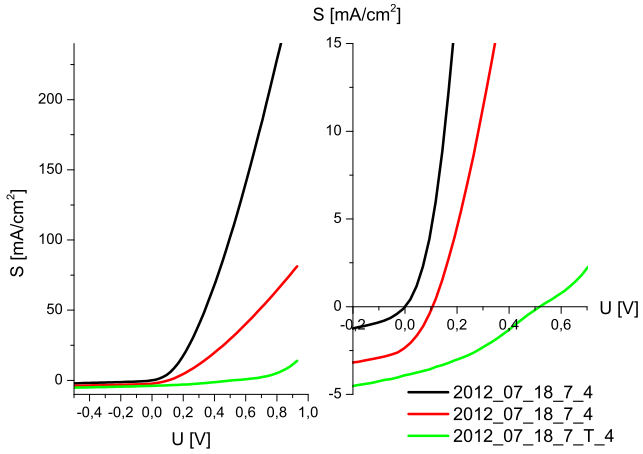

Fig. 6.15: P3HT:CNT:PCBM-C_{60} solar cell. The device architecture is ITO-Pedot:PSS-P3HT:CNT:PCBM-C_{60}-BPhen-Al. The thickness of the C_{60} layer is 60nm. Left: full graph of J-V characteristics, where black corresponds to dark, red represents under illumination, and green corresponds to illumination after thermal annealing. Right: magnification around the origin. The characteristic values are summarized in table 6.5.

sample		R_s [Ω]	R_{sh}[kΩ]	n	FF	J_{sc} $[mA/cm^2]$	V_{oc}[V]	η[%]
$C1_1$	as-is	187	14.37	2.79	0.33	-2.32	0.104	0.08
	annealed	359	15.61	4.61	0.33	-4.01	0.509	0.67
$C1_2$	as-is	622	21.10	4.46	0.26	-1.37	0.105	0.03
	annealed	460	21.48	4.71	0.32	-1.99	0.525	0.33
$C1_3$	as-is	401	12.82	2.79	0.31	-2.39	0.107	0.08
	annealed	284	18.34	4.94	0.32	-4.16	0.518	0.71
$C1_4$	as-is	213	13.80	3.11	0.32	-2.34	0.106	0.08
	annealed	70	9.74	6.01	0.34	-3.91	0.517	0.69

Tab. 6.5: Overview of the characteristic values of ITO-Pedot:PSS-P3HT:CNT:PCBM-C_{60}-BPhen-Al. samples. Tempering yields good results.

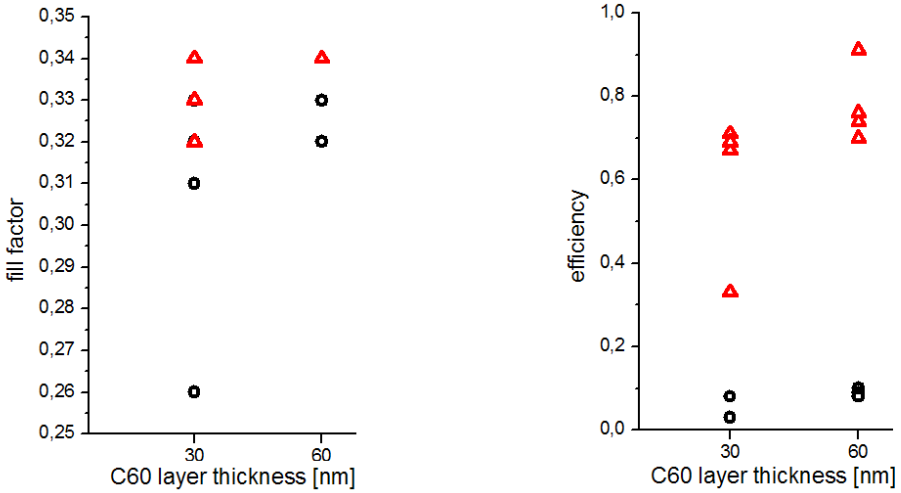

Fig. 6.16: Efficiencies and fill factors before and after thermal annealing of P3HT:CNT:PCBM-C_{60} solar cells(C1-C2). Thermal annealing significantly improved the device performances, if the solar cells contain a C_{60} layer.

6.2 CNTs in small molecule solar cells

Solution based organic solar cells with CuPc-TS were studied. The CuPc-TS showed a propensity to crystallize, which caused mash-grid like layers. Hence, the layers had to be spin coated. The forces due to the angular velocity cause the liquid to spread over the substrate, thus forming a thin layer right from the beginning of the spin process. This suppresses the mesh-grid formation and leads to the formation of films of high homogeneity. The layer thickness of the Pedot:PSS layer was 100nm. Also the layer thickness of the CuPc-TS:CNT blend layer was 100nm. The aluminium layer was

150nm thick. The layer thicknesses of these layers stood unchanged for all presented polymer solar cells. The CNT concentration was c=0.1mg/mL.

6.2.1 CuPc-TS:CNT

Functionalized SWCNTs were dispersed and added to the dye solution as explained in chapter 4.The solar cells produced with such mixtures showed similar properties. The band diagram of the following solar cells are shown in Figure 6.17.

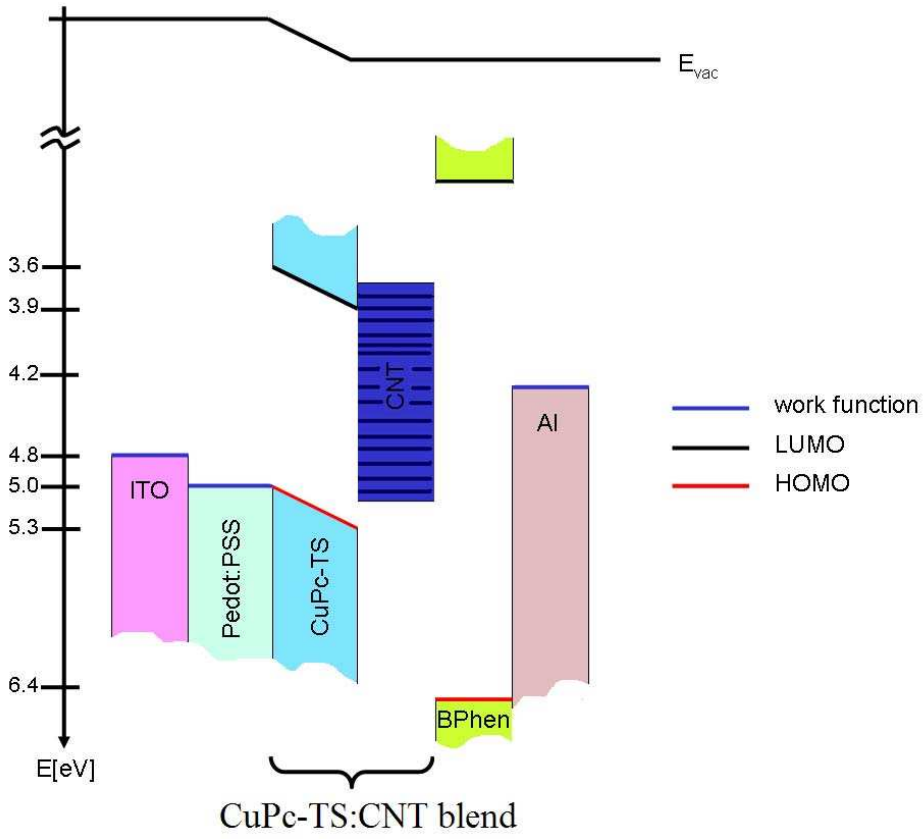

Fig. 6.17: Band diagram of the studied solar cells. The sample architecture consisted of ITO-Pedot:PSS-CuPc-TS:CNT-BPhen-Al. The work function of the CNTs is in the range from 3.75eV-4.8eV as reported by literature. The different energy levels of their work function are indicated by solid lines within the blue rectangle. The CuPc-TS:CNT blend is the active matrix.

sample		R_s [Ω]	R_{sh}[kΩ]	n	FF	J_{sc} [mA/cm^2]	V_{oc}[V]	η[%]
$E3_1$	as-is	190	18.59	4.91	0.24	-0.53	0.162	0.02
	annealed	525	45.32	4.60				
$E3_2$	as-is	205	13.52	4.73	0.21	-0.36	0.170	0.01
$E3_3$	as-is	231	14.78	3.41	0.22	-0.063	0.137	0.002
$E3_4$	as-is	145	14.88	4.36	0.24	-0.24	0.095	0.005

Tab. 6.6: Overview of the characteristic values of ITO-Pedot:PSS-CuPc-TS:CNT-BPhen-Al samples. Tempering destroyed most of the samples.

Thermal annealing yield bad J-V characteristics. Only one sample (shown in Figure 6.18) of this series of experiments yielded a J-V dependency after the annealing step. All other samples developed contact problems and could not be measured. The open circuit voltage for this one sample of $95mV < V_{OC} < 170mV$ is relatively low. The fill factor of 0.21<FF<0.24 is in agreement with the measured J-V dependency. Under illumination the photocurrent shows the significant influence of the series resistance. Nevertheless, the series resistances are in the range of $R_s = 145\Omega < R_s < R_s = 231\Omega$, which are quite good values for solar cells. The short circuit current density is small compared with the polymer cells. This implies that either the charge transfer state is restricted due to a poor match of the energy levels of the used materials, or recombination takes place.

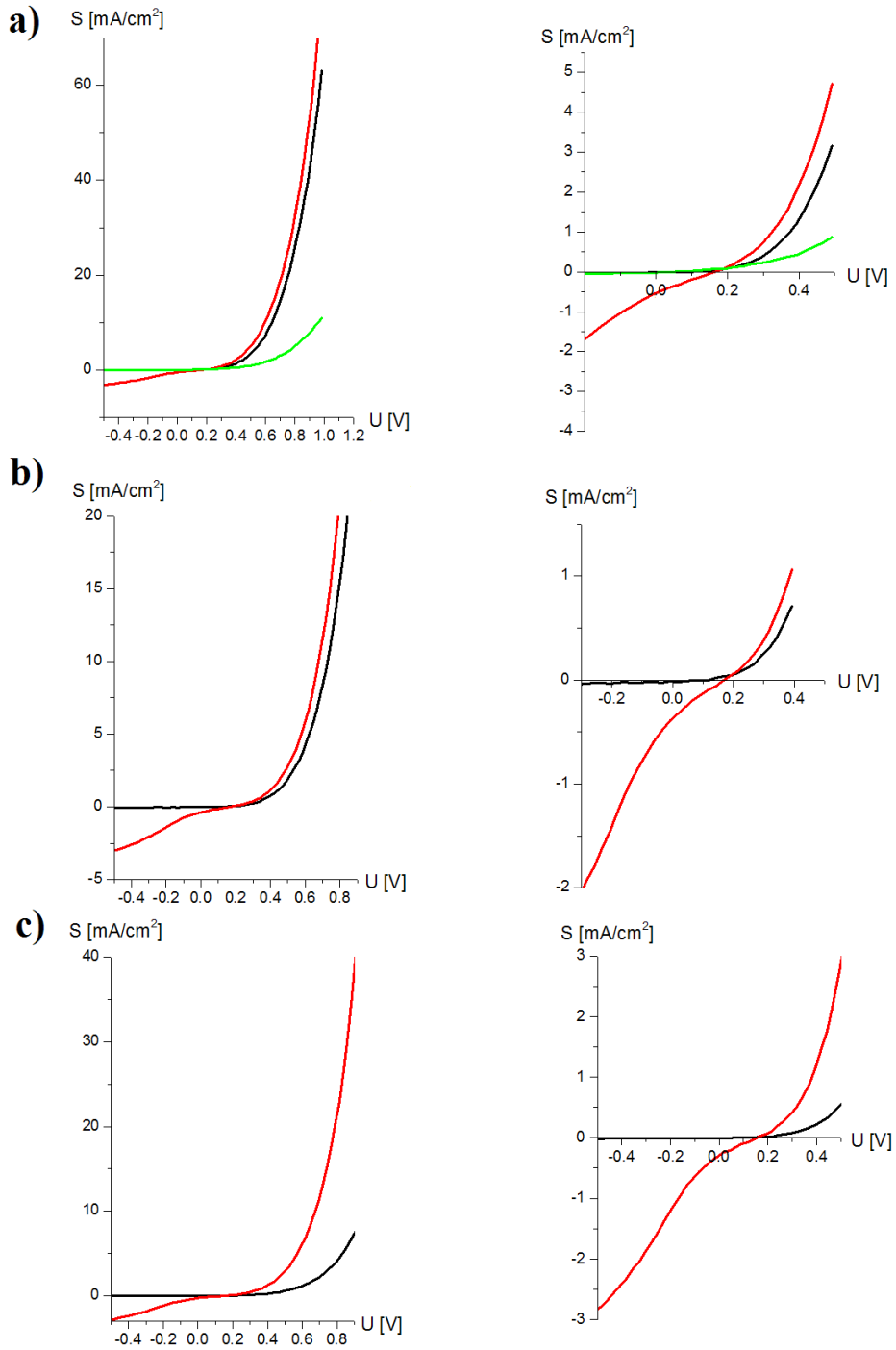

Fig. 6.18: CuPc-TS:CNT solar cells. CNTs are blended in the CuPc-TS layer. The device architecture consisted of ITO-Pedot:PSS-CuPc-TS:CNT-BPhen-Al. Left: full graph of J-V characteristics, where black corresponds to dark condition, red represents under illumination. Right: magnification around the origin. The characteristic values are summarized in table 6.6.

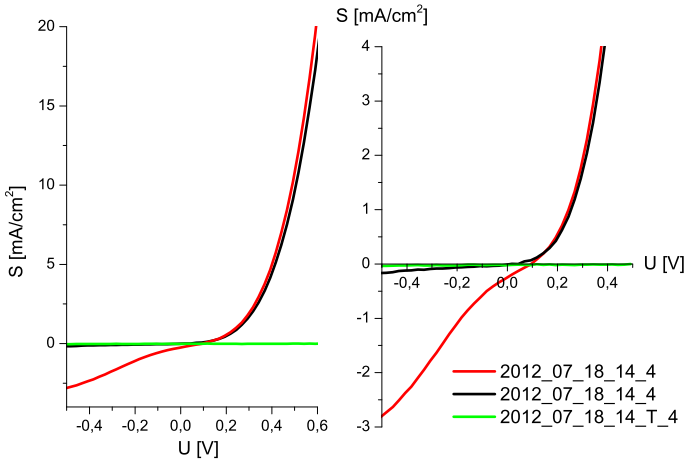

Fig. 6.19: CuPc-TS:CNT solar cell. The device architecture consisted of ITO-Pedot:PSS-CuPc-TS:CNT-BPhen-Al. Left: full graph of J-V characteristics, where black corresponds to dark, red represents under illumination and green corresponds to illumination after thermal annealing. Right: magnification around the origin. The characteristic values are: $V_{OC} = 0.095V$, $J_{SC} = -0.24mA/cm^2$, FF=0.24, $\eta = 0.005\%$, $R_s = 145\Omega$, $R_{sh} = 14886\Omega$, n=4.36.

6.2.2 CuPc-TS:CNT-C60

These samples had a 30nm thick C_{60} on top of the CuPc-TS:CNT composite layer used in the previous section. The C_{60} layer caused an upward leap of the short circuit current density to $J_{SC} = -1.66mA/cm^2$. This was a 400% increase compared with samples without the C_{60}. For these samples charge transfer is the most improved mechanism. The band diagram of the following solar cells are shown in Figure 6.20. In these samples the photocurrent

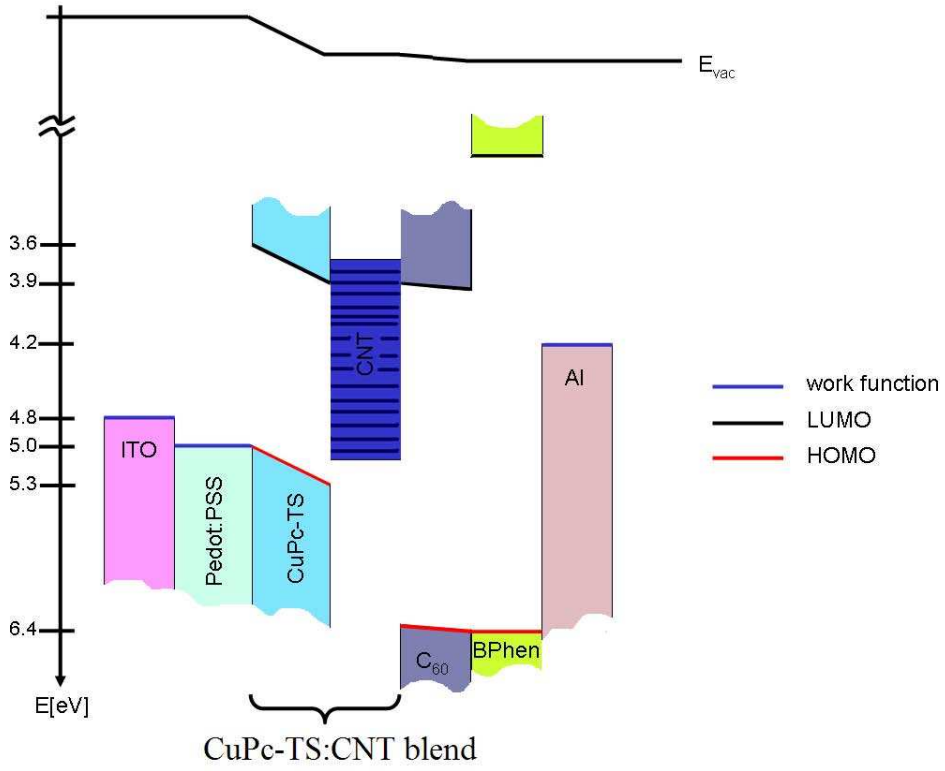

Fig. 6.20: Band diagram of the studied solar cells. The sample architecture consisted of ITO-Pedot:PSS-CuPc-TS:CNT-C_{60}-BPhen-Al. The work function of the CNTs is in the range from 3.75eV-4.8eV as reported by literature. The different energy levels of their work function are indicated by solid lines within the blue rectangle. The CuPc-TS:CNT blend covered with the C_{60} layer is the active matrix.

was influenced by series resistance, although the values were in the useful range of $R_s = 144\Omega < R_s < R_s = 144\Omega$. However, the open circuit voltage was almost in the same range of the samples without a C_{60} layer. The diode ideality factor is also in the same range of 3.9<n<5.10 as the sample without this layer, which can be attributed to the resistance influence in the J-V dependency. The fill factor stayed below FF=0.3, which implies that the C_{60} layer enhances the short circuit current density. However, from the

sample		R_s [Ω]	R_{sh}[kΩ]	n	FF	J_{sc} $[mA/cm^2]$	V_{oc}[V]	η[%]
$E2_1$	as-is	194	12.10	3.90	0.25	-1.66	0.210	0.09
$E2_2$	as-is	154	15.80	5.00	0.24	-1.05	0.165	0.04
$E2_3$	as-is	144	16.56	4.88	0.23	-0.96	0.151	0.03
$E2_4$	as-is	153	12.01	4.37	0.26	-0.65	0.108	0.01
	annealed	559	24.72	5.10				

Tab. 6.7: Overview of the characteristic values of ITO-Pedot:PSS-CuPc-TS:CNT-C_{60}-BPhen-Al samples. The thickness of the C_{60} layer is 30nm. Tempering destroyed most of the samples.

measurements it is clear that the current density-voltage dependencies are dominated by the CuPc-TS:CNT blend. This is seen clearly when Figures 6.18-6.19 are compared with Figures 6.21-6.22. Another possible explanation of the J-V dependencies of the small molecule solar cells takes traps into account. In general, every trap can function as a recombination centre for charge carriers. However, whether this occurs depends on the relevant time constants for recombination and detraping. If the detraping time is shorter than the recombination time, detrapping of the temporarily trapped charge carriers takes place. These charge carriers are once more part of the photocurrent of the device. On the other hand, if the recombination time is shorter than the detrapping time, the trapped charge carriers recombine and are lost from the photocurrent. Therefore, traps working as recombination centres have the most detrimental influence of all traps on the device performance.
The influence of trapped charge carriers on the built-in field of an organic solar cell device mainly is not field weakening, because a certain amount of trapped charges have to exist. Organic solar cell layers are usually of a thickness of 100nm to 200nm, which is simply too thin to place enough traps in for an effective weakening of the field. So the weakening of the built-in field takes place over the whole organic semiconductor layer.
Field weakening can occur when the ambivalent current flow of holes and electrons are not balanced. This happens when the mobility of the different charge carriers significantly differ from each other, or when the injection barriers at the respective electrodes are not balanced causing one type of charge carrier to be favourably injected into the electrode. Consequently, one type of charge carrier accumulates in the bulk semi-conductor material at the interface of the other (non-injecting) electrode. Depending on the height of the injection barrier, the built-in field can be significantly weakened resulting in a small device photocurrent. Thus the photocurrent is a SCLC due these "parked" charge carriers.
The CuPc-TS exists as an ion when dissolved in distilled water. The sodium on the molecule is positively charged in the liquid. When the layer of

sample		R_s [Ω]	R_{sh}[kΩ]	n	FF	J_{sc} $[mA/cm^2]$	V_{oc}[V]	η[%]
$E1_1$	as-is	71	25.21	3.36	0.30	-3.20	0.210	0.2
$E1_2$	as-is	88	16.33	3.09	0.27	-2.43	0.160	0.1
$E1_3$	as-is	112	17.18	4.10	0.28	-1.52	0.116	0.04
$E1_4$	as-is	545	19.09	6.37	0.28	-0.90	0.093	0.02

Tab. 6.8: Overview of the characteristic values of ITO-Pedot:PSS-CuPc-TS:CNT-C_{60}-BPhen-Al samples. Tempering destroyed the samples.

CuPc-TS is spin-coated onto the substrate, the ionized sodium stays within the layer. As sodium has an ionization potential of 5.14eV the sodium will easily attract one electron from the CuPc, as its HOMO level is around 5.2eV. Therefore, the CuPc is positively ionized in the bulk. The ionized sodium acts as a p-dopant, which is favourable for the donor layer.
The J-V curve can be interpreted in terms of the Poole-Frenkel effect, as the log(J) versus $\sqrt{V}$ dependency in the third and fourth quadrants is linear, [65]. This linear dependency of the logarithm of the current density versus the square root of the voltage is shown in Figure 6.23. The Pool-Frenkel effect is a bulk related mechanism in which a field assisted thermal detrapping of the carriers take place. The next series of experiments include a 60nm thick C_{60} layer.

6.3 Impact of CNTs on the presented organic solar cells

The solar cells which contain CNTs in the active matrix tend to show better initial device performance after deposition. For such solar cells a post deposition treatment such as thermal annealing was shown to only be effective for one series of samples. Efficiencies of $\eta = 0.6\%$ were reached after thermal annealing. CNTs were added to both solar cells based on small molecules and polymers. An overview of the averaged measured parameters of the different solar cell combinations are shown in Table 6.9 and Table 6.10.

6.3.1 Impact of CNTs on small molecule solar cells

Solar cells consisting of either CuPc-TS or a CuPc-TS:CNT blend layer were compared. In some cases a C_{60} layer was deposited onto the CuPc-TS or CuPc-TS:CNT blend layer.
The efficiency for devices which included CNTs increased were four times larger than devices without CNTs or a C_{60} layer. The FF for these devices was 1.6 times larger for the samples which included CNTs. The FF for devices was largely unchanged with the deposition of a C_{60} layer of 30nm or 60nm thickness onto the CuPc-TS or CuPc-TS:CNT blend layer. The efficiency for devices with a 30nm C_{60} layer and CNTs was 15.5 times larger than for devices without CNTs. The efficiency for devices with a 60nm C_{60}

c_{60}	post treatment	CuPc-TS		CuPc-TS:f-CNT	
		η	FF	η	FF
0nm	as-is	0.00225	0.1425	0.00925	0.2275
	annealed	-	-	-	-
30nm	as-is	0.00275	0.24	0.0425	0.2425
	annealed	0.0001	0.36	-	-
60nm	as-is	0.0295	0.285	0.09	0.2825
	annealed	$5.6{\cdot}10^{-6}$	0.233	-	-

Tab. 6.9: Overview of the efficiencies (η) and FF of the various solar cells consisting of small molecules, CuPc-TS as absorber material fabricated in this work. The impact of the CNTs on the device performance can be seen in this data. The CNTs yield an increase of the efficiency of the as-prepared samples compared to the same samples without CNTs.

c_{60}	post treatment	P3HT:CNT		P3HT:PCBM		P3HT:CNT:PCBM	
		η	FF	η	FF	η	FF
0nm	as-is	0.02675	0.3125	0.017	0.29	-	-
	annealed	-	-	0.056	0.2375	-	-
30nm	as-is	0.1525	0.33	0.083	0.323	0.09	0.325
	annealed	-	-	0.78	0.42	0.7775	0.34
60nm	as-is	0.1375	0.345	-	-	0.0675	0.305
	annealed	0.63	0.3575	-	-	0.6	0.3275

Tab. 6.10: Overview of the efficiencies (η) and FF of the various solar cells with the polymer P3HT as absorber material fabricated in this work. The impact of the CNTs on the device performance can be seen in this data. Like the samples having small molecules as absorbing material, for polymer solar cells the CNTs yield an increase of the efficiency of the as-prepared samples compared to the same samples without CNTs.

layer increased 3 times if CNTs were blended in the CuPc-TS layer in comparison to devices without CNTs.
The larger efficiencies for solar cells with blended CNTs in the CuPc-TS layer can be linked to the enhanced charge carrier transport properties in the CuPc-TS layer. This enhancement decreases the resistances for charge carriers travelling in the dye layer towards the outer electrodes. In addition, an increase of the efficiency is derived from the enhanced exciton dissociation at the CNT-CuPc-TS interface, which caused an increase in the photo-generated short circuit current density, J_{sc}. The averaged short circuit current density increased from $J_{sc} = 0.3225 ma/cm^2$ for devices without CNTs to $J_{sc} = 0.78 ma/cm^2$ for devices including CNTs. This is a 2.4 times increase of the short circuit current density.

6.3.2 Impact of CNTs on polymer solar cells

Devices with a P3HT:CNT blend layer were compared with devices consisting of a P3HT:CNT:PCBM blend layer. These devices had either no C_{60} layer or a C_{60} layer that was 30nm or 60nm thick. For devices without a C_{60} layer the as deposited efficiency tended to be 1.6 times larger for the devices containing CNTs compared to the devices containing no CNTs . Thermal annealing increased the efficiency of the devices containing PCBM to $\eta = 0.056\%$, which was twice as high as the efficiency of the devices containing CNTs before the thermal annealing treatment. Thermal annealing destroyed these devices. The measured fill factor of FF $\approx$ 0.33 was approximately the same for all samples (samples with or without CNTs). The fill factor for devices with a 30nm C_{60} layer was approximately the same for samples with or without CNTs as long as these samples were not thermal annealed. The efficiency of devices containing CNTs was shown to be 1.7-1.8 times larger compared to devices containing no CNTs. After the thermal annealing treatment devices containing PCBM reached efficiencies of $\eta = 0.78\%$. This is 5.1 times higher than the initial efficiency of the sample containing CNTs. The fill factor for devices made of P3HT:PCBM reached FF=0.42. This was the highest averaged value for the fill factor of all series of experiments. The fill factor for devices containing a 60nm C_{60} layer stayed roughly constant for all samples before and after the thermal annealing treatment. For the device with this thicker C_{60} layer, the fill factor for samples containing CNTs reached FF=0.35 and samples without CNTs reached fill factors of FF=0.3-FF=0.32. The last series of experiments showed that samples containing PCBM and/or CNTs reach similar efficiencies after a thermal annealing treatment. The results can be explained by morphology changes in the photovoltaic active matrix, as the experimental conditions were the same for all samples. CNTs show to have as good acceptor properties for exciton dissociation as PCBM shows to have.

6.4 Summary

In this chapter organic solar cells containing carbon nanotubes have been fabricated. The absorber materials either were small molecules or polymers. Blends of CNT and P3HT, CNT with P3HT and PCBM as well as CNT and CuPc-TS were investigated. These blends form different device architectures. The device architectures studied were bulk-heterojunction and a combination of a bulk-heterojunction and heterojunction. The latter both (e.g., P3HT and CNT or CuPc-TS and CNT blend (forming the bulk-heterojunction) covered with a layer of C_{60} (forming the heterojunction) yield the BHJ-HJ architecture). The J-V curve show different curve shapes after thermal annealing. For some devices the efficiency increase due to thermal annealing. Other devices were destroyed due to annealing. However, the applied thermal treatment was identical for all devices. Efficiencies of $0.001 < \eta < 1\%$ were achieved. The achieved efficiencies and fill factors were summarized. The impact of CNTs on the fill factors and the efficiencies of the devices is presented in detail.

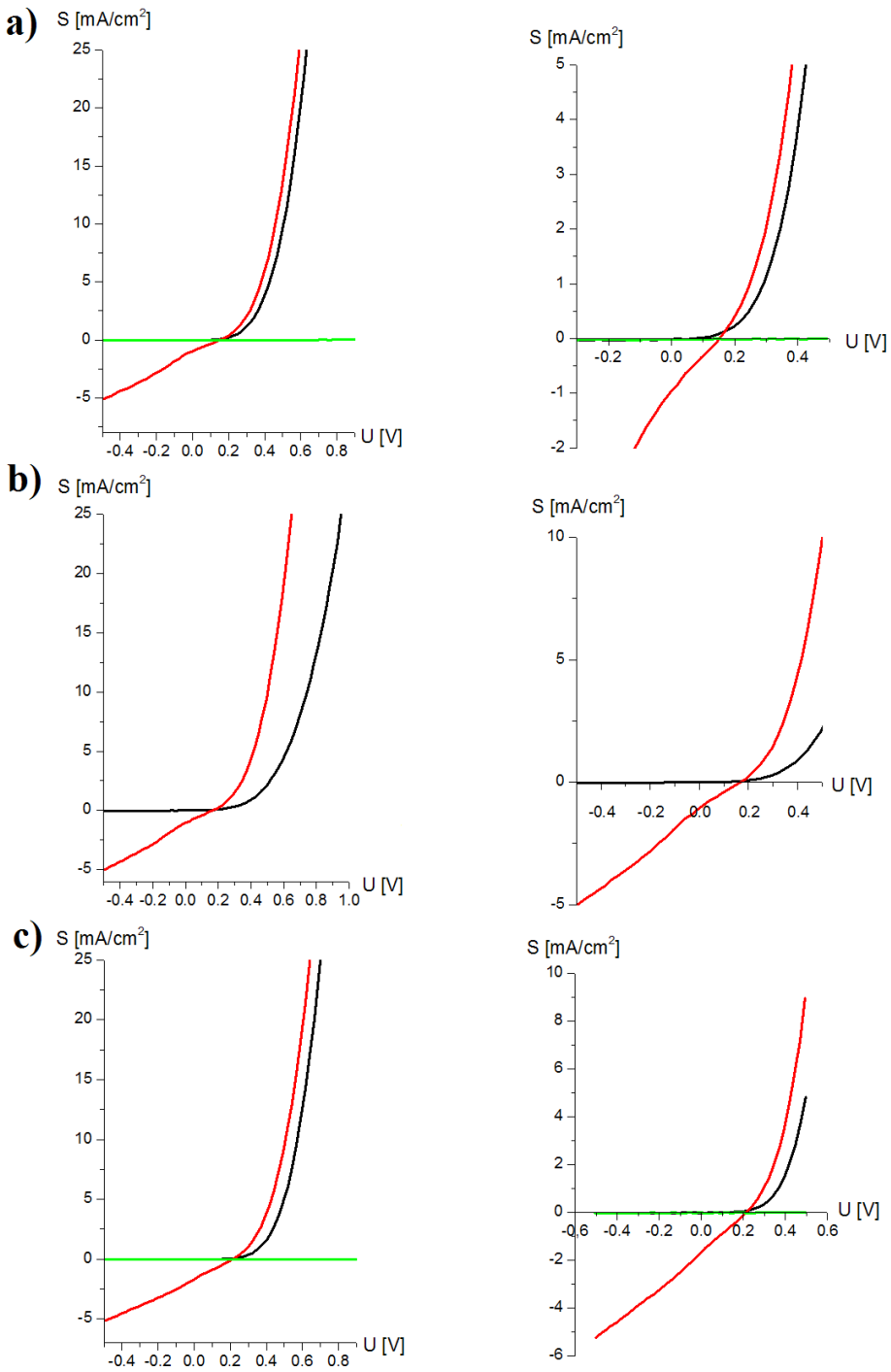

Fig. 6.21: CuPc-TS:CNT-C_{60} solar cell. The thickness of the C_{60} layer is 30nm. The device architecture is ITO-Pedot:PSS-CuPc-TS:CNT-C_{60}-BPhen-Al. Left: full graph of J-V characteristics, where black corresponds to dark condition, red represents under illumination. Right: magnification around the origin. The characteristic values are summarized in table 6.7.

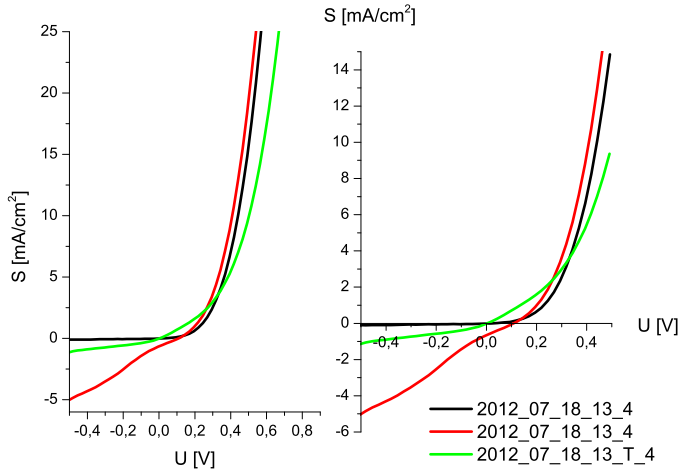

Fig. 6.22: CuPc-TS:CNT-C_{60} solar cell. The device architecture is ITO-Pedot:PSS-CuPc-TS:CNT-C_{60}-BPhen-Al.The thickness of the C_{60} layer is 30nm. Left: full graph of J-V characteristics, where black corresponds to dark, red represents under illumination and green corresponds to illumination after thermal annealing. Right: magnification around the origin. The characteristic values are summarized in table 6.7. After thermal annealing the values are: $R_s = 559\Omega$, $R_{sh} = 24724\Omega$, n=5.10. After annealing the device works as diode without a Photocurrent (J_{sc} is of positive integer).

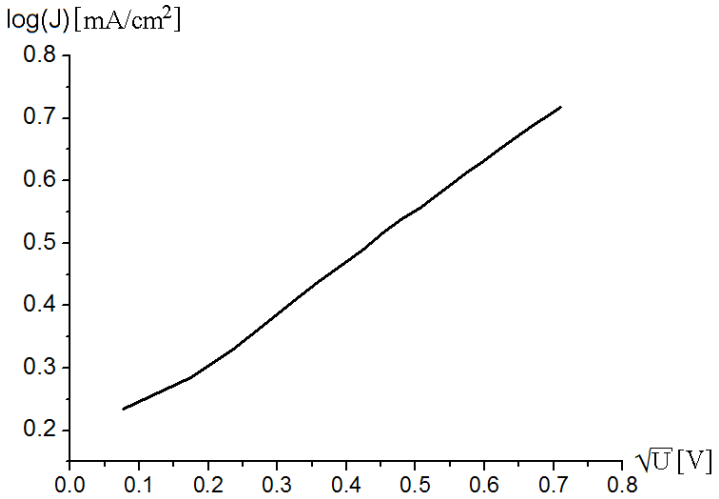

Fig. 6.23: J-V characteristic of sample shown in Figure 6.21 a). First absolute values were calculated then the graph was plotted. The log(J) versus $\sqrt{U}$ graph corresponds to the original voltage range from -0.5V-0V.

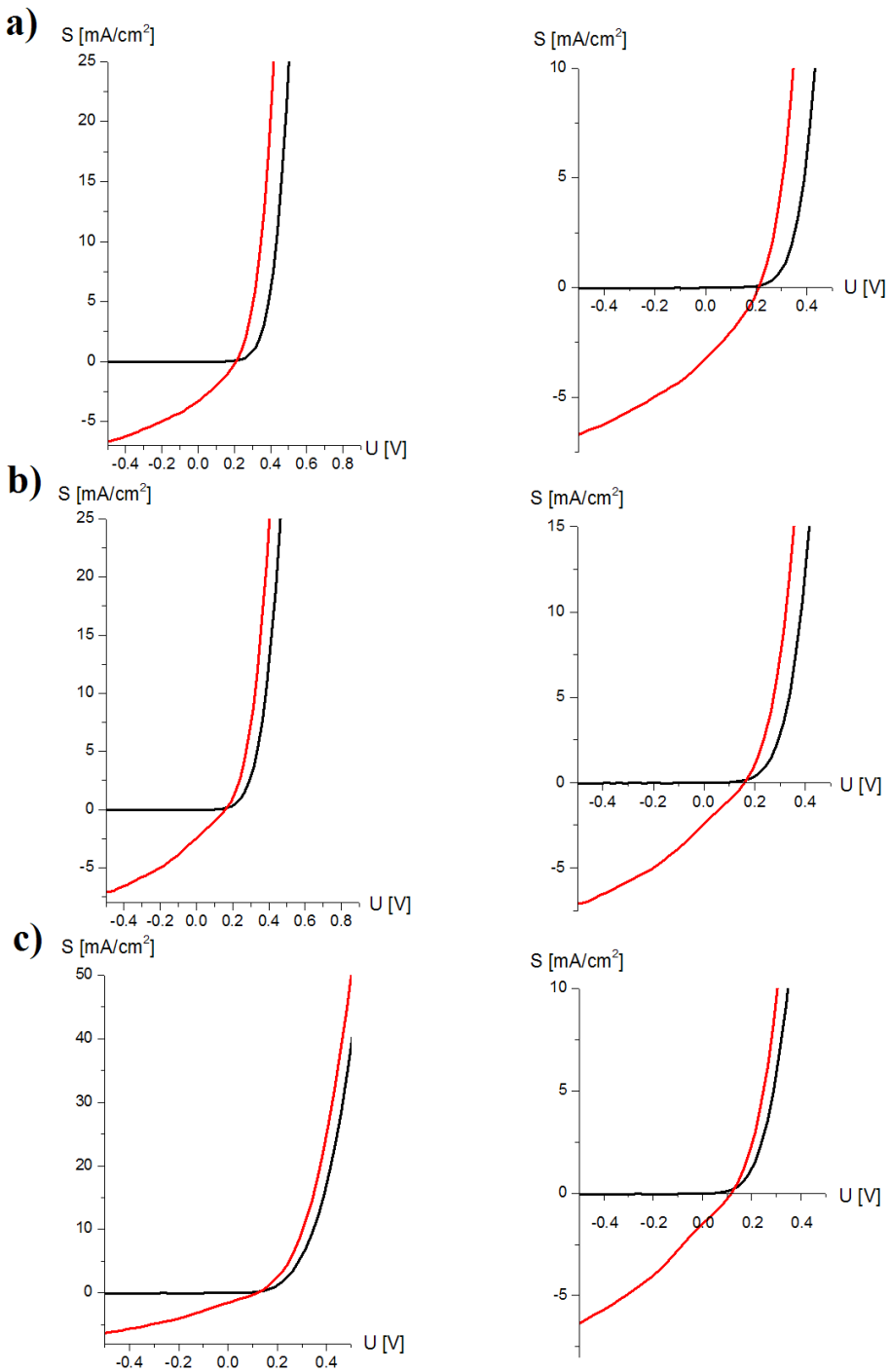

Fig. 6.24: CuPc-TS:CNT-C_{60} solar cell. The thickness of the C_{60} layer is 60nm. The device architecture is ITO-Pedot:PSS-CuPc-TS:CNT-C_{60}-BPhen-Al. Left: full graph of J-V characteristics, where black corresponds to dark condition, red represents under illumination. Right: magnification around the origin. The characteristic values are summarized in table 6.8.

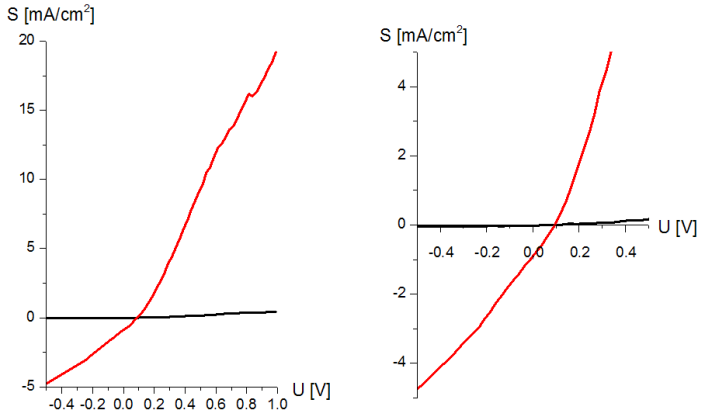

Fig. 6.25: CuPc-TS:CNT-C_{60} solar cell. The thickness of the C_{60} layer is 60nm. The device architecture is ITO-Pedot:PSS-CuPc-TS:CNT-C_{60}-BPhen-Al. Left: full graph of J-V characteristics, where black corresponds to dark condition, red represents under illumination. Right: magnification around the origin. The characteristic values are summarized in table 6.8.

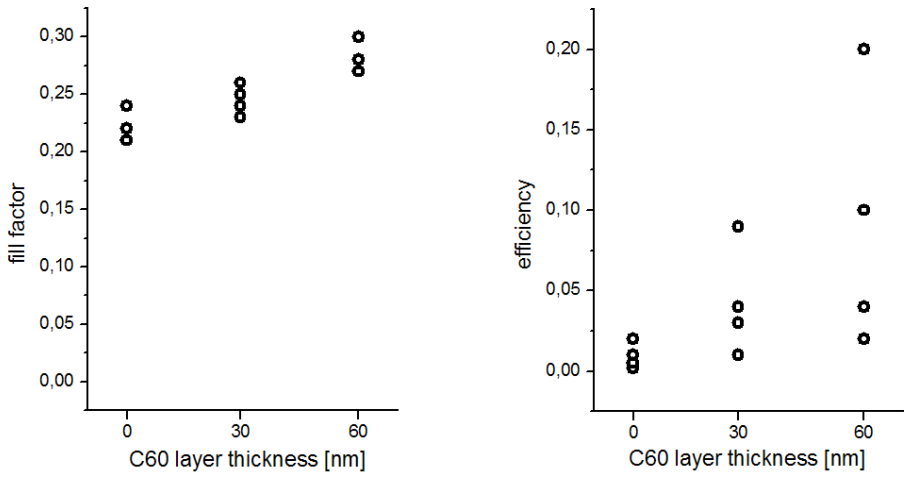

Fig. 6.26: Efficiencies and fill factors of the devices containing either CuPc-TS:CNT or CuPc-TS:CNT-C_{60} (E1-E3). The thicknesses of the C_{60} layer were either 30nm or 60nm.

7. VERTICALLY ALIGNED CARBON NANOTUBE SOLAR CELLS

Organic solar cell device architecture has been attracting much interest recently in the field of organic bulk-heterojunctions, in which the donor and acceptor material is blended within one layer. Such a structure enables exciton dissociation to occur over the whole active matrix (in contrast to a common heterojunction solar cell structure), because the average distance between a donor and acceptor molecule is less than the exciton diffusion length of ≈10nm. After the dissociation process the charge carriers hop in their respective n- or p-layer towards the electrodes along percolation paths. These pathways are in most case randomly distributed in the layer. A thermal annealing treatment after the deposition of the layers enables crystal growth in the organic materials and increases the nano-crystallinity of the morphology. In addition, phase separation of the donor and acceptor material takes place and the nano crystals are randomly distributed in the layer. Charge transportation is much better in a crystalline grain due to the stronger overlap of the molecular orbitals, however, if the number of grain boundaries increases the conductivity of the layers decreases, due to the significant resistive contribution caused by the grain boundary interfaces [242]. Therefore, two important challenges have to be addressed during the morphology optimization process driven by the thermal annealing treatment:

- the grain orientation has to be aligned along the built-in electric field direction in order to achieve optimized charge carrier transport and
- the grain size should be ideally comparable with the layer thickness in order to avoid grain boundary interface resistances in the absorber layer.

An electrode constructed from a vertically aligned carbon nanotube forest (see Figure 7.1) can be used to solve this challenge, at least for one type of charge carrier of the ambivalent current flow in the device if the blend is embedded in the forest. The va-CNT arrays used in this thesis were grown in the FHG-Fraunhofer Institute for Ceramic Systems and Technology (IKTS), Dresden. The separation of the nanotubes was about 10nm-40nm, which means the charge carriers would have to cover a distance of 5nm-20nm before reaching a nanotube. The nanotube array was synthesized by a pe-CVD technique. In this process the length of the tubes can reach up to tens of

microns. The nanotubes were grown on a 150nm TiN layer, which has a metallic conductivity of $5 \cdot 10^5 S/m$.

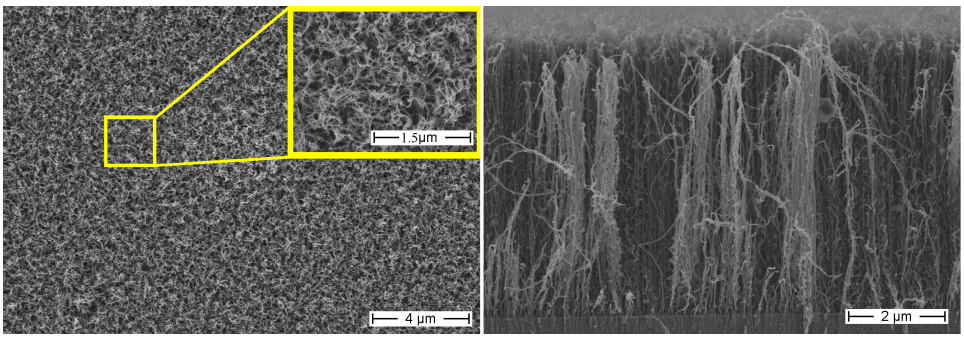

Fig. 7.1: va-CNT forest. Left: top-view, right: cross-section.

7.1 Fabrication

The va-CNT forest is supported by Dr. Endler from the IKTS, Dresden. Silicon wafers (thickness: $500\mu m$)served as the substrates for the production of aligned carbon nanotube films <100>, On top of these a TiN layer (150nm) was deposited directly onto the silicon by physical vapour deposition (PVD), explicitly via magnetron sputtering. For the nanotube growth iron particles were used as the catalyst. The particles were deposited by pulsed laser deposition. The synthesis of the wires was made using a pe-CVD tool which included a horizontal quartz tube (diameter 75mm). For the synthesis of the tubes the substrates were heated-up in a mixture of H_2 and Argon. Once the temperature had stabilized at the reaction temperature of 750°C, methane was introduced into the reaction chamber. Methane starts the CNT growth process, which was done at atmospheric pressure. A mixture of carbon source gas (methane) and the carrier gases (H_2 and Argon) was used. The volume ratio between methane and the carrier gases was fixed to 1:16. After a deposition time of 20 minutes, the gas flows were turned off. Subsequently, the samples were cooled down under an argon atmosphere. The arrays produced by this method consisted of SWCNTs and MWCNTs. Their presence was established by making Raman measurements (see Figure 7.2).
Iron is used as the CNT growth catalyst. The catalyst layer of 3nm thickness is deposited under high vacuum by magnetron sputtering. The forests were synthesized by pe-CVD. In this process the chamber is evacuated to $10^{-7} mbar$ and the substrate is heated up to $700°C$-$750°C$. The process gases are hydrogen (H_2), ethene (C_2H_2) and argon (Ar). The va-CNT growth rate is non linear. In the first 70s time interval of synthesis no CNT growth takes place. The first 70s are a process dead-time, t_{dead}. After a total synthesis time of $t_{synthesis} = 80s$ va-CNT with a height of 800nm to $1{,}2\mu m$ were syn-

thesized. This high sensitivity to the synthesis time is due to the 150nm TiN layer. This can be assumed by synthesis results of va-CNT growth on Al_2O_3. The va-CNTs grown on Al_2O_3 do not show this non-linear high sensitive dependency of synthesis time and CNT length.
Samples of va-CNTs grown on an Al_2O_3 buffer layer do not show this strong nonlinear growth behaviour. By replacing the TiN layer with an Al_2O_3 layer allows a controlled synthesis of va-CNT layer thickness in the range of 200nm is possible. This second va-CNT growth possibility is based on a $500\mu m$ silicon wafer , coated with a 200nm aluminium oxide layer with a 3nm iron layer on top. This route enables the synthesis of va-CNTs with the required height but the aluminium oxide layer restricts this design for electrical applications. Approaches used to strip away the infiltrated va-CNTs from the wafer, for the purpose of the thermal evaporation of the electrode on the bottom of the removed infiltrated va-CNT, often damage the layer.
The va-CNTs had a mass density of $\approx 0.03g \cdot cm^{-3}$ an open volume around

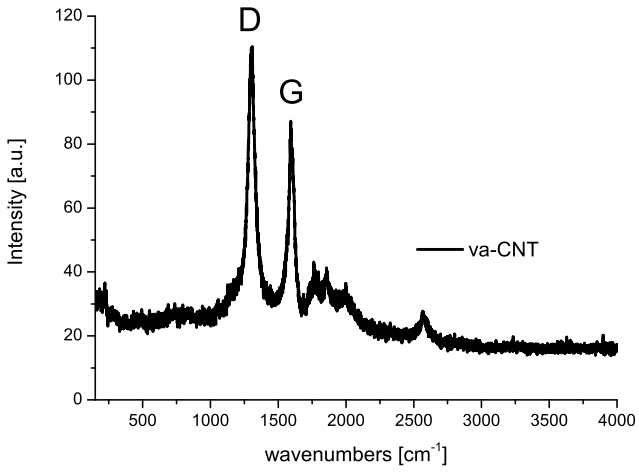

Fig. 7.2: Raman spectra of va-CNT. The D- and G-bands clearly identify the CNTs. The increase of the signal around $250cm^{-1}$ indicate the presents of SWCNTs on the va-CNT array.

the tubes of around 90%. Slight variations of the process parameters during the pe-CVD synthesis of the va-CNT samples yielded differences between the va-CNT samples. These variations, however, were not optically visible. Thus, AFM measurements were needed in order to prove these differences in sample homogeneity. An AFM image of such samples is shown in Figure 7.3. The surface roughness, R_{ms}, is R_{ms}=0.105μm. The height profiles prove inhomogeneous CNT length across the substrate. The va-CNT array has regions with super-long CNT bundles sticking out, or vice versa, the array exhibits regions with super-short CNT. These regions appear as "holes"

in the top view of the CNT forest. Mostly hole free samples of comparable quality to the one shown in the Figure 7.3 were used were used for all subsequent studies. The TiN layer has to fulfill two requirements

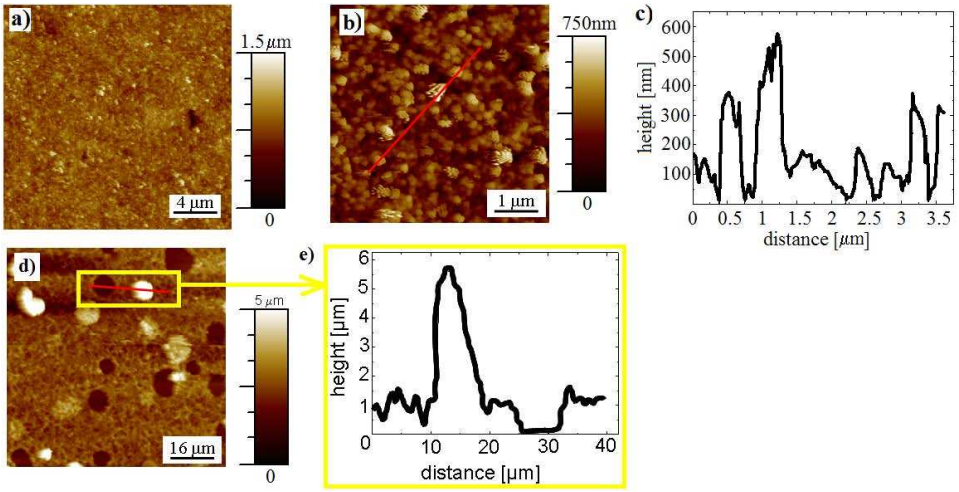

Fig. 7.3: a) AFM image of a "good" CNT array, its surface roughness is R_{ms}=0.105μm. b) magnification of a). c) corresponding height profile from b). d) "poor" samples. Their surface roughness is 0.65 μm. At particular locations either holes exist or super-long bundles stick out above the surface. The average CNT length here is around 1μm; e) corresponding height profile of va-CNT array along marked line in d). Images d) and e) taken from [143].

- the layer has to be electrically conductive, and
- the layer has to act as a diffusion barrier for catalyst materials of the CNT synthesis.

This is necessary in order to get all va-CNTs electrically connected with the bottom electrode (TiN layer) and to suppress a diffusion of the CNT growth catalysts (usually nickel or iron) into the silicon wafer. The TiN layer has different resistances over the wafer size. This can be caused by either local variations of the process parameters during synthesis yielding a variation in the ratio of titanium and nitrite within the TiN layer or by a variation in the thickness of the TiN layer over the substrate. The TiN layer was electrically characterized by using the 4-point contact arrangement shown in Scheme 7.4. The electrodes were arranged in-line or with a quadratic geometry. The measurements were then compared with each other. The electrical measurements and calculated resistances are shown in Figure 7.5. The location of each measurement on the substrate is shown in Figure 7.6.

Route towards va-CNT solar cells

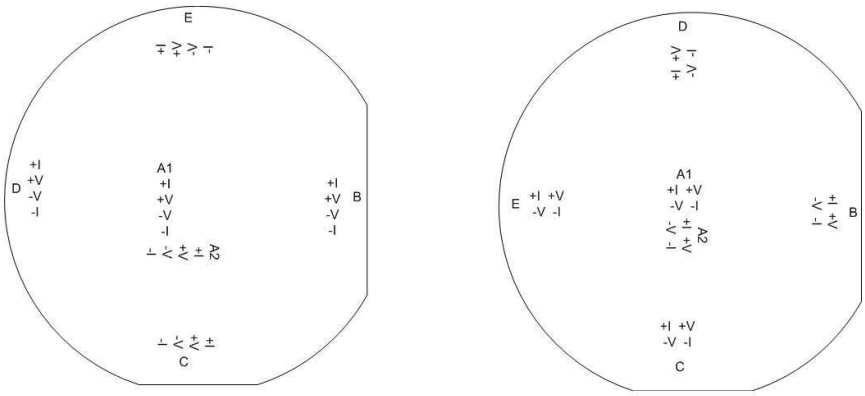

Fig. 7.4: The TiN layer was investigated on five different parts in order to investigate the homogeneity of the resistivity over the wafer.

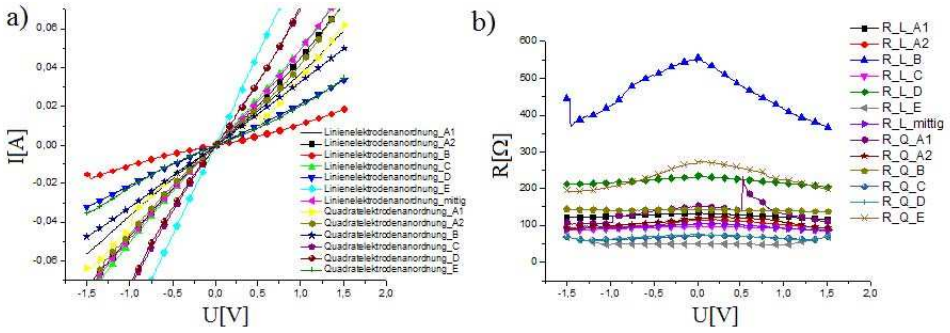

Fig. 7.5: Electrical measurements and calculated resistances. a) I-V characteristics of TiN layer measured by 4-point method with two different electrode geometries. b) resistances of the TiN layer. Values vary more than 100%.

Once the va-CNT has been synthesized it should be purified in order to remove carbonaceous impurities and the growth catalysts. This is necessary as the performance of organic solar cells is highly sensitive to the impurities. In addition, the layer thickness is crucial for device performance. Consequently, precise tailoring of va-CNT array height is important. This can be achieved by using different techniques such as an oxygen plasma treatment and an rapid thermal annealing (RTA) treatment. The CNTs also can be functionalized by the method of gas phase fluorination in a NF_3-plasma. This enlarges the bandgap of the CNTs and decrease their work function [243]. An expected benefit of such a process is enhanced solar cell performance. Subsequently, the array can be infiltrated with a dye which was done by liquid phase wetting. The OSC based on the va-CNT forest had the following layer ordering: 500μm silicon wafer - 150nm TiN - 1,3μm va-CNT - 150nm

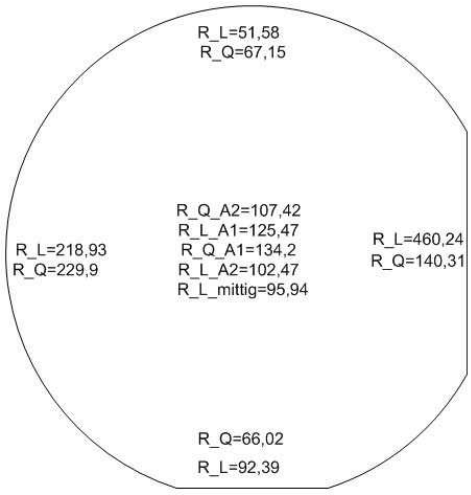

Fig. 7.6: Resistances of the TiN layer. Values vary over the wafer.

to 500nm dye cover layer - Pedot:PSS (see Figure 7.7). This architecture is classified as an inverted OSC design. The cathode of this device is the TiN layer at the bottom and the anode is the Pedot:PSS layer on top of the device. The generated excitons are dissociated at the donor-acceptor interface and the positive charge carriers hop to the Pedot:PSS layer whilst the electrons are transported along the CNT sidewall towards the TiN layer. In order to avoid electrical shorts during the electrical characterization under the sun equivalent source (air mass 1.5 (AM1.5)) the edge of the infiltrated substrate was dipped into resin before the Pedot:PSS layer was deposited onto it (see Scheme 7.7).

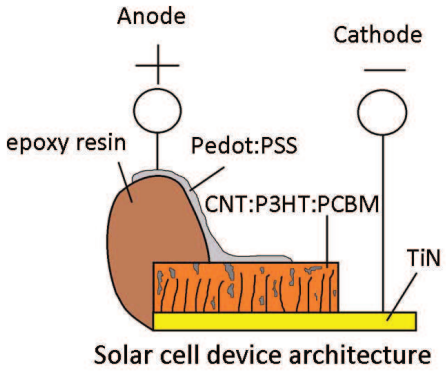

Fig. 7.7: Scheme of the 3D organic solar cell used in the electrical characterization measurements. Image taken from [244].

7.2 Purification

The used CVD synthesis method involved a catalyst-assisted decomposition of ethene in the presence of helium carrier gas and the growth of the CNTs by iron catalyst (as transition metal) at a temperature of 750°C. Although the CVD method has the advantage that vertically aligned tubes can be synthesized, it has the drawback that it causes a high defect density in the obtained CNTs. The cause of this is the low synthesis temperature in comparison with arc discharge and laser ablation which produce CNTs with less defects. The typical SWCNT content in as-prepared samples by CVD is ≈30–50 $wt\%$ for synthesis optimized for SWCNT growth. The content of MWCNTs is in the range of ≈30–99 $wt\%$ depending on their diameters, if the synthesis is optimized for MWCNTs growth. Usually CNT are purified using liquid acids, sonication, or thermal treatments [245]. The CNT tips can be opened, [246], and closed again [247]. The application of a smooth thermal annealing reduces the number of defects of the CNT.

7.2.1 Liquid Phase purification

For the va-CNT forest a treatment with liquid acids will destroy the vertical alignment of the CNTs over all the sample, as can be seen in Figure 7.8. When a va-CNT comes into contact with a liquid, two different physical

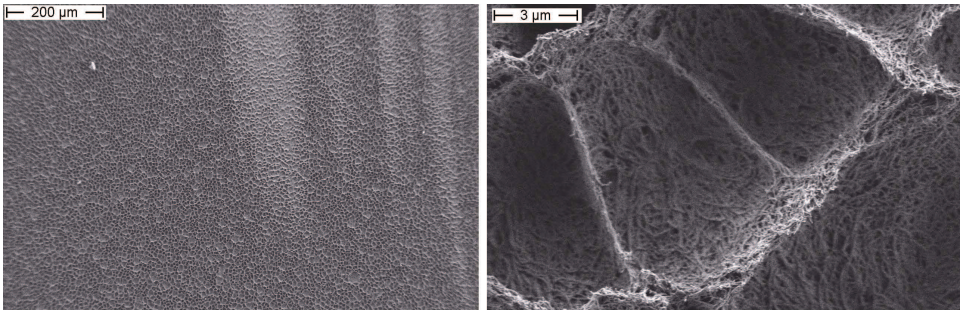

Fig. 7.8: Wetted va-CNT forest. Left: overview, right: magnified excerpt from image given on the left hand side.

phenomena can occur:

- due to unfavourable surface tension the lotus effect appears, or
- wetting takes place and the liquid infiltrates the pores of the va-CNT forest. forest.

Both phenomena can be described by Young's law

$$cos\theta = (\sigma_s - \sigma_{ls})/\sigma_l, \tag{7.1}$$

where σ_s, σ_{ls} and σ_l are the surface energy, interfacial tension, and the surface tension, respectively.

Electrochemical oxidation by cyclic voltammetry

Electrochemical oxidation is selective towards defects on a surface. The production process generally results in the CNTs having fewer defects than the carbonaceous impurities. Consequently, these impurities are much more quickly oxidized than the CNTs. It can be, therefore, assumed that CNTs have a higher electrochemical resistance than the impurities. If the solution used for the cyclic voltametry is acidic, the CNT tips can be opened, which exposes the metal catalyst to the acid solution. This allows the metal to be dissolved by the acid. All liquid phase purification methods will destroy the alignment, if no further innovative drying step is used. For example, if the array is kept in a wetting liquid the alignment is preserved. Because no meniscus is formed between the liquid and the CNT and hence, no driving force generated, which leads to a collapse of the CNTs. This was approach was taken by [248]. The cyclic voltammetry bath contains 57% H_2SO_4. The electrochemical treatment was made for 20s at 1mA current at room temperature. Afterwards, the purified CNT array was washed several times with distilled water and ethanol. Subsequently, it was quickly put into a autoclave filled with ethanol. The ethanol was then replaced with liquid CO_2 until the residual ethanol was at or below the 10ppm level. This was followed by an increase of the temperature of the autoclave to $45°C$ over 2h. The pressure in the autoclave reached about 100bar during the processing. This conditions was maintained for 3h. Finally, by decreasing the pressure to atmospheric pressure whilst keeping the temperature at 45°C the CO_2 was transformed to the gas phase [248]. Figure 7.9 shows the MWCNTs after this purification treatment.

7.2.2 Gas phase purification

Gas phase based purification methods were applied in order to preserve the va-CNT alignment in the purification process as well as transform the impurities into the gas phase. SWCNTs and MWCNTs differ with regard to their oxidation activity for two reasons: one is the larger curvature of the graphene sheet in the SWCNT; the other reason is metal impurities catalyze low-temperature oxidation of carbon (and SWCNT use to consist of only one single wrapped graphene sheet).

Oxygen plasma purification

An oxygen plasma transforms amorphous carbon into CO_2 according to equation (7.2):

$$C + O_2^{2-} \rightarrow CO_2. \tag{7.2}$$

If the parameters of the oxygen plasma treatment are not appropriately chosen, either the impurities stay unaffected on the sample or the CNTs

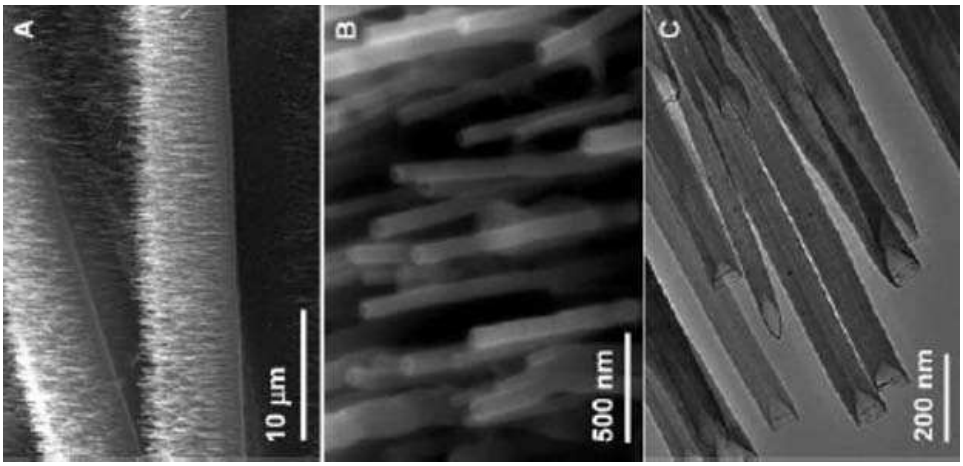

Fig. 7.9: A) and B) SEM images taken after liquid phase purification and CO_2 drying. C) TEM image of open-tipped CNTs. "Reprinted (adapted) with permission from (X. R. Ye, L. H. Chen, C. Wang, J. F. Aubuchon, I. C. Chen, A. I. Gapin, J. B. Talbot, and S. Jin, Electrochemical modification of vertically aligned carbon nanotube arrays, Journal of Physical Chemistry B, 110(26):12938–12942). ©(2006) American Chemical Society." [248].

themselves are badly stressed resulting in a graphene-like fringes on top of the forest (see Figure 7.10). Consequently, the energy density in the plasma chamber has to be tuned in order to remove impurities and preserve the va-CNT.

Thermal annealing under an ambient atmosphere

Gentle thermal treatment under an ambient atmosphere leads to similar purification results. Depending on the epitaxy, temperatures of 150°C-250°C are enough to start the oxidation process of converting amorphous carbon to CO_2. This can be described by:

$$2\mathrm{C} + \mathrm{O}_2 \rightarrow 2CO_2. \tag{7.3}$$

A crucial control parameter during the annealing process is the oxygen supply. This is crucial because, firstly, the size of the individual CNT decreases due to material removal by the oxidation process. Secondly, the diameter of the CNT increases during this treatment, which indicates that the single tubes are covered with a small shell during this process. This shell is expected to consist of amorphous carbon as an improper oxidation during the annealing process can be assumed.

Initial size [μm]	final size [μm]	power [W]	process time [s]	oxygen flux [sccm]	argon flux [sccm]	helium flux [sccm]	reflected power [W]
4,3	2,8	150	360	50	5	16	10
4,3	1,3 - 1,8	200	360	50	5	16	10
4,3	1,55	225	360	50	5	16	10
4,3	0,4 - 0,8	150	600	30	5	16	10
4,3	2,7 - 3,0	125	600	30	5	16	10
4,3	3,3 - 3,7	100	600	30	5	16	10

Tab. 7.1: Overview of the correlation between oxygen plasma power, plasma treatment process time and height of the va-CNT array.

Impact of gas phase purification on the va-CNT

The oxygen plasma causes stresses in the va-CNT array from the top downwards. This results in the rolling up of the upper part of the CNT as well as the formation of graphitic carbon flakes (see Figure 7.10). Table 7.1 shows

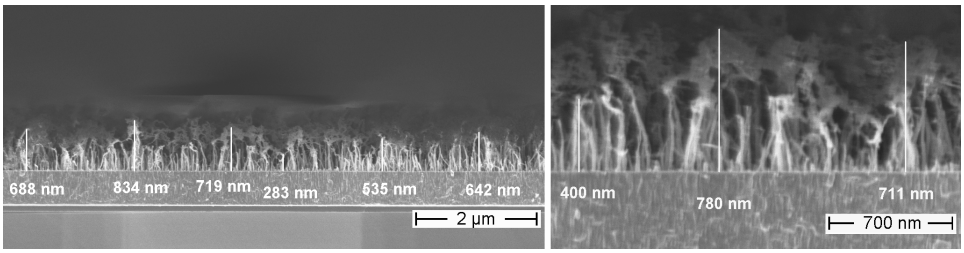

Fig. 7.10: Left: plasma treated va-CNT array. Right: magnification of left image. The detrimental aspects of an oxygen plasma treatment are clearly visible. The sidewall of the upper part of the CNT has cracked and rolled up. It appears as though the grapheme has undergone a flocculation process. It looks like graphene-like fringes of graphene.

the correlation between the input power, the process time of the oxygen plasma, and the height of the va-CNT array. The oxidation rate of the forest is higher for lower plasma powers over longer process time than for higher plasma powers used over shorter process times.

The control of the height delivered by this process indicates that this is a promising approach for the height control. However, an unfortunate side effect is the damage caused to the va-CNTs by this process. Afterwards, they have to be gently annealed in order to heal the damage. By optimizing the process parameters a significant decrease of amorphous carbon was also observed.

The metal catalyst is transformed in the oxygen plasma treatment to rust,

in accordance with the equation

$$3Fe + 2O_2^{2-} \rightarrow Fe^{II}O + Fe_2^{III}O_3. \tag{7.4}$$

Hence, it will stay in the va-CNT array as the impurity rust (solid).
Thermal annealing of such a processed sample causes an increase in the diameter of the CNT (see Figure 7.11). This happens, because amorphous carbon is a by-product of the thermal oxidation of carbonaceous materials when there is an insufficient oxygen supply. This can be additionally confirmed by the Raman measurements shown in Figure 7.12. Ferrari and

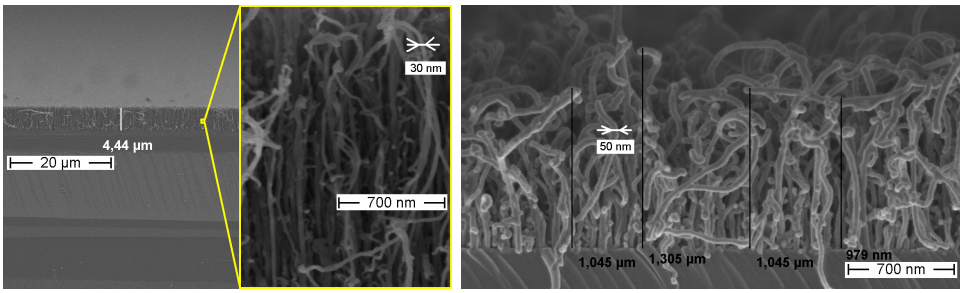

Fig. 7.11: Thermal treatment on a va-CNT sample ($434 - 1_4$). Left: untreated va-CNT array. Right: thermal annealed va-CNT array. The increase in diameter is caused by amorphous carbon deposition around the CNTs. The diameter of the CNTs almost doubles.

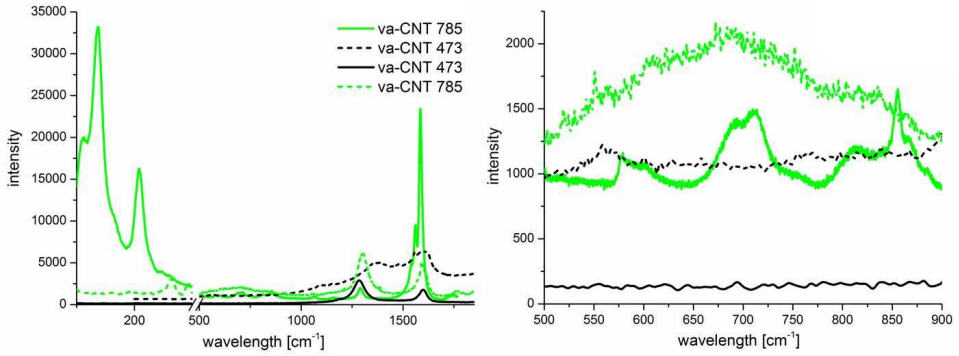

Fig. 7.12: Raman measurements of two different va-CNT samples before (solid line) and after a thermal annealing treatment (dashed line). a) the increase of the signal between the D and G bands ($1200cm^{-1}$-$1700cm^{-1}$) due to this treatment corresponds to diamond-like and amorphous carbonaceous material. b) the increase of the signal between $500cm^{-1}$-$900cm^{-1}$ due to this treatment corresponds to an increase in hydrogen freed, amorphous carbonaceous material, [249] [250], [251], and [249].

Robertson noted that the fit of the D peak (especially its position) is the least accurate for many amorphous carbons. The D peak is hard to be

clearly determined, because it is often only a low- frequency shoulder of the G peak [251].

Carbonylation

Iron can be transformed into iron pentacarbonyl when car- bon monoxide is present, according to the equation

$$Fe + 5CO \rightarrow Fe\,(CO)_5\,. \tag{7.5}$$

Therefore, this can be used for the purification of the va-CNT forest (see Figure 7.13).

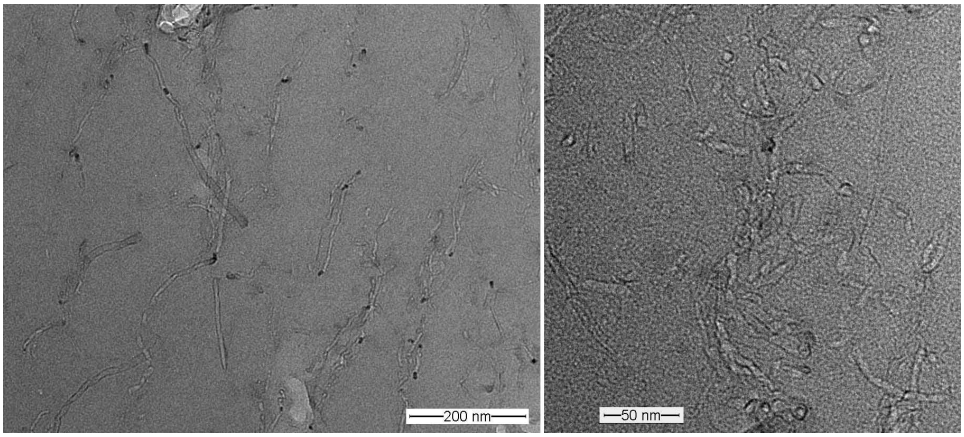

Fig. 7.13: TEM image of va-CNT as deposited (left) and after purification (right).

7.3 Functionalization

As one third of the CNTs are metallic and in the pe-CVD process MWCNTs are synthesized a covalent functionalisation should be undertaken in order to enhance the amount of semi-conducting CNTs in the array. Fluorination of the CNTs enhances their band gap. As this process is executed in a plasma chamber it is reasonable to combine both the purification and fluorination, with eventually the thermal annealing step. The thermal annealing process removes lattice defects, e.g. defect sites, where a carbon atom is missing, from a CNT. The results of EDS measurements made on the samples after the NF_3-plasma treatment are shown in Figure 7.14. Only the outer sidewall of a CNT, more specifically the MWCNT, is chemically functionalized in the NF_3-plasma. All pristine MWCNTs are known to have metallic like electrical conductivity, due to either interwall interactions or due to at least one of the tubes, which form the MWCNT, being metallic and somehow electrically connected with the bulk. If the latter is true, MWCNTs are

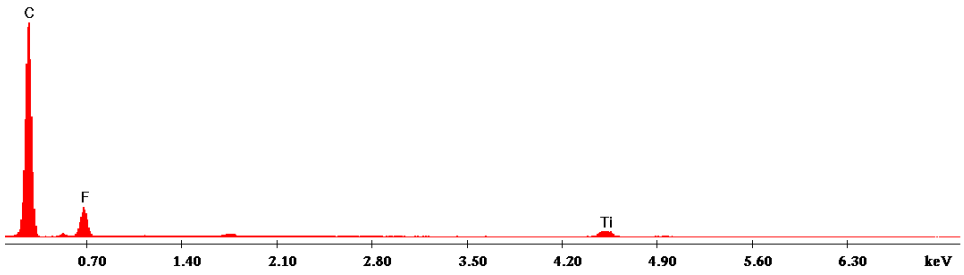

Fig. 7.14: EDS analysis of fluorinated va-CNT array. The amount of fluorine is 9.02 At %. Iron catalyst residues are not detected.

not metallic in nature. Only the outermost sidewall of every CNT forms the heterojunction with the enclosing dye. This means the heterojunction interface between semiconducting CNTs formed during fluorination and the dye increases significantly due to this treatment.
The EDS measurements confirm that there is no iron within the va-CNT sample.

7.4 Infiltration

For the infiltration of the va-CNT different approaches such as thermal evaporation, spin coating, drop coating and plotting were investigated. Due in part to limitations of the equipment only drop coating and plotting emerged as the best techniques for the layer deposition. Wetting studies for the three liquid based infiltration techniques have been described in the theoretical background section on wetting (chapter 4). All liquid based infiltration experiments were conducted in an UV shielded clean room (22°C, 60% humidity, clean room category ISO-3).

7.4.1 Infiltration via thermal evaporation

A standard method for layer deposition in the organic field is thermal evaporation due to its easy utilization, precise thickness control and high purity. In this technique single molecules are evaporated. The porosity (P) of a va-CNT forest can be estimated according to [252] as:

$$P = 1 - \frac{\pi}{4} \cdot \frac{d}{D}2 \approx 91\%, \tag{7.6}$$

where D is the average CNT separation and d is the average CNT diameter. The average spacing of around 30nm between neighbouring CNTs is expected to be large enough to allow the infiltration by single dye molecules of CuPc. In the best case the va-CNT forest will be infiltrated from bottom up due to this process.

Experiments, however, have shown that the spacing is not large enough for the infiltration process. This is caused by the dye condensing at the top of the forest and not penetrating further into the porous surface (see Figure 7.15). This behaviour is caused by the temperature difference between the heated dye molecules, $\approx$ heated up to 300-400°C, and the relatively cool va-CNT forest ($\approx 30 - 50°C$), which causes the molecules to condense at the surface. Furthermore, the CuPc has a strong intrinsic driving force to crystallize, which also enhances this condensing behaviour.

Consequently, the layer morphology is highly crystalline, see Figure 7.16.

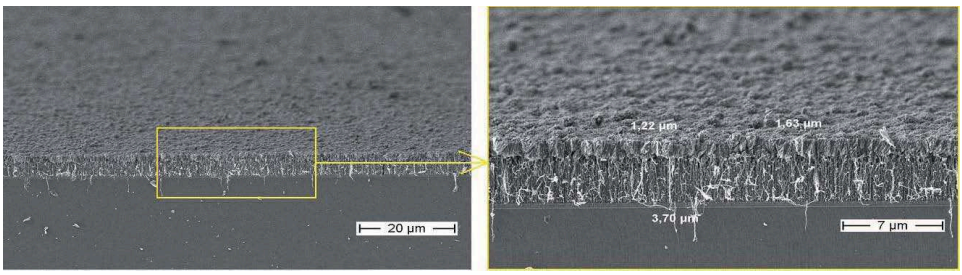

Fig. 7.15: Cross section of a va-CNT forest after the evaporation process. The figure on the right is an enlargement of the box marked in the figure on the left. Right image taken from [143].

The cross-sections in this figure show grain growth along the z-axis (vertical direction - perpendicular to the wafer plane). This ordered morphology refers the advantage of a controlled optimized electrical conduction in the CuPc layer. The anisotropic electrical conduction behaviour of CuPc has an influence on the behaviour of the device. The cross sections of Figures

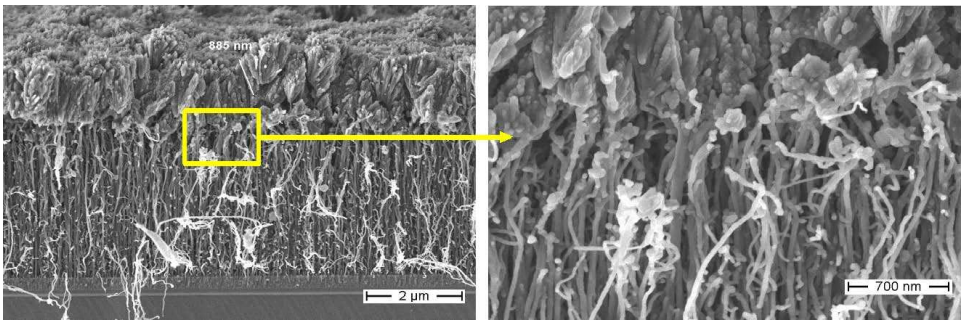

Fig. 7.16: Cross section, on the left, of va-CNT forest after the evaporation process. The high resolution image on the right shows clearly the crystallinity of the evaporated CuPc. Image taken from [143]

7.15 and 7.16 convey the impression that the top layer is homogeneous and non-porous. However, they are in fact porous, as shown in Figure 7.17. All darker areas are pores of the va-CNT forest which are covered with CuPc. The va-CNT forest is not fully covered in these pores due to shadow mask

effects. As a consequence shorts will be created when a top electrode is deposited on the partly covered va-CNT forest. Shorts of this kind were observed during the electrical characterisation of the devices. In Figure 7.17

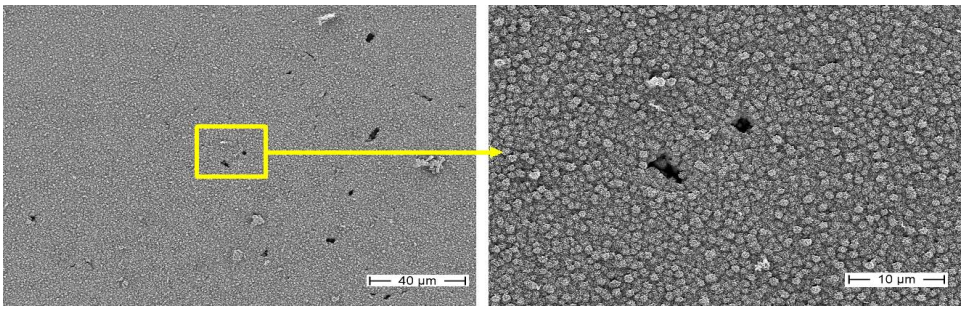

Fig. 7.17: Top view of the va-CNT forest after evaporation on the left and a magnification of the marked area on the right. The CuPc layer is not fully closed. The darker areas are pores which may cause shorts in the device after the deposition of the top electrode.

the pores appear like non coated holes in the forest. But this impression deceives, as the CuPc infiltrates these pores as can be seen in Figure 7.18. Despite further investigations the infiltration and cover layer formation could not be developed such that no shorts were observed. This means in all cases the whole device is shunted by these pores.

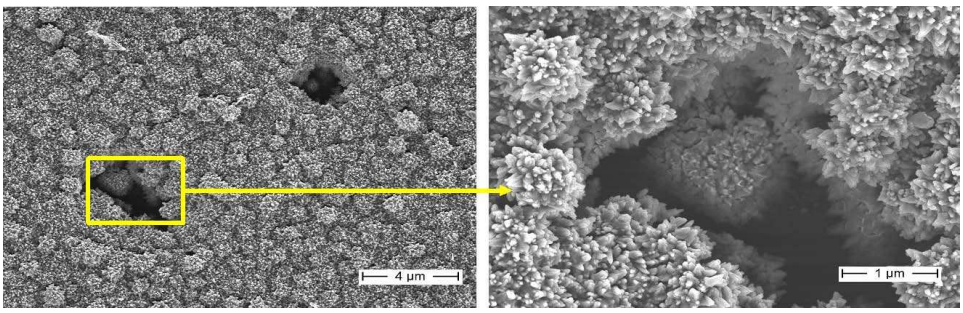

Fig. 7.18: A high resolution SEM micrograph of the top layer on the left and the enlargement of the marked area on the right. These show the infiltration of CuPc in the pores. Electrical characterisation has shown the resulting short circuit response.

7.4.2 Wetting of the va-CNT

All liquid phase based infiltration approaches rely on good wetting properties on the surface of the va-CNT forest. In order to overcome the lotus effect, wetting on the individual CNTs had to be improved. Goniometric data were obtained from the static contact angle, which was measured with

a Krüss DSA20 goniometer. In this method, a water droplet with a volume of 20-40μL was placed on top of the CNT forest using a needle. A picture was subsequently taken and the contact angle was determined from a mathematical fit of the drop shape. The fitting process either used the Young-Laplace equation or the tangent fitting method. The forest surface is composed of the CNT tips and a fraction of their sidewalls (see Figure 7.1, left image). The height of the va-CNT array varies by about ±500nm over the whole substrate and by about ±150nm locally along a 0,5μm line length on the substrate surface. The latter finding indicates that the surface roughness is large. When interpreting the results of a wetting study the surface roughness has to be considered in order to correctly interpret the results. Then the super hydrophobic surface of va-CNT forests can be infiltrated with certain solvent-dye combinations. Infiltration leads to the preservation of the vertical alignment.

Static wetting regimes

This section is based upon [143]. The results and discussion of that paper ([143]) was used to write this section. Figure 7.19 shows a sketch of the wetting process of a solvent with dissolved dye into a va-CNT array. The wetting behaviour of a va-CNT can be explained by introducing two different wetting regimes which depend on the residence time of the liquid, [224]. These two wetting regimes are either homogeneous (Wenzel state) or heterogeneous (Cassie-Baxter state), [253], [254], and [255]. Wenzel's theory

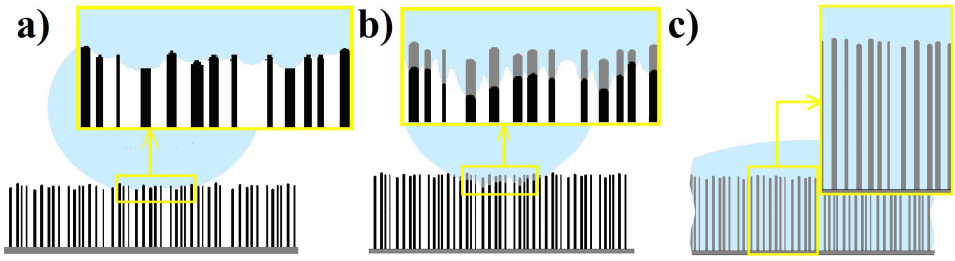

Fig. 7.19: "Wetting according to Wenzel and Cassie Baxter. (a) $\theta > 90°$: Cassie-Baxter regime; (b) $90° > \theta > 15°$: slight wetting occurs in the still heterogeneous wetting regime; (c) $\theta < 15°$: homogeneous wetting takes place (Wenzel regime)." Taken from [143].

describes the impact of surface roughness in terms of a simple extension of the liquid-solid interface. The degree of extension of the surface is expressed by the ratio factor (r). This is defined as the fraction of real interface length with respect to the ideal interface length. The ideal length corresponds to the length of the orthogonal projection of the surface roughness onto the surface. This theory works well for the contact angles $0° < \theta < 90°$, but if contact angles are measured in the interval $90° < \theta < 180°$ the liquid

does not penetrate very well the surface and into the gaps between the CNTs. Hence, liquid-solid and liquid-air interfaces are formed over the surface. The trapped air in the gaps between the CNTs has to be taken into account in the wetting analysis. The theory of Cassie and Baxter includes such behaviour. In general, wetting itself can be expressed as the ability of a liquid to spread over a solid surface. The liquid on a surface will spread until the cohesion forces of the liquid, the surface tension and gravity are in equilibrium. This leads to a stable contact angle, θ, at the triple point of solid, liquid and air interface. The angle can be expressed by Young's relation:

$$\cos\theta = \frac{\gamma_{\mathrm{sg}} - \gamma_{\mathrm{ls}}}{\gamma_{\mathrm{lg}}}, \tag{7.7}$$

where γ_{sg} is the surface tension coefficient of the solid-gas interface, γ_{sl} that of the solid-liquid interface, and γ_{lg} that of the liquid-gas interface, [256]. However, this is applicable only for an ideally flat surface. Therefore, it must be adjusted for surface roughness, as discussed above. In Wenzel's theory the relationship becomes:

$$\cos\theta_A = r \cdot \frac{\gamma_{sg} - \gamma_{sl}}{\gamma_{\mathrm{lg}}}, \tag{7.8}$$

where θ_A is the apparent contact angle and r is the ratio of the real rough surface length to the ideal smooth surface length. The apparent contact angle is, thus, adjusted with the correction factor, r. For rough surfaces r increases ($r > 1$) and for ideal smooth surfaces r = 1 (which means $\cos\theta_A = \cos\theta$). The approach made by Cassie and Baxter describes the contact angle for a composite material by:

$$\cos\theta_A = \Phi_1 \cdot \cos\theta_1 + \Phi_2 \cdot \cos\theta_2, \tag{7.9}$$

where Φ_1 is the fraction of interface length and θ_1 is the contact angle for the first component, and Φ_2, θ_2 are the corresponding values for the second component. In the special case (va-CNT wetted by aqueous solution) where a liquid on a rough surface encloses gas pockets (hence, $\theta_2 = 180°$) this equation reduces to:

$$\cos\theta_A = \Phi_{ls}(\cos\theta - 1) + 1, \tag{7.10}$$

where Φ_{ls} is the fraction of the liquid-solid interface and 1-Φ_{ls} is the fraction of liquid-air interface. If the liquid spreads over the CNT forest, i.e. wets it, the Wenzel state is applicable. In this regime the CNT forest is infiltrated by the liquid. If the gap between the CNTs is considered to be capillary like, then an equilibrium condition is reached when the hydrostatic pressure equals the capillary force. If a circular capillary is wetted then:

$$A \cdot \rho \cdot g \cdot h = U \cdot \gamma \cdot \cos\theta, \tag{7.11}$$

where A is the area of the capillary, ρ the density of the liquid, g the gravitational acceleration, h the maximum rise height of liquid, γ the liquid surface tension, θ the contact angle and U the circumference of the capillary. For the CNT forest some modification should be made to this simple idea due to the exact geometry of the forest, see Figure 7.20. The geometry is explained

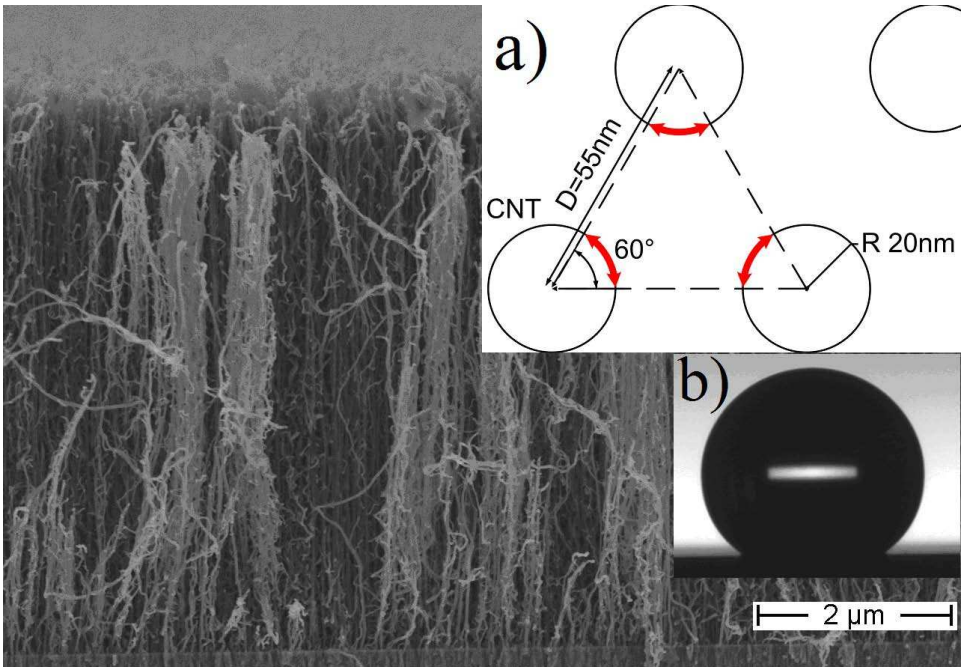

Fig. 7.20: The triangular CNT base cell shown in a) consists of three single CNTs of the forest at each corner. They have an average diameter of R=20nm. Their average separation between each other is D=55nm. Each CNT contributes a 60° surface fraction to the capillary (red coloured). This yields a CNT capillary surface of $A = \frac{D}{2} \cdot D \cdot \sin(60°)$ (see text). Image taken from [143].

in terms of a base cell. The base area of the "capillary" equals that of a triangle spanning the three triangularly arranged nearest neighbour CNTs. The wetted area of the CNT equals just a sixth of the circumference of each of the cornering three CNTs. Together, these describe the base cell of the va-CNT. These simplifications result in

$$\frac{D}{2} \cdot D \cdot \sin(60°) \cdot \rho \cdot g \cdot h = \left(\frac{2\pi R}{6} \cdot 3 \right) \cdot \gamma \cdot \cos\theta, \tag{7.12}$$

where D is the average distance from CNT to CNT, R the average diameter of the CNT and $\frac{2\pi r}{6} \cdot 3$ is the fraction of surface of the capillarity formed by the CNT triangles. Equation (7.12) can be rewritten as:

$$A_{eff} \cdot \rho \cdot g \cdot h = U_{eff} \cdot \gamma \cdot \cos\theta, \tag{7.13}$$

where: A_{eff} is the effective area and U_{eff} is the effective contact surface contour on the va-CNT. In this description the tubular geometry of a common capillary is replaced by a pattern of "triangular pillars" in the va-CNT array. An example of such a va-CNT capillary base cell is shown in Figure 7.20. The total contacting line segments form the effective contact surface contour according to:

$$U_{eff} = \frac{2\pi R}{6} \cdot 3 = \pi \cdot r \tag{7.14}$$

and the effective area equals:

$$A_{eff} = \frac{D^2}{2} \cdot \sin(60^\circ). \tag{7.15}$$

A number of solvents, dyes and their combinations have been shown to infiltrate the CNT array. The degree of polarity varies between the various solvents. Consequently, their particular combination determines the wetting regime. Variations in CNT length do not interfere with the wetting behaviour. It also do not influence the changes in the vertical alignment of the CNTs due to the wetting process.

Dynamic wetting regimes

If wetting occurs on a va-CNT surface then the Washburn equation is applicable to the wetting of the capillaries between the CNTs. This is given as:

$$h^2 = \frac{\gamma_l \cdot \cos\theta}{2\eta} \cdot r \cdot t \tag{7.16}$$

can be used to explain the wetting of the capillaries in the CNT forest, where γ_l is the surface tension of the liquid, θ is the contact angle at the three phase point, η is the liquids viscosity, t is the residence time and r is the radius of the capillary, [257]. However, the investigation made in this work of the water wetting phenomenon on va-CNT substrates yielded a slightly different behaviour. In order to investigate the initial wetting behaviour, a dye was dissolved in water. The dye, CuPc-TS, precipitates during the evaporation process. Consequently, a film of the dye remained after the solvent had evaporated. In detail, a 5μL drop was dropped on top of the array. It evaporated fully after several minutes under clean room conditions at room temperature. The dye concentration, c=0.5mg/mL, was high enough to cause the formation of a thin film after the evaporation process. The droplet showed similar drying behaviour to pure water, [252]. This implies that the extension of the wetted area is constant during solvent evaporation. During evaporation the effective droplet (sphere) radius increases, because the spherical droplet flattens out over this constant contact area, [252]. However, the droplet surface area decreases. It has been reported that the vertical alignment of the CNT array in the wetted area collapses during drying due to capillary forces.

These forces drive the CNTs into bundles and to eventually fall over despite one end of the CNT being still fixed to TiN layer on the substrate. The films produced in this study were homogenous, as shown in Figure 7.21. In the figure it is clear that only the CNT tips were wetted by the solution and the film itself maintains a constant thickness relative to the substrate. Hence, it appears that the wetting process stays in the Cassie-Baxter regime at all times. This implies that air always resides in between all the CNTs. It is expected that the shrinkage of the droplet during the film formation process drives the collapse of the array due to the shear forces. Due to precipitation of dye the vertically alignment of the array keeps preserved. The dye layer supports each single va-CNT horizontally and a collapse of the structure is suppressed. In the case that partial or complete infiltration occurred the

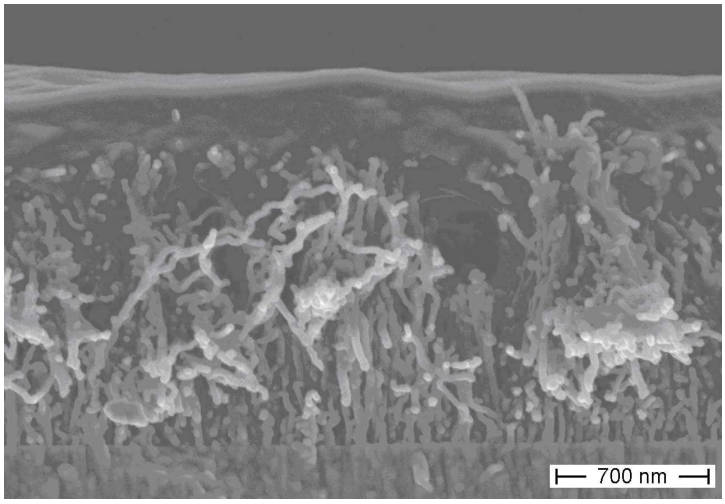

Fig. 7.21: va-CNT array infiltrated by CuPc-TS (aqueous solution). A dye layer is formed on top of the array, which supports the macroscopic structure of the va-CNT array and keeps the alignment stable. Image taken from [143].

precipitated dye mostly maintained the vertical alignment of the va-CNT. If the CNT ordering is preservation or not depends on the amount of dye precipitated (and, therefore, the dye concentration, c, in the solvent).
The surface roughness amplifies the interfacial interaction of liquid and surface. This means, that if wetting occurs, the surface roughness enhances the wetting behaviour. If anti-wetting occurs on a surface the surface roughness enhances the hydrophobicity to super-hydrophobicity. Hence, the hydrophobicity of the CNT shows super-hydrophobicity for aqueous liquids when in the form of a va-CNT array. This causes the lotus effect for aqueous liquids on the surface of the forest, see Figure 7.22. This results in heterogeneous wetting (Cassie-Baxter regime) of the surface. The total value and the polarity of the surface energies of the va-CNT arrays measured in the wetting

sample	surface energy [Nm/mm]			polarity	variation	
	total	polar	disperse		total	relative
va-CNT 816	59.40	16.26	43.23	0.27	0	0
va-CNT 811	59.83	16.07	43.76	0.27	0.51	1.88
va-CNT 435	52.61	10.54	42.07	0.20	7.34	26.81
va-CNT 46	58.89	11.05	47.84	0.19	8.61	31.45

Tab. 7.2: The sample va-CNT 816 was used as the reference for the determination of the variation.

study varied within a range caused by the random spread of the synthesis parameters, see Table 7.2.

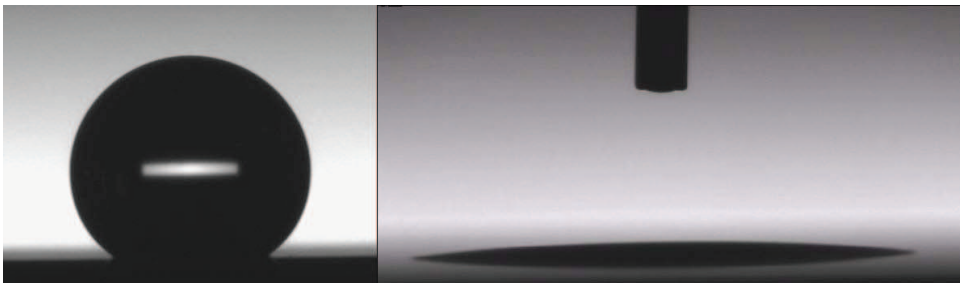

Fig. 7.22: Contact angle measurements of a va-CNT forest. Left: wetting with distilled water. Image taken from [143]. Right: wetting with diiodomethane.

7.4.3 Infiltration via spin coating

This study showed dichlorobenzene to be a good solvent for the infiltration of the va-CNTs. However, other organic solvents were tested. Due to their favourable wetting and solubility properties these solvents can be used to deposit a thin film by the spin coating technique. The homogeneity of the deposited layers is controlled by the spin parameters, such as acceleration, spin time and speed. For the processing tests, chips of purified va-CNT samples were fixed onto larger carrier silicon wafers. The silicon carrier wafer was sucked onto the chuck by the application of a vacuum. The liquid blend of organic material (donor and acceptor) and solvent was deposited onto the va-CNT with a μL-pipette. In addition to the organic solvents, the CNT arrays can also be wetted by a mixture of distilled water and surfactants. Surfactants decrease the surface tension of water, which enables wetting. However, surfactants will remain on the sample after solvent evaporation as they themselves do not evaporate under the used processing conditions. As a consequence, the active matrix of donor-acceptor material is "contaminated" with surfactants. Contamination of the active matrix is in most cases unwanted for reasons of device performance.

Experiments show that it is impossible to reach phase II and III conditions of the spin coating process (cf. Chapter 4), because in phase I the liquid wets the carrier silicon wafer and spreads over it. Hence, a controlled reduction of the amount of liquid on the sample is impossible. This leads to non-reproducible spin coating results. Spin coating also usually resulted in the flattening of the vertical array onto the substrate. This happened most significantly for high spin speeds, as shown in Figure 7.23. Spin coated layers of several micron thickness, which is equivalent to the height of the va-CNT, could not be produced due to the poor solubility of the dissolved OPV materials. This meant that the desired concentrations could not be achieved. Hence, spin coating was found not to be an applicable technique for film deposition on va-CNT arrays.

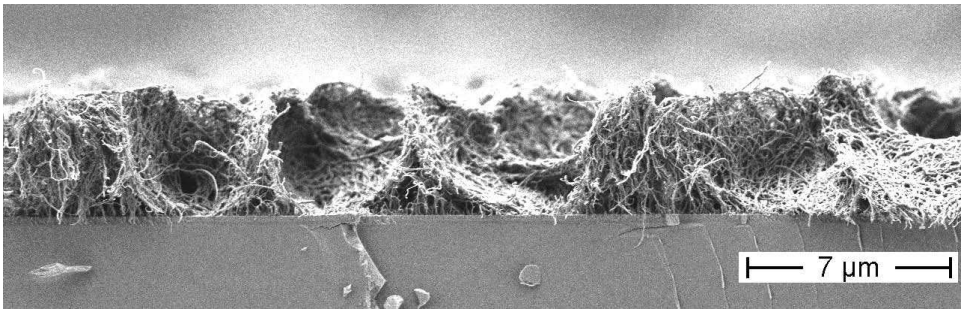

Fig. 7.23: Influence of the spin-coating of dissolved dyes on va-CNT. This figure shows the influence of CuPc-DMA dissolved in toluene. It is representative for all spinning experiments. Image taken from [143].

7.4.4 Infiltration via drop coating

This section is based on [143]. Drop coating offers the advantage that the initial amount of solvent - as well as the dissolved materials - will remain until complete evaporation of the solvent. This allows the determination of the optimum correlation between the four main aspects of va-CNT infiltration with a dye for the formation of non-porous composite layers. These aspects are:

- dye concentration in solvent,
- amount of dropped solvent,
- substrate size, and
- height of composite layer.

This study also showed that the solvents viscosity and composition of surface tension, i.e. the fraction of polar and dispersive component, as well as environmental parameters like humidity, temperature, dye concentration, and

many more have an influence on the structural integrity of the CNT forest. For this study several solvents were used to dissolve dye and to infiltrate the forest. For an appropriate choice of solvent, the infiltration was found to work up from top to bottom of the va-CNT array yielding completely embedded forest. 1,2-dichlorobenzene turned out to be the most suitable solvent for the infiltration. During the evaporation of the solvent a uniform composite matrix of va-CNT and dye was formed (see Figure 7.58). This composite can work as an organic solar cell because the dye absorbs light, which leads to the generation of excitons. These excitons dissociate at the donor-acceptor interface [258], [259], [260], [261]. Ideally, this heterojunction is formed between the dye and the CNTs. In the case of this infiltrated dye a structural ordered bulk-heterojunction organic solar cell was formed which included separate pathways for the carrier transport of holes and electrons. In principle, this configuration (CNT-dye) could also work as a light sensor or as an organic light emitting diode, if the energy levels of the used materials are appropriately configured.
In order for this composite configuration to function a conducting transparent top electrode has to be deposited. The CNTs (bottom electrode) are already conductively connected to the outside world as they are synthesized directly onto the conductive titanium nitrate layer. Its conductivity is $\kappa = 5 \cdot 10^6 S/m$. Goniometric measurements yielded a CA of $\theta = 139.9°$ for water (HPLC grade) and $\theta = 19.8°$ for diiodomethane by using the tangent fitting method. The surface energy of the va-CNT array was calculated to be $\gamma_s = 58.89 mN/m$, and the ratio of the polar and disperse fractions were $\gamma_{sp} = 11.05 mN/m$ and $\sigma_{sd} = 47.84 mN/m$, respectively. Hence, the polarity of the surface is $P = \frac{\gamma_{sp}}{\gamma_s} \approx 0,19$. Experiments have shown that this fraction and the viscosity of the solvent have a major influence on the preservation of the vertical alignment of the CNT forest during the wetting process. In order to infiltrate a CNT forest with an aqueous solution the surface tension has to be reduced. Consequently, a 0.05%wt solution of TritonX and distilled water with a surface tension of $\gamma_l = 30 mN/mm$ was used (see 7.26). An infiltration depth of around $1 \mu m$ was subsequently achieved. However, the vertical alignment differs from the non infiltrated forest. The CNTs themselves appear to be more crisscrossed than before. Depending on the solvent composition (i.e. polarity and/or ingredients) the array can macroscopically transform into various shapes after the infiltration process. Although the lengths of the CNTs varied in the study, this had no significant influence on the resulting macroscopic shapes of the infiltrated arrays (unless in the extreme case that the tubes were very short). The best replica was achieved for a methanol-water mixture of 1:1 wt.% containing dissolved CuPc-TS (c=0.5mg/mL), as shown in Figure 7.24. Mushroom like shapes appeared depending on the different surface tensions and polar (dispersive fraction). The tested solvent-dye combinations are shown in Table 7.3.

dye / solvent	solvent-substrate	CuPc-TS	CuPc-DMA	Toluylene red	Ferrocene	P3HT	CuPc
water and TritonX	Figure 7.25	Figure 7.26, 9^b, 1^c	X	Figure 7.27, 10^b, 1^c	X	X	X
toluene	Figure 7.28	X	Figure 7.29, 4^b, 1^c	Figure 7.30, 1^b, 4^c	Figure 7.31, 4^b, 1^c	O	X
1-decanole	Figure 7.32	X	Figure 7.33, 6^b, 1^c	Figure 7.34, 1^b, 4^c	Figure 7.35, 10^b, 1^c	O	X
diiodomethane	Figure 7.36	X	Figure 7.37, 4^b, 1^c	o	o	o	X
water and methanol	Figure 7.38	Figure 7.39, 3^b, 1.5^c	X	X	X	X	X
chlorobenzene	Figure 7.40	X	Figure 7.41, 5^b, 1^c	Figure 7.42, 1^b, 4^c	Figure 7.43, 10^b, 1^c	Figure 7.44, 10^b, 1.5^c	X
chlorobenzene and trifluoroacetic acid (TFA)	Figure 7.45	X	X	X	X	X	Figure 7.46, 5^b, 1.5^c

Tab. 7.3: "Overview of tested solvents and dye combinations. The corresponding figures are given in the table. *X* marks a combination that was not possible due to the solvents being incompatible, O marks an experiment that was not done, ^{b} concentration of dye in solvent (mg/mL); ^{c} solvent amount per CNT array area ($\mu L/mm^2$)." Table taken from [143].

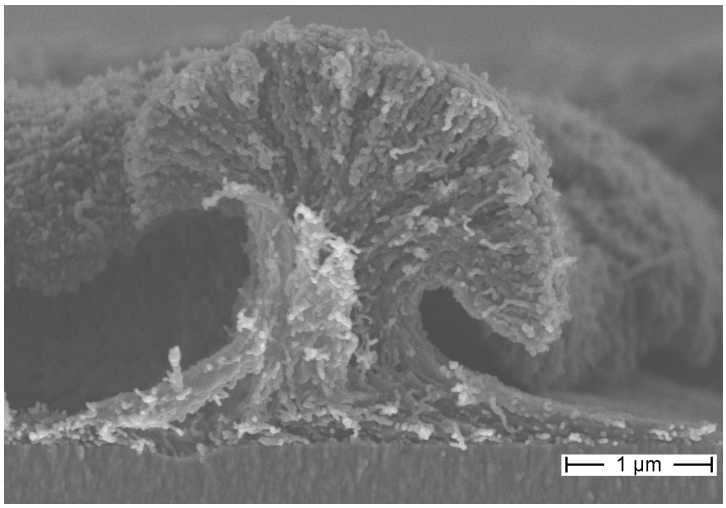

Fig. 7.24: "Mushroom shaped macro structure of a dried CNT array after being wet by methanol-water (1:1 wt% mixture) and dissolved CuPc-TS." Text and image taken from [143].

Water and TritonX

Goniometric contact angle measurements yielded a contact angle θ=155° for water and a surface energy of 59.7mN/m on the array. Consequently, the surface tension of aqueous liquids has to be reduced in order to obtain wetting. This is usually achieved using surfactants. SEM images in Figures 7.25-7.27 show experimental results for a solvent of 0.5wt.% TritonX in distilled water. The CuPc-TS deposited by using the solvent combination forms a uniform film with a constant height over several microns. Moreover, the precipitated CuPc-TS preserves the vertical alignment of the CNTs. The toluyene red deposited by using this solvent, shown in Figure 7.27, on the other hand did not mechanically support the array.

Toluene

Figures 7.28-7.31 display the obtained results when toluene was used as the solvent. The structure in Figure 7.28 is a pre-form of the mushroom shape shown in Figure 7.24. This kind of profile is generated during the drying process due to the capillary forces driving the CNTs together. The precipitating dye causes the retention of the vertical alignment of the array during infiltration and drying, see Figure 7.29. The CNT matrix is completely filled with CuPc-DMA and only a very thin cover layer exists. CuPc-DMA has been shown to adapt well to the CNT surface roughness [58]. The observed faceting of the CuPc-DMA at the fracture surface indicates a certain degree of crystallinity. In general, crystallinity improves the charge transport in the organic layers. The infiltration with dissolved toluyene red yielded a

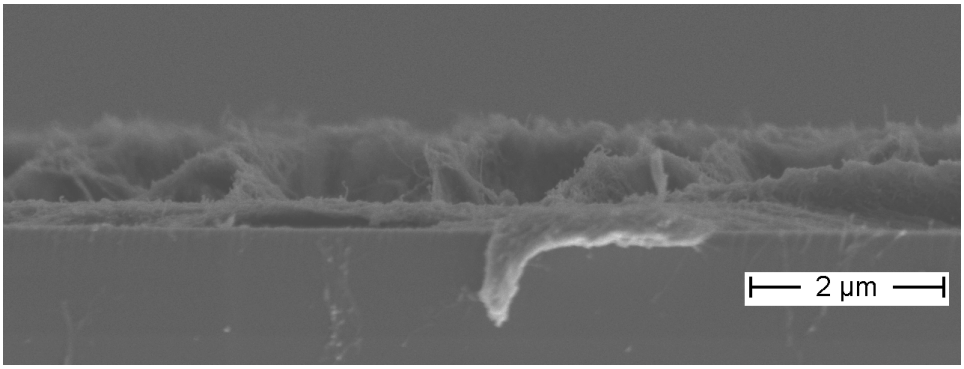

Fig. 7.25: "This image shows the ability of the pure solvent water + TritonX (0.5wt.%) to wet the CNT-forest with the dissolved dyes. It shows a tendency to mix up the vertical alignment of the CNT forest." Text and image from [143].

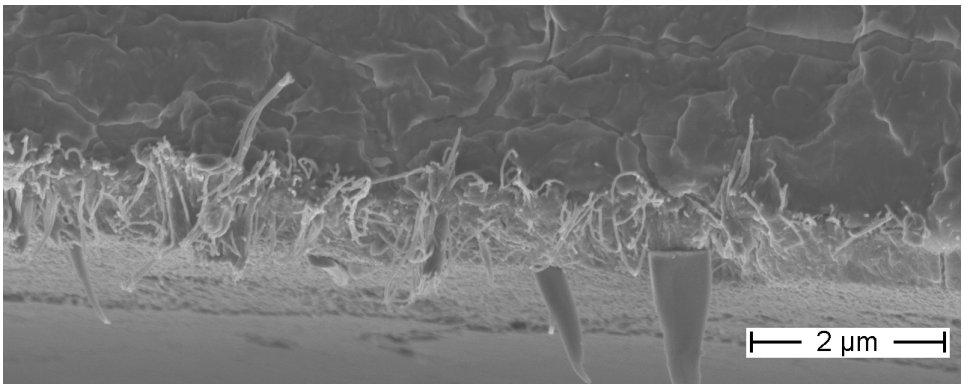

Fig. 7.26: CuPc-TS and CNT array. The combined layer detached from the substrate during solvent (water-TritonX, 0.5wt.%) evaporation. Image taken from [143].

homogenous composite matrix of dye and CNT (Figure 7.30). In this case the CNTs maintained their alignment. However, several tube tips were observed to stick out of the surface. In comparison with CuPc-DMA Figure 7.29, toluyene red does not adapt to the rough surface of the va-CNT array tips. Therefore, either another dye or solvent has to be chosen in order to reach a smoothly infiltrated and evenly cover layer. Ferrocene evaporates when the sample is thermally annealed after the infiltration process. This is done in order to reduce solvent residues in the CNT-dye composite, as it has a low vapour pressure (2.6 hPa at 100°C). Consequently, almost no dye layer is found in Figure 7.31. In this case the post-infiltration structure shows that the alignment of the CNTs is well preserved, particularly in comparison with Figure 7.28.

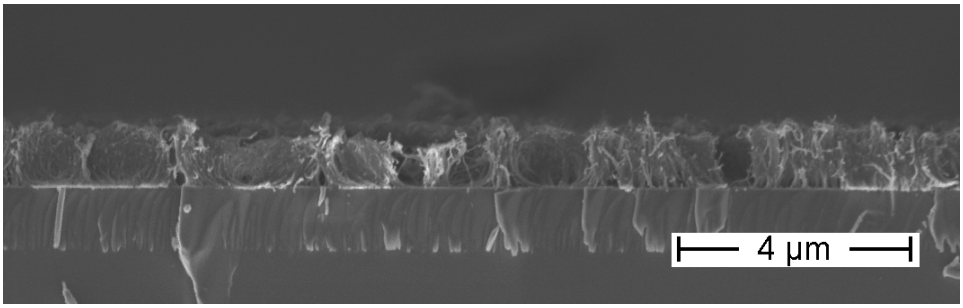

Fig. 7.27: Toluyene red dissolved in water-TritonX (0.5wt.%) did not form a homogeneous layer with the CNT matrix. Taken from [143].

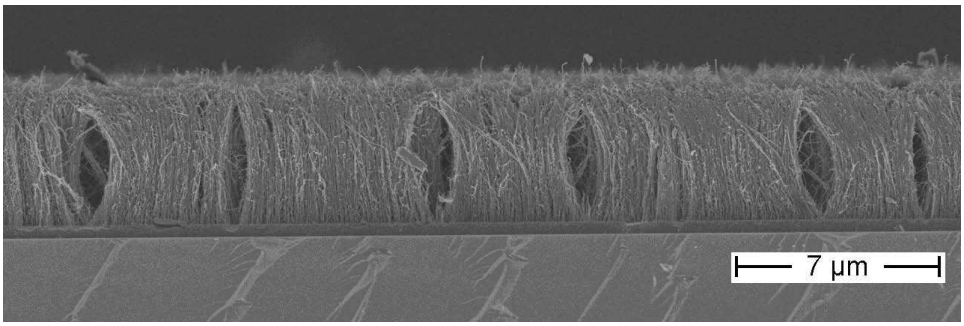

Fig. 7.28: Influence of wetting by toluene on the va-CNT array. The vertical alignment is relatively well preserved in comparison with the influence of water + TritonX (0.5wt.%) to the vertical alignment of the va-CNT array. Image taken from [143].

1-Decanole

1-decanole, like toluene, merely showed a negative impact on the array alignment as a result of the wetting process. In Figure 7.32 the alignment of the array is interrupted by several trench-like structures. In between the trenches the CNTs are bent and pressed together. A thick, homogeneous, non-porous and smooth composite matrix of CuPc-DMA and CNT is shown in Figure 7.33. The array is well infiltrated from the bottom to the top. The fractograph indicates a preserved vertical alignment of the CNT within the macro structure. The adhesive forces of the titanium nitrite substrate, CNT and CuPc-DMA suppress the mechanical forces generated by the dye in the layer. This is comparable to the processes observed within fibre reinforced composites. Two things were achieved by using these infiltration parameters: firstly the layer itself remains intact and, secondly, the layer is not detached from the titanium nitrite substrate as happened in Figure 7.26. Toluyene red was also shown precipitate during the solvent evaporation process. It formed a composite with the array as shown in Figure 7.34. The layer contains air pockets and/or caverns. The dye concentration and amount of solvent was

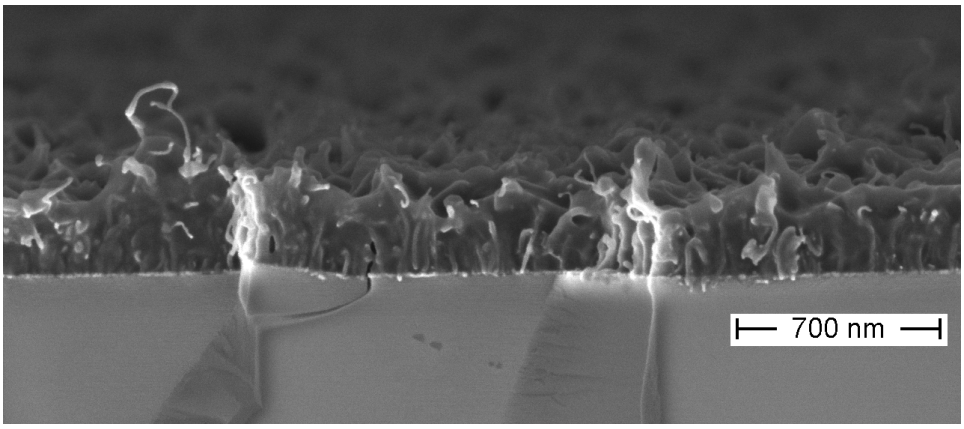

Fig. 7.29: CuPc-DMA dissolved in toluene. The array is well infiltrated with CuPc-DMA from the top to the bottom. The maximum composite height is 896nm. Single nanotubes stick out of the fractograph. Image taken from [143].

not matched properly to the substrate area. This occurs as the concentration limit, for the dissolving of toluyene red in 1-decanole, caps the amount of dye present and thus causes incomplete filling of the structure. Ferrocene, see Figure 7.35, could be made to form a thin cover layer of approximately 10-20nm on the CNTs. Moreover, most of the dye crystallized on top of the CNT array forming long needle-like structures.

Diiodomethane

Diiodomethane causes the formation of trenches and holes/caverns in the array, see Figure 7.36. Despite this the CNTs are still generally aligned from the bottom to the top, although a certain degree of bundling up occurs due to capillary forces increasing the CNT packing density at certain places within the array. By using CuPc-DMA as the dye, see Figure 7.37, the formation of trenches and caverns is limited. The CNTs, consequently, display a zigzag deformation. The big cover layer on top on the CNTs points to the top of the array being the preferred precipitation location of the dye. In this case, a gradient of the precipitated dye concentration arises in the infiltrated array (between the top and bottom). Lines of transition in between regions of different concentration appear. These lines are more or less parallel to the substrate and generate the shear band visible. The CNT themselves are bent due to the interacting forces of involved in the dye layer formation in the array.

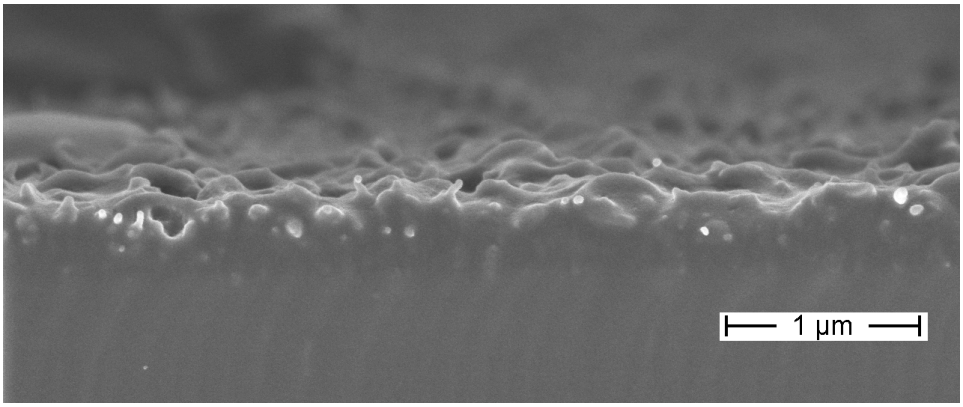

Fig. 7.30: Layer formed via infiltration of va-CNT with toluyene red dissolved in toluene. Single nanotubes stick out of the fractograph. Image taken from [143].

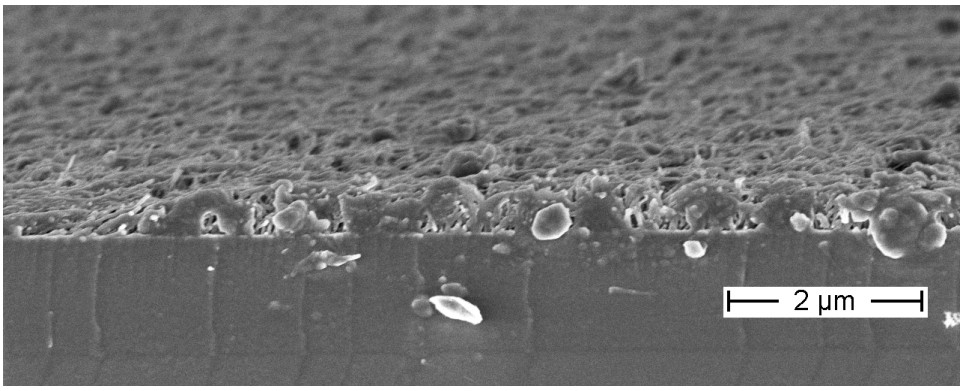

Fig. 7.31: Ferrocene dissolved in toluene. Ferrocene evaporated during the annealing process. The post-infiltrated array contained almost no dye. Image taken from [143].

Water-methanol

An azeotropic mixture of distilled water with methanol in the ratio (2:1)wt.% was observed to dissolve CuPc-TS and wets the array (Figure 7.39). The solubility of CuPc-TS was found to be very sensitive to the water-methanol ratio. The dye was found to mainly deposit on top of the array. The infiltrated array also formed trenches and was partly compressed. Compared to Figure 7.21 and Figure 7.37, this implies that the array is wetted but preferably patterned during solvent evaporation. The CuPc-TS does not preserve the alignment. The solvent possibly segregates during the evaporation process. This yields an increase of the CuPc-TS concentration in the parts with higher water concentrations.

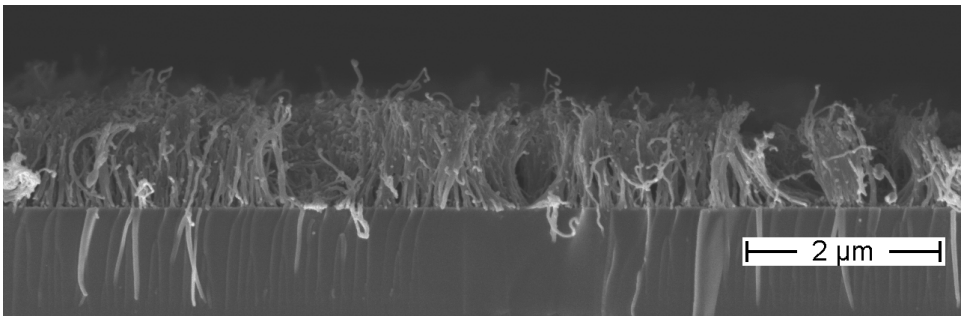

Fig. 7.32: Impact of wetting with 1-decanole. Trench-like structures are caused by the capillary forces. Image taken from [143].

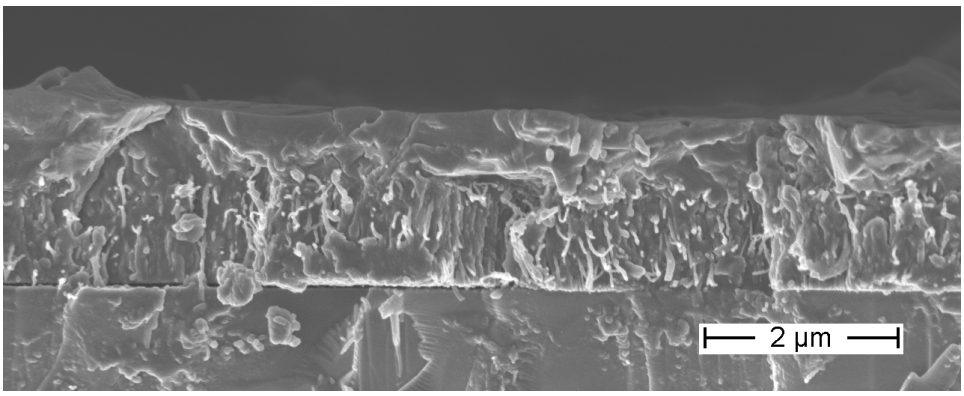

Fig. 7.33: CuPc-DMA dissolved in 1-decanole. Dye-CNT combination forms a smooth homogenous layer. Image taken from [143].

Chlorobenzene

The use of chlorobenzene as the solvent yields the deformation of the macro structure of the va-CNT array into holes and trenches, as shown in Figures 7.40-7.44. By dissolving small molecule dyes into the solvent the composite structure is still not stabilized, see Figures 7.41-7.43. Only the introduction of CuPc-DMA caused some limited performance improvements with regard to alignment preservation. As it performed much better in the 1-decanole or toluene solvents, the layer building process in this case can be attributed to the solvent. For this solvent the best results with regard to the vertical alignment of the CNT and homogeneity of the layer thickness in the resulting composite were achieved with the P3HT dye. In addition, a smooth cover layer of the P3HT on top of the CNT array was also achieved. This composite material is applicable to organic solar cells if the cover layer thicknesses can be fabricated to be within the exciton diffusion length. The performance of CNT-P3HT organic solar cells has already been reported by [244].

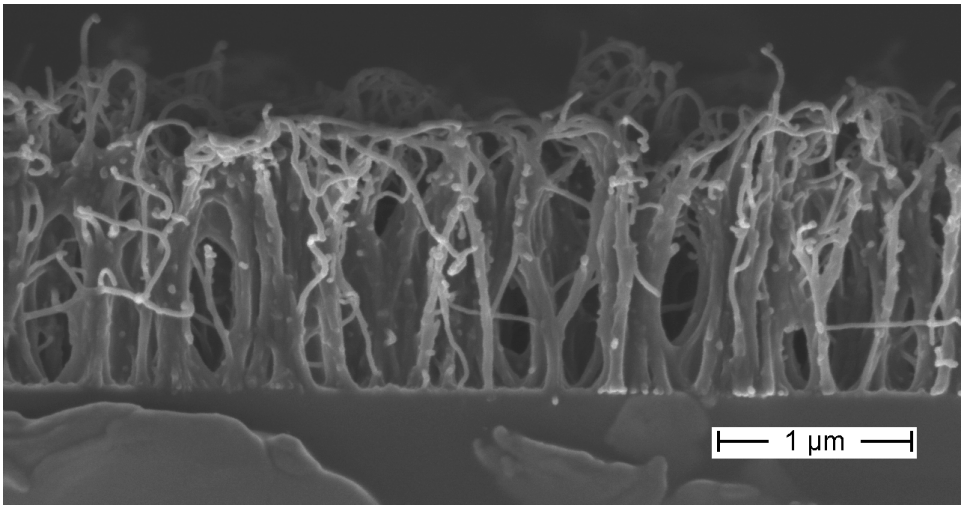

Fig. 7.34: Toluyene red infiltrates the va-CNT array, if dissolved in 1-decanole. Single CNT are covered with a thin dye layer. The infiltration parameters were not optimal, which resulted in the observed porosity and inhomogeneities. Image taken from [143].

Chlorobenzene and trifluoroacetic acid mixture

Because non functionalized CuPc is almost insoluble, the CuPc can be transformed into its protonated form by using a mixture of chlorobenzene and trifluoroacetic acid in a ratio of 1:1 wt.%, making it soluble [262]. The deformation of the array observed by using the mixture, see Figure 7.45, resembles the results of the spin-coating experiments. The CuPc precipitated out on the top of the array and formed several stacked hundred nanometer thick polycrystalline layers, see Figure 7.46. The crystallization caused the layer to be porous and flaky. Protonated CuPc has a large tendency to crystallize. According to these results, layer deposition with protonated CuPc or pristine CuPc should be done using thermal evaporation. However, for the other dyes such as CuPc-DMA and CuPc-TS it was found to be possible to deposit these by spin or drop coating.

Layer building process

The wetting of the CNT forest occurs in accordance with either the Young, Wenzel, Cassie and Baxter regimes. During the evaporation of the solvent the dissolved dye precipitates when the saturation limit in the deposited droplet on the forest is reached. The dye precipitates at the droplet's outer edge, which at the beginning of the process is always at the outer edge of the CNT forest substrate. Depending on the CA the droplet contracts early or later resulting in a thin or thicker layer part at the substrate's edge (see scheme 7.47). Subsequently, the droplet contracts causing its outer edge

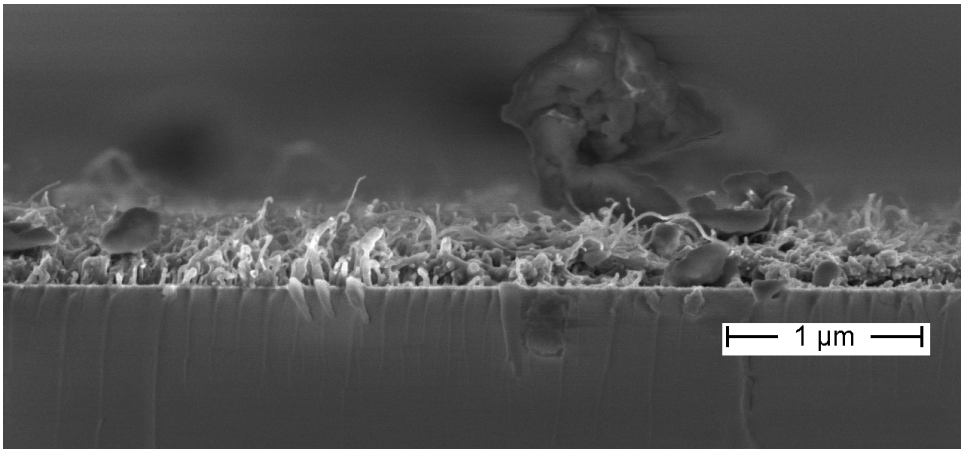

Fig. 7.35: Ferrocene dissolved in 1-decanole covered the individual CNTs as a thin layer. Image taken from [143].

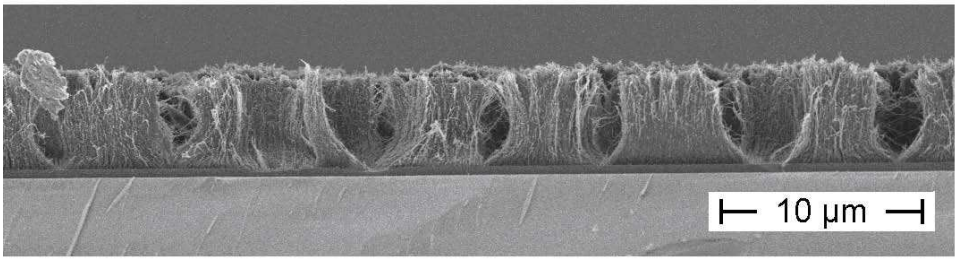

Fig. 7.36: The results of the interaction of the CNT array with diiodomethane; trenches and holes are visible. Image taken from [143].

to move from the substrate's edge towards its centre. The solution stays saturated at the outer edge and the dye precipitates homogenously during the further contraction until the droplet is fully evaporated. In order to obtain a homogenous layer and constant thickness of the dye-CNT forest composite, the following parameters have to be correctly matched:

- solution dye concentration,
- amount of solvent,
- substrate size, and
- CNT forest length.

In order to determine the correlation of the aforementioned four parameters the mass of the resulting layer has to be taken into account. It can be calculated by

$$m = \rho_{dye} \cdot V, \tag{7.17}$$

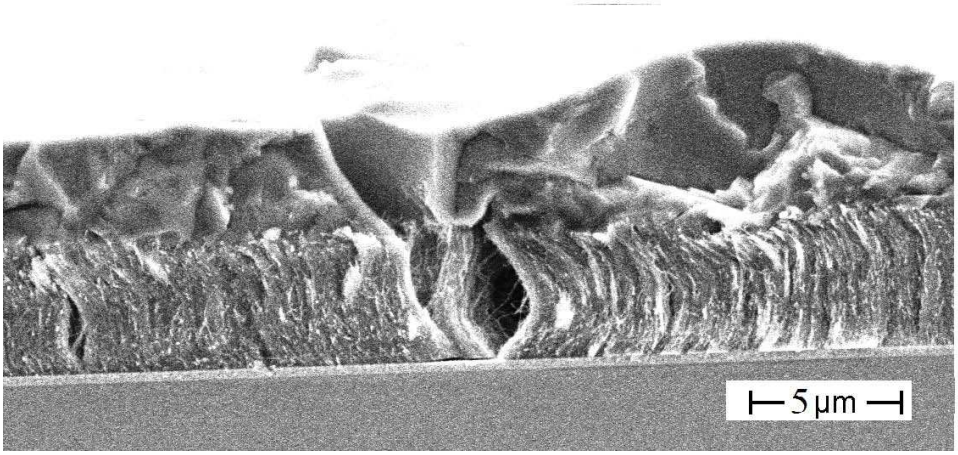

Fig. 7.37: A thick cover layer is formed by the introduction of CuPc-DMA dye in the diiodomethane solvent. This reduces the amount of trenching. The partial infiltration of the array and concentration gradients generate zigzag shaped CNT arrangements. Image taken from [143].

where m is the mass of the dye layer on the substrate, ?dye the specific density of the respective dye and V the volume of the layer. This can be further broken down into

$$m = \rho \cdot l \cdot b \cdot h, \tag{7.18}$$

where l, b and h are the length of the edges of the formed layer (see scheme in Figure 7.48). The layer is formed by the evaporation of the solvent from the deposited droplet. Therefore, the mass deposited corresponds to the amount of solvent (V) dropped on the substrate and its dye concentration (c).

$$m = c \cdot V_{liquid} \tag{7.19}$$

Combining this with equation (7.18) gives

$$c \cdot V_{liquid} = \rho \cdot l \cdot b \cdot h. \tag{7.20}$$

homogenous layer thickness was achieved equation (7.20) can be written as

$$h = \frac{c \cdot V_{liquid}}{\rho \cdot l \cdot b} \tag{7.21}$$

For this equation to be applicable to the produced composites two corrective factors have to be taken into account:

- volume of va-CNT on the substrate and
- volume of oversized dye layer on the substrate edges.

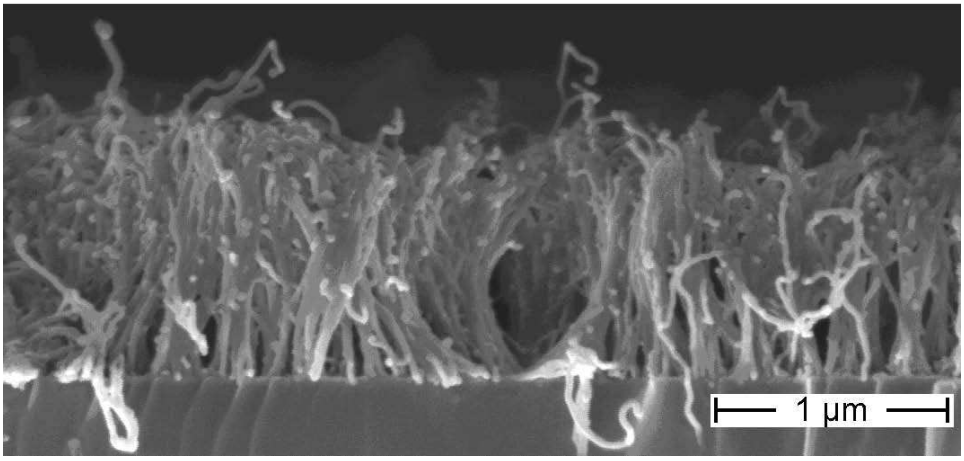

Fig. 7.38: Influence of water-methanol (2:1)wt.% on the va-CNT array. Image taken from [143].

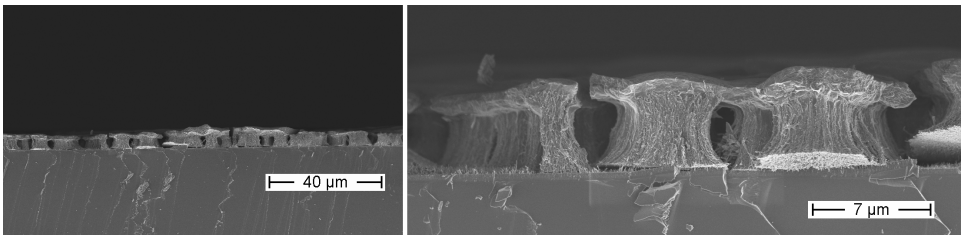

Fig. 7.39: CuPc-TS dissolved in water and methanol (2:1wt.%, respectively). The solvent mixture causes a texture and dye layer deposition process. These processes could be caused by poor wetting and bad evaporation behaviour of the solvent mixture although the pure solvent wets well.

These corrections give:

$$m = \rho \cdot V_{dye\,layer} + m_{va-CNT} - m_{layer\,oversize\,at\,margin}, \tag{7.22}$$

whereas the mass of the CNTs, m_{va-CNT}, has to be add up (as they fill the homogenous composite layer) and the mass of the layer oversize at the substrate's edge, $m_{layer\,oversize\,at\,margin}$, has to be subtracted. On the basis of the density of the va-CNT array, determined to be $d = 10^8 - 10^{10}\mathrm{CNT}/cm^2$, and total forest size the CNT correction factor can be estimated to be

$$m_{va-CNT} = d \cdot A \cdot l_{va-CNT} \cdot \rho_{CNT}. \tag{7.23}$$

The second corrective factor can be obtained optically from SEM images (see Figure 7.49). The rampart at the substrate edge was typically $200\mu m$ long with a largest thickness of $5.4\mu m$. The thinnest end of the rampart had a thickness of $1.7\mu m$ (normal film thickness). This shape was approximated by a V-block (prism), see Figure 7.50. The mass was calculated from the

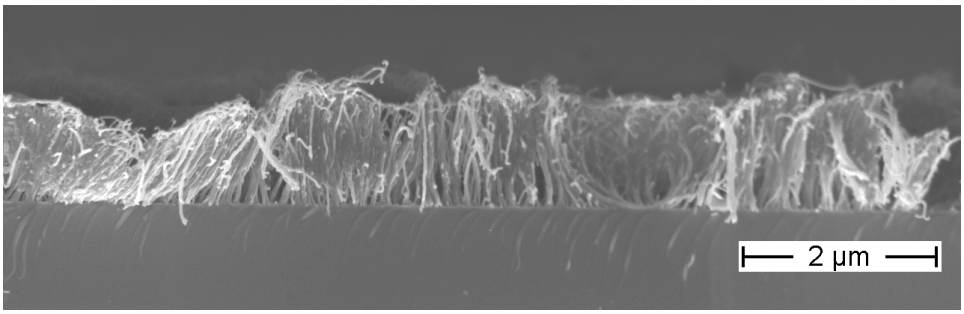

Fig. 7.40: Infiltration result when using chlorobenzene as the solvent. The macroscopic vertical alignment of the CNT is destroyed. Image taken from [143].

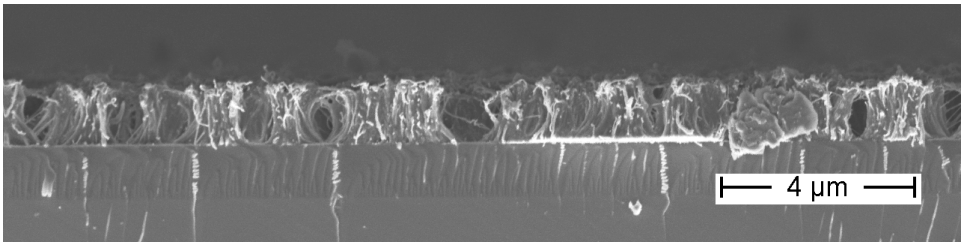

Fig. 7.41: Infiltration results of CuPc-DMA dissolved in chlorobenzene. Poor layer forming ability of the small molecule dye occurs. Image taken from [143].

multiple of the cross-section area with the length of respective substrate edge and specific density.

$$m_{layer\,oversize\,at\,margin} = \rho_{dye} \cdot A \cdot l + \rho_{dye} \cdot A \cdot b = \rho_{dye} \cdot \frac{z \cdot c}{2} \cdot 2 \cdot l + \rho_{dye} \cdot \frac{z \cdot c}{2} \cdot 2 \cdot b. \tag{7.24}$$

The correlation between the solvent parameters, dye concentration, substrate area and CNT height can be, thus, expressed as

$$c \cdot V_{liquid} = \rho_{dye} \cdot l \cdot b \cdot h + d \cdot l \cdot b \cdot l_{va-CNT} \cdot \rho_{CNT} - \left(\rho_{dye} \cdot \frac{z \cdot c}{2} \cdot 2 \cdot l + \rho_{dye} \cdot \frac{z \cdot c}{2} \cdot 2 \cdot b \right). \tag{7.25}$$

Solving equation (7.25) to give the dye layer height, h, on the substrate of the composite with the va-CNT forest yields

$$h = \frac{c \cdot V_{liquid} - d \cdot l \cdot b \cdot l_{va-CNT} \cdot \rho_{CNT} + \left(\rho_{dye} \cdot \frac{z \cdot c}{2} \cdot 2 \cdot l + \rho_{dye} \cdot \frac{z \cdot c}{2} \cdot 2 \cdot b \right)}{\rho_{dye} \cdot l \cdot b}. \tag{7.26}$$

The accuracy of the fit of equation (7.26) depends on the used dye and solvent combination. In particular, for CuPc based dyes the layer building process was highly sensitive to the CNT height and match in the dispersive and polarity rate of surface tension and solvent. Small molecule dyes showed poor layer building properties in comparison with the polymers.

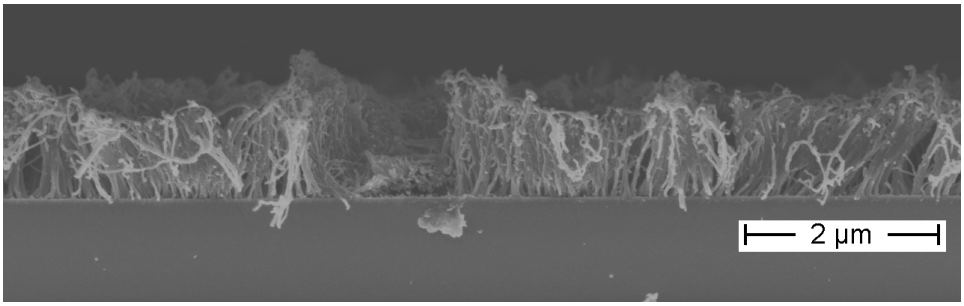

Fig. 7.42: Infiltration results of toluyene red dissolved in chlorobenzene. Toluyene red covers single CNT. The cover layer is extremely thin. Image taken from [143].

Epoxy resin

The infiltration with epoxy resin is used to rip the va-CNTs off the substrate after having cured the resin. This facilitates the deposition of an electrode onto the bottom side of the ripped off va-CNTs. These va-CNTs are then stuck on a substrate. Figure 7.52 shows the infiltrated va-CNTs before and after being ripped off the substrate. For further processing the epoxy resin should be removed. Then the va-CNT array should be infiltrated with dye and a transparent top electrode should be deposited onto the top. This procedure failed due to experimental difficulties by ripping the va-CNTs off the substrate. The epoxy resin tend to break into indefinable pieces. This made a further processing impossible.

7.4.5 Infiltration via plotting

The device used for the infiltration of the CNTs with a plotting method was a nanoplotter from GeSim. This plotter can dispense droplets from 2pL up to 15nL in volume. In order to achieve these small volumes a piezoactuator is embedded in the glass tips. This presses the droplets out of the tip according to the adjusted frequency. A pattern overview is given in Figure 7.53. The plotting area is divided into a matrix of single points. Each point represents one plotted droplet. The frequency and the density of the droplets can be adjusted, such that the layer thickness can be controlled. The density of points determines the amount of solvent plotted on the area. Moreover, the plotting regime can also be adjusted, such that the chronological order of the plotted droplets can be set. Examples of two different plotting regimes are shown in Figure 7.53. Due to the wetting properties of the liquid the droplets spread over the va-CNT array (not shown in Figure 7.53). In order to accelerate the drying process of the plotted droplets the substrate was heated up in-situ to 80°C - 120°C. This allowed the sample to be annealed during the printing process. The merging of single droplets is shown in Figure 7.54.

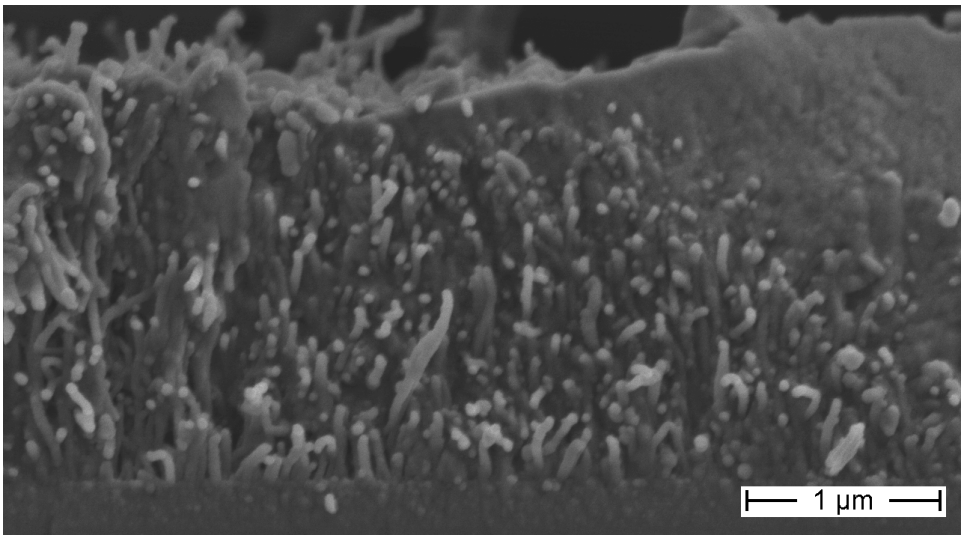

Fig. 7.43: Infiltration results of ferrocene dissolved in chlorobenzene. Ferrocene forms a good composite matrix with the va-CNT. Formation of a homogeneous layer thickness failed. The thickness varied from 1μm-3.5μm. Image taken from [143].

The driving forces of the droplets to merge were strong enough to merge even when the droplets are plotted at 100°C. Different plotting regimes yield different layer structures as shown in Figure 7.55. The composite layer of PCBM:P3HT plotted on heated substrates (100°C) yield optically same layers as plotted under room temperature 7.56. The va-CNT array was also infiltrated by plotting. Figure 7.57 shows the plotted layer. A defined area of the va-CNT array can be infiltrated by plotting as shown in Figure 7.57. Less amounts of plotted ink yields an inhomogeneous layer at the edge of the plotted area. The small grains between the large grains originate from phase separation of PCBM and P3HT, when the substrate has been annealed. These grains occur, when being poorly dissolved in the solvent, if these grains occur without an annealing treatment. Hence, the origin of these grains cannot be determined explicitly as the grains in Figures 7.55 and 7.56 appear the same.

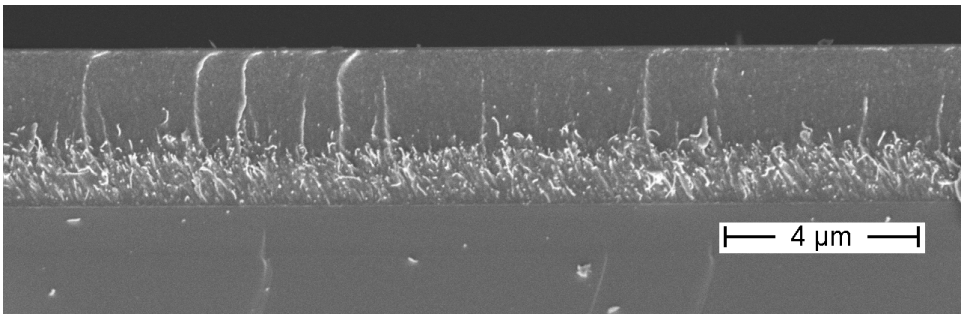

Fig. 7.44: Infiltration results of P3HT dissolved in chlorobenzene. A non- porous layer with a good thickness homogeneity was achieved. Good vertical alignment preservation was also gained. The solvent chlorobenzene is the best solvent for the infiltration. Together with P3HT an excellent layer is formed. Image taken from [143].

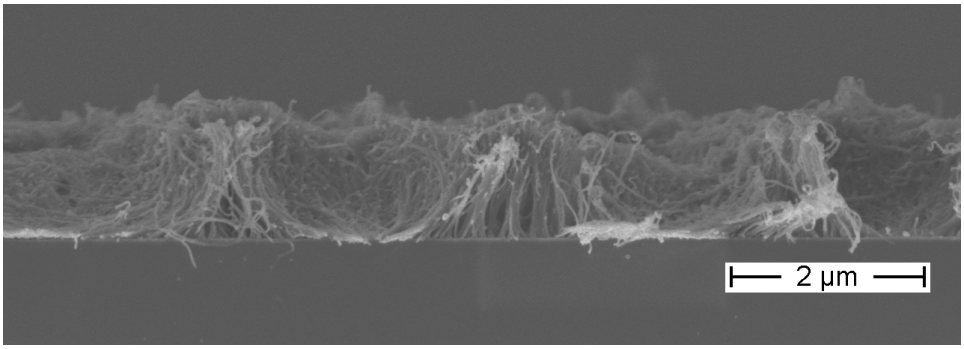

Fig. 7.45: The results of wetting with chlorobenzene and trifluoroacetic acid in a 1:1 wt.% ratio. Image taken from [143].

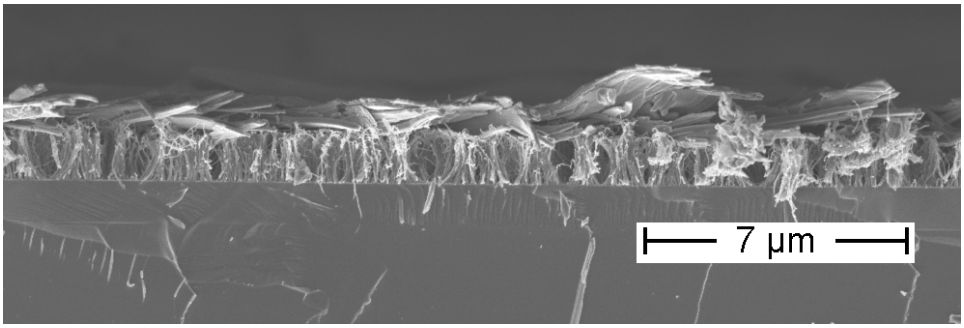

Fig. 7.46: Protonated CuPc was observed to precipitate on top of the array. A flaky layer appears. Although the solvent spreads over the va-CNT, the precipitated CuPc does not form a composite layer with the va-CNT forest. Image taken from [143].

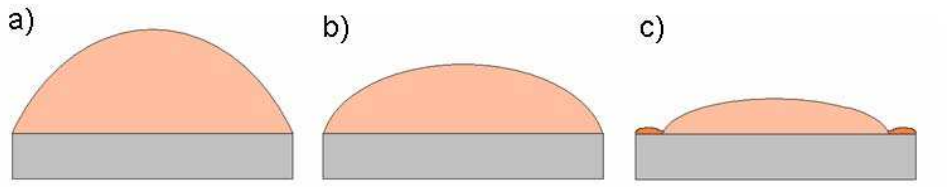

Fig. 7.47: The droplet contracts due to solvent evaporation (a-c).The dissolved dye precipitates and form a thicker layer at the substrate's edge followed by a homogenous layer size over the rest of the substrate.

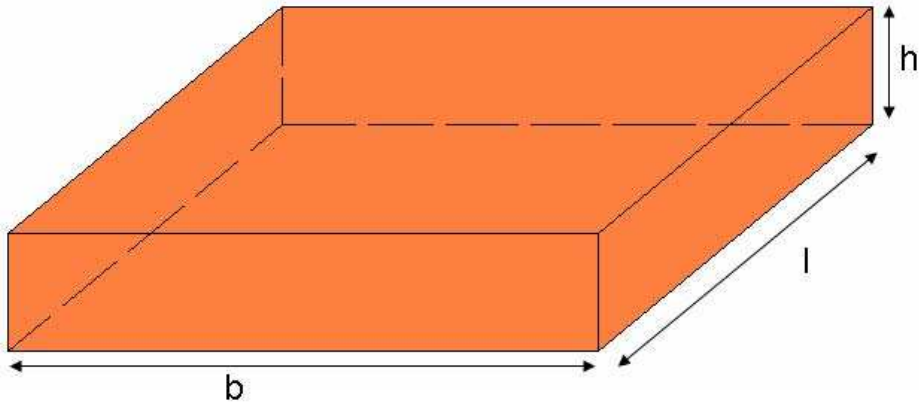

Fig. 7.48: Scheme of the formed composite layer.

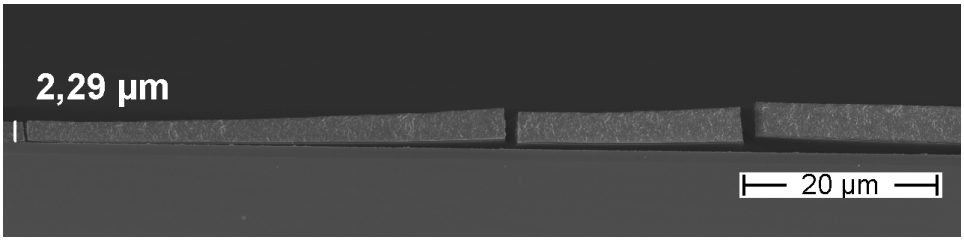

Fig. 7.49: Edge region on the wafer of infiltrated va-CNT forest substrate. The dye forms a rampart leading to a mismatch of concentration and layer size. Therefore, a correction for this has to be introduced. The rampart is around $200\mu m$ long, the thickest part is $5.4\mu m$ and the homogenous layer thickness is $1.7\mu m$.

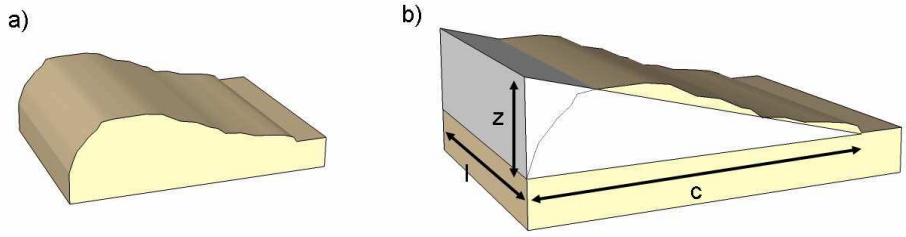

Fig. 7.50: The cross section area is approximated by a triangle, see (b), spanned by a) the difference in initial and final layer size, z, and b) the length of the rampart, c. The whole volume is obtained by multiplying the cross section by the length of the outer edge of the wafer, l.

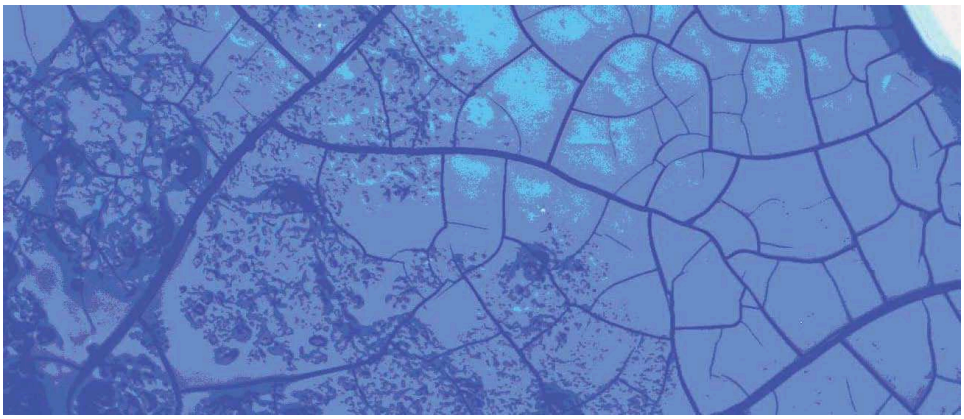

Fig. 7.51: Top view of infiltrated va-CNT forest. Image taken with an incident light microscope.

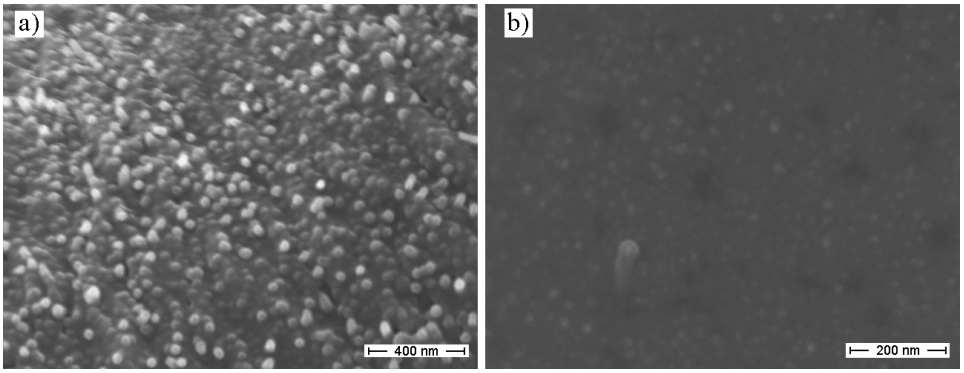

Fig. 7.52: Infiltrated va-CNT array with epoxy resin. a) top view of the array. Single CNT tips stick out of the surface. b) bottom view of the infiltrated va-CNT array. The array was ripped off the substrate. The bottom tips of the va-CNTs are visible. None of them stick out of the surface.

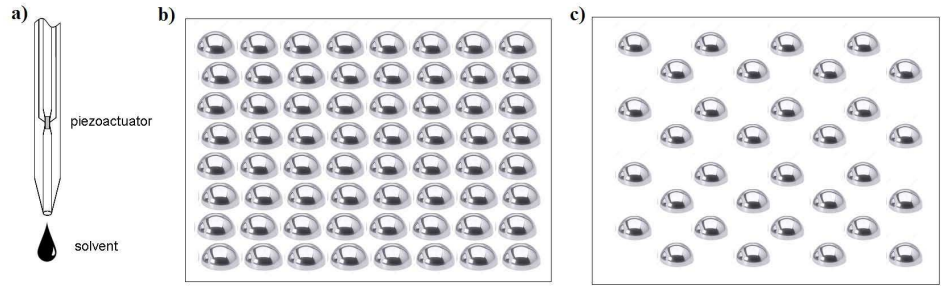

Fig. 7.53: a) Scheme of used (pico- and nano-litre) glass tip of nanoplotter. b) and c) two different plotting regimes used for adjusting the layer thickness.

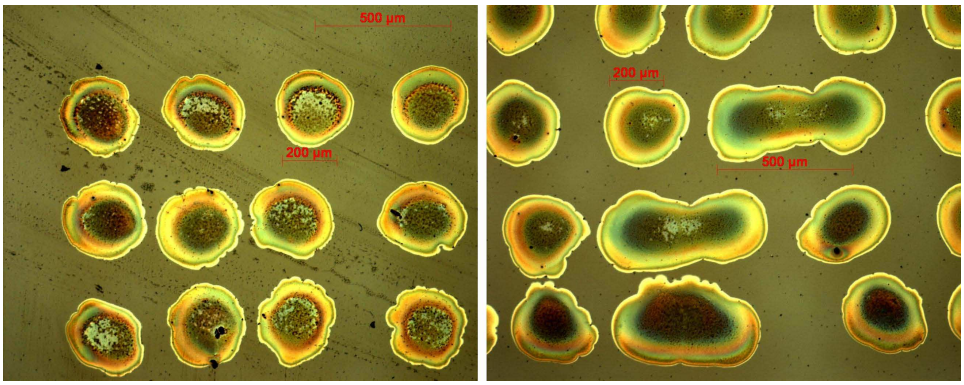

Fig. 7.54: Droplets of PCBM:P3HT printed on glass by a nanoplotter. Left: mesh-grid plotting regime at room temperature. Right: printed droplets have merged.

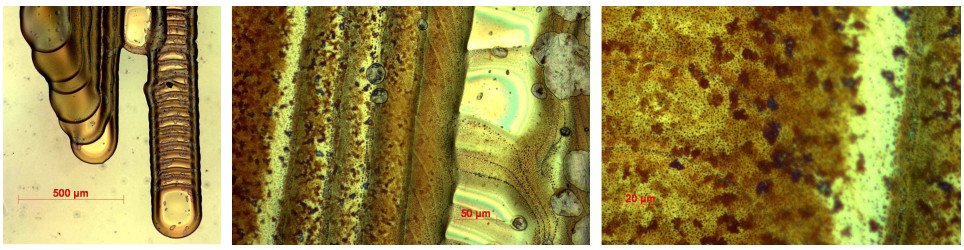

Fig. 7.55: Printed stripes of PCBM:P3HT on glass by a nanoplotter. Left: Several individual stripes forming one film. Middle: magnification of left. Grains are visible in the polymer matrix. Right: magnification of middle. The In between the large grains small grains occur.

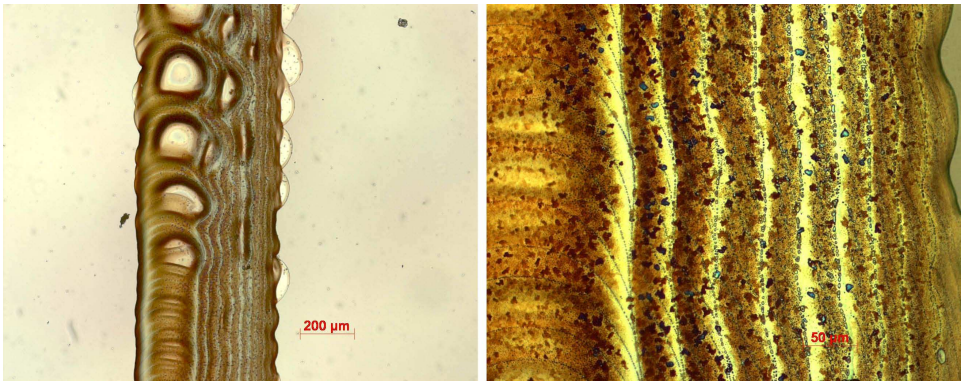

Fig. 7.56: Printed stripes of PCBM:P3HT on glass by a nanoplotter. Left: Several individual stripes forming one film. The droplets were printed closer to each other compared with the printing regime shown in Figure 7.55. The substrate was heated to 100°C during plotting. Right: magnification of the image shown on the left. Grains occur in the film.

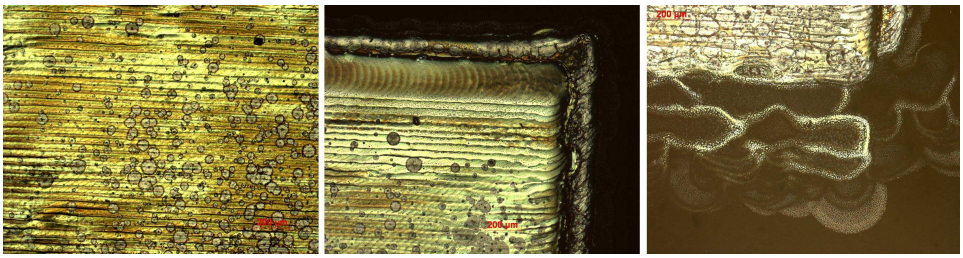

Fig. 7.57: Droplets of PCBM:P3HT printed on va-CNT array by a nanoplotter. Left: homogeneous layer plotted at 100°C. Middle: magnifications of left. Right: Less amount of plotted ink yields an inhomogeneous layer at the edge of the homogeneous layer.

7.5 Potential device

"For appropriate infiltration parameters, a homogenous smooth composite layer of the dye and CNT array was achieved, with homogenous vertical alignment of the CNTs and a dye cover layer over the entire substrate" [143] (Figure 7.58). However, in order to turn these layers into useful organic solar cell devices the addition of electrical contacts is necessary. The conductive but non-transparent TiN layer serves as the bottom electrode. Consequently, the top electrode has to be not only conductive but also transparent. "Furthermore, the deposition technique for the top electrode has to be gentle in order to protect the organic composite layer." [143] This prohibits the use of high energy methods such as sputtering. In this work both thermal evaporation and printing technique were tested. As a result, all these requirements are met by choosing Pedot:PSS. The composite thickness from the tips of the CNTs to the counter electrode have to be in the range of 100-200nm in order to take into account the limitations imposed by the high absorption coefficients of organic dyes. The match of dye concentration, substrate area and layer size yield $1mm^2$ of va-CNT array has to be wetted by 0.6μL solvent with dye concentration of c=12.5mg/mL for the layer shown in Figure 7.58.

7.5.1 Characterisation

The Measurement of the CNT-TiN interface was done under room temperature. A round electrode of copper with a diameter of 3mm was put on the tip of a micrometer test prod. Conductive silver lacquer was add to improve contact of copper and prod. The copper was cleaned with acid to remove impurities. The copper electrode was placed with the adjustment of micrometer screws. Conductive AFM measurements were done to prove these macroscopic results on a microscopic scale. The I-V characteristics of the prepared va-CNT solar cells via infiltration with different dyes imply

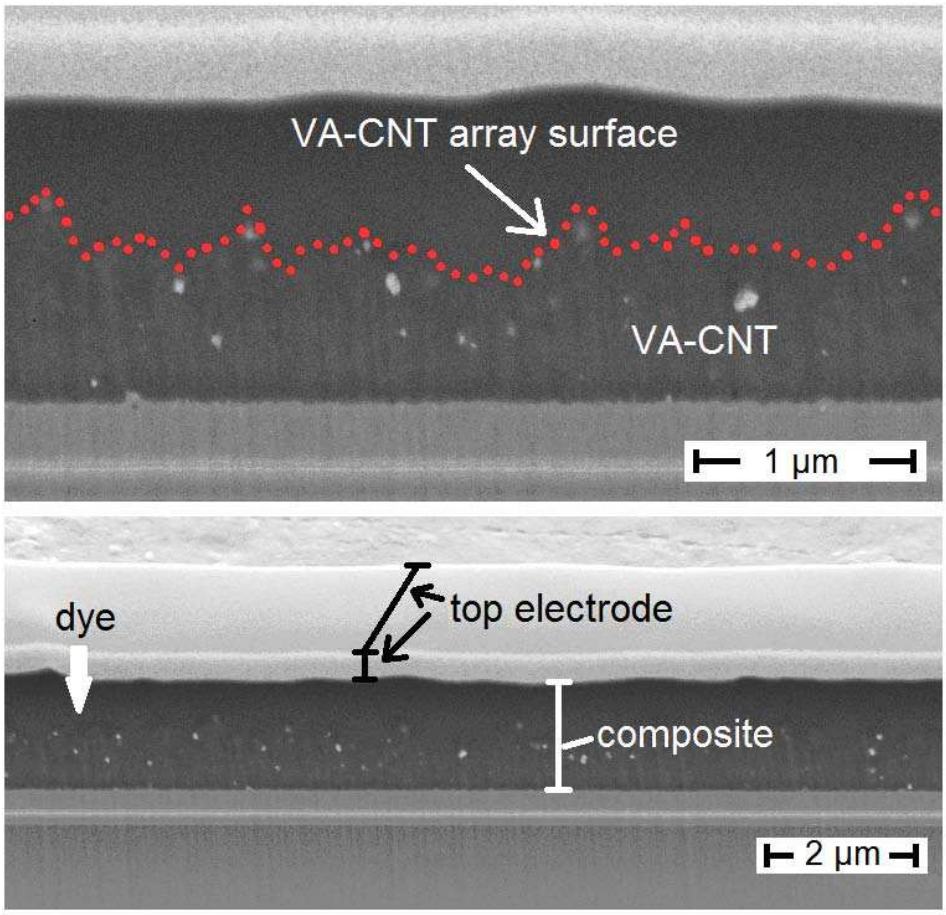

Fig. 7.58: "FIB slice of CNT array infiltrated with P3HT for a perfect match of infiltration parameters. The brighter stripes represent the CNT array. Light particles are catalyst residuals." Image and text taken from [143].

that different devices are finally made by the same preparation method. The different types of devices are resistors, diodes, backward diodes and proof of principle of organic solar cells. The graphs axes are scaled in the typical way for organic solar cells, which means the y-axis corresponds to the current density S.

7.5.2 Solar cells

According to the structure given in Figure 7.58 the layer thickness fits and the electrical measurements give a clear solar cell response. The band diagram of the va-CNT solar cell is shown in Figure 7.61. Although the short circuit current density is small ($J_{sc} = -6.85 \cdot 10^{-4} mA/cm^2$), the open circuit voltage reaches $V_{oc} = 157mV$. This is pretty enough to prove the principal

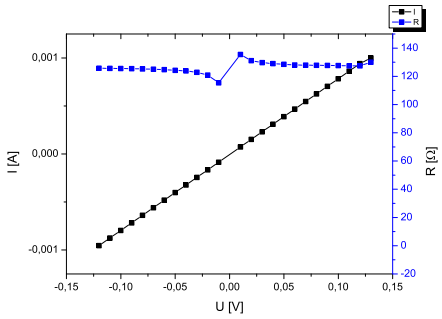

Fig. 7.59: Resistance of CNT-TiN interface. The average resistance equals 126.5Ω (standard deviation $\sigma = 3.74$).

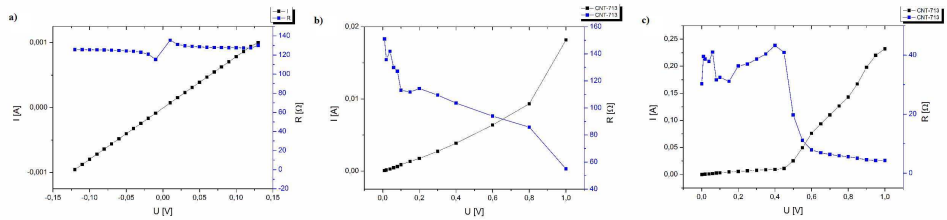

Fig. 7.60: Resistance of CNT-TiN interface. Three measurements were done using a copper electrode. The diameter of the electrode was $11mm^2$. a)-c) Different results were obtained due to different contact formation of CNT array and copper electrode.

functioning.

Effective area adaption

Due to the large absorption coefficient of $\alpha = 10^5 cm^{-1}$ the penetration depth of incident light is 100nm-300nm. Film thicknesses larger than 300nm act as optical filter, because the light is completely absorbed. The film thickness which covers the infiltrated va-CNT array from the CNT tips to the top electrode varies from 150nm-800nm. Subsequently, the parts of the infiltrated va-CNT array which are covered with a dye layer larger than 250nm are shadowed. These parts do not contribute to the photovoltaic active area. Figure 7.63 shows the active area adjusted I-V characteristics. Subtracting the inactive areas from the active areas yields corrective factors, K_1, K_2. The effective areas are three to four magnitude of orders smaller than the original area, which is the area of the top electrode. Figure 7.64 shows the active area marked with black rectangles. Two different assumptions of photovoltaic active areas have been done. These assumptions yield two different corrective factors, K_1, K_2. The corresponding efficiencies, fill factors, open circuit voltages, and short circuit current densities are listed in table 7.4.

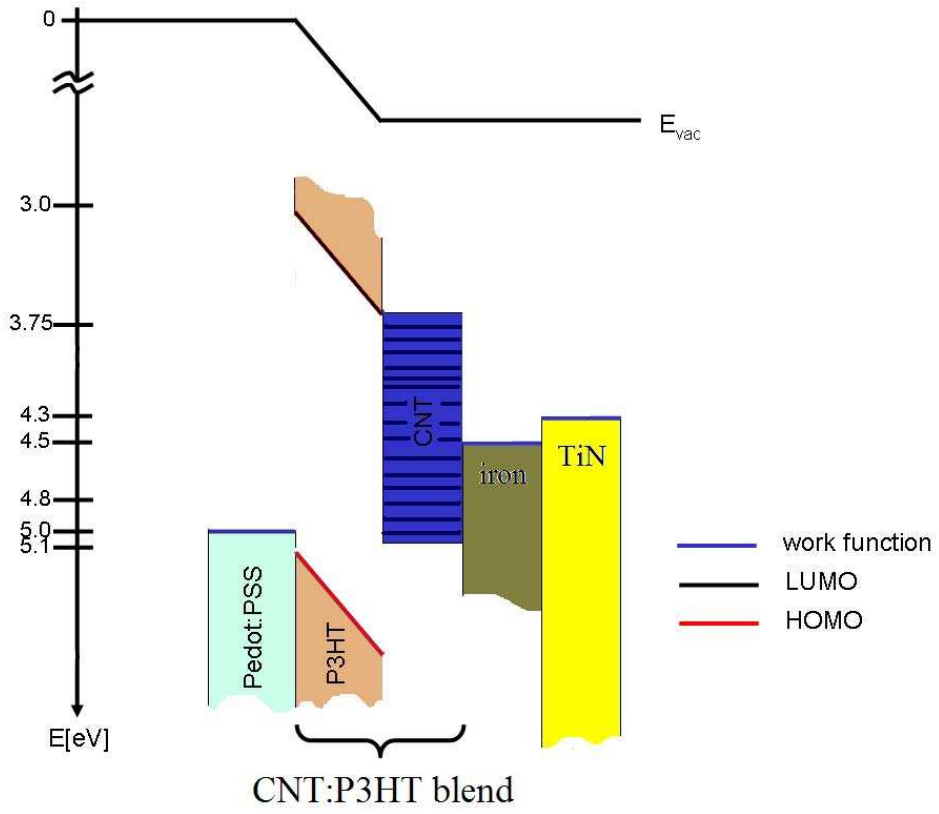

Fig. 7.61: Scheme of the band diagram of the va-CNT solar cell. The work function of the CNTs is assumed to vary in the range reported by literature. PCBM was added to enhance homogeneous layer formation. Additionally, the PCBM enhances the exciton dissociation. Dissociated charge carriers are expected to hop from the PCBM onto the CNTs. The work function of the CNTs is in the range from 3.75eV-4.8eV as reported by literature. The different energy levels of their work function are indicated by solid lines within the blue rectangle.

7.6 Summary

The va-CNT was purified using a gas phase method. This method preserves the vertical alignment of the CNT forest. The va-CNT array was treated by oxygen plasma. This yield to the carbonylation of iron catalyst due to the presence of carbon monoxide. Carbon monoxide is a byproduct of insufficient carbon oxidation during the plasma treatment. The purified va-CNT array was plasma-assisted functionalized. Fluorine atoms were covalently bonded to the CNT by NF_3-plasma. A wetting study of a va-CNT array was presented. Different infiltration techniques were studied and a homogeneous infiltration of the va-CNT forest achieved. Prototypes of organic solar cells made of the va-CNT forest were fabricated and analysed.

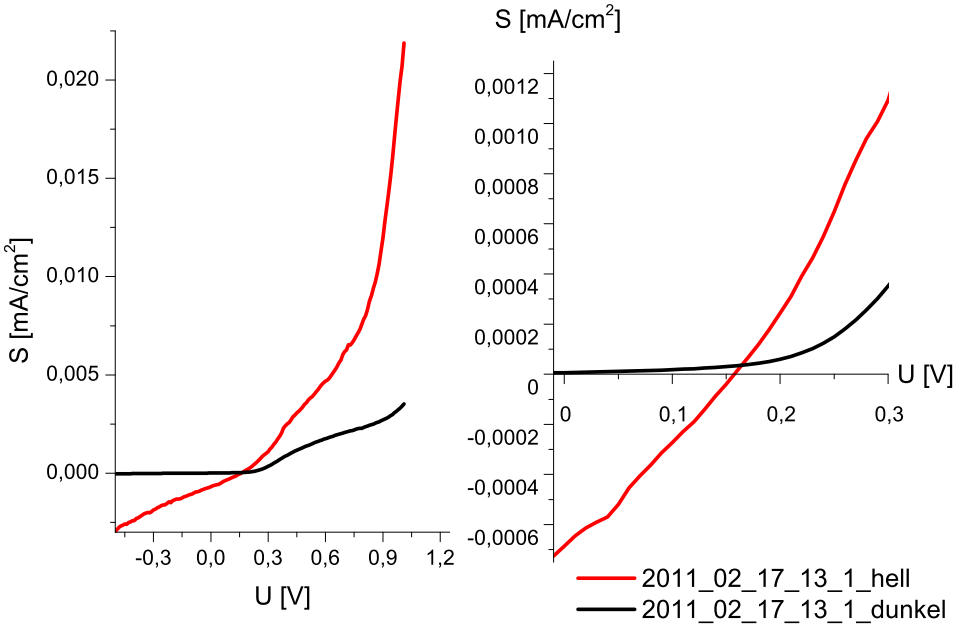

Fig. 7.62: J-V characteristics of a P3HT:va-CNT organic solar cell. Left: full graph of J-V characteristics, where black corresponds to dark condition and red represents under illumination. Right: magnification around the origin. The characteristic values are: $V_{OC} = 0.157V$, $J_{SC} = -6.85 \cdot 10^{-4} mA/cm^2$, FF=0.27, $\eta = 2.89 \cdot 10^{-5}\%$, $R_s = 859\Omega$, $R_{sh} = 17722\Omega$, n=2.89.

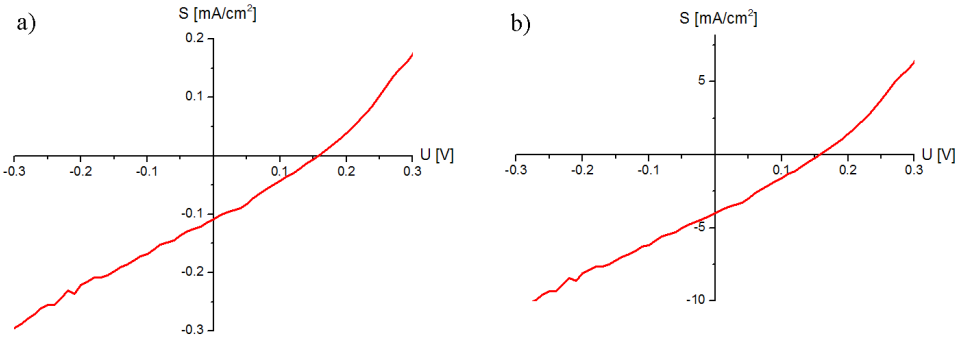

Fig. 7.63: J-V characteristics of a P3HT + va-CNT organic solar cell after correction of the effective area. a) J-V characteristics with adjustment of $K_1 = 0.0063$. b) J-V characteristics with adjustment of $K_1 = 1.73 \cdot 10^{-4}$.

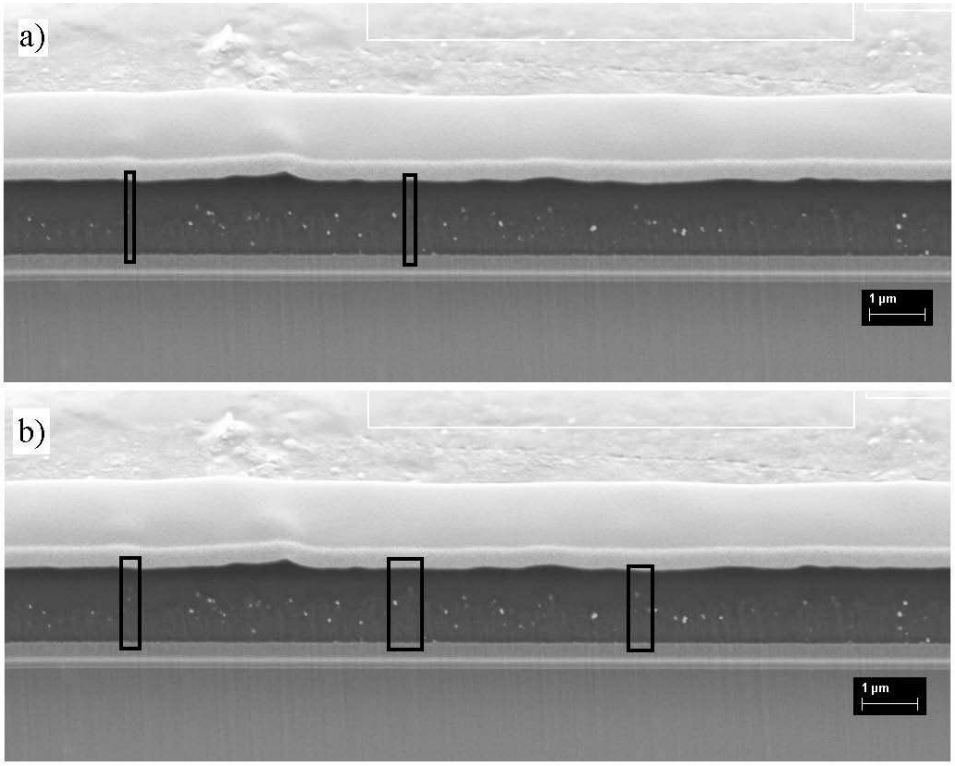

Fig. 7.64: J-V characteristics of a P3HT + va-CNT organic solar cell. The active areas are indicated with black coloured rectangles. a) the corrective factor equals $K_2 = 1.73 \cdot 10^{-4}$. b) more areas have been assumed to be photovoltaic active due to fuzzy cover layer thickness and va-CNT heights. The corrective factor equals $K_1 = 0,0063$.

sample		FF	J_{sc} $[mA/cm^2]$	V_{oc}[V]	η[%]
$va-CNT$	as-is	0.27	-0.000685	0.157	0.0000289
$va-CNT$	K_1	0.27	-0.108	0.157	0.0046
$va-CNT$	K_2	0.27	-3.96	0.157	0.167

Tab. 7.4: Overview of the characteristic values of the va-CNT solar cell with different corrective factors. These factors adjust the difference between the electrode areas and effective photovoltaic active area. The values of the factors are: K_1=0.0063 and $K_2 = 1.73 \cdot 10^{-4}$.

8. CONCLUDING REMARKS

8.1 Conclusions

The results reported and discussed in this thesis confirm the capability to fabricate organic solar cells can be fabricated by using the combination of CNT and an organic absorber, which enhances absorption of light in the visible range. The absorption properties and energy levels at the various interfaces yield diverse current current density-voltage (J-V) dependencies. Thus, organic solar cells with efficiencies of up to 1% were produced. In the current work, different dyes and acceptor material combinations were investigated for their performance. For such investigations devices with different architectures were fabricated and studied. The solution processed solar cells were annealed in order to optimize layer morphology.

The small molecules of CuPc and its derivatives showed different layer building properties by spin-coating technique as the polymer P3HT. The CuPc tends to form crystallites which greatly improves the transport properties for charge carriers due to the periodic lattice structure. It was found that for a larger number of crystal grains within the layer there was an increase in the series resistance in the layer due to the increased number of grain boundaries. This corresponds well with the literature, [263]. Best device performances were achieved from devices built with P3HT.

The surface roughness of the devices, as analyzed on AFM, is RMS=0.105μm. The height of the va-CNT forest varies about $\pm 0.5 \mu m$ along the length of the substrate - confirmed with FE-SEM. Thus, the CNTs of the va-CNT forest are not of equal length. The va-CNT array has regions where super-long CNT bundles either stick out above the surface or alternatively, the array exhibits regions with super-short CNTs. These regions appear as "holes" from the top view of the CNT forest forest shown in Figure 7.3. This causes a lot of difficulties when fabricating working devices because constant layer thicknesses are crucial for organic solar cells. The device performances vary extremely - up to several percent - due to layer thickness variations of a few tens of nanometres.

The va-CNT array are purified from catalyst residues (i.e. iron) through a process of plasma assisted oxidation. During the plasma treatment carbon monoxide is created. This carbon monoxide triggers a carbonylation. The carbonylation transforms the solid iron into a gas phase. EDS and TEM measurements were used to confirm the absence of iron within the va-CNT

sample after the plasma process .
The wetting studies revealed a variation in the surface energy of the synthesized va-CNT forests and an influence of the polar-dispersive ratio of the used solvent on the layer building process. The infiltration studies showed the influence of the composition of the solvent and dye on the resulting composite layer. Aqueous mixtures of solvents cause a collapse of the vertically alignment of the CNT forest. A mixture of water and methanol induces a ruptured layer, which is full of trenches (see Figure 7.24). Furthermore, the CNT-dye composite locally forms a button-mushroom shape. The va-CNT wetting behaviour occasionally varied between samples, despite there being no change in all the infiltration parameters such as type of dye, concentration, solvent and atmosphere. These differences appear due to variations in the process parameters during the pe-CVD synthesis of the va-CNT forests. These variations are not optically visible but AFM measurements can reveal these differences in sample homogeneity (see Figure 7.3).
Partial wetting occurs if pure distilled water is used as the solvent. The precipitated dye formed a thin layer on top of the va-CNT array. Only the tips of the CNTs are wetted by water. The dye layer did not penetrate the forest further than the wetting depth.
The ultra hydrophobic surface of the va-CNT arrays can be infiltrated only with certain solvent-dye combinations whilst preserving the vertical structure of the array. The various solvents have a differing degree of polarity. It is the particular combination that determines the wetting regime. Variations in the homogeneous CNT forest height neither interfere with the wetting behaviour nor influence the changes in the vertical alignment of the CNT due to the wetting process. The wetting regime is either heterogeneous or homogeneous. Wetting the va-CNT array by water stays heterogeneous as shown in Figure 7.21. The dried dye formed a film which supported each single va-CNT in the horizontal direction and, thereby, suppressed the collapse of the structure. The films produced in this study stayed homogenous.
The wetting of different solvent dye combinations on CNT arrays was investigated. In some case the choice of solvent-dye combination can modify the alignment of the CNT array. Combinations can be found where CNT array alignment is preserved, or trenches, zigzag and mushroom profiles are formed. The wetting of water on va-CNT is heterogeneous (Cassie-Baxter regime) which causes, for instance CuPc-TS, layer to reside on top of the array. In this case full infiltration can be achieved by the addition of surfactants. Less polar solvents yield a reduced wetting affinity. Several dyes such as CuPc, CuPc-DMA, CuPc-TS, toluyene red, ferrocene and P3HT have been studied. The polymers showed much better layer building properties in comparison to the small molecule dyes. The optimized values for dye concentration with respect to wetted substrate area were found to lie in range of 10mg/mL and $1\mu L/mm^2$. Fully infiltrated smooth layers were obtained and incorporated into a functional device assembly which included

a substrate, back electrode, blocking layer and top electrode.
The CNT array grown on TiN are very sensitive to synthesis parameter variation. In order to synthesize an array of height 100-300nm short synthesis times should just be needed. However, the synthesis either resulted in no CNTs or their average length was 1-1.3μm. CNTs grown on Al_2O_3 does not have such a sensitivity like TiN. Hence, they could be synthesized in the desired range. However, the infiltrated CNT array must separated from the substrate after the infiltration process in order to deposit a bottom electrode contact for the CNTs, because Al_2O_3 is an insulator. The actual approach used was:

- infiltrate the CNT array,
- deposit a top electrode on it,
- cover the CNT-dye composite with a cover material (for structural reinforcement),
- separate the CNT-dye composite from the substrate (structural cohesion of the composite is maintained by the cover material), and
- add a bottom electrode.

In some instances, this failed in some sense because the mechanical cohesion of the CNT-dye composite covered with epoxy resin could not be maintained for a sufficient sample size. Nevertheless, in principle, an infiltrated CNT array can be covered by a transparent epoxy resin and separated from a silicon substrate.
Infiltration of the va-CNT array could not be achieved by thermal evaporation. The va-CNT substrate could not be heated up during the thermal evaporation of the dye (CuPc). This caused there to be a big temperature difference between the temperature of the sublimated dye (around 400°C) and the substrate (estimated to be slightly higher than room temperature). The dye, in the study only CuPc, immediately condensed for this reason on top of the surface of the CNT array, and crystallized there. Furthermore, due to the uncontrollable va-CNT synthesis the array contains regions where some CNTs are much shorter than their neighbouring CNTs. This appears macroscopically as holes of several microns in diameter on the surface of the array. These holes are not filled with dye sufficiently during the evaporation process. Consequently, these non-coated regions cause short circuits when the transparent top electrode is deposited onto the CuPc layer. These short-circuited devices cannot work as organic solar cells (OSCs).
The va-CNT array could be infiltrated with different dyes. The layer homogeneity depended on the structure of the dye (small molecule or polymer, planar or spherical) and its affinity to retain its initial form (powder) instead of remaining as a homogeneous layer. The infiltration of the array was made

either by drop coating or printing. Drop coating yielded good homogeneous layers when a small amount of PCBM was added to P3HT. The PCBM acts as a lubricant as its football like molecular shape makes it easy to rotate. Consequently, it can act as a "ball bearing" for the polymer P3HT during the drying process and reduce the mechanical stress in the final layer.
Only the outer sidewall of a CNT is chemically functionalized with NF_3-plasma. In this case the outermost sidewall of every MWCNT is functionalized. All pristine MWCNT are known to be metallic due to either interwall interactions or to at least one of the tubes (of the interlaced tubes, which form the MWCNT) being metallic and electrically connecting the ends of the MWCNT. If the latter assumption is true, MWCNT are not metallic in nature. Only the outermost sidewall of every CNT forms the heterojunction with the surrounding dye. As a consequence the possible energy yield of the heterojunction interface of the semiconducting CNT and dye is significantly increased by the fluorination with the NF_3.
The observed contact angle of the infiltrated va-CNT array shown in Figure 5.10 fits well with the contact angle of a single CNT reported in the literature by [227]. The surface energy of a single CNT was calculated to be γ_{CNT}=24.4mN/m, with a polarity p=0.22. The polar surface energy equals γ_s^p=5.4mN/m. Hence, the dispersive fraction of the surface energy γ_s^p=19mN/m. The absolute value of the surface energy of a CNT found in this study agrees closely with that of graphite. The same is also true for the polarity.
CNT dispersion appeared to be a major challenge without the addition of surfactants. Strategies to add functional groups or single atoms to the CNT sidewall, which are known to change the CNT from being super-hydrophobic to a more hydrophilic state, were investigated. MWCNTs were much more easily dispersed in different liquids than SWCNTs. All dispersion related functionalisations seemed to work better for the MWCNTs. The improvements of the dispersing properties were more significant for MWCNTs in the various tested aqueous and organic solvents. As a result the SWCNTs were much more difficult to disperse. The reproducibility of the functionalisation with regard to comparable results was a hard task. The only way to achieve this was by increasing the tolerance towards the dispersebility, although UV-vis data proved similar results for CNT concentrations of different CNT dispersions.
The introduction of the CNT into the organic matrix in an OSC device causes in some cases a plateau in the first quadrant of the J-V dependency. In this case the device is working as a tunnel diode. The CNTs influence the band alignment of the device, which allows the electrons to tunnel backwards. This results in a decrease in the current and the knob shape forms in the J-V curve.

8.2 Outlook

In the light of the results of the investigations undertaken in this work several further studies are suggested. The influence of the SWCNT length on the CNT dispersion should be investigated. The dispersion properties showed to depend much on CNT length. Short CNT are even disperseable in water, [264] and [265] (additionally, an oxidation treatment was made prior to the dissolution).
Infiltrated CNT arrays have the potential to be applied in organic solar cells as part of an ideal bulk-heterojunction cell structure, where the CNT provides the acceptor and the dye works as the donor. In order to achieve an idealised architecture the top layer thickness still needs to be reduced, the work function / ionization energy of the CNT has to be tuned, and arrays of purely semiconducting CNT should be used, if there availability is ever achieved. Infiltration of the dye in the CNT array is not the limiting process step. Only the purity of the layers is expected to be the main issue once the previously listed factors have been optimized.
The CNT array can be infiltrated with various soluble materials. By using different functional fillers the CNT structures can also be applied to sensory, Organic light emitting diodes (LEDs), or other nanostructured functional devices.
Generally, the CNT forest can be infiltrated via evaporation of the source material [266]. The temperatures of the evaporated source material and the substrate (the CNT forest) have to be the same, or close to each other. This is necessary to suppress the dye to condense on the top of the CNT array. Subsequently, the infiltration via thermal evaporation can be achieved using substrate heating.
The electrical transport properties of the CNTs are based upon their delocalized π-system. This delocalized π-system exists due to covalent bonded carbon atoms as described in chapter 3. E.g., for transparent electrodes CNTs are spin coated onto a glass substrate. These thin films of CNTs have sheet resistances in the range of $1 \cdot 10^2 \Omega$. These relatively high sheet resistances exist, because the π-systems of the single CNTs do not overlap well with each other, resulting in high resistances for charge carriers travelling from one CNT to another. Subsequently, the π-systems of neighbouring single CNTs have to be bond chemically with alternating sp^1- and sp^2-hybridized carbon bonds to create one large π-system spread over several single CNTs. This can be achieved with acid-base and plasma treatments, or with combinations of both treatments.
CNTs can be used as sensors as well. Their application as chlorine sensor looks prospering. First prototypes have been manufactured already, [267], and [268]. Consequently, CNTs can be applied as low-cost alternative chlorine sensors for isolated application for water purification, because commercial sensors cost about 150 € and have to be changed after an operation time

of six month.

BIBLIOGRAPHY

[1] C. W. Tang. 2-layer organic photovoltaic cell. *Applied Physics Letters*, 48(2):183–185, 1986.

[2] Website. Available online at `http://www.nrel.gov/ncpv/images/efficiency_chart.jpg`. Visited on November 11th 2012.

[3] Website. Available online at `http://www.bmu.de/fileadmin/bmu-import/files/pdfs/allgemein/application/pdf/energiekonzept_bundesregierung.pdf`. Visited on November 9th 2012.

[4] Website. Available online at `http://www.ier.uni-stuttgart.de/publikationen/arbeitsberichte/Arbeitsbericht_04.pdf`. Visited on November 11th 2012.

[5] Website. Available online at `http://www.bdew.de/internet.nsf/id/DE_Energiedaten`. Visited on November 8th 2012.

[6] Website. Available online at `http://www.tecson.de/historische-oelpreise.html`. Visited on November 8th 2012.

[7] Website. Available online at `http://www.sapa-solar.com/germany/EineversprechendeLösung/Photovoltaik.html`. Visited on November 10th 2012.

[8] Website. Available online at `http://ec.europa.eu/energy/strategies/2008/doc/2008_11_ser2/strategic_energy_review_wd_cost_performance.pdf`. Visited on June 27th 2012.

[9] Website of Plextronics, Inc. Available online at `http://www.plextronics.com/article/13`. Visited on November 13th 2012.

[10] Volker Quaschning. *Regenerative Energiesysteme / Technologie, Berechnung, Simulation ; mit 113 Tabellen*. Hanser, München, 7., aktualisierte aufl. edition, 2011.

[11] Website. Available online at `http://www.wittmann-travel.de/uploads/pics/H-alpha_Sonne.gif`. Visited on July 5th 2012.

[12] Website. Available online at `http://www.idtechex.com/research/reports/organic-photovoltaics-opv-2012-2022-technologies-markets-players-000319.asp`. Visited on August 17th 2012.

[13] Website. Available online at `http://www.heliatek.com/newscenter/latest_news/heliatek-erzielt-mit-107-effizienz-neuen-weltrekord-fur-seine-organische-tandemzelle/` Visited on August 18th 2012.

[14] A. Pochettino. *Acad. Lincei Rend.*, 15:355, 1906.

[15] D. Bilby, B. G. Kim, and J. Kim. Recent design strategies for polymer solar cell materials. *Pure and Applied Chemistry*, 83(1):127–139, 2011.

[16] C. J. Brabec, M. Heeney, I. McCulloch, and J. Nelson. Influence of blend microstructure on bulk heterojunction organic photovoltaic performance. *Chemical Society Reviews*, 40(3):1185–1199, 2011.

[17] L. J. A. Koster. Charge carrier mobility in disordered organic blends for photovoltaics. *Physical Review B*, 81(20):205318, 2010. PRB.

[18] Website. Available online at `http://www.aaronsenvironmental.com/2009/07/mitsubishis-organic-photovoltaic-modules-solar-panels`. Visited on November 10th 2012.

[19] R. O. Loutfy and J. H. Sharp. Photo-voltaic properties of metal-free phthalocyanines .1. al-h2pc schottky-barrier solar-cells. *Journal of Chemical Physics*, 71(3):1211–1217, 1979.

[20] N. S. Sariciftci and A. J. Heeger. Reversible, metastable, ultrafast photoinduced electron-transfer from semiconducting polymers to buckminsterfullerene and in the corresponding donor-acceptor heterojunctions. *International Journal of Modern Physics B*, 8(3):237–274, 1994.

[21] P. Peumans, A. Yakimov, and S. R. Forrest. Small molecular weight organic thin-film photodetectors and solar cells. *Journal of Applied Physics*, 93(7):3693–3723, 2003.

[22] B. Maennig, J. Drechsel, D. Gebeyehu, P. Simon, F. Kozlowski, A. Werner, F. Li, S. Grundmann, S. Sonntag, M. Koch, K. Leo, M. Pfeiffer, H. Hoppe, D. Meissner, N. S. Sariciftci, I. Riedel, V. Dyakonov, and J. Parisi. Organic p-i-n solar cells. *Applied Physics A*, 79(1):1–14, 2004.

[23] G. Yu, J. Gao, J. C. Hummelen, F. Wudl, and A. J. Heeger. Polymer photovoltaic cells - enhanced efficiencies via a network of internal donor-acceptor heterojunctions. *Science*, 270(5243):1789–1791, 1995.

[24] Website. Available online at `http://www.sigmaaldrich.com/catalog/product/aldrich/702854?lang=de&region=DE`. Visited on November 10th 2012.

[25] Website. Available online at `http://www.sigmaaldrich.com/catalog/product/aldrich/698989?lang=de&region=DE`. Visited on November 10th 2012.

[26] S. J. Tans, M. H. Devoret, R. J. A. Groeneveld, and C. Dekker. Electron-electron correlations in carbon nanotubes. *Nature*, 394(6695):761–764, 1998.

[27] B. Q. Wei, R. Vajtai, and P. M. Ajayan. Reliability and current carrying capacity of carbon nanotubes. *Applied Physics Letters*, 79(8):1172–1174, 2001.

[28] S. Hong and S. Myung. Nanotube electronics - a flexible approach to mobility. *Nature Nanotechnology*, 2(4):207–208, 2007. 160DQ Times Cited:52 Cited References Count:8.

[29] C. T. White and T. N. Todorov. Carbon nanotubes as long ballistic conductors. *Nature*, 393(6682):240–242, 1998. 10.1038/30420.

[30] Website. Available online at `http://www.sigmaaldrich.com/catalog/product/aldrich/379646?lang=de&region=DE`. Visited on November 10th 2012.

[31] Website. Available online at `http://www.sigmaaldrich.com/catalog/product/aldrich/684457?lang=de&region=DE`. Visited on November 10th 2012.

[32] Peter Würfel. *Physics of solar cells : from principles to new concepts*. Physics textbook. Wiley-VCH, Weinheim, 2005.

[33] Markus Schwoerer and Hans Christoph Wolf. *Organische molekulare Festkörper : Einführung in die Physik von π-Systemen*. Lehrbuch Physik. Wiley-VCH, Weinheim, 2005. 05N051087 1140539 000 Markus Schwoerer; Hans Christoph Wolf. Ill., graph. Darst. ; 24 cm. Literaturangaben Pi-Systemen.

[34] V. Coropceanu, J. Cornil, D. A. da Silva, Y. Olivier, R. Silbey, and J. L. Bredas. Charge transport in organic semiconductors (vol 107, pg 926, 2007). *Chemical Reviews*, 107(5):2165–2165, 2007.

[35] J. Lee, S. Baek, J. B. Park, W. Lee, S. H. Han, and S. H. Lee. A facile method to prepare regioregular poly(3-hexylthiophene) nanorod arrays using anodic aluminium oxide templates and capillary force. *New Journal of Chemistry*, 33(5):986–990, 2009.

[36] X. Y. Zhu, Q. Yang, and M. Muntwiler. Charge-transfer excitons at organic semiconductor surfaces and interfaces. *Accounts of Chemical Research*, 42(11):1779–1787, 2009.

[37] C. Silva. Organic semiconductors a little energy goes a long way. *Nature Materials*, 9(11):884–885, 2010.

[38] N. Kim, B. Domercq, S. Yoo, A. Christensen, B. Kippelen, and S. Graham. Thermal transport properties of thin films of small molecule organic semiconductors. *Applied Physics Letters*, 87(24):–, 2005.

[39] J. Loos, X. N. Yang, M. M. Koetse, J. Sweelssen, H. F. M. Schoo, S. C. Veenstra, W. Grogger, G. Kothleitner, and F. Hofer. Morphology determination of functional poly[2-methoxy-5-(3,7-dimethyloctyloxy)-1,4-pheny[enevinylene]/poly[oxa-1,4-phenylene-1,2-(1-cyanovinylene)-2-methoxy,5-(3,7-dimethyloctyloxy)-1,4-phenylene]1,2-(2-cyanovinylene)-1,4-phenylene] blends as used for all-polymer solar cells. *Journal of Applied Polymer Science*, 97(3):1001–1007, 2005.

[40] N. Camaioni, G. Ridolfi, G. Casalbore-Miceli, G. Possamai, and M. Maggini. The effect of a mild thermal treatment on the performance of poly(3-allkylthiophene)/fullerene solar cells. *Advanced Materials*, 14(23):1735–+, 2002.

[41] Michael Hoffmann. Organische halbleiter. Unpublished, 2006. Vorlesungsmanusskript, nicht veröffentlicht.

[42] Michael Hoffmann. Organische halbleiter. Unpublished, 2007. Vorlesungsmanusskript, nicht veröffentlicht.

[43] A. Colsmann. *Ladungstransportschichten für effiziente organische Halbleiterbauelemente*. PhD thesis, Universität Karlsruhe, 2008.

[44] Martin Pope and Charles E. Swenberg. *Electronic processes in organic crystals and polymers*. Oxford University Press, New York [u.a.], 2. ed. edition, 1999.

[45] Martin Pfeiffer. *Controlled doping of organic vacuum deposited dye layers / basics and applications*. 1999.

[46] G. R. Desiraju and A. Gavezzotti. Crystal-structures of polynuclear aromatic-hydrocarbons - classification, rationalization and prediction from molecular-structure. *Acta Crystallographica Section B-Structural Science*, 45:473–482, 1989.

[47] Mattheus. *Polymorphism and electronic properties of pentacene*. PhD thesis, Groningen, 2002.

[48] Kuzma. Charge transport in thin layers of organic crystals. *Journal of Physics: Conference Series*, 30:307–320, 2006.

[49] R. L. Martin, J. D. Kress, I. H. Campbell, and D. L. Smith. Molecular and solid-state properties of tris-(8-hydroxyquinolate)-aluminum. *Physical Review B*, 61(23):15804–15811, 2000.

[50] Felix Gutmann and E. Lawrence. *Organic Semiconductors*. John Wiley and Sons, New York-London-Sydney, 1967.

[51] Philip A. Leighton. Electronic processes in ionic crystals (mott, n. f.; gurney, r. w.). *Journal of Chemical Education*, 18(5):249–null, 1941. doi: 10.1021/ed018p249.1.

[52] J. S. Bonham and D. H. Jarvis. New approach to space-charge-limited conduction theory. *Australian Journal of Chemistry*, 30(4):705–720, 1977.

[53] K. Hummer, P. Puschnig, and C. Ambrosch-Draxl. Ab initio study of anthracene under high pressure. *Physical Review B*, 67(18), 2003.

[54] T. Stübinger. *Optische Modellierung und Charakterisierung von organischen Donor-Akzeptor-Solarzellen*. Perspektivenverlag, 1. edition, 2005.

[55] Website. Available online at `http://en.wikipedia.org/wiki/Air_mass_%28solar_energy%29`. Visited on November 11th 2012.

[56] Website. Available online at `http://www.newport.com/Einführung-in-die-Sonnenstrahlung/411919/1031/content.aspx`. Visited on January 27th 2012.

[57] Website. Available online at `http://commons.wikimedia.org/wiki/File:Solar_spectrum_ita.svg`. Visited on November 9th 2012.

[58] T. Stübinger and W. Brütting. Exciton diffusion and optical interference in organic donor-acceptor photovoltaic cells. *Journal of Applied Physics*, 90(7):3632–3641, 2001.

[59] N. S. Sariciftci, L. Smilowitz, A. J. Heeger, and F. Wudl. Photoinduced electron-transfer from a conducting polymer to buckminsterfullerene. *Science*, 258(5087):1474–1476, 1992.

[60] B. A. Gregg and M. C. Hanna. Comparing organic to inorganic photovoltaic cells: Theory, experiment, and simulation. *Journal of Applied Physics*, 93(6):3605–3614, 2003.

[61] W. Ruppel and P. Würfel. Upper limit for the conversion of solar-energy. *IEEE Transactions on Electron Devices*, 27(4):877–882, 1980.

[62] J. Knobloch A. Goetzberger, B. Voß. *Sonnenenergie: Photovoltaik*. Teubner Verlag, 2 edition, 1997.

[63] P. Peumans and S. R. Forrest. Very-high-efficiency double-heterostructure copper phthalocyanine/c-60 photovoltaic cells. *Applied Physics Letters*, 79(1):126–128, 2001.

[64] Simon M. Sze. *Physics of Semiconductor Devices*. Wiley-VCH, 3rd edition, 2006.

[65] J. C. Bernede. Organic photovoltaic cells: History, principle and techniques. *Journal of the Chilean Chemical Society*, 53(3):1549–1564, 2008.

[66] R. C. Haddon, L. E. Brus, and K. Raghavachari. Electronic-structure and bonding in icosahedral c-60. *Chemical Physics Letters*, 125(5-6):459–464, 1986.

[67] Website. Available online at `http://www.ch.ic.ac.uk/local/projects/unwin/Fullerenes.html`. Visited on August 17th 2012.

[68] Website. Available online at `http://www.utcc.ac.th/public_content/files/001/P46_1.pdf`. Visited on August 15th 2012.

[69] W. Krätschmer. How we came to produce c60-fullerite. *Zeitschrift Für Physik D - Atoms, Molecules and Clusters*, 19(1-4):405–408, 1991.

[70] B. Gomez-Lor, G. Otero, G. Biddau, C. Sanchez-Sanchez, R. Caillard, M. F. Lopez, C. Rogero, F. J. Palomares, N. Cabello, M. A. Basanta, J. Ortega, J. Mendez, A. M. Echavarren, R. Perez, and J. A. Martin-Gago. Fullerenes from aromatic precursors by surface-catalysed cyclodehydrogenation. *Nature*, 454(7206):865–U19, 2008.

[71] C. M. Lieber and Z. Zhang. Physical properties of metal-doped fullerene superconductors. *Solid State Physics - Advances in Research and Applications, Vol 48*, 48:349–384, 1994.

[72] Website. Available online at `http://www.creative-science.org.uk/propc60.html`. Visited on August 15th 2012.

[73] Q. S. Xie, E. Perezcordero, and L. Echegoyen. Electrochemical detection of c-60(6-) and c-70(6-) - enhanced stability of fullerides in solution. *Journal of the American Chemical Society*, 114(10):3978–3980, 1992.

[74] V. D. Mihailetchi, J. K. J. van Duren, P. W. M. Blom, J. C. Hummelen, R. A. J. Janssen, J. M. Kroon, M. T. Rispens, W. J. H. Verhees, and M. M. Wienk. Electron transport in a methanofullerene. *Advanced Functional Materials*, 13(1):43–46, 2003.

[75] G. D. Sharma, P. Suresh, and John A. Mikroyannidis. Effect of thermal annealing and incorporating tio2 layer on the photovoltaic performance of single- and bi-layer bulk heterojunction devices based on phenylenevinylene copolymer and small molecule. *Organic Electronics*, 11(5):731–742, 2010.

[76] Yeonjin Yi and Seong Jun Kang. Interfacial electronic structures between fullerene and calcium for high performance n-type organic semiconducting devices. *Thin Solid Films*, 519(10):3119–3122, 2011.

[77] Zai-Quan Xu, Jin-Peng Yang, Fu-Zhou Sun, Shuit-Tong Lee, Yan-Qing Li, and Jian-Xin Tang. Efficient inverted polymer solar cells incorporating doped organic electron transporting layer. *Organic Electronics*, 13(4):697–704, 2012.

[78] S. Cook, H. Ohkita, Y. Kim, J. J. Benson-Smith, D. D. C. Bradley, and J. R. Durrant. A photophysical study of pcbm thin films. *Chemical Physics Letters*, 445(4-6):276–280, 2007.

[79] P. Peumans, S. Uchida, and S. R. Forrest. Efficient bulk heterojunction photovoltaic cells using small-molecular-weight organic thin films. *Nature*, 425(6954):158–162, 2003.

[80] B. Maennig, M. Pfeiffer, A. Nollau, X. Zhou, K. Leo, and P. Simon. Controlled p-type doping of polycrystalline and amorphous organic layers: Self-consistent description of conductivity and field-effect mobility by a microscopic percolation model. *Physical Review B*, 64(19):art. no.–195208, 2001.

[81] A. B. P. Lever C. C. Leznoff. *Phthalocyanines—Properties and Applications*, volume 1. Wiley-VCH, Weinheim, 1989.

[82] R. D. Gould. Structure and electrical conduction properties of phthalocyanine thin films. *Coordination Chemistry Reviews*, 156:237–274, 1996.

[83] S. C. Mathur and N. Ramesh. Non-applicability of band-model to beta-hydrogen phthalocyanine. *Chemical Physics Letters*, 37(2):276–278, 1976.

[84] J. Kaufhold and K. Hauffe. Uber das leitfahigkeitsverhalten verschiedener phthalocyanine im vakuum und unter dem einfluss von gasen. *Berichte Der Bunsen-Gesellschaft Fur Physikalische Chemie*, 69(2):168, 1965.

[85] Website. Available online at `http://www2.ocn.ne.jp/~cste/phtalocyanine.html`. Visited on November 10th 2012.

[86] Clifford C. Leznoff. *Phthalocyanines / properties and applications*. VCH, New York, NY ; Weinheim ; Cambridge, 1989.

[87] H. Abramczyk and I. Szymczyk. Aggregation of phthalocyanine derivatives in liquid solutions and human blood. *Journal of Molecular Liquids*, 110(1-3):51–56, 2004.

[88] K. Y. Law. Organic photoconductive materials - recent trends and developments. *Chemical Reviews*, 93(1):449–486, 1993.

[89] A. M. Schaffer, Gouterma.M, and E. R. Davidson. Porphyrins .28. extended huckel calculations on metal phthalocyanines and tetrazaporphins. *Theoretica Chimica Acta*, 30(1):9–30, 1973.

[90] V. P. Singh, S. Rajaputra, and S. Vallurupalli. Copper phthalocyanine based schottky diode solar cells. *Journal of Materials Science-Materials in Electronics*, 18(11):1147–1150, 2007.

[91] H. M. Ding, X. Q. Zhang, M. K. Ram, and C. Nicolini. Ultrathin films of tetrasulfonated copper phthalocyanine-capped titanium dioxide nanoparticles: Fabrication, characterization, and photovoltaic effect. *Journal of Colloid and Interface Science*, 290(1):166–171, 2005.

[92] I. Szymczyk and H. Abramczyk. Peripheral substituent and solvent effects on the aggregation and photochemical properties of copper(ii)phthalocyanine and copper(ii)phthalocyanine-3,4 ',4 ",4 "'-tetrasulfonic anion. *Pure and Applied Chemistry*, 76(1):183–187, 2004.

[93] T. S. Jones, S. Schumann, and R. A. Hatton. Organic photovoltaic: Devices based on water-soluble copper phthalocyanine. *Journal of Physical Chemistry C*, 115(11):4916–4921, 2011.

[94] S. H. Yang, A. S. Ma, J. Lu, and K. M. Ng. Quantitative non-covalent functionalization of carbon nanotubes. *Journal of Cluster Science*, 17(4):599–608, 2006.

[95] S. Rajaputra, G. Sagi, and V. P. Singh. Schottky diode solar cells on electrodeposited copper phthalocyanine films. *Solar Energy Materials and Solar Cells*, 93(1):60–64, 2009.

[96] K. M. Parida, N. Baliarsingh, B. S. Patra, and J. Das. Copperphthalocyanine immobilized zn/al ldh as photocatalyst under solar radiation for decolorization of methylene blue. *Journal of Molecular Catalysis a-Chemical*, 267(1-2):202–208, 2007.

[97] Website. Available online at `http://www.sigmaaldrich.com/catalog/product/aldrich/393886?lang=de&region=DE`. Visited on May 28nd 2012.

[98] Y. Yang, G. Li, V. Shrotriya, J. S. Huang, Y. Yao, T. Moriarty, and K. Emery. High-efficiency solution processable polymer photovoltaic cells by self-organization of polymer blends. *Nature Materials*, 4(11):864–868, 2005.

[99] A. J. Heeger, W. L. Ma, C. Y. Yang, X. Gong, and K. Lee. Thermally stable, efficient polymer solar cells with nanoscale control of the interpenetrating network morphology. *Advanced Functional Materials*, 15(10):1617–1622, 2005.

[100] R. D. Mccullough, R. D. Lowe, M. Jayaraman, and D. L. Anderson. Design, synthesis, and control of conducting polymer architectures - structurally homogeneous poly(3-alkylthiophenes). *Journal of Organic Chemistry*, 58(4):904–912, 1993.

[101] J. M. J. Frechet and B. C. Thompson. Organic photovoltaics - polymer-fullerene composite solar cells. *Angewandte Chemie-International Edition*, 47(1):58–77, 2008.

[102] F. Padinger, R. S. Rittberger, and N. S. Sariciftci. Effects of postproduction treatment on plastic solar cells. *Advanced Functional Materials*, 13(1):85–88, 2003.

[103] Website. Available online at `http://www.creative-science.org.uk/propc60.html`. Visited on August 15th 2012.

[104] A. Watanabe and A. Kasuya. Effect of atmospheres on the open-circuit photovoltage of nanoporous tio2/poly(3-hexylthiophene) heterojunction solar cell. *Thin Solid Films*, 483(1-2):358–366, 2005.

[105] Sanqing Huang, Li Li, Zhibin Yang, Lingli Zhang, Hexige Saiyin, Tao Chen, and Huisheng Peng. A new and general fabrication of an aligned carbon nanotube/polymer film for electrode applications. *Advanced Materials*, 23(40):4707–4710, 2011.

[106] Y. Kojima, S. Kishimoto, M. Okochi, H. Honda, and T. Mizutani. Fabrication of vertically-aligned carbon nanotube electrodes using grid-inserted plasma-enhanced chemical vapor deposition for chemical sensors. *Japanese Journal of Applied Physics*, 47(4):2028–2031, 2008.

[107] Biddut K. Sarker, Muhammad R. Islam, Feras Alzubi, and Saiful I. Khondaker. Fabrication of aligned carbon nanotube array electrodes for organic electronic devices. *Materials Express*, 1(1):80–85, 2011.

[108] Xian-Ming Liu, Zhen dong Huang, Sei woon Oh, Biao Zhang, Peng-Cheng Ma, Matthew M. F. Yuen, and Jang-Kyo Kim. Carbon

nanotube (cnt)-based composites as electrode material for rechargeable li-ion batteries: A review. *Composites Science and Technology*, 72(2):121–144, 2012.

[109] Website. Available online at `http://www.plexon.com/assets/pdf/CarbonNanotubes.pdf`. Visited on May 22nd 2012.

[110] E. Kymakis and G. A. J. Amaratunga. Single-wall carbon nanotube/conjugated polymer photovoltaic devices. *Applied Physics Letters*, 80(1):112–114, 2002.

[111] S. Bhattacharyya, E. Kymakis, and G. A. J. Amaratunga. Photovoltaic properties of dye functionalized single-wall carbon nanotube/conjugated polymer devices. *Chemistry of Materials*, 16(23):4819–4823, 2004. doi: 10.1021/cm0496063.

[112] E. Kymakis, I. Alexandrou, and G. A. J. Amaratunga. High open-circuit voltage photovoltaic devices from carbon-nanotube-polymer composites. *Journal of Applied Physics*, 93(3):1764–1768, 2003.

[113] B. J. Landi, R. P. Raffaelle, S. L. Castro, and S. G. Bailey. Single-wall carbon nanotube-polymer solar cells. *Progress in Photovoltaics*, 13(2):165–172, 2005.

[114] S. Kazaoui, N. Minami, B. Nalini, Y. Kim, and K. Hara. Near-infrared photoconductive and photovoltaic devices using single-wall carbon nanotubes in conductive polymer films. *Journal of Applied Physics*, 98(8):084314, 2005.

[115] Basudev Pradhan, Sudip K. Batabyal, and Amlan J. Pal. Functionalized carbon nanotubes in donor/acceptor-type photovoltaic devices. *Applied Physics Letters*, 88(9):093106, 2006.

[116] C. Li, Y. H. Chen, Y. B. Wang, Z. Iqbal, M. Chhowalla, and S. Mitra. A fullerene-single wall carbon nanotube complex for polymer bulk heterojunction photovoltaic cells. *Journal of Materials Chemistry*, 17(23):2406–2411, 2007.

[117] Taku Hasobe, Shunichi Fukuzumi, and Prashant V. Kamat. Organized assemblies of single wall carbon nanotubes and porphyrin for photochemical solar cells:? charge injection from excited porphyrin into single-walled carbon nanotubes†. *The Journal of Physical Chemistry B*, 110(50):25477–25484, 2006. doi: 10.1021/jp064845u.

[118] D. M. Guldi, G. M. A. Rahman, F. Zerbetto, and M. Prato. Carbon nanotubes in electron donor-acceptor nanocomposites. *Accounts of Chemical Research*, 38(11):871–878, 2005.

[119] D. M. Guldi, G. M. A. Rahman, M. Prato, N. Jux, S. H. Qin, and W. Ford. Single-wall carbon nanotubes as integrative building blocks for solar-energy conversion. *Angewandte Chemie-International Edition*, 44(13):2015–2018, 2005.

[120] Sumit Chaudhary, Haiwei Lu, Astrid M. Müller, Christopher J. Bardeen, and Mihrimah Ozkan. Hierarchical placement and associated optoelectronic impact of carbon nanotubes in polymer-fullerene solar cells. *Nano Letters*, 7(7):1973–1979, 2007. doi: 10.1021/nl070717l.

[121] S. Barazzouk, S. Hotchandani, K. Vinodgopal, and P. V. Kamat. Single-wall carbon nanotube films for photocurrent generation. a prompt response to visible-light irradiation. *Journal of Physical Chemistry B*, 108(44):17015–17018, 2004.

[122] Sebastiano Cataldo, Patrizio Salice, Enzo Menna, and Bruno Pignataro. Carbon nanotubes and organic solar cells. *Energy and Environmental Science*, 5(3):5919–5940, 2012.

[123] Sungjun Lee, Hajin Kim, Jhinhwan Lee, Young Kuk, Kwang Hwa Chung, Howon Kim, and Se-Jong Kahng. Donor and acceptor-like electronic states in a one-dimensional semiconductor. *Surface Science*, 600(22):4937–4940, 2006.

[124] S. Iijima. Helical microtubules of graphitic carbon. *Nature*, 354(6348):56–58, 1991.

[125] Website. Available online at `http://nanotube.korea.ac.kr/english/?page_id=49`. Visited on July 13th 2012.

[126] Website. Available online at `http://www.mecheng.osu.edu/netl/tem-single-wall-carbon-nanotube-array-image-1`. Visited on August 27th 2012.

[127] Y. J. Dappe, R. Oszwaldowski, P. Pou, J. Ortega, R. Perez, and F. Flores. Local-orbital occupancy formulation of density functional theory: Application to si, c, and graphene. *Physical Review B*, 73(23), 2006.

[128] R. Saito, M. Fujita, G. Dresselhaus, and M. S. Dresselhaus. Electronic-structure of chiral graphene tubules. *Applied Physics Letters*, 60(18):2204–2206, 1992.

[129] C. M. Lieber, M. Ouyang, J. L. Huang, and C. L. Cheung. Energy gaps in "metallic" single-walled carbon nanotubes. *Science*, 292(5517):702–705, 2001.

[130] P. Kim, T. W. Odom, J. L. Huang, and C. M. Lieber. Electronic density of states of atomically resolved single-walled carbon nanotubes: Van hove singularities and end states. *Physical Review Letters*, 82(6):1225–1228, 1999.

[131] W. A. de Heer, P. Poncharal, C. Berger, Y. Yi, and Z. L. Wang. Room temperature ballistic conduction in carbon nanotubes. *Journal of Physical Chemistry B*, 106(47):12104–12118, 2002.

[132] S. Frank, P. Poncharal, Z. L. Wang, and W. A. de Heer. Carbon nanotube quantum resistors. *Science*, 280(5370):1744–1746, 1998.

[133] Yuan Cheng and Otto Zhou. Electron field emission from carbon nanotubes. *Comptes Rendus Physique*, 4(9):1021–1033, 2003.

[134] R. B. Weisman, S. M. Bachilo, M. S. Strano, C. Kittrell, R. H. Hauge, and R. E. Smalley. Structure-assigned optical spectra of single-walled carbon nanotubes. *Science*, 298(5602):2361–2366, 2002.

[135] A. Jorio, A. P. Santos, H. B. Ribeiro, C. Fantini, M. Souza, J. P. M. Vieira, C. A. Furtado, J. Jiang, R. Saito, L. Balzano, D. E. Resasco, and M. A. Pimenta. Quantifying carbon-nanotube species with resonance raman scattering. *Physical Review B*, 72(7), 2005.

[136] Website. Available online at `http://ipn2.epfl.ch/CHBU/NTproduction1.htm`. Visited on November 11th 2012.

[137] Website. Available online at `http://www.teltec.biz/teltec_new/images/stories/pecvd.bmp`. Visited on November 11th 2012.

[138] Yosuke Kanai and Jeffrey C. Grossman. Role of semiconducting and metallic tubes in p3ht/carbon-nanotube photovoltaic heterojunctions: Density functional theory calculations. *Nano Letters*, 8(3):908–912, 2008.

[139] M. Ozkan, S. Chaudhary, H. W. Lu, A. M. Muller, and C. J. Bardeen. Hierarchical placement and associated optoelectronic impact of carbon nanotubes in polymer-fullerene solar cells. *Nano Letters*, 7(7):1973–1979, 2007.

[140] L. Q. Ren, S. R. Wang, M. Holtz, and J. J. Qiu. The synergistic effect of nanocrystal integration and process optimization on solar cell efficiency. *Nanotechnology*, 23(7), 2012.

[141] N. S. Sariciftci S. Sun. *Organic Photovoltaics: Mechanisms, Materials and Devices*. CRC Press, 2005.

[142] Sam-Shajing Sun N. S. Sariciftci, editor. *Organic Photovoltaics: Mechanisms, Materials, and Devices*. CRC Press, 2005.

[143] G. Lackner, T. Mayer-Uhma, I. Endler, R. Boucher, F. Meißner, S. Scholz, M. Krug, V. Bezugly, M. Mkandawire, A. Majumder, D.A. Kovalenko, S. Conze, S. Hildebrandt, A. Michaelis, and D.C. Lupascu. Dyes in carbon nanotube arrays. *Journal of Materials Science and Engineering. B*, 2(6):334–346, 2012.

[144] O. Groning, O. M. Kuttel, C. Emmenegger, P. Groning, and L. Schlapbach. Field emission properties of carbon nanotubes. *Journal of Vacuum Science and Technology B*, 18(2):665–678, 2000.

[145] Alper Buldum and Jian Ping Lu. Electron field emission properties of closed carbon nanotubes. *Physical Review Letters*, 91(23):236801, 2003.

[146] J. C. Nolasco, R. Cabre, J. Ferre-Borrull, L. F. Marsal, M. Estrada, and J. Pallares. Extraction of poly (3-hexylthiophene) (p3ht) properties from dark current voltage characteristics in a p3ht/n-crystalline-silicon solar cell. *Journal of Applied Physics*, 107(4):044505, 2010.

[147] J. L. Brédas W. R. Salaneck, S. Stafstrom. *Conjugated Polymer Surfaces and Interfaces*. Cambridge University Press, 1996.

[148] J. Frisch, M. Schubert, E. Preis, J. P. Rabe, D. Neher, U. Scherf, and N. Koch. Full electronic structure across a polymer heterojunction solar cell. *Journal of Materials Chemistry*, 22(10):4418–4424, 2012.

[149] P. G. de Gennes. Wetting: statics and dynamics. *Reviews of Modern Physics*, 57(3):827–863, 1985. RMP.

[150] Website. Available online at `http://de.wikipedia.org/wiki/Kontaktwinkel`. Visited on November 21st 2012.

[151] K. X. Ma, C. H. Ho, F. R. Zhu, and T. S. Chung. Investigation of surface energy for organic light emitting polymers and indium tin oxide. *Thin Solid Films*, 371(1-2):140–147, 2000.

[152] F. M. Fowkes. Determination of interfacial tensions, contact angles, and dispersion forces in surfaces by assuming additivity of intermolecular interactions in surfaces. *The Journal of Physical Chemistry*, 66(2):382–382, 1962. doi: 10.1021/j100808a524.

[153] Website. Available online at `http://home.wanadoo.nl/tom.peeters/Subpaginas/spin%20coating_parameters.htm#Parameters_of_the_spincoat_process`. Visited on March 21st 2012.

[154] Website. Available online at `http://large.stanford.edu/courses/2007/ph210/hellstrom1/`. Visited on March 21st 2012.

[155] Alfred G. Emslie, Francis T. Bonner, and Leslie G. Peck. Flow of a viscous liquid on a rotating disk. *Journal of Applied Physics*, 29(5):858–862, 1958.

[156] Dietrich Meyerhofer. Characteristics of resist films produced by spinning. *Journal of Applied Physics*, 49(7):3993–3997, 1978.

[157] W G Cochran and S Goldstein. The flow due to a rotating disc. *Mathematical Proceedings of the Cambridge Philosophical Society*, 30(03):365, 1934.

[158] D. E. Bornside, C. W. Macosko, and L. E. Scriven. Spin coating of a pmma/chlorobenzene solution. *Journal of The Electrochemical Society*, 138(1):317–320, 1991.

[159] J. P. Chong F. Kreith, J. H. Taylor. Heat and mass transfer from a rotating disk. *Journal of Heat Transfer*, 81:95, 1959.

[160] J. L. Gregg E. M. Sparrow. Heat transfer from a rotating disk to fluids of any prandtl number. *Journal of Heat Transfer*, 81:249, 1959.

[161] E. M. Sparrow and J. L. Gregg. Mass transfer, flow, and heat transfer about a rotating disk. *Journal of Heat Transfer*, 82(4):294–302, 1960.

[162] K. Denbeigh. *The principles of chemical equilibrium*. Cambridge, U.K.: Cambridge University Press, 4 edition, 1997.

[163] Website. Available online at `http://www.smtchn.com/html_news/Spin-Coating-Process-Troubleshooting-13.html`. Visited on November 21st 2012.

[164] J B Theeten and D E Aspnes. Ellipsometry in thin film analysis. *Annual Review of Materials Science*, 11(1):97–122, 1981.

[165] Website. Available online at `http://www.horiba.com/fileadmin/uploads/Scientific/Documents/TFilm/AR_SE02.pdf`. Visited on February 3rd 2012.

[166] C. J. Huang, Y. K. Su, and S. L. Wu. The effect of solvent on the etching of ito electrode. *Materials Chemistry and Physics*, 84(1):146–150, 2004.

[167] Website. Available online at `http://www.heraeus-clevios.com/en/technology/substrate-conditioning.aspx`. Visited on November 21st 2012.

[168] N. S. Sariciftci and H. Hoppe. Organic solar cells: An overview. *Journal of Materials Research*, 19(7):1924–1945, 2004.

[169] A. Kahn, I. G. Hill, Z. G. Soos, and R. A. Pascal. Charge-separation energy in films of pi-conjugated organic molecules. *Chemical Physics Letters*, 327(3-4):181–188, 2000.

[170] P. Peumans, A. Liu, S. Zhao, S. B. Rim, J. Wu, M. Konemann, and P. Erk. Control of electric field strength and orientation at the donor-acceptor interface in organic solar cells. *Advanced Materials*, 20(5):1065–+, 2008.

[171] C. Hein, E. Mankel, T. Mayer, and W. Jaegermann. Engineering the electronic structure of the cupc/bpe-ptcdi interface by wo(3) doping of cupc. *Physica Status Solidi a-Applications and Materials Science*, 206(12):2757–2762, 2009.

[172] A. Wagenpfahl, D. Rauh, M. Binder, C. Deibel, and V. Dyakonov. S-shaped current-voltage characteristics of organic solar devices. *Physical Review B*, 82(11), 2010.

[173] J. Schafferhans, A. Baumann, A. Wagenpfahl, C. Deibel, and V. Dyakonov. Oxygen doping of p3ht:pcbm blends: Influence on trap states, charge carrier mobility and solar cell performance. *Organic Electronics*, 11(10):1693–1700, 2010.

[174] J. Wagner, M. Gruber, A. Wilke, Y. Tanaka, K. Topczak, A. Steindamm, U. Hormann, A. Opitz, Y. Nakayama, H. Ishii, J. Pflaum, N. Koch, and W. Brütting. Identification of different origins for s-shaped current voltage characteristics in planar heterojunction organic solar cells. *Journal of Applied Physics*, 111(5), 2012.

[175] W. Tress, K. Leo, and M. Riede. Influence of hole-transport layers and donor materials on open-circuit voltage and shape of i-v curves of organic solar cells. *Advanced Functional Materials*, 21(11):2140–2149, 2011.

[176] W. Tress, A. Petrich, M. Hummert, M. Hein, K. Leo, and M. Riede. Imbalanced mobilities causing s-shaped iv curves in planar heterojunction organic solar cells. *Applied Physics Letters*, 98(6), 2011.

[177] Z. Ouennoughi and M. Chegaar. A simpler method for extracting solar cell parameters using the conductance method. *Solid-State Electronics*, 43(11):1985–1988, 1999.

[178] K. Bouzidi, M. Chegaar, and A. Bouhemadou. Solar cells parameters evaluation considering the series and shunt resistance. *Solar Energy Materials and Solar Cells*, 91(18):1647–1651, 2007.

[179] Y. F. Chen, X. M. Wang, D. Li, R. J. Hong, and H. Shen. Parameters extraction from commercial solar cells i-v characteristics and shunt analysis. *Applied Energy*, 88(6):2239–2244, 2011.

[180] A. Jain and A. Kapoor. Exact analytical solutions of the parameters of real solar cells using lambert w-function. *Solar Energy Materials and Solar Cells*, 81(2):269–277, 2004.

[181] Jl Ding. *Principle study and technique application of explicit solution for solar cell I-V equation*. Dissertation, University of Science and Technology of China, 2007.

[182] W. Shockley. The theory of p–n junction in semiconductors and p–n junction transistors. *Bell System Technical Journal*, 28:435–489, 1949.

[183] Shockley W Shah CT, Noyce RN. Carrier generation and recombination in p–n junctions and p–n junction characteristics. *Proceeding in IRE*, 45:1228–43, 1957.

[184] M.J. Buckingham E.A. Faulkner. Modified theory of the current/voltage relation in silicon p–n junction. *Electron Lett*, 4:259–260, 1968.

[185] E. Sanchez G.L. Araujo. Analytical expression for the determination of the maximun power point and the fill factor of a solar cell. *Solar Cells*, 5:377–386, 1982.

[186] H.J. Queisser W. Shockley. Detailed balance limit of efficiency of p–n junction solar cells. *32*, Journal of Applied Physics:510–519, 1961.

[187] Stirn RJ. Junction characteristics of si solar cells. *9th IEEE PVSC*, page 77–82, 1972.

[188] J.L. Gray. *The physics of the solar cell*. Handbook of Photovoltaic Science and Engineering. John Wiley and Sons, Ltd, 2003.

[189] P. G. Karagiannidis, D. Georgiou, C. Pitsalidis, A. Laskarakis, and S. Logothetidis. Evolution of vertical phase separation in p3ht:pcbm thin films induced by thermal annealing. *Materials Chemistry and Physics*, 129(3):1207–1213, 2011.

[190] Mirko Vogel. *Grenzflächen in Phthalocyanin-C60-Solarzellen*. Dissertation, Freie Universität Berlin, 2005.

[191] R. O. Loutfy, J. H. Sharp, C. K. Hsiao, and R. Ho. Phthalocyanine organic solar-cells - indium-x-metal free phthalocyanine schottky barriers. *Journal of Applied Physics*, 52(8):5218–5230, 1981.

[192] P. X. Hou, C. Liu, and H. M. Cheng. Purification of carbon nanotubes. *Carbon*, 46(15):2003–2025, 2008.

[193] P. Chaturvedi, P. Verma, A. Singh, P. K. Chaudhary, Harsh, and P. K. Basu. Carbon nanotube - purification and sorting protocols. *Defence Science Journal*, 58(5):591–599, 2008.

[194] Wencai Ren, Feng Li, Jian Chen, Shuo Bai, and Hui-Ming Cheng. Morphology, diameter distribution and raman scattering measurements of double-walled carbon nanotubes synthesized by catalytic decomposition of methane. *Chemical Physics Letters*, 359(3–4):196–202, 2002.

[195] H. T. Fang, C. G. Liu, L. Chang, L. Feng, L. Min, and H. M. Cheng. Purification of single-wall carbon nanotubes by electrochemical oxidation. *Chemistry of Materials*, 16(26):5744–5750, 2004.

[196] S. K. Pillai, S. S. Ray, and M. Moodley. Purification of single-walled carbon nanotubes. *Journal of Nanoscience and Nanotechnology*, 7(9):3011–3047, 2007.

[197] M. S. Dresselhaus, G. Dresselhaus, A. Jorio, A. G. Souza, and R. Saito. Raman spectroscopy on isolated single wall carbon nanotubes. *Carbon*, 40(12):2043–2061, 2002.

[198] M. E. Itkis, D. E. Perea, R. Jung, S. Niyogi, and R. C. Haddon. Comparison of analytical techniques for purity evaluation of single-walled carbon nanotubes. *Journal of the American Chemical Society*, 127(10):3439–3448, 2005.

[199] S. H. Jeong, K. K. Kim, S. J. Jeong, K. H. An, S. H. Lee, and Y. H. Lee. Optical absorption spectroscopy for determining carbon nanotube concentration in solution. *Synthetic Metals*, 157(13-15):570–574, 2007.

[200] M. Zheng and E. D. Semke. Enrichment of single chirality carbon nanotubes. *Journal of the American Chemical Society*, 129(19):6084–+, 2007.

[201] Xiaozhou Liao, Adriana Serquis, Quanxi Jia, Dean E. Peterson, Yuntian T. Zhu, and Huifang Xu. Relationship between catalyst composition and carbon morphology. *Microscopy and Microanalysis*, 9(SupplementS02):328–329, 2003.

[202] C. J. Lee, J. Park, and J. A. Yu. Catalyst effect on carbon nanotubes synthesized by thermal chemical vapor deposition. *Chemical Physics Letters*, 360(3-4):250–255, 2002.

[203] D. T. Colbert, J. Zhang, S. M. McClure, P. Nikolaev, Z. Chen, J. H. Hafner, D. W. Owens, P. G. Kotula, C. B. Carter, J. H. Weaver,

A. G. Rinzler, and R. E. Smalley. Growth and sintering of fullerene nanotubes. *Science*, 266(5188):1218–1222, 1994.

[204] H. Hu, B. Zhao, M. E. Itkis, and R. C. Haddon. Nitric acid purification of single-walled carbon nanotubes. *Journal of Physical Chemistry B*, 107(50):13838–13842, 2003.

[205] X. L. Zhao, M. Ohkohchi, S. Inoue, T. Suzuki, T. Kadoya, and Y. Ando. Large-scale purification of single-wall carbon nanotubes prepared by electric arc discharge. *Diamond and Related Materials*, 15(4-8):1098–1102, 2006.

[206] Y. Li, X. B. Zhang, J. H. Luo, W. Z. Huang, J. P. Cheng, Z. Q. Luo, T. Li, F. Liu, G. L. Xu, X. X. Ke, L. Li, and H. J. Geise. Purification of cvd synthesized single-wall carbon nanotubes by different acid oxidation treatments. *Nanotechnology*, 15(11):1645–1649, 2004.

[207] J. Liu, A. G. Rinzler, H. J. Dai, J. H. Hafner, R. K. Bradley, P. J. Boul, A. Lu, T. Iverson, K. Shelimov, C. B. Huffman, F. Rodriguez-Macias, Y. S. Shon, T. R. Lee, D. T. Colbert, and R. E. Smalley. Fullerene pipes. *Science*, 280(5367):1253–1256, 1998.

[208] I. W. Chiang, B. E. Brinson, R. E. Smalley, J. L. Margrave, and R. H. Hauge. Purification and characterization of single-wall carbon nanotubes. *Journal of Physical Chemistry B*, 105(6):1157–1161, 2001.

[209] R. Sen, S. M. Rickard, M. E. Itkis, and R. C. Haddon. Controlled purification of single-walled carbon nanotube films by use of selective oxidation and near-ir spectroscopy. *Chemistry of Materials*, 15(22):4273–4279, 2003.

[210] K. Denbeigh. *Kirk-Othmer Encyclopedia of Chemical Technology*, volume 26. J. Wiley and Sons: New York, 4 edition, 1998.

[211] J. H. Hafner, C. L. Cheung, T. H. Oosterkamp, and C. M. Lieber. High-yield assembly of individual single-walled carbon nanotube tips for scanning probe microscopies. *Journal of Physical Chemistry B*, 105(4):743–746, 2001.

[212] B. Gao, G. Z. Yue, Q. Qiu, Y. Cheng, H. Shimoda, L. Fleming, and O. Zhou. Fabrication and electron field emission properties of carbon nanotube films by electrophoretic deposition. *Advanced Materials*, 13(23):1770–1773, 2001.

[213] C. N. R. Rao, B. C. Satishkumar, A. Govindaraj, and M. Nath. Nanotubes. *Chemphyschem*, 2(2):78–105, 2001.

[214] A. G. Osorio, I. C. L. Silveira, V. L. Bueno, and C. P. Bergmann. H2so4/hno3/hcl-functionalization and its effect on dispersion of carbon nanotubes in aqueous media. *Applied Surface Science*, 255(5):2485–2489, 2008.

[215] G. X. Chen and H. Shimizu. Multiwalled carbon nanotubes grafted with polyhedral oligomeric silsesquioxane and its dispersion in poly(l-lactide) matrix. *Polymer*, 49(4):943–951, 2008.

[216] Alberto Bianco, Kostas Kostarelos, and Maurizio Prato. Applications of carbon nanotubes in drug delivery. *Current Opinion in Chemical Biology*, 9(6):674–679, 2005.

[217] Y. Li, Y. F. Chen, Y. Y. Feng, S. L. Zhao, P. Lu, X. Y. Yuan, and W. Feng. Progress of synthesizing methods and properties of fluorinated carbon nanotubes. *Science China-Technological Sciences*, 53(5):1225–1233, 2010.

[218] L. M. Yu, J. J. Zhao, J. S. Qiu, C. Hao, and H. Wang. Sidewall fluorination and hydrogenation of single-walled carbon nanotubes: a density functional theory study. *Frontiers of Physics in China*, 4(3):393–397, 2009.

[219] O. Lourie, D. M. Cox, and H. D. Wagner. Buckling and collapse of embedded carbon nanotubes. *Physical Review Letters*, 81(8):1638–1641, 1998.

[220] A. Thess, R. Lee, P. Nikolaev, H. J. Dai, P. Petit, J. Robert, C. H. Xu, Y. H. Lee, S. G. Kim, A. G. Rinzler, D. T. Colbert, G. E. Scuseria, D. Tomanek, J. E. Fischer, and R. E. Smalley. Crystalline ropes of metallic carbon nanotubes. *Science*, 273(5274):483–487, 1996.

[221] Website. Available online at `http://old.iupac.org/reports/2001/colloid_2001/manual_of_s_and_t/node33.html`. Visited on May 3rd 2012.

[222] Micah J. Green. Analysis and measurement of carbon nanotube dispersions: nanodispersion versus macrodispersion. *Polymer International*, 59(10):1319–1322, 2010.

[223] J. H. Walther, T. Werder, R. L. Jaffe, and P. Koumoutsakos. Hydrodynamic properties of carbon nanotubes. *Physical Review E*, 69(6), 2004.

[224] H. Liu, J. Zhai, and L. Jiang. Wetting and anti-wetting on aligned carbon nanotube films. *Soft Matter*, 2(10):811–821, 2006.

[225] L. Vaisman, H. D. Wagner, and G. Marom. The role of surfactants in dispersion of carbon nanotubes. *Advances in Colloid and Interface Science*, 128:37–46, 2006.

[226] Sang Won Kim, Taehoon Kim, Yern Seung Kim, Hong Soo Choi, Hyeong Jun Lim, Seung Jae Yang, and Chong Rae Park. Surface modifications for the effective dispersion of carbon nanotubes in solvents and polymers. *Carbon*, 50(1):3–33, 2012.

[227] A. H. Barber, S. R. Cohen, and H. D. Wagner. External and internal wetting of carbon nanotubes with organic liquids. *Physical Review B*, 71(11), 2005.

[228] A. H. Barber, S. R. Cohen, and H. D. Wagner. Static and dynamic wetting measurements of single carbon nanotubes. *Physical Review Letters*, 92(18), 2004.

[229] G. M. Wu, J. M. Schultz, D. J. Hodge, and F. N. Cogswell. Effects of treatment on the surface-composition and energy of carbon-fibers. *Polymer Composites*, 16(4):284–287, 1995.

[230] A. W. Adamson. *Physical Chemistry of Surfaces*. Whiley-VCH, New York, 5 edition, 1990. p. 397.

[231] D. K. Owens and R. C. Wendt. Estimation of surface free energy of polymers. *Journal of Applied Polymer Science*, 13(8):1741–ff, 1969.

[232] H. T. Ham, Y. S. Choi, and I. J. Chung. An explanation of dispersion states of single-walled carbon nanotubes in solvents and aqueous surfactant solutions using solubility parameters. *Journal of Colloid and Interface Science*, 286(1):216–223, 2005.

[233] K. D. Ausman, R. Piner, O. Lourie, R. S. Ruoff, and M. Korobov. Organic solvent dispersions of single-walled carbon nanotubes: Toward solutions of pristine nanotubes. *Journal of Physical Chemistry B*, 104(38):8911–8915, 2000.

[234] O. Matarredona, H. Rhoads, Z. R. Li, J. H. Harwell, L. Balzano, and D. E. Resasco. Dispersion of single-walled carbon nanotubes in aqueous solutions of the anionic surfactant naddbs. *Journal of Physical Chemistry B*, 107(48):13357–13367, 2003.

[235] Website. Available online at `http://www.sigmaaldrich.com/catalog/product/sigma/t0875?lang=de&region=DE`. Visited on October 14th 2012.

[236] Richa Rastogi, Rahul Kaushal, S. K. Tripathi, Amit L. Sharma, Inderpreet Kaur, and Lalit M. Bharadwaj. Comparative study of carbon

nanotube dispersion using surfactants. *Journal of Colloid and Interface Science*, 328(2):421–428, 2008.

[237] A. Ikeda, T. Hamano, K. Hayashi, and J. Kikuchi. Water-solubilization of nucleotides-coated single-walled carbon nanotubes using a high-speed vibration milling technique. *Organic Letters*, 8(6):1153–1156, 2006.

[238] Weijie Huang, Shelby Taylor, Kefu Fu, Yi Lin, Donghui Zhang, Timothy W. Hanks, Apparao M. Rao, and Ya-Ping Sun. Attaching proteins to carbon nanotubes via diimide-activated amidation. *Nano Letters*, 2(4):311–314, 2002.

[239] Jeffrey L. Bahr, Edward T. Mickelson, Michael J. Bronikowski, Richard E. Smalley, and James M. Tour. Dissolution of small diameter single-wall carbon nanotubes in organic solvents? *Chemical Communications*, 0(2):193–194, 2001.

[240] Website. Available online at `http://en.wikipedia.org/wiki/Beer-Lambert_law`. Visited on October 15th 2012.

[241] Michael W. Rowell, Mark A. Topinka, Michael D. McGehee, Hans-Jurgen Prall, Gilles Dennler, Niyazi Serdar Sariciftci, Liangbing Hu, and George Gruner. Organic solar cells with carbon nanotube network electrodes. *Applied Physics Letters*, 88(23):233506, 2006.

[242] N. Grossiord, J. M. Kroon, R. Andriessen, and P. W. M. Blom. Degradation mechanisms in organic photovoltaic devices. *Organic Electronics*, 13(3):432–456, 2012.

[243] Y. Li, Y. F. Chen, Y. Y. Feng, S. L. Zhao, P. Lu, X. Y. Yuan, and W. Feng. Progress of synthesizing methods and properties of fluorinated carbon nanotubes. *Science China-Technological Sciences*, 53(5):1225–1233, 2010.

[244] G. Lackner, I. Endler, F. Meissner, S. Scholz, T. Mayer-Uhma, R. Liebschner, V. Bezugly, J. Meiss, M. Mkandawire, R. Boucher, A. Michaelis, and Doru C. Lupascu. Dyes in vertically aligned carbon nanotube arrays for solar cell applications. *MRS Symposium Proceedings*, 389:MRSF11–1390–H03–47.R1, 2011.

[245] A. F. Ismail, P. S. Goh, J. C. Tee, S. M. Sanip, and M. Aziz. A review of purification techniques for carbon nanotubes. *Nano*, 3(3):127–143, 2008.

[246] D. Bonifazi, R. Marega, G. Accorsi, M. Meneghetti, A. Parisini, and M. Prato. Cap removal and shortening of double-walled and very-

thin multi-walled carbon nanotubes under mild oxidative conditions. *Carbon*, 47(3):675–682, 2009.

[247] O. Zhou, H. Shimoda, B. Gao, S. J. Oh, L. Fleming, and G. Z. Yue. Materials science of carbon nanotubes: Fabrication, integration, and properties of macroscopic structures of carbon nanotubes. *Accounts of Chemical Research*, 35(12):1045–1053, 2002.

[248] X. R. Ye, L. H. Chen, C. Wang, J. F. Aubuchon, I. C. Chen, A. I. Gapin, J. B. Talbot, and S. Jin. Electrochemical modification of vertically aligned carbon nanotube arrays. *Journal of Physical Chemistry B*, 110(26):12938–12942, 2006.

[249] M. A. Tamor and W. C. Vassell. Raman fingerprinting of amorphous-carbon films. *Journal of Applied Physics*, 76(6):3823–3830, 1994.

[250] Igor Chourpa, Laurence Douziech-Eyrolles, Lazare Ngaboni-Okassa, Jean-Francois Fouquenet, Simone Cohen-Jonathan, Martin Souce, Herve Marchais, and Pierre Dubois. Molecular composition of iron oxide nanoparticles, precursors for magnetic drug targeting, as characterized by confocal raman microspectroscopy. *Analyst*, 130(10):1395–1403, 2005.

[251] A. C. Ferrari and J. Robertson. Interpretation of raman spectra of disordered and amorphous carbon. *Physical Review B*, 61(20):14095–14107, 2000.

[252] C. T. Wirth, S. Hofmann, and J. Robertson. Surface properties of vertically aligned carbon nanotube arrays. *Diamond and Related Materials*, 17(7-10):1518–1524, 2008.

[253] R. N. Wenzel. Resistance of solid surfaces to wetting by water. *Industrial and Engineering Chemistry*, 28:988–994, 1936.

[254] A. B. D. Cassie and S. Baxter. Wettability of porous surfaces. *Transactions of the Faraday Society*, 40:0546–0550, 1944.

[255] D. Quere. Rough ideas on wetting. *Physica a-Statistical Mechanics and Its Applications*, 313(1-2):32–46, 2002. 10th International Summer School on Fundamental Problems in Statistical Physics AUG 20-SEP 02, 2001 ALTENBERG, GERMANY.

[256] T. S. Chow. Wetting of rough surfaces. *Journal of Physics-Condensed Matter*, 10(27):L445–L451, 1998.

[257] E. W. Washburn. The dynamics of capillary flow. *Physical Review*, 17(3):273–283, 1921.

[258] Y. Q. Xue and S. Datta. Fermi-level alignment at metal-carbon nanotube interfaces: Application to scanning tunneling spectroscopy. *Physical Review Letters*, 83(23):4844–4847, 1999.

[259] M. Shiraishi and M. Ata. Work function of carbon nanotubes. *Carbon*, 39(12):1913–1917, 2001.

[260] S. Kazaoui, N. Minami, N. Matsuda, H. Kataura, and Y. Achiba. Electrochemical tuning of electronic states in single-wall carbon nanotubes studied by in situ absorption spectroscopy and ac resistance. *Applied Physics Letters*, 78(22):3433–3435, 2001.

[261] H. Y. Si, C. H. Liu, H. Xu, T. M. Wang, and H. L. Zhang. Shell-controlled photoluminescence in cdse/cnt nanohybrids. *Nanoscale Research Letters*, 4(10):1146–1152, 2009.

[262] T. Komino, M. Matsuda, and H. Tajima. The fabrication method of unsubstituted planar phthalocyanine thin films by a spin-coating technique. *Thin Solid Films*, 518(2):688–691, 2009.

[263] Huanli Dong, Lang Jiang, and Wenping Hu. Interface engineering for high-performance organic field-effect transistors. *Physical Chemistry Chemical Physics*, 14(41):14165–14180, 2012.

[264] Y. P. Sun, K. F. Fu, Y. Lin, and W. J. Huang. Functionalized carbon nanotubes: Properties and applications. *Accounts of Chemical Research*, 35(12):1096–1104, 2002.

[265] D. Pantarotto, C. D. Partidos, R. Graff, J. Hoebeke, J. P. Briand, M. Prato, and A. Bianco. Synthesis, structural characterization, and immunological properties of carbon nanotubes functionalized with peptides. *Journal of the American Chemical Society*, 125(20):6160–6164, 2003.

[266] Deng Fei, Rujisamphan Noporn, Liu Chang, Stephen C. Hawkins, S.I. Sha, and Ni Chaoying. Light-induced polymer coatings on the surface of carbon nanotube forest and yarn. *MRS Fall Meeting and Exhibit*, Poster, 2012.

[267] Rosa Olivé-Monllau, Ana Pereira, Jordi Bartrolí, Mireia Baeza, and Francisco Céspedes. Highly sensitive cnt composite amperometric sensors integrated in an automated flow system for the determination of free chlorine in waters. *Talanta*, 81(4–5):1593–1598, 2010.

[268] Rosa Olivé-Monllau, Cynthia S. Martínez-Cisneros, Jordi Bartrolí, Mireia Baeza, and Francisco Céspedes. Integration of a sensitive carbon nanotube composite electrode in a ceramic microanalyzer for the

amperometric determination of free chlorine. *Sensors and Actuators B: Chemical*, 151(2):416–422, 2011.

LIST OF FIGURES

LIST OF TABLES